Ph. D. Thesis

A Search for the Decay $\mu^+ \to e^+\gamma$ Using a High-Resolution Liquid Xenon Gamma-Ray Detector

Yasuhiro NISHIMURA

Department of Physics, School of Science,
the University of Tokyo

December 2010

Abstract

Recent observations of neutrino oscillation indicated a lepton flavor mixing in neutrino sector, whereas charged lepton flavor violation has not been observed so far in past experiments. A rare decay with charged lepton flavor mixing, $\mu \to e\gamma$, is sensitive to new physics beyond the standard model. Many new physics models, which explain the hierarchy problem naturally, predict $\mu \to e\gamma$ in achievable branching-ratio region with a measurement.

The MEG experiment searches for $\mu^+ \to e^+\gamma$ at Paul Sherrer Institut (PSI) in Switzerland. Innovative detector technology was developed for the experiment, such as a liquid xenon gamma-ray detector, a positron spectrometer with a special gradient magnetic field for a high-rate positron measurement and a fast waveform sampler chip. In 2008 the first physics data was taken for three months. After upgrade for the detector, the data was taken for two months in year 2009.

The liquid xenon detector plays the most important role to suppress background events and showed excellent resolutions with a proper calibration. The light yield of liquid xenon greatly improved by a purification and was stable over the physics run in 2009. During the physics run in 2009, the detector was monitored with various calibration sources and operated stably.

The sensitivity of upper limit on the branching ratio at 90% confidence level (C.L.) is estimated in 2009 data to be

$$S_{2009} = 6.1 \times 10^{-12}.$$

On the 2009 data, a likelihood analysis was performed to set the upper limit on the branching ratio,

$$\mathrm{Br}(\mu^+ \to e^+\gamma) < 1.5 \times 10^{-11} \text{ at } 90\% \text{ C.L.}$$

The MEG experiment is currently running toward a 10^{-13} branching-ratio region for a next few years.

Contents

Introduction

Lepton is known to have three generations of particles. Charged leptons are classified as electron, muon and tauon with different masses, and corresponding electron-, muon- and tau-neutrino are known in neutrino sector. Quark also has three generations of particles and these is a mixing between generations. For a long time there had been no observation of lepton mixing, thus the lepton flavor number had been regarded as preserved. However, in neutrino sector, a mixing of lepton flavor was implied from atmospheric neutrino oscillation in 1998 at Super-Kamiokande, Japan [1]. There is still no observation of lepton-flavor mixing in charged lepton sector so far.

The Standard Model (SM) in particle physics can describe phenomena of particles well but a new physics beyond the SM is desired to overcome artificial features of the SM. Some new physics predict charged-lepton-flavor violation (cLFV) around an observable level.

The rare muon decay, $\mu^+ \to e^+\gamma$, is sensitive to new models of the SM extension around the current upper limit of branching ratio $\mathrm{Br}(\mu^+ \to e^+\gamma) < 1.2 \times 10^{-11}$ (90% C.L.) given by MEGA experiment in 1999 [2]. The MEG experiment aims to search for $\mu^+ \to e^+\gamma$ at a sensitivity better than the current limit by two orders of magnitude [3]. We started physics data taking in 2008 and reported the first physics result with three-month data, $\mathrm{Br}(\mu^+ \to e^+\gamma) < 2.8 \times 10^{-11}$ (90% C.L.) [4]. There were some updates of hardware before the 2009 run started, then the data was taken for two months in 2009. This thesis will describe the results from the run in year 2009.

Chapter I introduces the physics motivation of the MEG experiment. Then the detail of the MEG experiment and the MEG detectors are described in Chapter II. The calibration and the performance of the liquid xenon gamma-ray detector are described in Chapter III. The performance of the other detectors are shown in Chapter IV. In Chapter V the analysis and the result of $\mu^+ \to e^+\gamma$ search using 2009 data are shown.

Part I
Lepton Flavor

1 Lepton Flavor Physics and $\mu \to e\gamma$

1.1 Introduction

The behavior of fermions and gauge bosons are well described in the Standard Model (SM). A lot of evidence supports the SM, but it was mainly confirmed under TeV-scale energy and the hierarchy problem remains. The hierarchy implies that a fine tuning with cut-off energy or some extensions of the theory are needed. In addition, many parameters such as masses, mixing angles and the number of generation in the SM are determined by experimental observations without predictions from the SM. Therefore people tend to consider that the SM is localized up to GeV scale and is an approximation of a global theory.

Many extended models from the SM are proposed, such as supersymmetry or extra dimensions. One way to verify these models is a higher energy collisions of particles. In the near future the Large Hadron Collider (LHC) will operate at a collision energy of 14 TeV energy region. Another powerful approach to go beyond the SM is a search for rare mixings of lepton flavor, which is sensitive to many new physics models depending on flavors to be mixed. High-energy frontier and rare decays with lepton-flavor mixings are complementary to verify predictions in new models with different sensitivities for parameters such as energy scale, therefore both approaches are desired.

1.2 Lepton flavor mixing

The quarks and leptons are classified into three generations. The mixing of mass eigenstates in quark sector with Cabibbo-Kobayashi-Maskawa (CKM or KM) matrix is well known, while there had been no observation between leptons. However, if neutrinos have non-zero masses and mixing angles, neutrino oscillation appears with mixing lepton flavors. The oscillation was observed first at Super-Kamiokande and it proves lepton flavor violation (LFV) occurs in neutrino sector. So far, however, there is still no observation of charged-lepton-flavor violation (cLFV).

The cLFV process can occur in any weakly decaying particles of μ, τ and also π, K, B, D, W and Z particles. Because parameters of new physics models affect each decaying channel with different tendencies depending on its models, the multifaceted research of the cLFV with many channels would help a discrimination of the models.

Muon decay channels enable to search for the cLFV physics under less backgrounds than those of tauon decays. Some theories predict that rare muon decays are enhanced than other flavors by those mass ratio. In many popular theories, the decay, $\mu \to e\gamma$, tends to appear more frequently than other modes of $\mu \to eee$ and $\mu - e$ conversion. At the muon side current ongoing project is only the MEG experiment to search for $\mu \to e\gamma$ at Paul Sherrer Institut (PSI). A possibility of the Coherent Muon to Electron Transition (COMET) experiment to search for the $\mu - e$ conversion at the Japanese Proton Accelerator Research Complex (J-PARC) is under study. Intense source of B mesons provides many clues of lepton physics and B factory at High Energy Accelerator Research

Organization (KEK) has a plan to upgrade luminosity in future such as SuperKEKB, which has 40 times higher intensity than the current world most intense KEKB. The parallel search of flavor mixing in different sectors has different sensitivity to discriminate various extensions.

1.3 Neutrino and the see-saw mechanism

In order to describe too small masses of neutrinos some theories are suggested, for example Zee-mechanism, which produces radiative mass from one-loop radiative correction, allows a nonzero mass of the left-handed neutrino introducing one extra Higgs doublet and one charged singlet. Another strong candidate is the seesaw model.

The right-handed neutrino, which is a singlet of $SU(2)_L$ and noted as ν_R, can exist in the Lagrangian of the SM as a Yukawa coupling term, then it can obtain a mass with Higgs mechanism. The Majorana mass term is also added in the Lagrangian. The sea-saw mechanism can naturally explain the small masses of neutrinos such that the right-handed Majorana mass matrix, M_R, is much larger than the Dirac mass matrix, M_D and the left-handed Majorana mass is set to zero. One obtains the mass matrix of the light neutrinos,

$$M_\nu = -M_D^T M_R^{-1} M_D + O\left(\left(\frac{m_D}{m_R}\right)^2\right), \tag{1}$$

$$m_\nu \simeq \frac{m_D^2}{m_R}, \tag{2}$$

where $m_{D,R}$ is a scale of $M_{D,R}$ respectively and m_ν is that of neutrinos. For example an electroweak scale of $m_D \simeq 100$ GeV and an GUT scale of $m_R \simeq 10^{15}$ GeV gives a reasonable mass of neutrino m_ν, to be $O(10^{-2})$ eV. On the other hand an assumption of $m_D \sim m_{\mu,\tau}$ and $m_\nu \sim \sqrt{\Delta m^2_{atm}} \sim 0.05$ eV suggests m_R in a range of 10^8-10^{11} GeV.

The mixing in neutrino sector also suggests the cLFV decay. For example a $\mu^+ \to e^+\gamma$ decay arises when radiative neutrino mixing occurs with a weak interaction involving W boson while the lepton flavor changes between neutrinos (Figure 1.1). In such a case the branching ratio of $\mu^+ \to e^+\gamma$ is determined by a mass ratio of the mass difference of muon and positron to W boson mass, $(\Delta m^2_{21}/M^2_W)^2$,

$$B(\mu \to e\gamma) = \frac{3\alpha}{32\pi} \sum_i \left| U^*_{\mu i} U_{ei} \frac{\Delta m^2_{21}}{M^2_W} \right|^2 \tag{3}$$

$$\approx \frac{\alpha}{128\pi} \sin^2 2\theta_{12} \left(\frac{\Delta m^2_{21}}{M^2_W}\right)^2 < 10^{-54}, \tag{4}$$

where U is the Pontecorvo-Maki-Nakagawa-Sakaga (PMNS or MNS) matrix, $\sin^2 2\theta_{12} = 0.86$ and $\Delta m^2_{21} \sim 8 \times 10^{-5} eV^2$ are assumed. The branching ratio in the SM with massive neutrinos is too low to be reached experimentally. In other words, the signal of cLFV is definitely the evidence of the new physics beyond the SM. Many extensions of the SM enhance the mixing of lepton flavor and predict the existence of $\mu \to e\gamma$ near to the current upper limit of $\mathrm{Br}(\mu \to e\gamma)$.

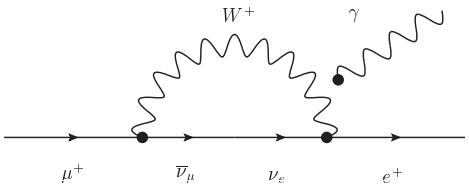

Figure 1.1: Feynman diagram for the $\mu^+ \to e^+\gamma$ in the Standard Model.

1.4 Motivation of $\mu^+ \to e^+\gamma$ search

The advantage of using muons to search for new physics is absence of strong interactions. Further, a low energy muon produces only electron, positron, gamma ray and neutrinos with only a few decay modes. Therefore only two types of detectors for positrons and gamma rays are required. A $\mu^+ \to e^+\gamma$ has a clear two-body decay and there is no missing particle in signal.

For $\mu - e$ conversion the branching ratio is about hundred times lower than that of $\mu^+ \to e^+\gamma$ in major cases of extended theories. Furthermore the observed number of muons limits the achievable branching ratio rather than the performance of a detector. Thus to be comparable with $\mu^+ \to e^+\gamma$, an intense muon source is required. On the other hand, because a $\mu^+ \to e^+\gamma$ search, as well as $\mu^+ \to e^+e^-e^+$, is limited by a resolution of detectors and pileup, an innovative upgrade of a detector enables to give a strict upper limit of the branching ratio.

The observation of LFV events should be the evidence of extended theories of the SM. Even though there is no LFV observed, the lower limit of branching ratio is able to distinguish a possible model and its parameters. The LFV search with τ lepton is also needed for a discrimination of models because the sensitivity of the LFV between different pairs of lepton family depend on models. However, the angular distribution from $\mu^+ \to e^+\gamma$ with polarized muons is also dependent on models, thus there is a possibility to discriminate models only in the $\mu^+ \to e^+\gamma$ search. Regarding the region around current upper limits of rare muon or tau lepton decays and other cLFV, the search for $\mu^+ \to e^+\gamma$ has a powerful ability to discriminate various models for new physics beyond the SM. If $\mu^+ \to e^+\gamma$ is discovered, it is the evidence of new physics because the SM does not predict it in the reachable region.

1.5 Physics of the $\mu^+ \to e^+\gamma$ decay

General SUSY The supersymmetric (SUSY) scenarios enhance LFV because of the misalignment between fermion and sfermion mass eigenstates. The LFV would occur by one-loop diagrams with the exchange of gauginos and sleptons, thus the branching ratio of $\mu \to e\gamma$ is determined by the ratio of corresponding elements in slepton mass matrix, a SUSY mass running in the loop and $\tan\beta$ that is the ratio of the two MSSM-Higgs vacuum expectation values (VEVs).

SUSY GUT SU(5) In the grand-unified theory (GUT), the electroweak interaction and the strong interaction are globally treated in a group, such as SU(5), SO(10) or $E_{6,7,8}$ (E series of Lie groups). The SU(5) is a minimal expression but can not unify the

gauge couplings of the SM and it was excluded by the longer proton decay time than its expectation as experimentally proved at KAMIOKANDE [5]. However, the minimum SUSY extension of the SM (MSSM) solves the hierarchy problem and agrees with all observations. Figure 1.2 shows the relation of branching ratio [6]. The possibility of $\mu \to e\gamma$ discovery in this model is low but exists only in the case of light SUSY particles and large values of $\tan\beta$ and A_0. The input parameters are given as $m_0, M_{1/2} < 1\,\text{TeV}$, $|A_0| < 3\,m_0$, $3 < \tan\beta < 50$ and $\mu > 0$. For the neutrino sectors, we assume a hierarchical spectrum for both light and heavy neutrinos and we take $m_{\nu_3} = 0.05$ eV, $10^{10} < M_3 < 10^{15}$ GeV. The gray regions are excluded by the current experimental upper bounds on $\text{Br}(\mu \to e\gamma)$.

With right-handed neutrinos of singlet $(\text{SU}(5)_{RN})$, SU(5) model gets a natural enhancement of the branching ratio due to the left-handed sleptons mass matrix. Figure 1.3 shows the correlation between branching ratios between $\mu \to e\gamma$ and $\tau \to \mu\gamma$ for three different values of $U_{e3} = (0.001, 0.01, 0.1)$, which is the element of the MNS matrix and a crucial parameter to determine $\text{Br}(\mu \to e\gamma\ )$.

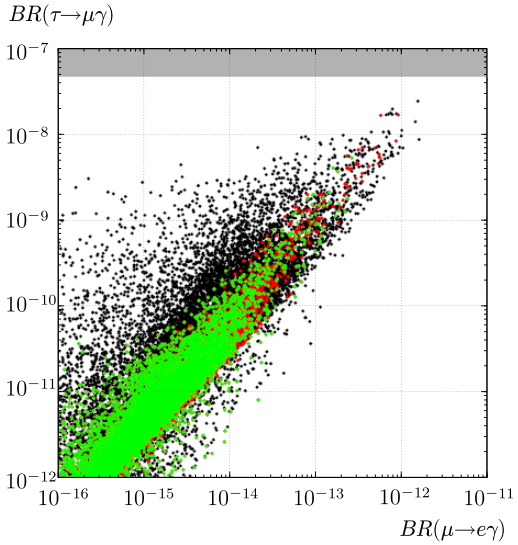

Figure 1.2: Branching ratios of $\mu \to e\gamma$ and $\tau \to \mu\gamma$ in SU(5) SUSY GUT without right-handed neutrinos. Red and green dots satisfy the $B \to X_s\gamma$ constraints at the 99% C.L. limit while black dots do not. Green dots additionally satisfy $m_{h^0} > 111.4$ GeV. All the points satisfy $\Delta a_\mu^{\text{SUSY}} \leq 5 \times 10^{-9}$.

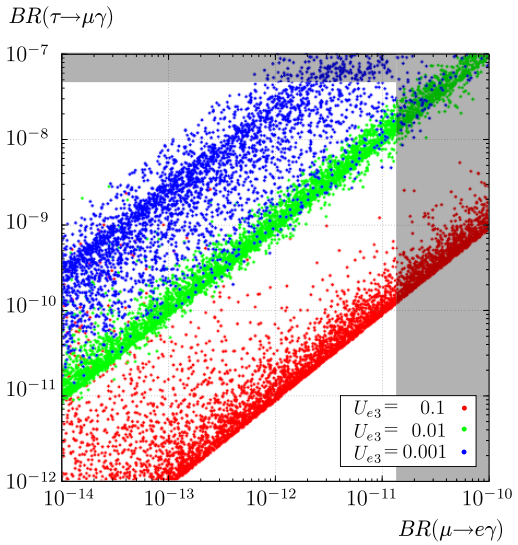

Figure 1.3: Branching ratios of $\mu \to e\gamma$ and $\tau \to \mu\gamma$ in the $\text{SU}(5)_{RN}$ model. The input parameters are given as $m_0, M_{1/2} < 1$ TeV, $|A_0| < 3\,m_0$, $3 < \tan\beta < 50$ and $\mu > 0$, and for both light and heavy neutrinos, $m_{\nu 3} = 0.05$ eV and $10^{10} < M_3 < 10^{15}$ GeV are set.

Gray regions are excluded by the experimental upper limit.

SUSY GUT SO(10) Compared to the minimal SU(5) SUSY GUT, naturally a large mixing of lepton flavor is introduced in SO(10) with see-saw mechanism, because Yukawa

couplings of neutrino relates with those in quark sector and both the left-handed and right-handed sleptons receive LFV effects. For example, the branching ratio of $\mu \to e\gamma$ is enhanced by $(m_\tau/m_\mu)^2$ compared to the minimal SU(5) SUSY GUT. The correlation of branching ratio between $\mu \to e\gamma$, $\tau \to \mu\gamma$ and $\mu Ti \to eTi$ are described with $A_0 = 0$ in Figure 1.4, by various five models of different higgs content, flavor symmetry and different M_R hierarchy [7]. The assumption for each model on SO(10) for $(\tan\beta,\ \sin\theta_{13})$ is that Albright - Barr (AB)[8], Chen - Mahanthappa (CM)[9], Cai - Yu (CY)[10], Dermisek - Raby (DR)[11] and Grimus - Kuhbock (GK)[12] have (5, 0.002), (10, 0.013), (10, 0.0029), (50, 0.0024) and (10, 0.00059), respectively.

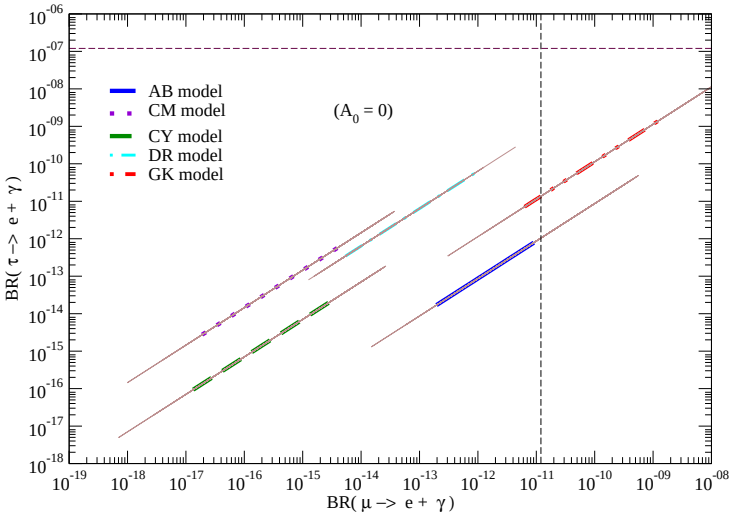

(a) $\mu \to e\gamma$ and $\tau \to e\gamma$

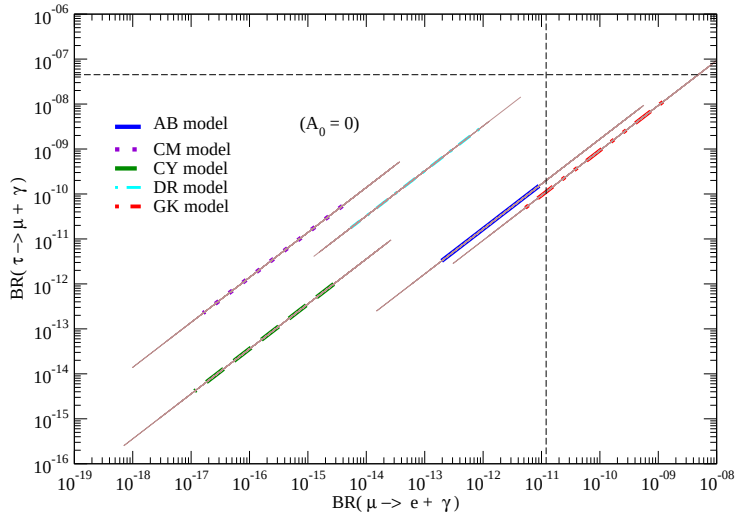

(b) $\mu \to e\gamma$ and $\tau \to \mu\gamma$

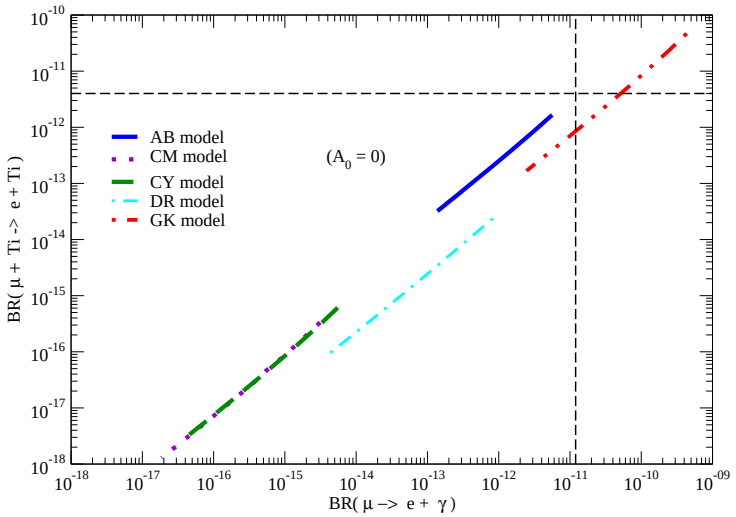

(c) $\mu \to e\gamma$ and $\mu + Ti \to e^+ + Ti$

Figure 1.4: Relation between branching ratios of muon rare decays in SO(10) SUSY GUT. The present experimental constraints are indicated by the dashed lines [7].

Part II
MEG Experiment

This part introduces a principle and an apparatus of the MEG experiment with its advantages. Details of expected signal and background, detectors and the status are described.

Recent experiments to search for the $\mu^+ \to e^+\gamma$ are shown in Table 1. The previous experiment by MEGA gave the limit of $\mathrm{Br}(\mu^+ \to e^+\gamma) < 1.2 \times 10^{-11}$ (90% C.L.) in 1999 [2]. The parameters in the table determine the ability to search $\mu \to e\gamma$, and suggest a possibility to reach unexplored region with new experiments. The MEG experiment aims at two orders of magnitude lower than the limit with innovative detectors and a highly efficient measurement.

Table 1: Progress of 90 % C.L. upper limits of $\mathrm{Br}(\mu^+ \to e^+\gamma$) and performance in full width at half maximum (FWHM).

Year	Site	Beam rate (sec^{-1})	ΔE_e (%)	ΔE_γ (%)	$\Delta t_{e\gamma}$ (nsec)	$\Delta\Theta_{e\gamma}$ (mrad)	Upper Limit $\mathrm{Br}(\mu \to e\gamma)$	Ref.
1977	TRIUMF	2×10^5 π^+	8.7	9.3	1.4		3.6×10^{-9}	[13]
1980	SIN	5×10^5 μ^+	10	8.7	6.7		1.0×10^{-9}	[14]
1979	LAMPF	2.4×10^6 μ^+	8.8	8	1.9	37	1.7×10^{-10}	[15]
1986	LAMPF	4×10^5 μ^+	8	8	1.8	87	4.9×10^{-11}	[16]
1999	LAMPF	1.3×10^7 μ^+	1.2	4.5	1.6	15	1.2×10^{-11}	[2]
2008	PSI	3×10^7 μ^+	1.6	4.7 [1]	0.35		2.8×10^{-11}	[4]

[1] FWHM from upper part of sigma.

2 Principle and Overview of the MEG Experiment

2.1 Signal and background of $\mu \to e\gamma$

2.1.1 Signal

The MEG experiment utilizes positive muons in order to avoid a formation of a muonic atom and a process such as $\mu - e$ conversion. The $\mu^+ \to e^+\gamma$ signal is a clear two-body decay from a positive muon at rest on a stopping target and decays to back-to-back direction at a coincident time. Both a positron and a gamma ray have energies at a half muon mass, $m_\mu/2 = 52.8\,\mathrm{MeV}/c^2$. Therefore observed parameters of a time difference, $t_{e\gamma}$, an opening angle, $\Theta_{e\gamma}$, and each energy from half muon mass, $m_\mu/2 - E_e$ and $m_\mu/2 - E_\gamma$ can distinguish a signal from backgrounds by selecting events with these parameters around zero. The distinctive signal is an advantage to detect the $\mu \to e\gamma$ decay.

2.1.2 Backgrounds

Even though a pure positive muon beam is introduced into the target, there are several backgrounds from muon decay by itself. Figure 2.1 shows energy spectra of positrons and

gamma rays from muon decays. The most dominant muon decay mode is $\mu^+ \to e^+\nu_e\overline{\nu}_\mu$, which is called Michel decay (MD) named after Louis Michel, and it produces many positrons around the signal energy region. The positron itself and the gamma ray from radiative muon decays or annihilation of positrons make a source of $\mu^+ \to e^+\gamma$ background when a positron and a gamma ray get accidentally coincident with back-to-back direction around the signal energy region, 52.8 MeV. For a $\mu^+ \to e^+\gamma$ searching experiment there are two main backgrounds and this accidental background is the most dominant.

Second one is a prompt background from a physical decay $\mu^+ \to e^+\nu_e\overline{\nu}_\mu\gamma$. Another decay mode of radiative muon decay (RD, RMD), $\mu^+ \to e^+\nu_e\overline{\nu}_\mu\gamma$, emits both a positron and a gamma ray at coincident time with a branching ratio $\mathrm{Br}(\mu^+ \to e^+\nu_e\overline{\nu}_\mu\gamma) = (1.4 \pm 0.4)\%$ ($E_\gamma > 10$ MeV). This forms a coincident background of back-to-back positron and gamma ray if two neutrinos get less energies.

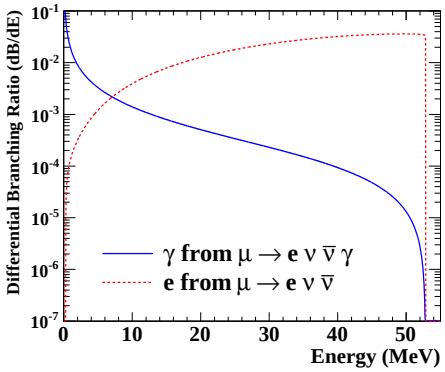

Figure 2.1: Energy spectra of a positron from $\mu^+ \to e^+\nu_e\overline{\nu}_\mu$ [17] and a gamma ray from $\mu^+ \to e^+\nu_e\overline{\nu}_\mu\gamma$ [18]. Other variables are integrated.

Prompt background The differential branching ratio of the radiative muon decay was calculated at the rest frame of a muon,

$$dB_{RD}(\mu \to e\nu\bar{\nu}\gamma) = \frac{\alpha}{64\pi^3}\beta dx\frac{dy}{y}d\Omega_e d\Omega_\gamma [F(x,y,d) - \beta P_\mu \cdot \hat{p_e} G(x,y,d) - P_\mu \cdot \hat{p_\gamma} H(x,y,d)], \quad (5)$$

$$\beta = \frac{|\vec{p_e}|}{E_e},\ d = 1 - \beta\hat{p_e}\cdot\hat{p_\gamma}, \quad (6)$$

$$x = \frac{2E_e}{m_\mu},\ y = \frac{2E_\gamma}{m_\mu}, \quad (7)$$

where P_μ is a polarization vector of a muon and functions of $F(x,y,d)$, $G(x,y,d)$ and $H(x,y,d)$ are described in Appendix A.1 ([19, 20, 21]).

Our interest is a background around the $\mu^+ \to e^+\gamma$ signal region, therefore the dB_{RD} is integrated in ranges of $1-\delta x \le x \le 1$, $1-\delta y \le y \le 1$ and $0 \le z \le \delta z$, where the parameter z is defined as $z = \pi - \Theta_{e\gamma}$ and δx, δy and δz mean detector resolutions

for the signal discrimination. There is an assumption of uniform performance about any directions, $\delta z = \delta z_\phi = \delta z_\theta$. The partial branching ratio is expressed as,

$$\begin{aligned} dB_{RD}(\mu \to e\nu\bar{\nu}\gamma) &= \int_{1-\delta x}^{1} dx \int_{1-\delta y}^{1} dy \int_{0}^{min[\delta z, 2\sqrt{(1-x)(1-y)}]} dz \frac{dB(\mu^+ \to \mathrm{e}^+\nu\bar{\nu}\gamma)}{dxdydz} \\ &= \frac{\alpha}{16\pi}[J_1(1-|P_\mu|\cos\theta) + J_2(1+|P_\mu|\cos\theta)]d(\cos\theta), \end{aligned} \tag{8}$$

$$\begin{aligned} J_1 &= \frac{8}{3}(\delta x)^3(\delta y)\left(\frac{\delta z}{2}\right)^2 - (\delta x)^2\left(\frac{\delta z}{2}\right)^4 + \frac{1}{3}\frac{1}{(\delta y)^2}\left(\frac{\delta z}{2}\right)^8, \\ J_2 &= 8(\delta x)^2(\delta y)^2\left(\frac{\delta z}{2}\right)^2 - 8(\delta x)(\delta y)\left(\frac{\delta z}{2}\right)^4 + \frac{8}{3}\left(\frac{\delta z}{2}\right)^6, \end{aligned} \tag{9}$$

where θ is the angle between the muon spin and the positron direction [22].

Accidental background With a realistic muon rate and detector's resolution, the accidental background is the most dominant as a background of $\mu^+ \to e^+\gamma$ decay. The positrons come from normal Michel decay, while the gamma rays from the radiative muon decays, annihilation in flight (AIF) of positrons or external bremsstrahlung.

With taking each detection probability of a positron and a gamma ray in the $\mu^+ \to e^+\gamma$ signal region into account, the ratio of the accidental background (B_{acc}) over total muons, by integrating a muon rate R_μ, is

$$N_{acc} = \int_{DAQ} dT \left(R_\mu \cdot f_e^0 \cdot \eta_e \cdot \frac{\Omega_e}{4\pi} \cdot \epsilon_e\right) \cdot \left(R_\mu \cdot f_\gamma^0 \cdot \eta_\gamma \cdot \frac{\Omega_\gamma}{4\pi} \cdot \epsilon_\gamma\right) \cdot \frac{\delta\omega_{e\gamma}}{\Omega_{e\gamma}} \cdot (2\delta t_{e\gamma}), \tag{10}$$

$$B_{acc} = \frac{N_{acc}}{\int_{DAQ} dT (R_\mu \cdot (\Omega_{e\gamma}/4\pi) \cdot \eta_{e\gamma} \cdot \epsilon_e \cdot \epsilon_\gamma)} \tag{11}$$

$$= R_\mu \cdot f_e^0 \cdot f_\gamma^0 \cdot \left(\frac{\delta\omega_{e\gamma}}{4\pi}\right) \cdot (2\delta t_{e\gamma}) \cdot \eta, \tag{12}$$

where the effect of polarization determined by detector's acceptance is included in η as the suppression factor by a muon polarization. It is maximized to $\eta = 1$ in the case of 100% depolarized muon. The fraction of energy spectrum around $\mu^+ \to e^+\gamma$ signal region is expressed as f_e^0 and f_γ^0 for positrons and gamma rays, respectively.

In order to consider the f_γ^0, in a theoretical aspect, the differential branching ratio of the radiative muon decay is considered after the integration of the positron energy and the opening angle [23],

$$dB_{RD}(\mu \to e\nu\bar{\nu}\gamma) \simeq \frac{dy}{y} d(\cos\theta)[J_+(y)(1+|P_\mu|\cos\theta) + J_-(y)(1-|P_\mu|\cos\theta)], \tag{13}$$

where the term of order $\sqrt{r} \equiv m_e/m_\mu$ is neglected and $J_+(y)$ and $J_-(y)$ are defined by

$$\begin{aligned} J_+(y) &= \frac{\alpha}{6\pi}(1-y)\left[\left(3\ln\frac{1-y}{r}-\frac{17}{2}\right)\right. \\ &\left.+\left(-3\ln\frac{1-y}{r}+7\right)(1-y)+\left(2\ln\frac{1-y}{r}-\frac{13}{3}\right)(1-y)^2\right], \qquad (14) \\ J_-(y) &= \frac{\alpha}{6\pi}(1-y)^2\left[\left(3\ln\frac{1-y}{r}-\frac{93}{12}\right)\right. \\ &\left.+\left(-4\ln\frac{1-y}{r}+\frac{29}{3}\right)(1-y)+\left(2\ln\frac{1-y}{r}-\frac{55}{12}\right)(1-y)^2\right]. \qquad (15) \end{aligned}$$

With using above relations, the fractions are estimated as

$$f_\gamma^0 = \int_{1-\delta y}^{1-r} dy \frac{dB_{RD}(\mu^+ \to e^+\nu\bar{\nu}\gamma)}{dy} \approx \frac{\alpha}{2\pi}(\delta y)^2[\ln(\delta y)+7.33], \qquad (16)$$

$$f_e^0 = \int_{1-\delta x}^{1+r} dx \frac{dB_{MD}(\mu^+ \to e^+\nu\bar{\nu})}{dx} \approx 2(\delta x), \qquad (17)$$

thus the effective branching ratio of accidental background is approximately given by

$$B_{acc} \approx R_\mu \cdot (2\delta x) \cdot \left[\frac{\alpha}{2\pi}(\delta y)^2(\ln(\delta y)+7.33)\right] \cdot \frac{(\delta z)^2}{4} \cdot (2\delta t_{e\gamma}) \cdot \eta. \qquad (18)$$

2.2 Strategy of the MEG experiment

2.2.1 Requirement

A search for a rare decay of muons requires an intense muon beam and an excellent performance of detectors for both a gamma ray and a positron in order to avoid pileup and reach the interesting region. As described in Section 2.1, the better resolution of the detector can suppress main backgrounds from accidental pileup, which would limit the sensitivity of the search.

2.2.2 Muon source

Because muons are finally stopped on a target without including a beam momentum into decay products, a low-energy muon beam is allowed. A direct current (DC) of a muon beam is efficient to suppress the accidental background compared to alternating current (AC) muons, because the accidental background depends on effective beam rate in a bunch and the observed number is accumulated by averaged rate.

We select the world's most intense DC muon beam from 590 MeV proton ring cyclotron facility of $\sim$2 mA intensity at Paul Sherrer Institut in Switzerland.

2.2.3 Positron tracking

Many positrons are produced from Michel decays around a signal energy, thus pileup is a critical problem. Therefore, in the positron detector, it is desired to avoid too long tracking time and to select only the interesting signal region. In addition, a material thorough

tracking should be as less as possible to avoid scattering, energy loss or annihilation of low positron momentum, around 52.8 MeV.

As a solution, we developed a special magnet with a gradient magnetic field, which enables a momentum cut with its geometry and a suitable tracking length. Undesired low momentum positrons is outside the detector, then effective measurement is possible. To detect positrons low mass drift chambers are also developed and plastic-scintillator bars support a timing determination.

2.2.4 Scintillator for a gamma-ray measurement

Equation 18 suggests that the energy resolution for a gamma ray (δy) is crucial to suppress the background level. Thus, the gamma-ray detector is the most important part to determine a final sensitivity.

The gamma-ray measurement in the MEGA experiment has a good energy performance but a low detection efficiency of photon spectrometer about 2.4%, because it detects a photon via charged particles [2]. It is considered that the performance of photon detector could improve from the list in Table 1, with a proper selection of scintillators, especially as timing and efficiency.

Performance of various scintillators is shown in Table 2. Some crystals with good timing performance are typically small size and not suitable for a large detector to measure ten-MeV scale. We adopt a xenon in a liquid state with a fast signal and a high density. It is a new frontier with a use of a large 900-liter (2.7-ton) liquid xenon as a detector, so that innovative liquid xenon gamma-ray detector was developed for the MEG experiment as later described in Section 3.6.

Table 2: Comparison of various scintillators.

	LXe	LAr	NaI (Tl)	CsI (Tl)	BGO	LSO (Ce)	$LaBr_3$ (Ce)	$PbWO_4$
Density (g/cm^3)	2.98	1.40	3.67	4.51	7.13	7.40	5.29	8.3
Radiation length (cm)	2.77	14	2.59	1.86	1.12	1.14	2.1	0.89
Mollier radius (cm)	4.2	7.2	4.13	3.57	2.23	2.07	2.85	2.00
Decay time (ns)	45	1620	230	1300	300	40	25	30/10[1]
Emission peak (nm)	178	127	410	560	480	420	380	425/420[1]
Relative output	75	90	100	165	21	83	130	0.083/0.29[1]

[1]slow/fast component

2.3 Sensitivity and goal

Although we would estimate a sensitivity of the MEG experiment with a measured performance and a likelihood method later, it makes a sense to obtain an overview of time scale toward our goal beforehand. The single event sensitivity (SES) of $\mu^+ \to e^+\gamma$, defined in Equation 19, is a sensitivity of background-less single-signal discovery,

$$SES(\mu^+ \to e^+\gamma) = \frac{1}{R_\mu \cdot T \cdot (\Omega_{e\gamma}/4\pi) \cdot \epsilon_e \cdot \epsilon_\gamma \cdot \epsilon_{e\gamma}}, \tag{19}$$

where R_μ is the muon stopping rate, T is the total effective run time, $\Omega_{e\gamma}$ is the detector acceptance with considering a muon polarization, ϵ_γ and $\epsilon_{e\gamma}$ are detection efficiencies of a gamma-ray and positron detector and $\epsilon_{e\gamma}$ is the total efficiency to select back-to-back $e\gamma$ of trigger, analysis and selection.

Actual branching-ratio sensitivity of null-signal observation starts a saturation when a total time reaches a region that SES becomes comparable with the dominant background of B_{acc}. As a function of total time T, B_{acc}/SES can be regarded as the number of accidental backgrounds in a certain signal window for B_{acc}. Around the region of the current limit, an achievable region in $\mu^+ \to e^+\gamma$ search is limited by B_{acc}, not by statistics.

There are shown estimation of backgrounds approximately by assuming a detector performance. In the case of MEGA experiment, Table 1 gives

$$\begin{aligned} &\delta x = 0.0084,\ \delta y = 0.032,\ \delta z = 0.02,\ \delta t_{e\gamma} = 1.12 \text{ ns}, \\ &R_\mu = 1.3 \times 10^7 \text{ (DC rate for } SES),\ R_\mu = 2.6 \times 10^8 \text{ (for } B_{acc}), \\ &(\Omega_{e\gamma}/4\pi) \cdot \epsilon_e \cdot \epsilon_\gamma \cdot \epsilon_{e\gamma} = 0.003, \end{aligned} \tag{20}$$

where AC beam rate with 6-7% duty cycle is considered in R_μ only for B_{acc} but not for SES and we assume 1.4 FWHM region as 90% region. Then each background is estimated to be

$$B_{RD} = 9.1 \times 10^{-15}, B_{acc} = 4.4 \times 10^{-12}, SES(T = 1 \text{ year}) = 8.1 \times 10^{-13}. \tag{21}$$

On the other hand, the current performance of the MEG experiment are typically

$$\begin{aligned} &\delta x = 0.012,\ \delta y = 0.033,\ \delta z = 0.02,\ \delta t_{e\gamma} = 0.25 \text{ ns}, \\ &R_\mu = 3 \times 10^7,\ (\Omega_{e\gamma}/4\pi) \cdot \epsilon_e \cdot \epsilon_\gamma \cdot \epsilon_{e\gamma} = 0.017, \end{aligned} \tag{22}$$

where we assume the same δz as the MEGA because a comparison is difficult and these are not so different each other. The backgrounds and SES are calculated as

$$B_{RD} = 9.2 \times 10^{-15},\ B_{acc} = 4.4 \times 10^{-14},\ SES(T = 1 \text{ year}) = 6.0 \times 10^{-14}. \tag{23}$$

Although the definition of resolutions slightly differs between two experiments, we can see lower accidental backgrounds for the MEG experiment by two order of magnitude thanks to the intense DC muon beam and the high resolution of timing. The energy resolutions are comparable each other, but detection efficiencies of the MEG detector are much better. Especially, the gamma-ray detector in MEGA detects charged particles from converted gamma rays, thus the efficiency is low.

The SES and B_{acc} in Equation 23 indicate that the MEG experiment needs a few years run, considering available beam time of nine months per year, effective DAQ time, a calibration and a maintenance. The upper-limit sensitivity for null signal obtained in 2009 analysis will be shown later in Section 10.5 by our analysis method. The strategy to acquire the sufficient performance in MEG will be shown in next section.

3 Detector and Setup

3.1 Detectors overview

3.1.1 MEG detector

Detectors consist of the positron spectrometer inside the magnet and the liquid xenon (LXe) gamma-ray detector. The C-shaped LXe detector is located outside the magnet and the positron detectors, which consist of a drift chamber (DCH) and a scintillation timing counter (TIC), are mounted around a lower position from a target as shown in Figure 3.1. Two sets of TIC are located at the upstream and downstream side, each of which consists of two layers of arrays along the beam axis and the azimuthal axis.

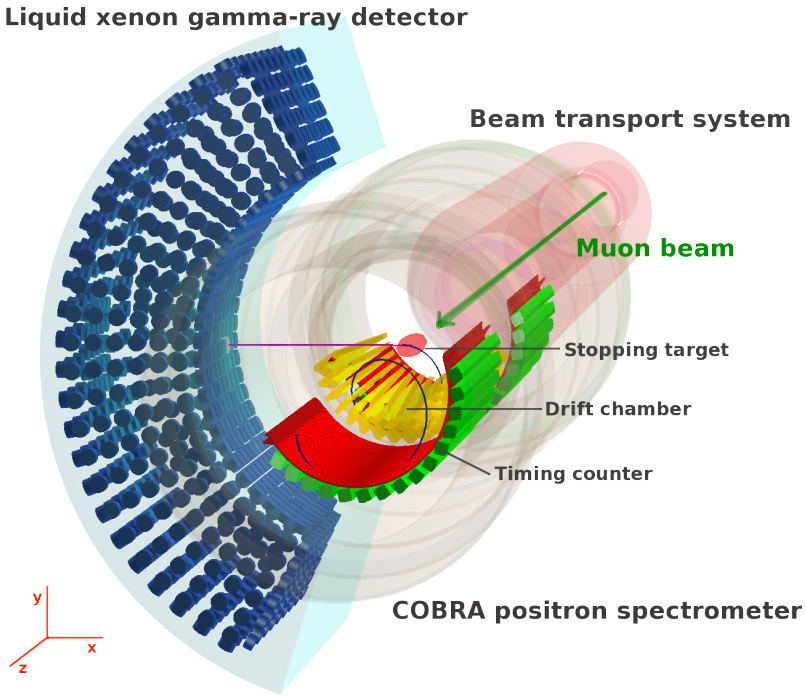

Figure 3.1: Overview of detectors in the MEG experiment.

3.1.2 MEG coordinate system

We define an orthogonal coordinate system by (x, y, z) as a global coordinate system of the MEG (Figure 3.2). The origin is defined as the center of COBRA magnet and also at the central position of the MEG target. The z-axis is parallel to the muon beam with the beam direction. The y-axis is vertical so the x-axis penetrates perpendicularly the central detection face of the LXe detector at negative x. The θ parameter is defined as the polar angle from the z-axis, that means the beam direction is presented with $\theta = 0$. The ϕ is an azimuth of the z-axis and takes zero on the positive x-axis. For example, a direction from the target to the center of the LXe detector is $(\phi, \theta) = (\pi, \frac{\pi}{2})$. The spherical polar coordinates and the cylindrical polar coordinates are defined by θ and ϕ.

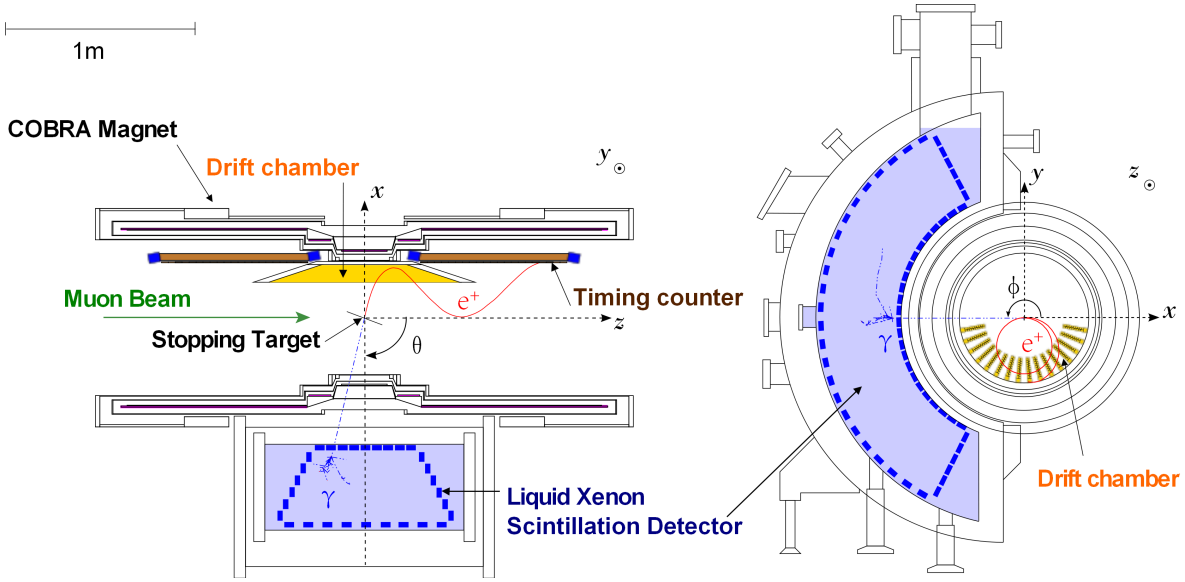

Figure 3.2: Layout of detectors in the MEG experiment.

3.2 Beamline

3.2.1 Proton accelerators at PSI

The facility to provide protons at PSI consists of three accelerators (Figure 3.3). At first the PSI Cockcroft-Walton Pre-Injector generates 870 keV protons from a source made up of hydrogen atoms. Then PSI Injector 2 cyclotron with four spectromagnets provides 72 MeV protons with 0.2% FWHM spread, 50.63 MHz frequency (19.75 ns interval) and 0.3 ns width of a bunch from the 870 keV injector.

Finally the Proton Ring Cyclotron with a diameter of approximately 15 meters, which consists of eight sector magnets and four accelerator cavities (Figure 3.4), accelerates the 72 MeV proton beam up to 590 MeV kinetic energy. The accelerator normally delivers 2.0 or 2.2 mA protons, sometimes 1.8 mA. With some resonators' upgrades for the Injector 2 and cyclotron, the operational current is planned to be increased to 2.6 mA and finally to 3.0 mA within a few years [24].

Table 3: Characteristics of 590 MeV Ring Cyclotron [25].

Injection Energy	72 MeV
Extraction Energy	590 MeV
Extraction Momentum	1.2 Gev/c
Energy spread (FWHM)	ca. 0.2 %
Beam Emittance	ca. 2 π mm $\times$ mrad
Beam Current	2.0 - 2.2 mA (in DC)
Accelerator Frequency	50.63 MHz
Time Between Pulses	19.75 ns
Bunch Width	ca. 0.3 ns
Extraction Losses	ca. 0.03 %

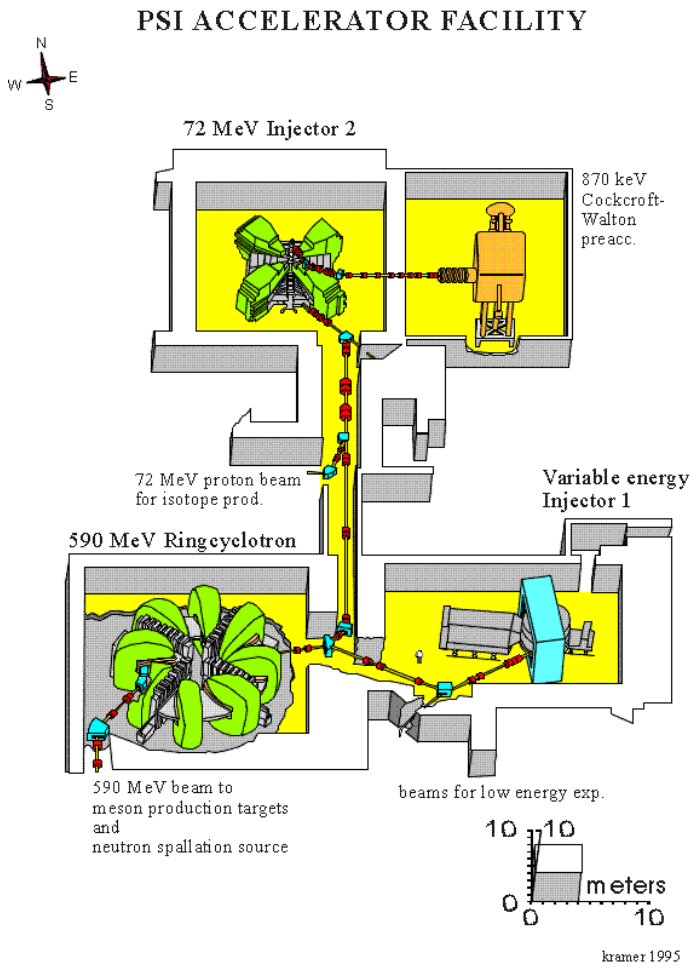

Figure 3.3: Proton Accelerators at PSI. Injector 1 is unused.

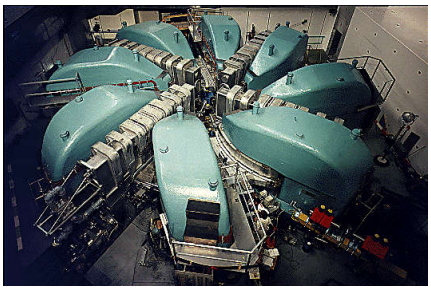

Figure 3.4: The 590 MeV Ring Cyclotron of PSI.

3.2.2 Proton target and surface muon

The proton beam reaches the target station M and E, then the Spallation Neutron Source (SINQ) target or a beam dump. The E target has a 1 Hz rotating truncated cone of polycrystalline graphite. Its length along beam direction is 40 mm (Figure 3.5). The rotation is to avoid a heat and the graphite is replaced by a few months.

A lifetime of charged pion at rest is about 26 ns, which is comparable with the time between beam pulse of 19.75 ns. A muon is produced by a charged pion decay, $\pi^{\pm} \to \mu^{\pm}\nu_{\mu}$, with a muon neutrino, thus these two are polarized by opposite direction each other. The momentum of $\mu^{\pm}$ from $\pi^{\pm}$ decay at rest is $E_{\mu} \sim E_{\nu} = (m_{\pi^{\pm}}^2 + m_{\nu_{\mu}}^2 - m_{\mu}^2)c/2m_{\pi^{\pm}} = 29.8$ MeV/c. The muons from stopped pions around a surface of the target within a few μm is called surface muon, which has a low energy loss and a trivial depolarization during a short pass length in a target and has an upper edge at 29.8 MeV/c. Sub-surface muons, which come from pions in the bulk of the target, are also generated with lower momentum and cloud muons with higher momentum originate from pions outside the target. The intense surface muons are used for the MEG experiment.

3.2.3 Area πE5

The MEG experiment uses πE5 area, which is one of five branches from target E. By viewing the target E at 175° with respect to the primary proton beam, positive or negative pions, muons and electrons or positrons are provided with a lower momentum 10-120 MeV/c. The πE5 area has a suitable channel to obtain surface muons. Figure 3.6 shows the πE5 branch, which has two subbranches U and Z to switch the beam for two setups in πE5 area by a bending magnet. The Z branch of the left-hand side in the figure has the last bending magnet and the first degrader in it. MEG uses Z branch to extract the surface positive muon beam.

Figure 3.5: Target E (40 mm thickness).

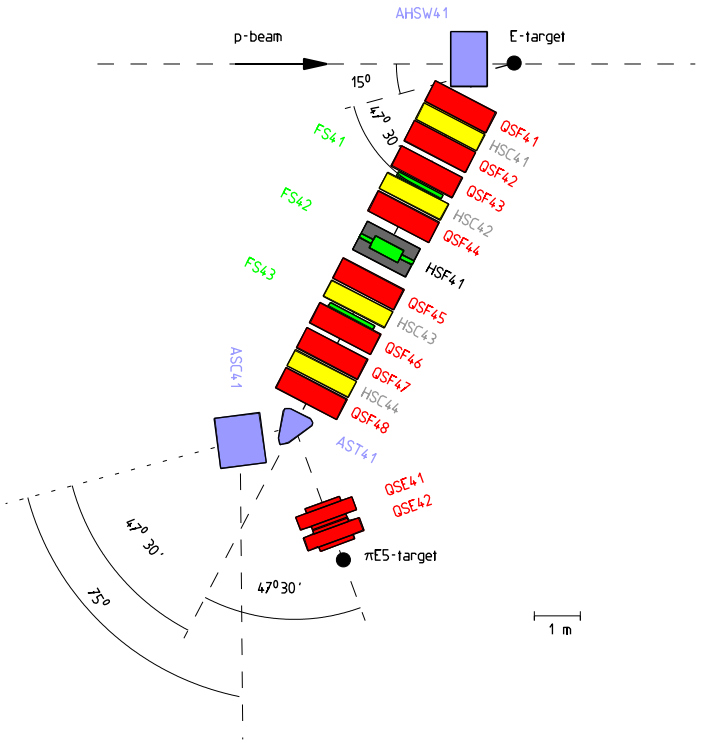

Figure 3.6: Branch to the πE5 area.

The πE5 beam line in Figure 3.6 consists of bending, quadrupole, hexapole magnets and slits, and it can transfer pions and muons with fluxes shown in Figure 3.7. Especially surface muons make a peak around 28 MeV/c down to 10 MeV/c. In the middle of the beam line, three sets of horizontal and one set of vertical slits can determine the momentum and the acceptance of beam.

3.2.4 Beam transport system

Figures 3.8 and 3.9 show the MEG beam transport system in the πE5 area to bring the muon beam to stopping target. It consists of a quadrupole triplet (Triplet I), a velocity separator using a Wien filter, a second quadrupole triplet (Triplet II) and a beam transport solenoid (BTS) with superconducting magnet from a view of the beam

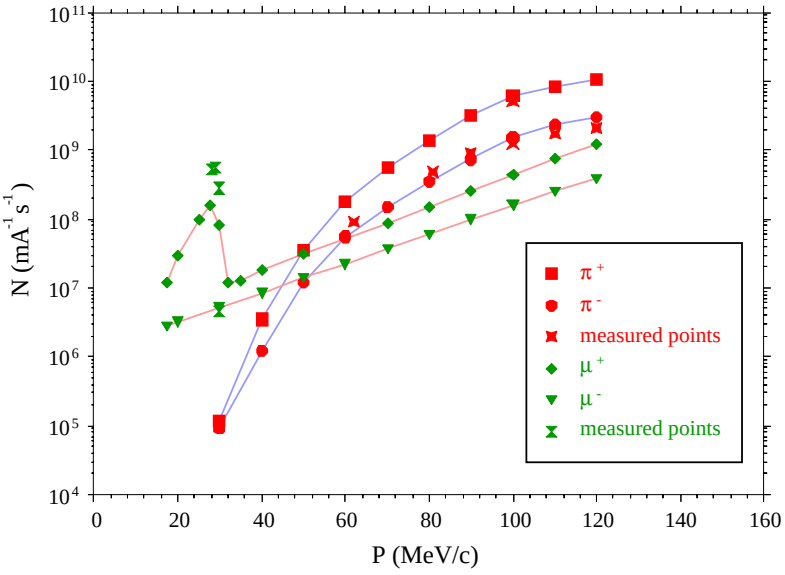

Figure 3.7: Pion and muon beam intensity at πE5 beam line.

direction. The purpose of the system is to focus positive surface muons at the center of the muon stopping target with selecting and degrading momentum and to suppress other particles. A momentum degrader at the center of the BTS is made of Mylar with a thickness between 200 and 450 μm which can be optimized to maximize stopping efficiency with less backgrounds.

With a horizontal magnetic field of 133 Gauss and a vertical electric field of 195 kV, the Wien filter separates positive muons from positron contamination by 7.5 σ and also from others. The beam spot size at the center of the target is $\sigma_x = 9.5$ mm and $\sigma_y = 10.2$ mm.

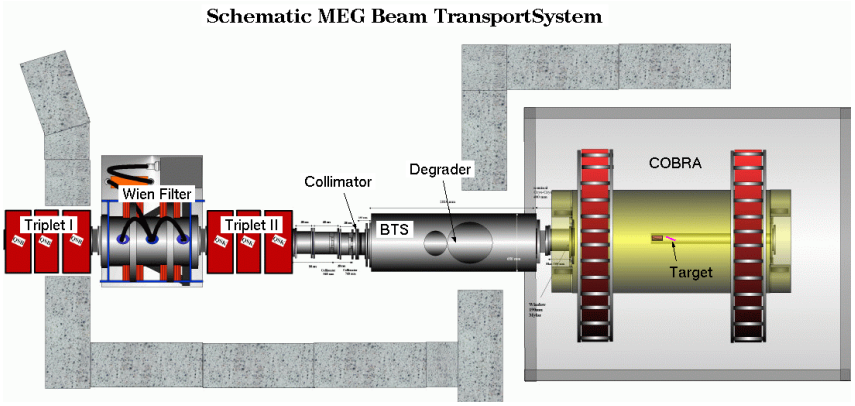

Figure 3.8: Schematic view of MEG beam transport system.

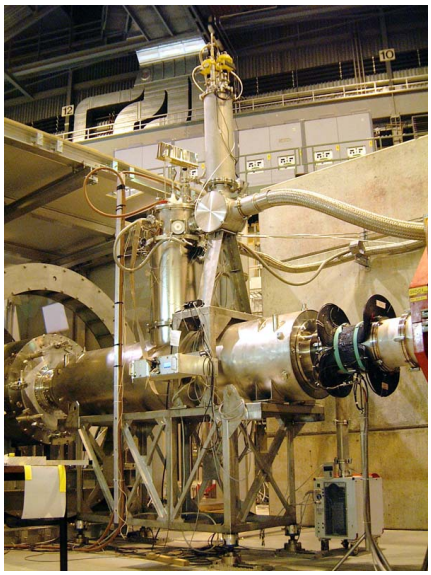

Figure 3.9: Beam transport solenoid (BTS).

3.2.5 Muon stopping target

The target has to efficiently stop the muon. On the other hand it should be as thin as possible in order to avoid scattering, annihilation and energy loss of positrons in the target. Thus an elliptical shaped plane with a large slant angle from a vertical plane of muon beam direction is suitable to have a enough thickness for a muon stopping as well as a less thickness for positrons' emission to the detector. In addition, inside of the COBRA magnet, except for around the detectors, is filled with helium and a few percent air for that. A narrow spread of positron momentum by the Wien filter allows to control a precise stopping point with using a degrader at the center of BTS.

The dimension of the target is 79.8 mm along vertical axis and 200.5 mm along the long axis (Figure 3.10). The target is slanted with 20.5° relative to the beam axis. The target has six holes of 10 mm diameter to align the target and to estimate the resolution of the vertex position reconstructed with the positron tracking.

The target is made of a material with light Z, that is a sheet of polyethylene and polyester with a 205 μm thickness corresponding to 18 mg/cm^2 on plane and gives an 82% stopping efficiency. The target is supported with a frame made of Rohacell (0.895 g/cm^3) and is remotely operated with an insertion system to move between the mounted position and a stay position apart from the center. Figure 3.11 shows the location of the target and the insertion bar around an upper position.

This insertion system of the muon target allows a background study without the target and another target or another beam line from down stream side. The other insertion systems are equipped at the down stream side, which allow a beam scanning at the center with using APD, a proton beam line and a target insertion of a proton accelerator for a photon calibration and a hydrogen target for a pion charge exchange run.

Figure 3.10: Muon stopping target.

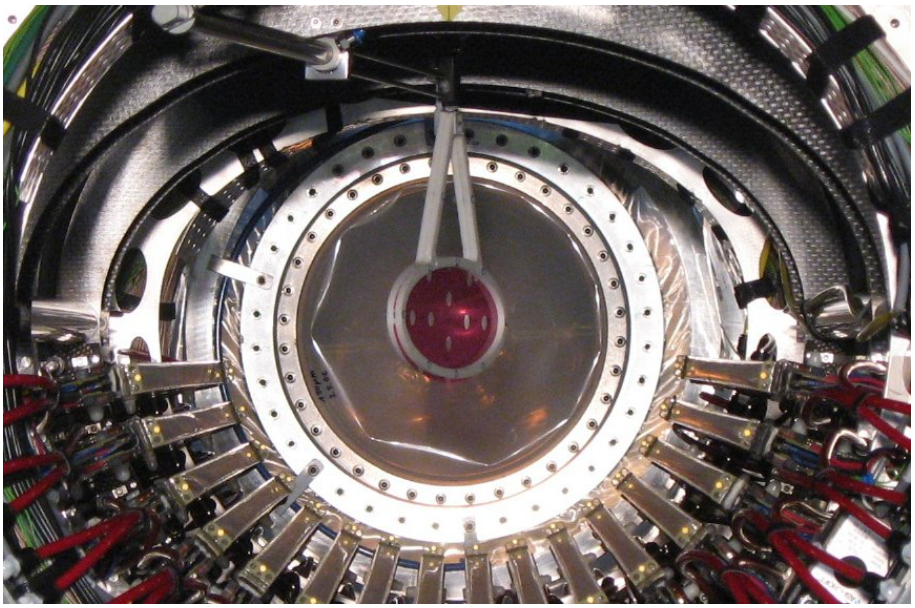

Figure 3.11: Mounting position of the target.

3.3 COBRA magnet

3.3.1 Design

The positron spectrometer consists of drift chamber, two types of timing counter and a special superconducting magnet with a gradient magnetic field dedicated to the MEG experiment. The magnet is called COBRA (COnstant-Bending-RAdius) (Figure 3.12) [26]. All the positron detectors are mounted in the magnet and the LXe detector is put outside. Thus a window for a gamma ray on COBRA wall should be very thin for a gamma-ray transmission.

The most important issue is a reduction of high-rate positrons around 10^8 sec^{-1} rate. An optimization of a geometry and an alignment of positron detectors make it possible to select a high energy region around the 52.8 MeV signal from high-rate positrons. However, because the dominant muon decay, $\mu^+ \to e^+\nu_e\overline{\nu}_\mu$, emits a positron largely in a high energy

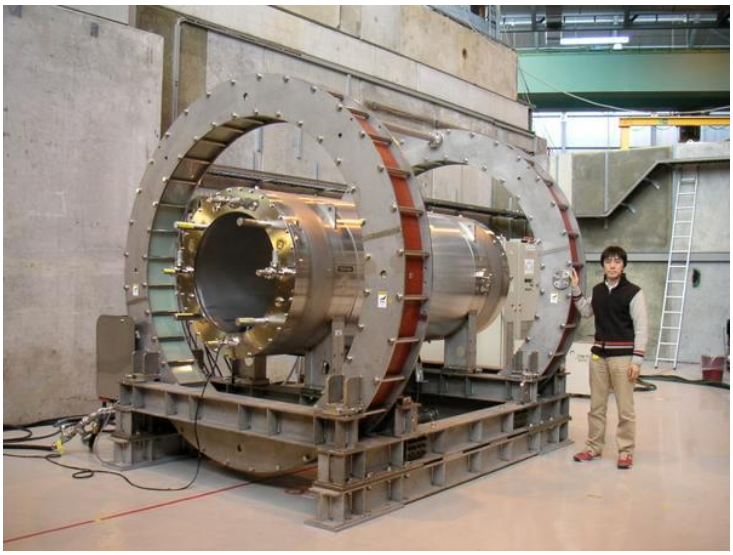

Figure 3.12: The COBRA magnet.

region near the signal, an additional idea is desired.

There are two solutions to avoid high-rate hits in the COBRA magnet. Figure 3.13 illustrates a difference between a simple solenoid (a, b) and the solenoid with gradient field in the MEG experiment (c, d). In a uniform solenoidal magnetic field, there is no force along a cylindrical axis therefore a helical trajectory has a constant pitch, which makes many pileups (Figure 3.13 a). While a non-zero radial component of the magnetic field forces to sweep positrons away quickly (Figure 3.13 c).

In a normal solenoidal magnetic field, the radius of a charged particle's trajectory relates to its momentum. However, the momentum selection is poor in the field because the radius depends on its emission angle, too. Second advantage of the COBRA gradient field is that tracks of the same momentum have the same radius and are independent of emission angles (Figure 3.13 d), which enables a precise and strict momentum cut as shown in Figure 3.14. In usual solenoidal magnet, radii of tracks depend on a momentum component on a vertical plane of cylinder. The radius of the same momentum is therefore not constant by emission angles (Figure 3.13 b).

Superconducting solenoidal magnet with step structure of different radii forms the gradient magnetic field. Mainly the COBRA consists of one central coil, two gradient coils and two end coils shown in Figure 3.15. At the both ends of the COBRA, a pair of two large resistive coils cancel the stray field from the COBRA magnet around the photo-multiplier tubes (PMTs) of the LXe detector less than 50 Gauss as shown in Figure 3.16.

The superconducting cable is made of NbTi multifilament embedded in copper matrix with a 0.59 mm diameter and covered with high-strength aluminum stabilizer with a 0.8 $\times$ 1.1 mm^2 dimension, which is insulated with a Kapton polyimide. The overall cross section is 0.9 $\times$ 1.2 mm^2.

The central coil and the gradient coils have four layers and the end coils have three. The high-strength cable allows a thin support structure and total thickness of the magnet including its cryostat is estimated to be 0.197 X_0, corresponding to 85% transmission efficiency of gamma-rays at the signal energy (52.8 MeV).

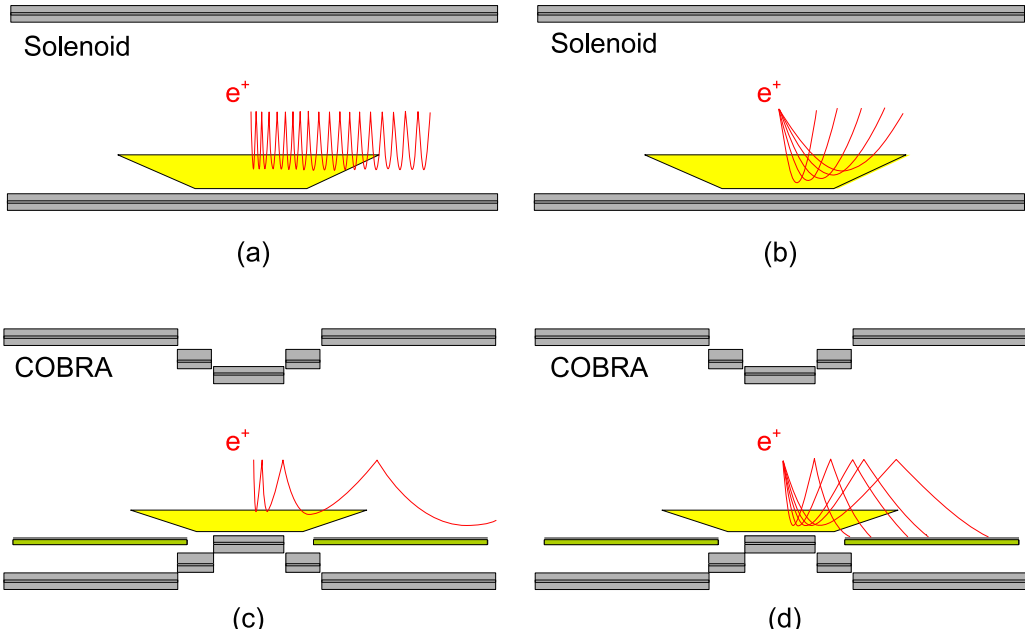

Figure 3.13: Principle of COBRA magnet.

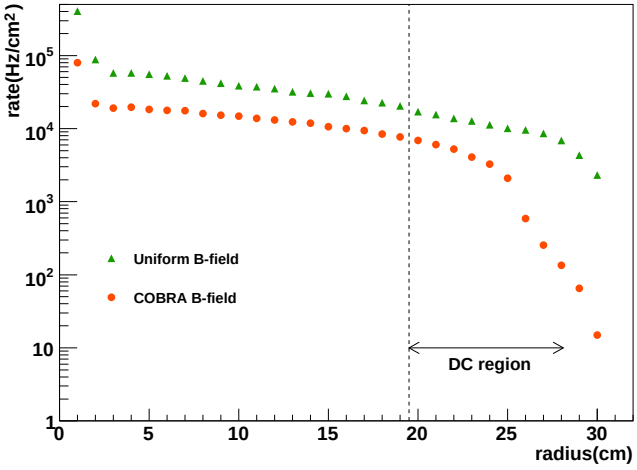

Figure 3.14: Positron rate on drift chamber in COBRA magnetic field.

3.3.2 Magnetic field

In a normal operation at 360 A current (about half of critical current of the superconducting cable) the central field is 1.27 T at $z = 0$ and slowly decreasing, as $|z|$ increases, to 0.49 T at edge (Figure 3.17). Figure 3.18 shows the magnetic field of B_z and $|B_r|$ inside the COBRA magnet.

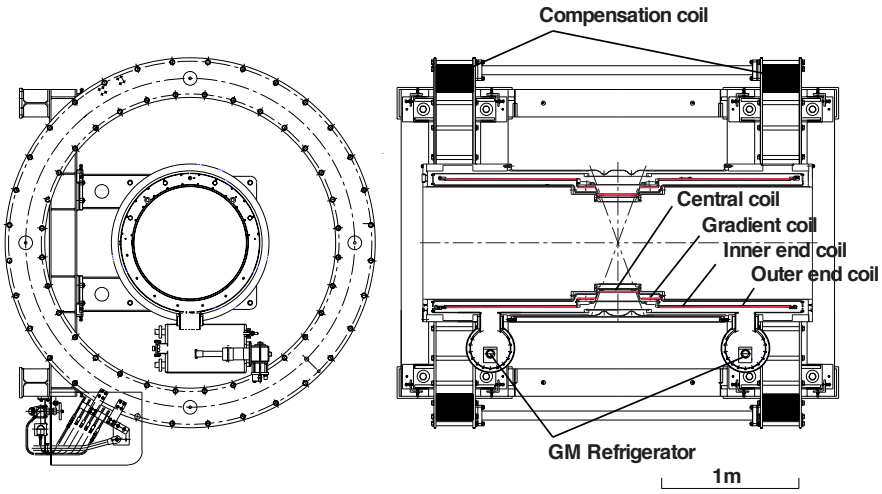

Figure 3.15: Design of the COBRA magnet [26].

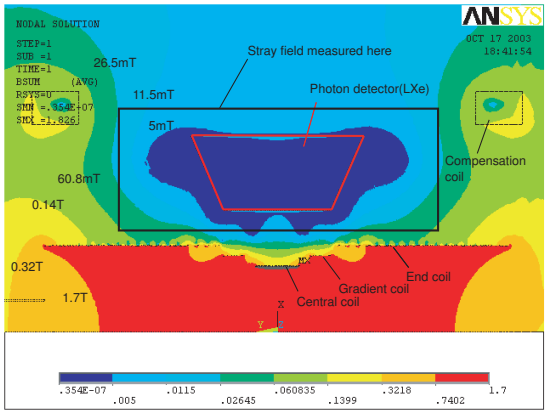

Figure 3.16: Map of COBRA magnetic field [26].

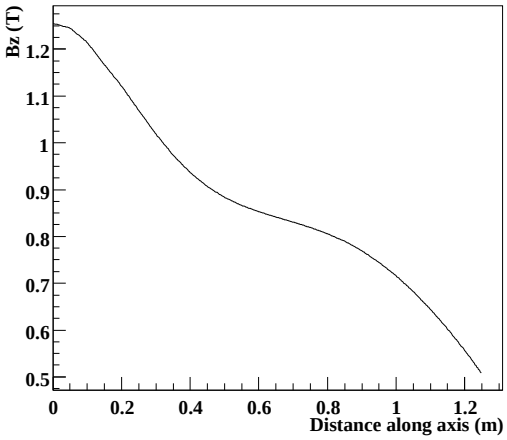

Figure 3.17: Magnetic field (B_z) along beam axis ($x = y = 0$).

3.4 Drift chamber

3.4.1 Required performance

The drift chamber (DCH) measures a momentum, a decay vertex and an emission angle of a positron. A time property of a positron is determined by the timing counter at the end of its track. The main purpose of DCH is to obtain the track of a positron. We require following items for the MEG positron tracker:

1. Low mass structure to avoid positron energy loss and multiple scattering
2. High rate tolerance for high rate positron hit, up to $\sim$10 kHz/cm^2
3. Selection over 40 MeV/c to $\mu^+ \to e^+\gamma$ signal positron momentum

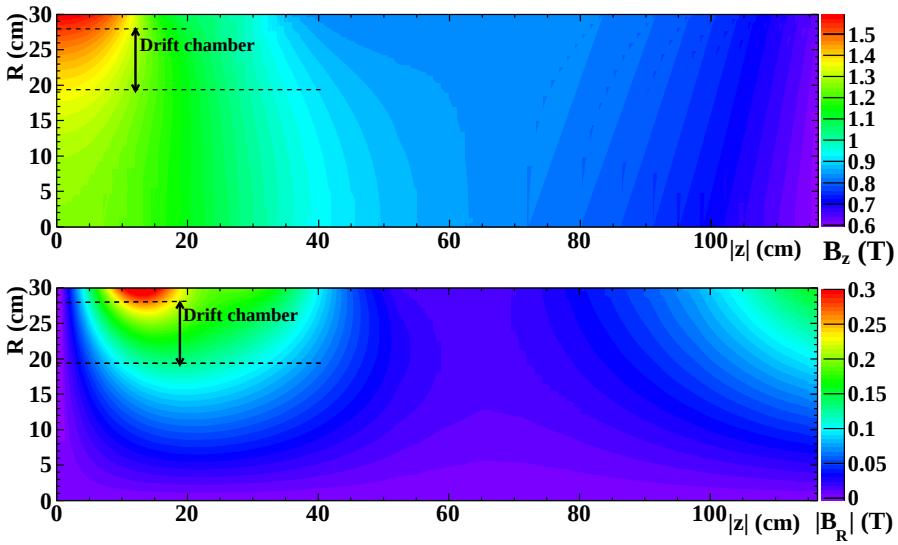

Figure 3.18: Map of COBRA magnetic field (B_z, B_r) on $r - |z|$ plane.

4. Sensitive for both along transverse and longitudinal directions

Thanks to highly efficient selection of positron momentum by the COBRA, we can select momenta by simply optimizing a geometry of DCH. Even after a reduction by momentum, coming positrons still have a high rate. The material of DCH makes both the efficiency and the resolution worse, thus it should be as less as possible. The design of DCH is specially optimized for the MEG experiment.

3.4.2 Design of chamber

The drift chambers consist of 16 modules radially aligned with 10.5° intervals in the azimuthal angle. The radius is from 19.3 cm to 27.9 cm in order to select only positrons around the signal region. In helium gas inside the COBRA magnet, all modules are installed at a lower part (Figure 3.2).

Each module consists of a support frame, a foil with a cathode pattern and anode wires as shown in Figure 3.19, and is composed of two layers with isolated by the cathode foil with 3.0 mm gap enough to suppress a cross talk. The layers contains nine axial sense wires, ten grounded potential wires and nine drift cells (Figure 3.20). The two types of wires are shifted each other between the two layers in order to resolve ambiguity along a radial direction. The field map and drift lines are calculated by a GARFIELD simulation (Figures 3.21 and 3.22) [27].

With a 4.5 mm pitch, a carbon-fiber frame stretches sense wires by 50 g tension and potential wires by 120 g alternately (Figure 3.23) [28]. The sense wire, with positive high voltage, and the potential wire have a 25 μm diameter made of Ni/Cr (80:20) and 50 μm of Be/Cu (2:98) respectively. The wires are surrounded with a cathode pad made of thin 12.5 μm-thickness polyimide with aluminum deposition (Figure 3.24).

For a chamber active gas, the helium based gas mixture, He:C_2H_6 = 50:50, is adopted. The mean of total radiation length inside the tracking volume for a signal positron is about 2×10^{-3} X_0. It mainly comes from a material of chambers such as cathode foil

Figure 3.19: Element of a drift chamber module.

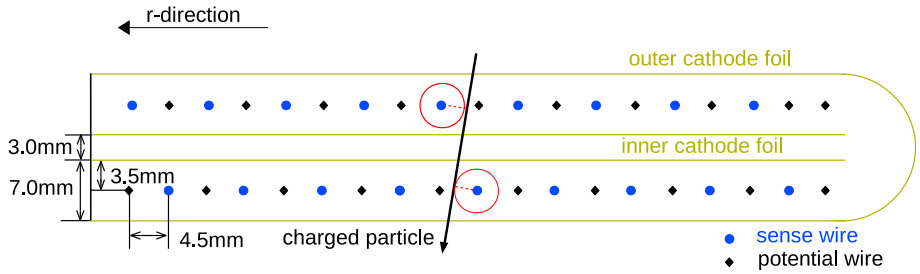

Figure 3.20: Section of wires in two layers.

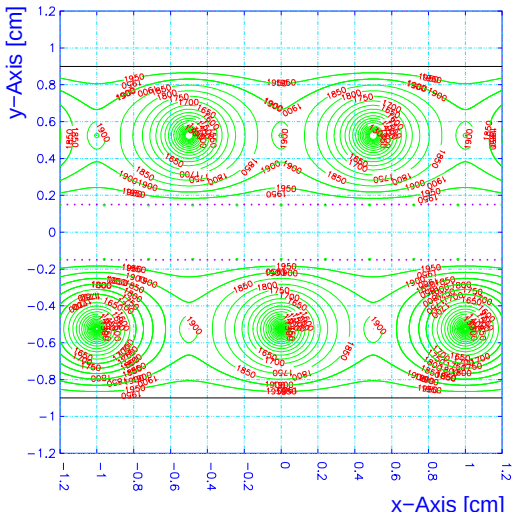

Figure 3.21: Contour line of the potential.

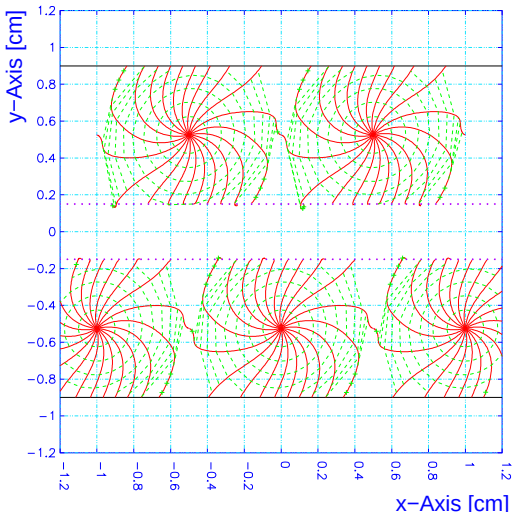

Figure 3.22: Particle drift line to each wire.

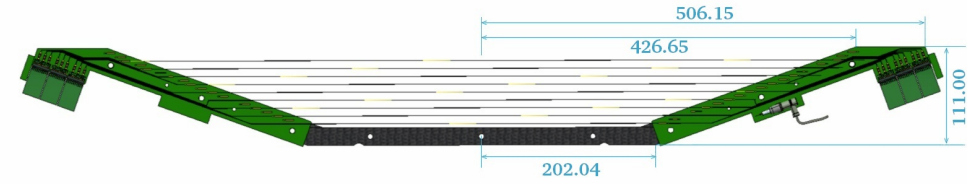

Figure 3.23: Stretched wires on a drift chamber module (mm). There is no support frame at the target side.

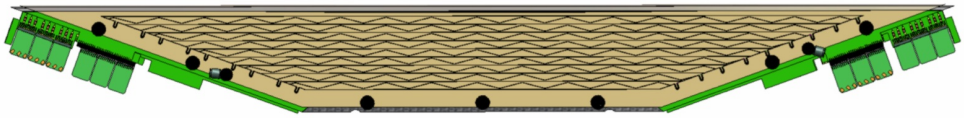

Figure 3.24: Cell and support of drift chamber.

and wires (1.9×10^{-3} X_0) and other little contribution is from the helium atmosphere and the chamber gas (0.26×10^{-3} X_0).

The drift chamber measures two-dimensional hit positions along z and ϕ direction and rough hit timings. For the geometrical reason, all wires are aligned in parallel with z axis and there is no crossing wire. To reconstruct two-dimensional positions, a special periodical shape of cathode named 'Vernier Pad' is adopted with the same direction of wires for z measurement. Figure 3.25 shows a schematic view of the vernier-pad method on cathode using a 'zig-zag' shape strip.

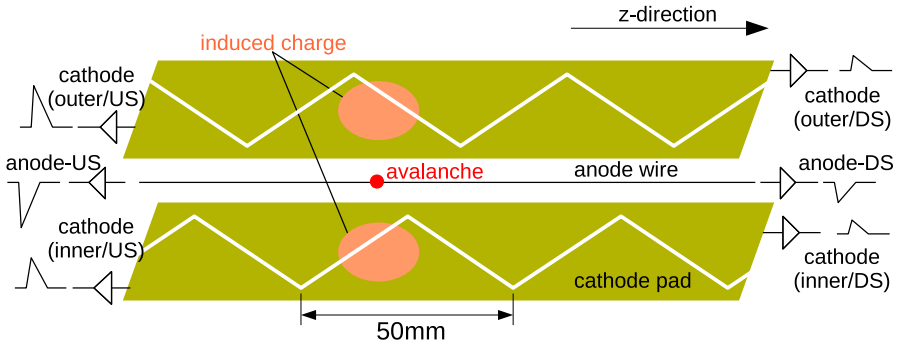

Figure 3.25: View of vernier pad.

There are four cathode channels to be read out per one anode sense wire. The isolation of cathodes is formed by etching on two cathode foils at both upper and lower side. At first the hit wire with a resistance, 2200 Ω/m, tells the z position by the ratio of the charges at both ends of the wire with an accuracy of 1 cm. Further the vernier structure of a 5 cm zig-zag period determines a more accurate z position within that period because of different phases of verniers at both sides. The layers are shifted each other by one-half

cell along a longitudinal direction in order to resolve ambiguity. Section 4.3.2 explains the details of the reconstruction.

3.4.3 Readout electronics

For the readout at the pre-amplifiers, the anode wire is decoupled with 2.7 nF capacitor with biased by typically 1850 V through 1 MΩ protection resistance. Because a waveform sampler for the DCH accepts only a positive signal, two different amplifiers of inverting and non-inverting types are developed for anode and cathode output respectively. The amplifier is fabricated on a 20.5 mm × 30.5 mm mini card with three input channels and each consists of two operational amplifiers, OPA691 (current-feedback type, 190 MHz bandwidth, Texas Instruments Inc.). The amplifier has a gain of 52 and works under ±6 V.

In a chamber with double layers, read channels of anode at both sides of nine wires needs totally 36 inputs, corresponding to 12 inverting mini-cards and decoupling capacitors. On the other hand four cathodes per a wire require 24 non-inverting mini-cards, therefore totally 18 cards are mounted at one side (Figure 3.26).

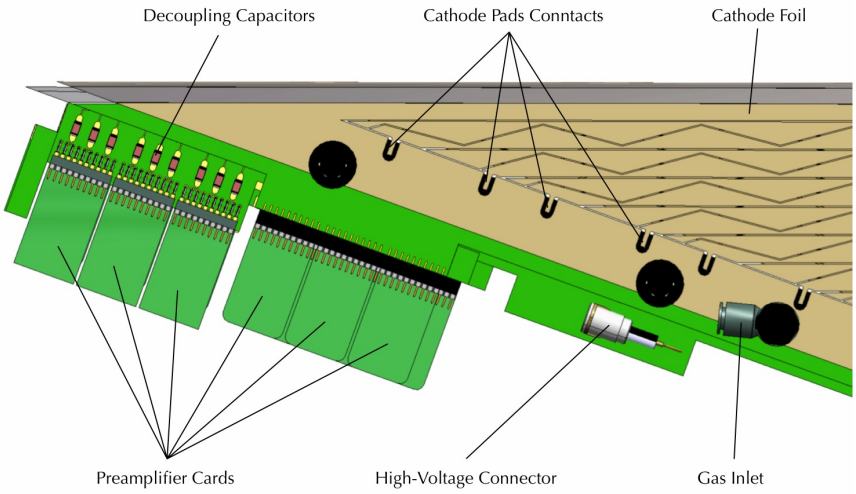

Figure 3.26: Preamplifier cards at one side of drift chamber.

3.5 Timing counter

3.5.1 Design of timing counter

Timing counter (TIC) arrays detect a positron in the angular range of $0.08 < |\cos\theta| < 0.35$ after hitting the drift chamber (Figure 3.1). The arrays consist of two layers of different plastic scintillators along z direction and ϕ direction. The inner layer along ϕ direction is made of a fine bending scintillation fiber and an avalanche photo diode (APD) in order to tag z position with a precision of its pitch, thus it is called timing counter

z (TICZ). The outer layer along z direction gives the timing information of the final hit of the positron from the drift chamber and also ϕ positions, therefore it is called timing counter ϕ (TICP). TICP takes an important role to determine positron timing and TICZ contributes for an efficient trigger and a z determination, while TICP can also measure z position roughly. The two sets of timing counter arrays are installed at down stream and up stream outside the drift chamber. In the 2009 run timing z counter was not used. A plastic bag surrounds whole TIC detector and is filled with nitrogen gas to protect PMTs of TICP from the helium gas.

3.5.2 Timing ϕ-counter

The ϕ counter is an array of 15 plastic scintillation bars, each of which is made of BC-404 by BICRON (SAINT-GOBAIN), with a $4 \times 4 \times 80$ cm^3 dimension. Figure 3.27 shows that the bars are aligned with the same angular pitch as the DCH (10.5°) along ϕ from $-150°$ to 10° at a radius of 32 cm. It covers 160° ϕ-acceptance between $-150°$ and 10°. To make path lengths of positrons uniform, the bars are mounted with slant angle of 20° and formed into a hexagonal shape so that positrons do not graze the edge of bars as shown in Figure 3.28.

At both side of the bar, fine-mesh PMTs of 2 inches, R5294 made by Hamamatsu Photonics with an active area of 39 mm diameter, are attached with a tilting angle of 10° such that the angle between the PMT axis and the magnetic field is 30° where the PMT gain is maximized.

Figure 3.27: Picture of timing ϕ counter.

3.5.3 Timing z-counter

Bending 128 scintillating fibers of 6×6 BCF-20 by BICRON (SAINT-GOBAIN) form the z counter as shown in Figure 3.29. At both end of the fiber, 5×5 mm^2 silicon

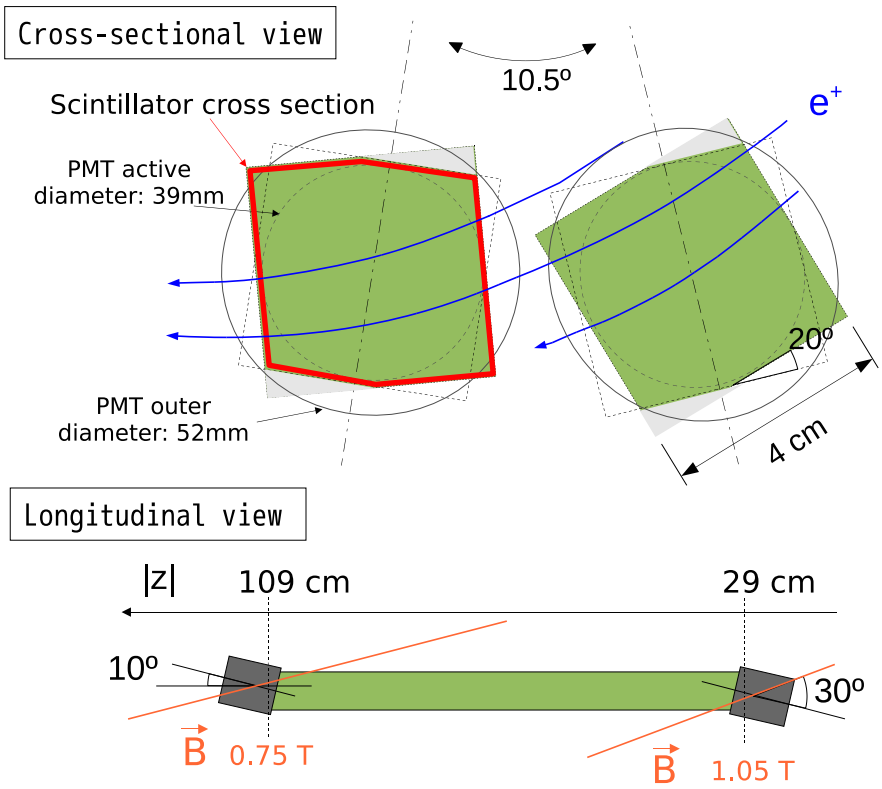

Figure 3.28: Design of timing ϕ counter.

avalanche photo-diodes, S8664-55 by Hamamatsu Photonics, are attached. The fiber is optically separated at a center.

3.6 Liquid xenon detector

3.6.1 Property of liquid xenon scintillator

For the MEG experiment we constructed the world's largest liquid xenon detector of 900-liter volume (2.7 tons in weight) by developing innovative technologies. That allows the excellent sensitivity for a $\mu \to e\gamma$ search.

The use of liquid xenon as a scintillator has many advantages compared with other scintillators. Its excellent property takes important roles on various ongoing projects such as a dark matter search, a neutrinoless double beta decay search, a gamma ray astronomy, medical applications such as positron emission tomography (PET) and so on. A short summary of the advantage is listed as follows:

- High density 2.95 g/cm^3 and short radiation length $X_0 = 2.77$ (cm)
- High light yield, 80% of NaI(Tl)
- Fast response of 45 ns for gamma rays
- No absorption of scintillation light in liquid xenon

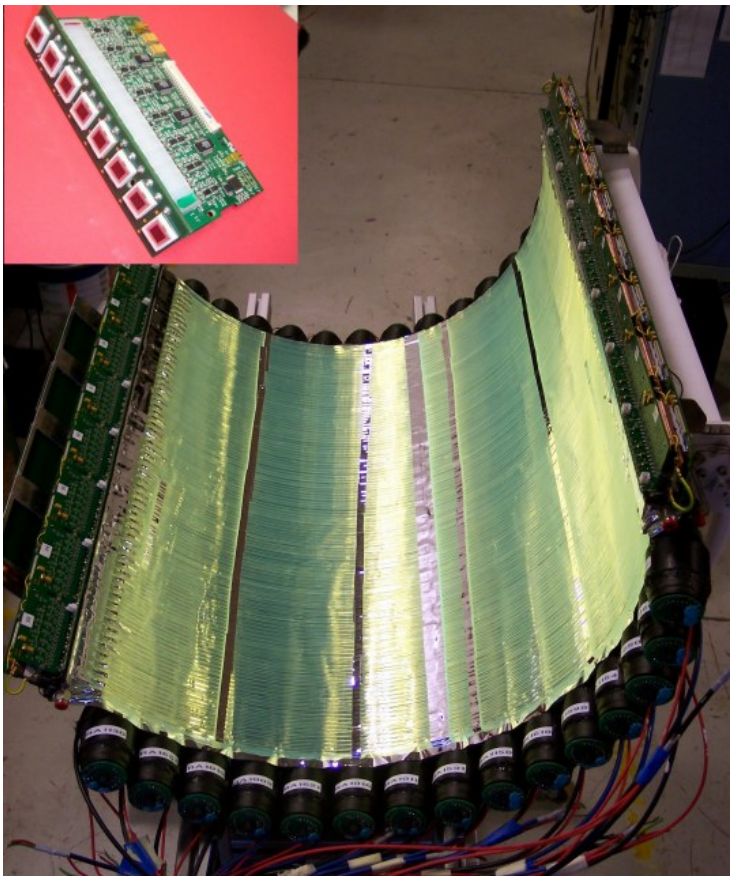

Figure 3.29: Timing z counter and 1 cm $\times$ 1 cm APD for scintillation fibers. The fibers are mounted on timing ϕ bars.

- Uniform because of liquid
- Particle discrimination

There are, however, some difficulties for the following reasons:

- Expensive
- Stable cooling in liquid phase at low temperature
- High purity to avoid absorption of the scintillation light by contaminations
- Detection of vacuum ultraviolet (VUV) scintillation light

Thanks to various studies with prototype detectors, all concerning were solved in the MEG LXe detector [29, 30].

3.6.2 Liquid xenon

The scintillation light in noble gases is attributed to the decay of excited dimers (Xe_2^*), or excimers in other words, but not a excited atoms (Xe^*) to the ground state, thus there is no absorption by itself. For argon, krypton and xenon, the luminescence emission bands,

that is scintillation wavelength, are almost identical between liquid, solid, and gas phases, except for neon. The characteristics of liquid rare gases are listed in Table 4 and liquid xenon shows the highest stopping power and shortest decay time with high scintillation light yield, however the scintillation light with a short wave length (VUV, $\lambda = 175$ nm) is difficult to detect. The property of xenon is summarized in Table 5.

Table 4: The main characteristics of Ar, Kr and Xe as scintillators.

	Ar	Kr	Xe
ρ (g/cm^3)	1.39	2.45	2.98
Z	18	36	54
λ (nm)	128	147	178
Boiling T(K)	87.3	119.9	167.1
dE/dx (m.i.p.) (MeV/cm)	2.11	3.45	3.89
X_0(cm)	14.0	4.76	2.87
Moliere radius (cm)	7.3	4.7	4.1
τ(ns)	6 / 1000	2 / 91	4 / 22 / 45

Scintillation process Injection of ionizing radiation into xenon produces excited atoms (Xe^*) or ions (Xe^+). Accordingly, there are two types of scintillation processes with a different W value and decay time. The ratio of two is determined by a deposited energy density, thus it depends on injected particles. The scintillation pulse from alpha particles is faster than that from gamma rays or electrons because of its large dE/dx, and this property is useful to discriminate particles.

At final stage, however, the scintillation light is emitted from a decay of the excimer, $Xe_2^* \rightarrow 2Xe + h\nu$, for all the scintillation processes. The excimer has mainly two excited molecular state of singlet $^1\Sigma_u^+$ and triplet $^3\Sigma_u^+$. The decay time of singlet state has much shorter than triplet state, therefore two different time constants appear depending on the process. In the case of alpha particle, singlet state has 4.2 ns decay time and triplet has 22 ns, while these depends on excited species.

The faster scintillation process occurs in such a way that excited atoms instantly form excimers and then emit photons,

$$\begin{aligned} Xe^* + Xe + Xe &\rightarrow Xe_2^* + Xe, & (24)\\ Xe_2^* &\rightarrow 2Xe + h\nu. & (25) \end{aligned}$$

Another electron-ion recombination process from Xe^+ is slower than direct excitation,

$$\begin{aligned} Xe^+ + Xe &\rightarrow Xe_2^+, & (26)\\ Xe_2^+ + e^- &\rightarrow Xe^{**} + Xe, & (27)\\ Xe^{**} &\rightarrow Xe^* + \text{heat}, & (28)\\ Xe^* + Xe + Xe &\rightarrow Xe_2^* + Xe, & (29)\\ Xe_2^* &\rightarrow 2Xe + h\nu. & (30) \end{aligned}$$

Table 5: Properties of LXe.

Material Properties	Value & Unit	Ref.
Atomic Number	54	
Atomic Weight	131.293	[31]
Density at 161.4 K	2.978 g/cm^3	[32]
Boiling point	165.1 K	[31]
Melting point	161.4 K	[31]
Triple point (temperature)	161.3 K	[33]
Triple point (pressure)	0.805 atm	[33]
Radiation length	2.77 cm	[31]
Critical Energy	14.5 MeV	[34]
Mollier radius	4.2 cm	[34]
Scinti. wavelength (peak±FWHM)	(178 ± 14) nm	[35]
Refractive index at 175 nm	1.57 to 1.72	[36, 37, 40]
W_{ph} for electron	21.6 eV	[38]
W_{ph} for α particles	17.9 eV	[38]
Decay time (recombination)	45 ns	[39]
Decay time (fast components)	4.2 ns	[39]
Decay time (slow components)	22 ns	[39]
Absorption length	> 100 cm	
Scattering length	29 cm to 50 cm	[40, 41, 42, 43]

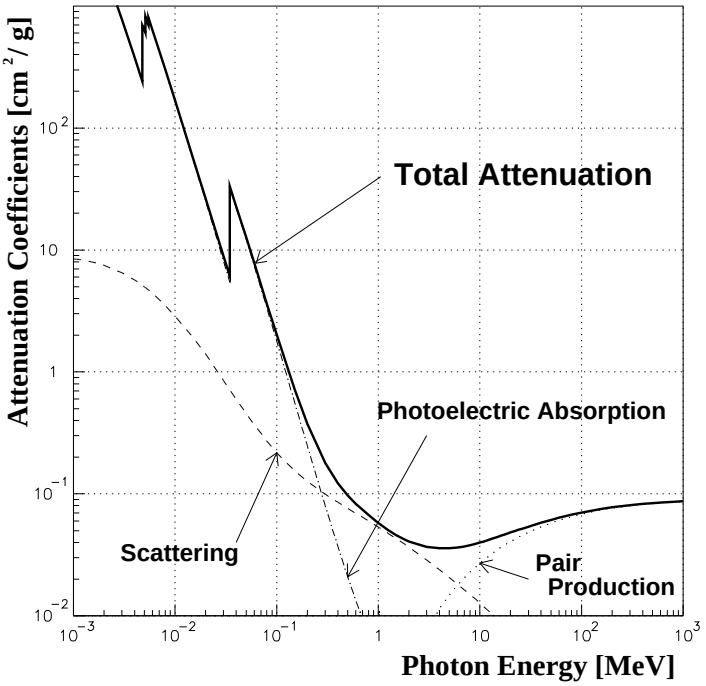

Figure 3.30: Photon reaction in liquid xenon.

The recombination process with 45 ns slower decay component is dominant in scintillation light from electrons and also from gamma rays. For gamma rays the pair production occurs around MeV scale as shown in Figure 3.30.

The liquid state has the benefit of homogeneity, however, to keep liquid state needs special technique because of its narrow temperature range. Figure 3.31 shows phase diagram of xenon and liquid phase should be kept between 161 and 165 K at 1 atom.

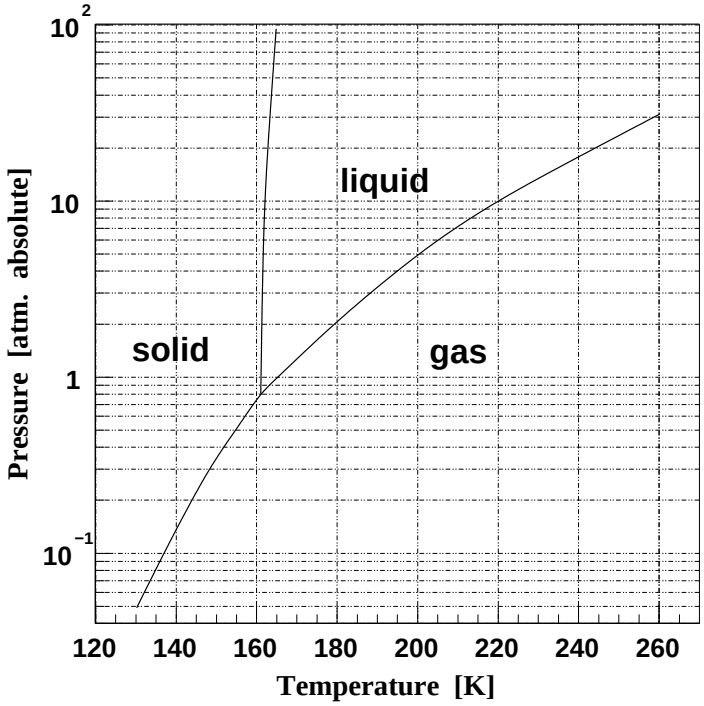

Figure 3.31: Xenon phase diagram.

The effect of radioisotope of xenon is negligible in our case from the viewpoint of the rate and the energy. The impurities in the liquid xenon should be removed with a purification system not to lose a xenon scintillation light by absorption. There is no self absorption in xenon, but contaminations such as oxygen, nitrogen and water decrease a light yield of short-wavelength scintillation light (Figures 3.32 and 3.33). Not only a purification system but also a light yield monitor is needed for a stable operation of the liquid xenon detector.

3.6.3 Photo-multiplier tube

Under 50 Gauss magnetic field the PMT for the LXe detector has to work in the 165 K liquid xenon up to absolute pressure of 0.3 MPa and also has to detect high-rate VUV ($\lambda \sim$ 178 nm) photons. Materials of PMTs should be low because the gamma-ray has to traverse the PMTs on the gamma-ray entrance face. Furthermore the MEG experiment requires a low current operation because a heat generation accumulated by many 846 PMTs makes it hard to cool xenon. A new PMT with metal channel dynodes was developed for the MEG experiment in collaboration with Hamamatsu Photonics (Table 6, Figure 3.34).

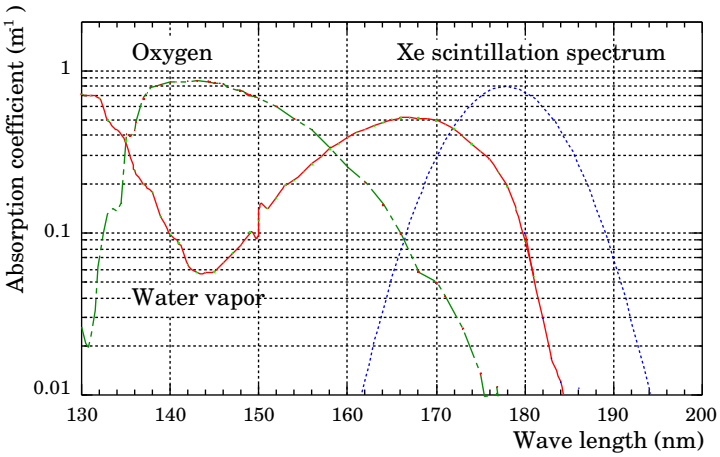

Figure 3.32: Absorption spectrum by each contamination in liquid xenon [44].

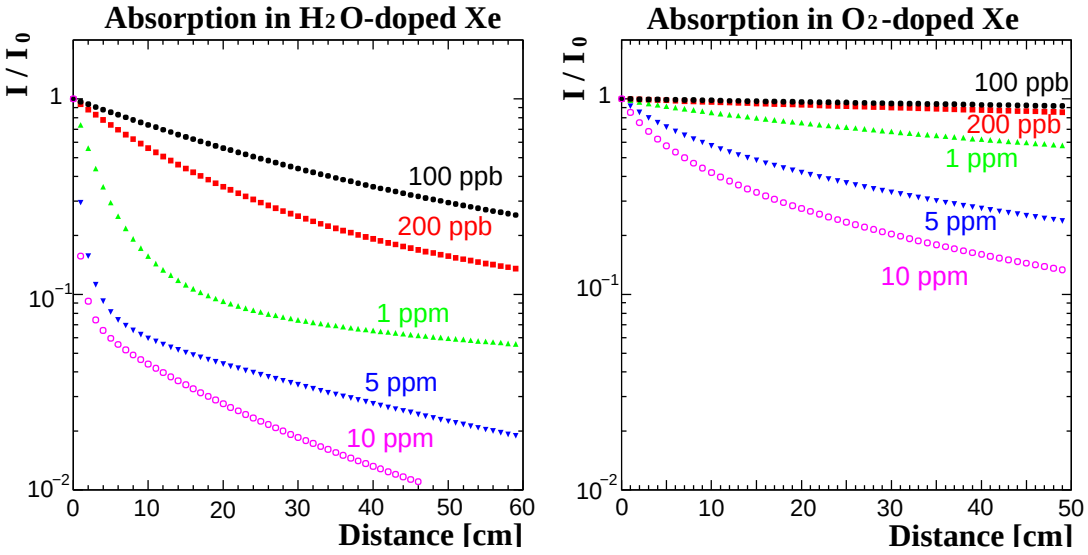

Figure 3.33: Absorption by distance and contamination.

The window of the PMT is made of synthetic quartz glass, which is transparent between 160 and a few thousands nano-meter wavelength, with a 80% transparency around $\lambda \sim 178$ nm without using a wavelength shifter. The photo-cathode material is bi-alkali K-Cs-Sb, which has better sensitivity than Rb-Cs-Sb adopted in the initial version of PMT. Bialkali has a high resistance and its large dependence by temperature. To make a uniform response for temperature and on cathode, aluminum stripes of 4% area are deposited on the photo-cathode to avoid the resistivity of bialkali (Figure 3.35). The QE is estimated to be about 15%.

High-resistance resistors are used in the voltage divider of the PMT in order to minimize the heat dissipation (Figure 3.36). In order to avoid the problem of the over-linearity at high-rate environment, Zener diodes are inserted in parallel to the last two stages of the resistive divider for twelve-step dynodes and keep a voltage around 85 V.

Thanks to the compensation coils of the COBRA the magnetic field becomes weak under 50 Gauss around the LXe detector as shown in Figure 3.16. The effect of magnetic

Table 6: Properties of the PMT (R9869). These are typical values.

Size	57 mm ϕ
Active area size	45 mm ϕ
PMT length	32 mm
Photo-cathode material	K-Cs-Sb
Dynode type	Metal channel
Number of dynode	12
Typical HV	900 V
Typical gain	1×10^6
Typical QE	15 %
Rise time	2 nsec
Typical Transit time	12.5 nsec
Typical Transit Time Spread	0.75 nsec

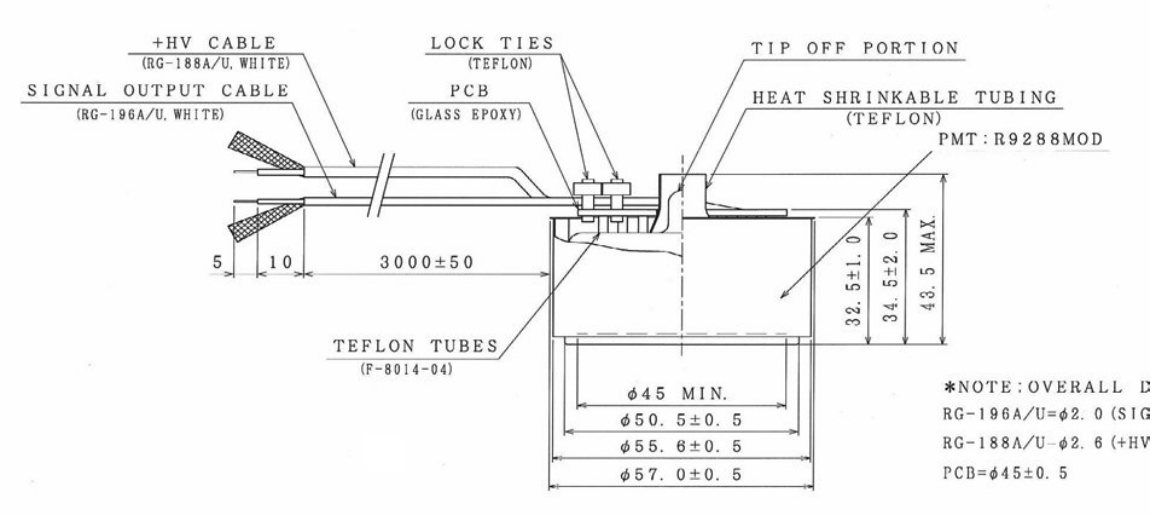

Figure 3.34: Schematic view of PMT R9288.

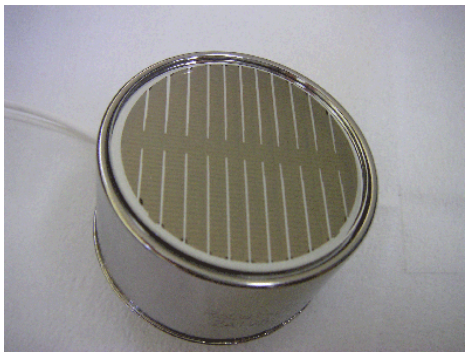

Figure 3.35: Photo-multiplier tube for the LXe detector. Aluminum stripe makes a flat response.

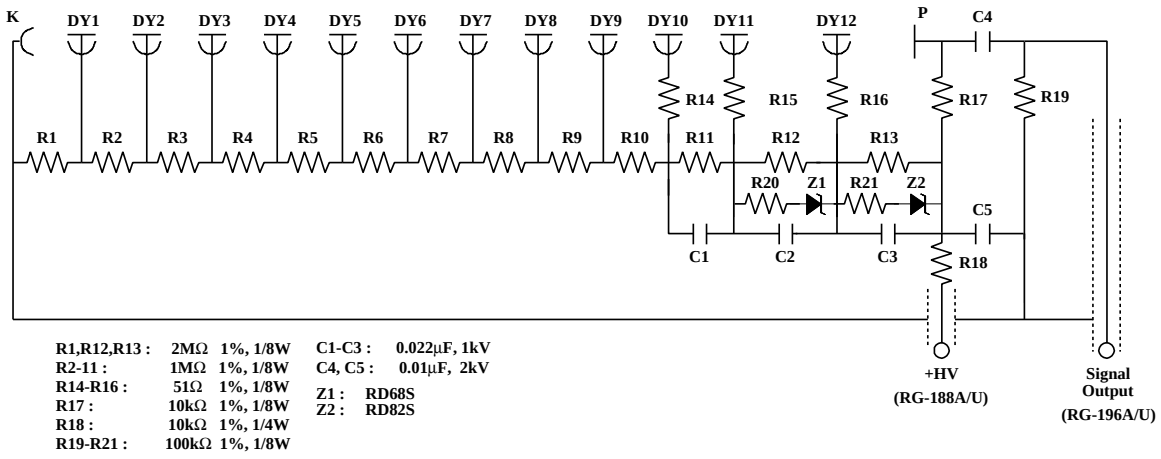

Figure 3.36: Divider circuit of photo-multiplier tube.

field was measured by three directions shown in Figure 3.37, because the PMTs are mounted on six different faces. There are larger decreases on lateral faces than others but no significant change on inner face as displayed in Figure 3.38. The measured decrease of gains from COBRA off to on is about 10% on average and sufficiently small.

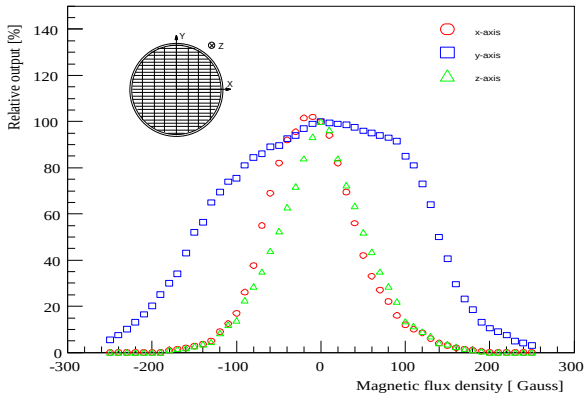

Figure 3.37: Response of PMT against magnetic field. Relative gain decrease is shown by three axes with different magnetic flux densities.

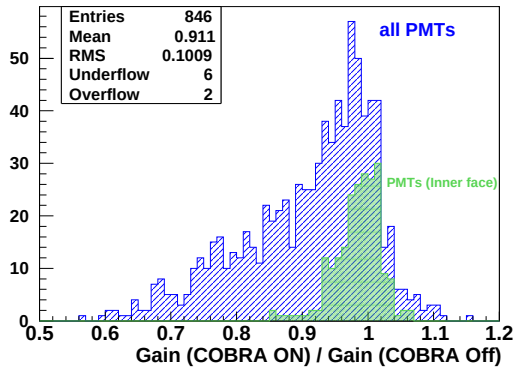

Figure 3.38: PMT gain ratios for COBRA magnetic field on / off. The ratio is measured with LEDs and shown by all PMTs. The gains of PMTs in the inner face have small changes as shown by a superimposed distribution around 1.

3.6.4 The 900-liter liquid xenon detector

The LXe detector uses liquid xenon of 900 liter volume (∼800 liter in active volume). In the liquid xenon 846 PMTs are mounted on all the six faces in liquid xenon. Figure 3.39 shows the C-shaped detector, which is mounted outside the magnet and covers 11% of the solid angle.

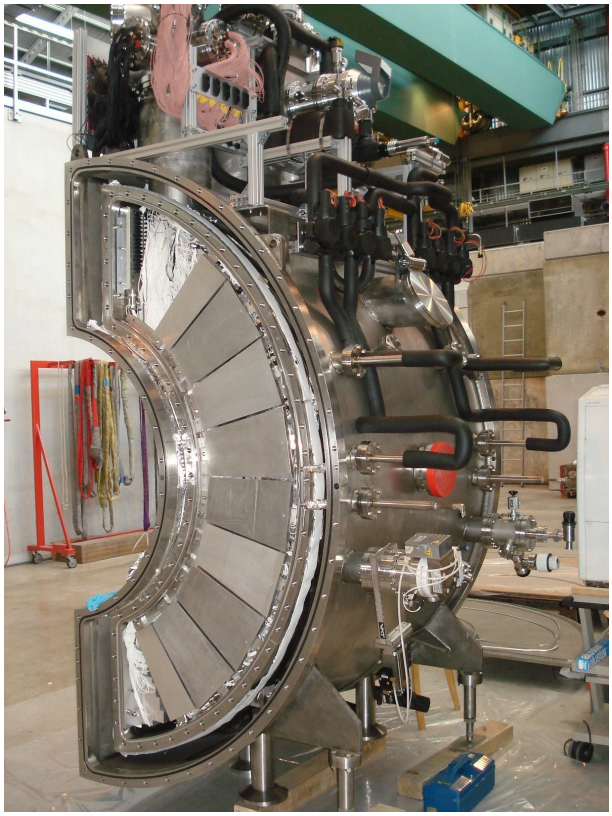

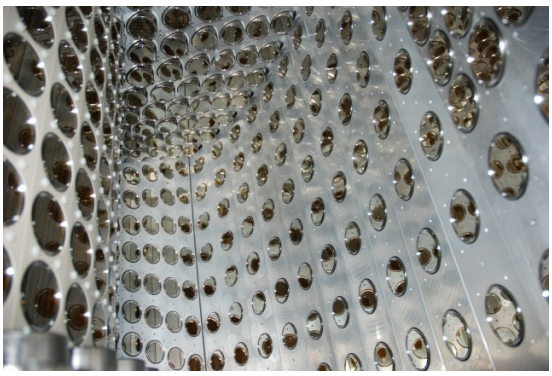

Inside of the liquid xenon detector shows the inner face on the left hand side and the outer face on the right.

Figure 3.39: The liquid xenon detector.

Figure 3.40 shows schematic view of the LXe detector. The inner face and the outer face are in a cylindrical shape with a radius of 67.85 cm and 106.35 cm respectively, while top and bottom face are on the planes of $\phi = \pm 60°$ and lateral down stream and up stream face are on $\theta = (\pm 30 + 90)°$. The 38.5 cm depth of liquid xenon is corresponding to 14 X_0. Development view of all faces is shown in Figure 3.41, where it can be seen that PMTs on the detection inner face are arrayed most densely. A special coordinate (u, v, w) based on the inner face is defined to describe a position of gamma-ray vertex in the detector.

$$R_{inner} = 67.85 \text{ (cm)} \tag{31}$$

$$u = z \tag{32}$$

$$v = R_{inner} \times \arctan(y/x) \tag{33}$$

$$w = \sqrt{x^2 + y^2} - R_{inner} \tag{34}$$

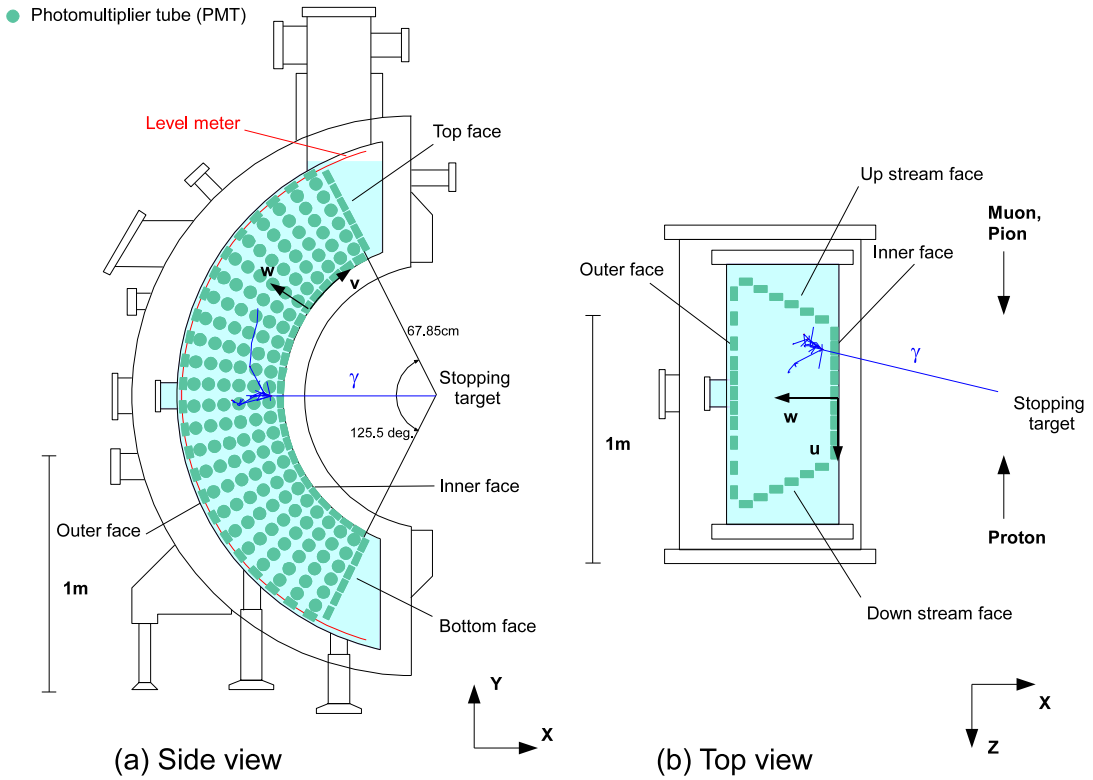

Figure 3.40: Schematic view of the liquid xenon detector.

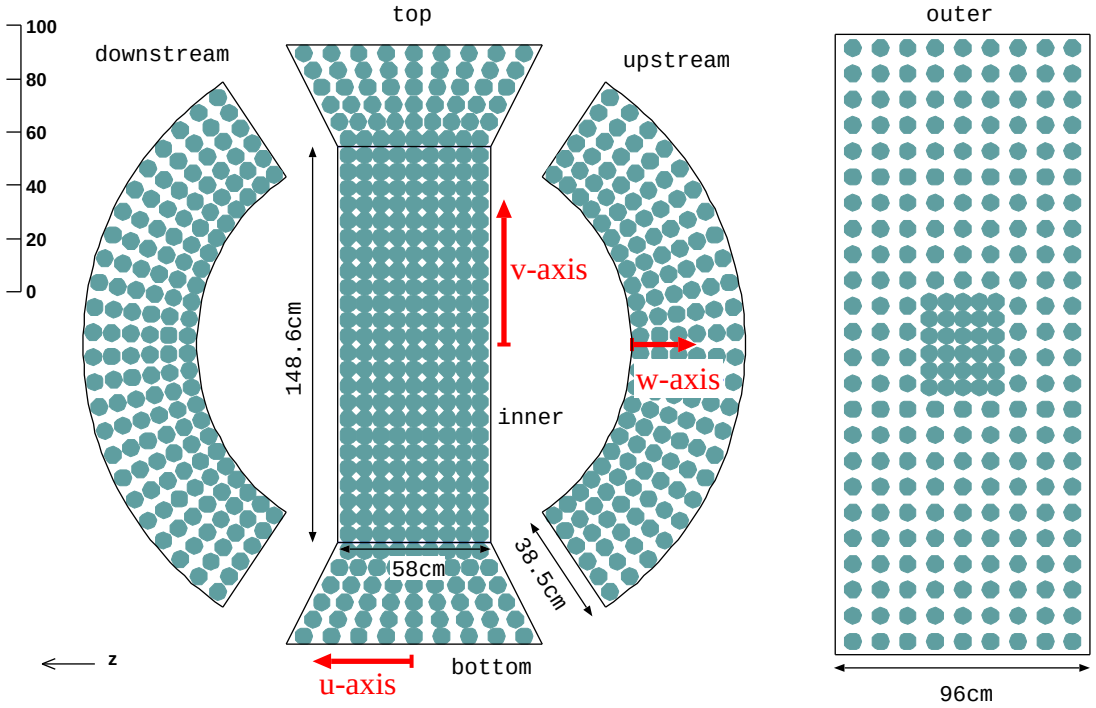

Figure 3.41: Development view of the faces of liquid xenon detector. Each face is equipped with 216, 234, 144 × 2 and 54 × 2 PMTs for inner, outer, lateral and top or bottom.

3.6.5 Constant calibration source in detector

The detector is equipped with LEDs and alpha sources in liquid xenon. The picture and location are shown in Figures 3.42 and 3.43.

^{241}Am source The point-like source of radioactive ^{241}Am had been developed for the MEG experiment [45]. It emits alpha ray at 5.485 MeV (84.5%) and 5.443 MeV (13.0%). The long 432-year life time is suitable for a year-long operation. Each source is optimized to be $\approx$ 200 Bq activity. Backgrounds from sources are negligible because we are measuring the events at the energy above a few tens of MeV. Five alpha sources are attached on a thin tungsten wire of 100 μm diameter with 12.4 cm interval as shown in Figure 3.44, and five wires are stretched from both lateral sides.

LED The blue-light LEDs with 470 nm wavelength are installed for the PMT gain calibration. They are flashed at 100 Hz for the gain measurement and constantly flashed at 1 Hz during the physics data taking for the gain monitoring. The light from LEDs is attenuated with pin hole and Teflon to illuminate PMTs more uniformly and to operate stable voltage with suppressing light intensity. Each lateral face has six mounted positions and five are in normal use for a constant calibration as shown in Figure 3.43.

3.6.6 Cryogenics

The cryostat of the MEG LXe detector requires thin window for the gamma-ray detection, non-magnetic materials, good thermal insulation and cooling system. The cryostat consists of two different inner and outer vessels to keep xenon cooling in liquid state. The insulation layer between two vessels is in vacuum state and super insulation sheets are installed to prevent a radiant heat from coming.

The entrance window for the gamma ray is made as thin as possible to suppress gamma-ray conversion inside. Thanks to aluminum honeycomb panel covered with carbon fiber plate at the inner vessel, the stainless steel part of the window is a thin of only 0.4 mm at the inner vessel with a high-pressure tolerance up to 0.5 MPa, the entrance window at the outer vessel is made of 0.7 mm-thick stainless steel. Its total thickness is 0.075 X_0.

Aluminum spacers are installed outside the PMT arrays to avoid scintillation light from the outside of the active volume and to save expensive xenon. A capacitance level meter is installed along outer face and 27 resistances of Pt-100 temperature sensors are attached to monitor the xenon temperature. All cables for HVs, signals, sensors and LEDs, with Teflon isolation to keep xenon clean, come out of the cryostat through the feedthroughs at the top of the detector. A 200 W pulse-tube refrigerator, a turbo molecular pump and a cryo-pumps are mounted at the top chimney of the detector [46]. The refrigerator shown in Figure 3.45 was specially developed for the liquid xenon cooling in the MEG. It enables to stably keep xenon in liquid with a help of the heater in the detector. In order to cool down the vessels quickly for a transportation of xenon or to help the refrigerator in normal operation, cooling pipes with liquid nitrogen are attached outside the outer and the lateral faces. In actual operation pipes on lateral side are sometimes used to cool down xenon in addition to constant cooling of refrigerator.

The detector has two storages to keep whole amount of xenon outside the detector for a maintenance or repair of the detector (Figure 3.46). One of the storages is a 1000-

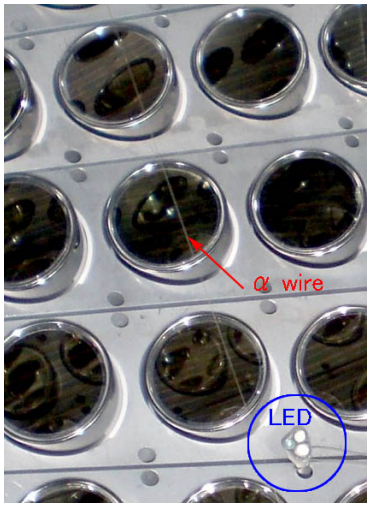

Figure 3.42: Inside view of the detector shows ^{241}Am source on wire and LED on wall. Three LEDs with different attenuations are mounted by each points on lateral faces.

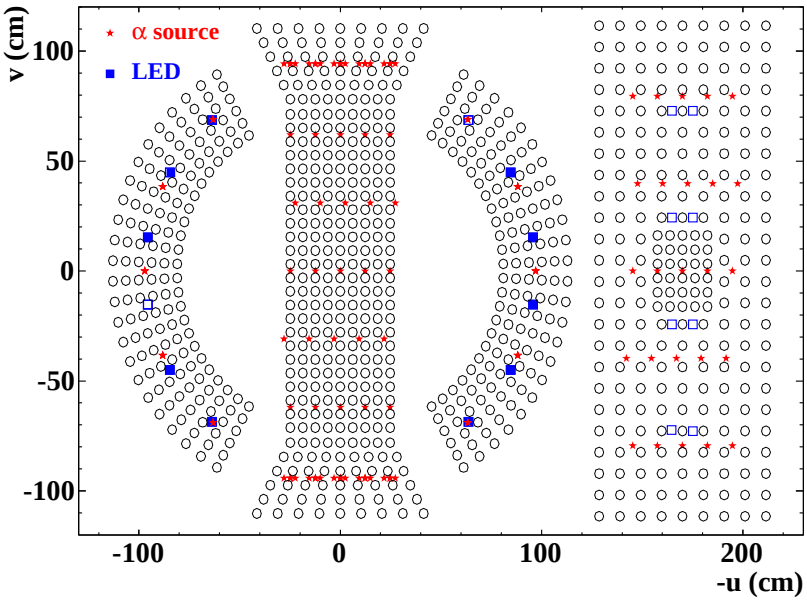

Figure 3.43: Projection view of 25 alpha sources on 5 wires and LEDs at 20 positions on the wall in the LXe detector. Filled 10 squares as LEDs are constantly used for a gain measurement and others are not used.

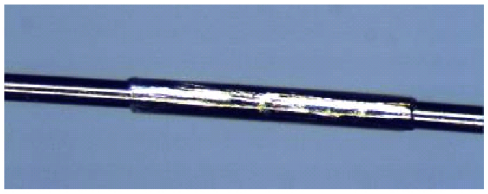

Figure 3.44: Close-up view of ^{241}Am source on tensioned wire along beam axis. Diameter is 100 μm and longitudinal dimension is about 2 mm.

liter dewar in Figure 3.47 to keep xenon as a liquid with a refrigerator [47]. The quick transfer and recovery is possible thanks to the liquid transportation and storage with a liquid pump. Another storage system consists of eight high-pressure gas tanks as shown in Figure 3.48 to store high-pressure gas of xenon stably for a long maintenance.

3.6.7 Purification system

In order to purify xenon, two types of purification system in liquid and gaseous phase were developed [48]. The liquid purifier system has oxidization-reduction filter made of copper and molecular sieves, which removes oxygen and water with 180 liter/h circulation by piston-type liquid pump. The system was installed at the back side of the detector (Figure 3.49). Another purification system in gas phase uses metal-heated getter to remove

Figure 3.45: Pulse tube refrigerator for liquid xenon.

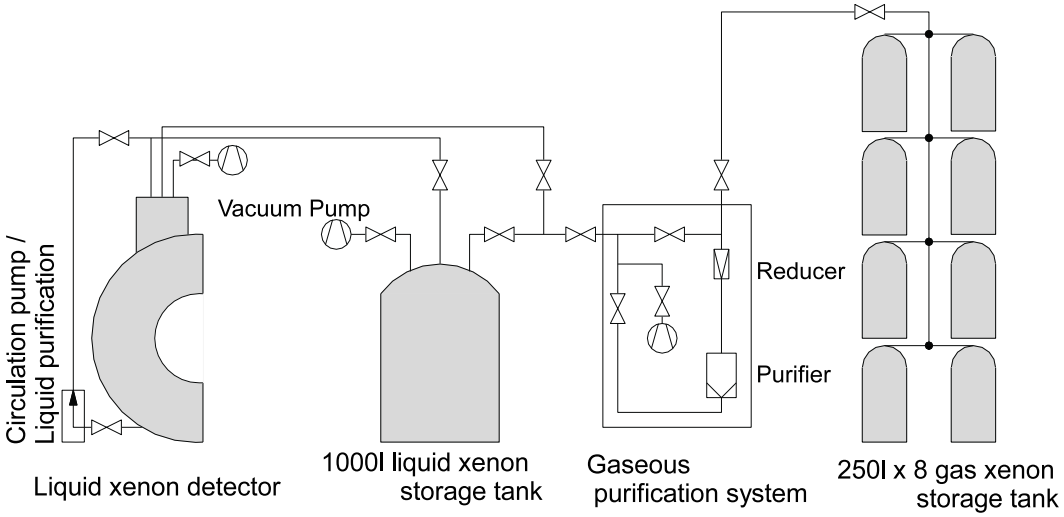

Figure 3.46: Cryogenics of the liquid xenon detector.

H_2O, O_2, CO, CO_2, N_2, H_2 and hydro-carbon molecules from gaseous xenon down to 1.0 ppb level with slow circulation speed lower than 100 cm^3/hour in liquid.

3.7 Setup for π^0 run

3.7.1 Purpose and principle

The gamma ray from π^0 decay is the most important calibration source for the energy, timing and positron with the LXe detector. The PSI beam facility can supply charged pions as well as muons and electrons or positrons to the πE5 area. The π^- beam is introduced to the center of the MEG detector with the same beam line and there are

Figure 3.47: Liquid xenon tank and gaseous purification system.

Figure 3.48: Gas xenon storage tank.

two processes occurred. One is the charge exchange reaction ($\pi^- p \to \pi^0 n \to 2\gamma n$) and another is the radiative capture reaction ($\pi^- p \to \gamma n$). The energy region from π^0 decays is between 54.9 MeV and 82.9 MeV, while a 129.4 MeV monochromatic gamma ray and a 8.9 MeV neutron are produced from the radiative capture. In addition the Dalitz decay of neutral pion ($\pi^0 \to \gamma e^+ e^-$) is a coincident event of a gamma ray and a positron or an electron. Thus it is useful to calibrate the drift chamber, too.

The energy range of the gamma-ray from the π^0 decay arises from the momentum of 28 MeV/c at the decay of the π^0 in the laboratory frame, after the charged pion π^- exchanges a charge with a proton of a hydrogen at rest. It is interested that the energies of generated two gamma rays from the π^0 decay are determined by the opening angle of $\theta_{\gamma\gamma}$ between two gammas,

$$\cos\theta_{\gamma\gamma} = \frac{m_{\pi^0}^2}{2E_\gamma(E_{\pi^0} - E_\gamma)}, \tag{35}$$

$$E_{\pi^0} = \frac{(m_{\pi^-} + m_p)^2 + m_{\pi^0}^2 - m_n^2}{2(m_{\pi^-} + m_p)} = 137.85 \text{ (MeV)}, \tag{36}$$

$$(m_{\pi^-}, m_{\pi^0}, m_p, m_n) = (139.57, 134.97, 938.27, 939.57) \text{ (MeV}/c^2), \tag{37}$$

where E_γ is the energy of the gamma rays (Figure 3.51). Equation 37 shows masses of charged pion, neutral pion, proton and neutron respectively. Monochromatic gamma-rays

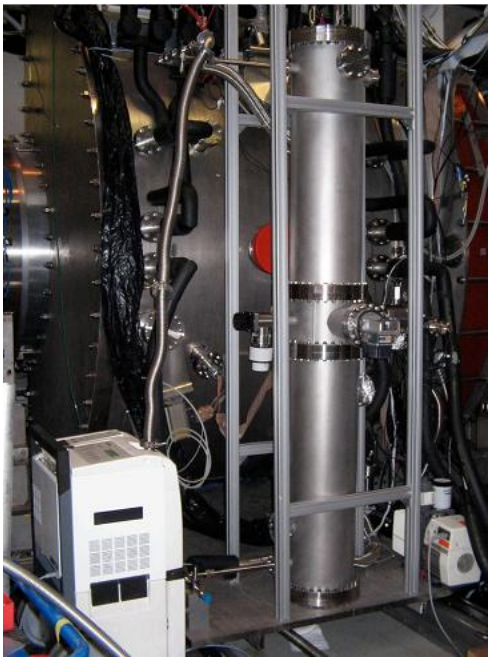

Figure 3.49: Liquid purifier in 2009.

of 54.9 MeV and 82.9 MeV are obtained by selecting back-to-back events (Figure 3.52). The lower peak of 54.9 MeV is very near to the signal energy from $\mu^+ \to e^+\gamma$, that is why we use it for the performance evaluation.

Because the LXe detector has a $2/3\pi$ acceptance along a ϕ direction, we need a tagging detector with the same coverage at opposite side in order to detect the back-to-back two-gamma-ray decay (Figure 3.50). A liquid hydrogen target placed at the center of the MEG detector instead of a muon stopping target.

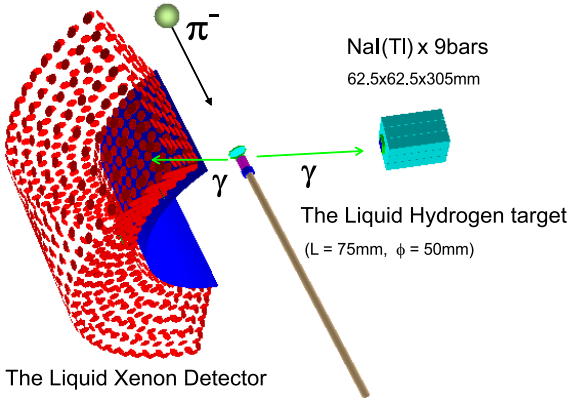

Figure 3.50: Overview of the setup in π^0 run.

3.7.2 Negative pion beam

In π^0 run a charged pion, π^0, decays into two gamma rays from after a single-charge exchange reaction of a negative charged pion and a proton. To obtain a monochromatic

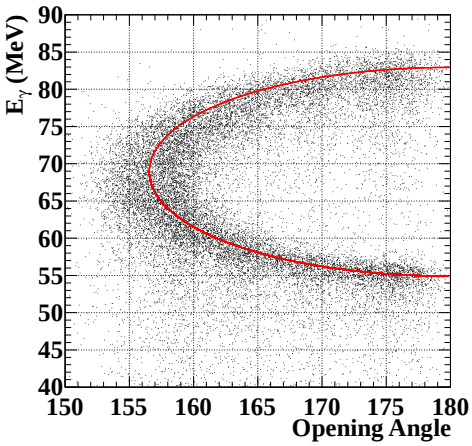

Figure 3.51: Gamma-ray energy and opening angle of two gamma rays in 2009 π^0 run at the LXe detector.

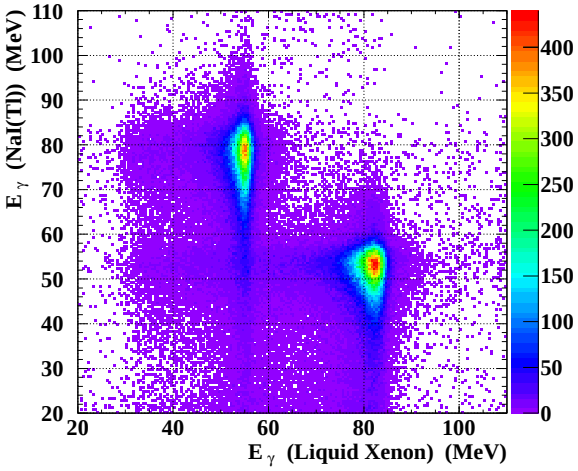

Figure 3.52: Energy distribution of two gamma rays from a π^0 decay with selecting back-to-back decays in the LXe detector and in the NaI detector.

π^0 momentum of 28 MeV/c, we select a liquid hydrogen as a stopping target from the at-rest charge exchange reaction (CEX) reaction, $^1\mathrm{H}(\pi^-, \pi^0)n$. The $\pi^- p$ system also results in a radiative capture to a neutron and a gamma ray, $n\gamma$.

The ratio of two channels is known as Panofsky ratio,

$$P = \frac{\sigma(\pi^- p \to \pi^0 n)}{\sigma(\pi^- p \to \gamma n)}, \tag{38}$$

which was measured in the previous experiments to be 1.5 [49, 50].

By a different configuration of BTS magnet and turning off the Wien filter, the negative pion beam is tuned to have a 70.5 MeV/c momentum and the measured spot size at the hydrogen target of $\sigma_x \sim 8.5$ mm and $\sigma_y \sim 7.5$ mm. Because negative pions come from a bunch of the pulse beam with many contaminations of electrons and cloud muons, more backgrounds are observed than in the muon beam. We optimized the beam intensity testing several conditions of the beam slits to consider some effects in the LXe detector such as a pileup.

3.7.3 Liquid hydrogen target

The liquid hydrogen (LH_2) target has a cylindrical cell of a 50 mm diameter with a 75 mm length filled with ~150 cc LH_2 in 20 K cooling (Figure 3.53). The window of the target cell is made of a thin 135 μm mylar window. The target is inserted from down stream side with a two meter long pipe.

A hydrogen buffer of two bottles with 47 liters each is connected to the LH_2 cell constantly with 2.5 bar in gas or 1.2 bar after the liquefaction. A flow of the liquid helium from the 250 liter dewars enables liquefaction of hydrogen with a pressure control.

The setup of the LH_2 target takes about three days to remove the proton beam line of Cockcroft-Walton accelerator, assemble the target system and cool a hydrogen. One

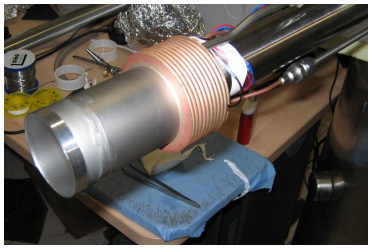

Figure 3.53: Liquid hydrogen target.

helium dewar is exhausted per a few days during π^0 run with a decrease of about 2.4% per hour and the exchange of the dewar needs for a few hours. The π^0 run is usually planned less than a few times per year because of its long running time about one or two weeks.

3.7.4 NaI tagging detector

Because the LXe detector has the acceptance with 120° along ϕ direction and ±30° along θ, it detects only one gamma ray from a back-to-back decay of π^0. In order to obtain monochromatic gamma-rays from the back-to-back decays, another calorimeter is required at opposite side of the LXe detector. It allows the LXe detector to measure a lower gamma-ray energy near to $\mu \to e\gamma$ signal. The selection of opening angle depends on the geometry of the detectors' setup and it determines the energies of two gamma rays (Figure 3.51). Therefore the only important issue for the tagging detector is to identify higher energy of two gamma rays in a certain precision at the back-to-back position opposite to a measured position of the LXe detector and a high performance of the tagging detector does not required. We adopted the movable NaI detector for that.

The tagging detector for one of two gamma rays consists of nine crystals of NaI(Tl) scintillator and two layers of plastic scintillator for the timing measurement. In order to scan the whole acceptance of the LXe detector, the NaI detector is mounted on a mover that can get the same coverage of the LXe detector. The NaI mover has three movements along ϕ direction from $-57°$ to 57°, z direction from -350 mm to 350 mm corresponding θ direction from $-24°$ to 24° and θ-rotation from $-22°$ to 22° to always face the target. Figure 3.54 (a) shows a picture of the mover. The array of the 3 × 3 NaIs is put on the stage and the plastic timing counter is attached in front of the central NaI.

There are some difficulties in the readout of the scintillation photons from the NaI crystal by a PMT. The PMT gain varies depending on the position of the NaI due to the magnetic field and it is difficult to mount PMTs due to the limited space. Therefore, for the detection of the scintillation photons, APDs and charge amplifiers are adopted. On the other hand for the plastic scintillator, fine-mesh PMTs are used for a photon detection because there is no need of a severe energy selection for the plastic scintillators from a trigger point of view.

Each NaI crystal has a size of 62.5 mm × 62.5 mm × 305 mm (11.8 X_0) and its acceptance of 6° or 0.07% solid angle per crystal is almost the same as the 1 PMT size on the inner face of the LXe detector. For the timing measurement the two plastic scintillators of 60 mm × 60 mm × 7 mm are attached in front of the central NaI crystal. A lead converter of 50 mm × 50 mm × 5 mm is put on the plastic with 2.2 X_0. About

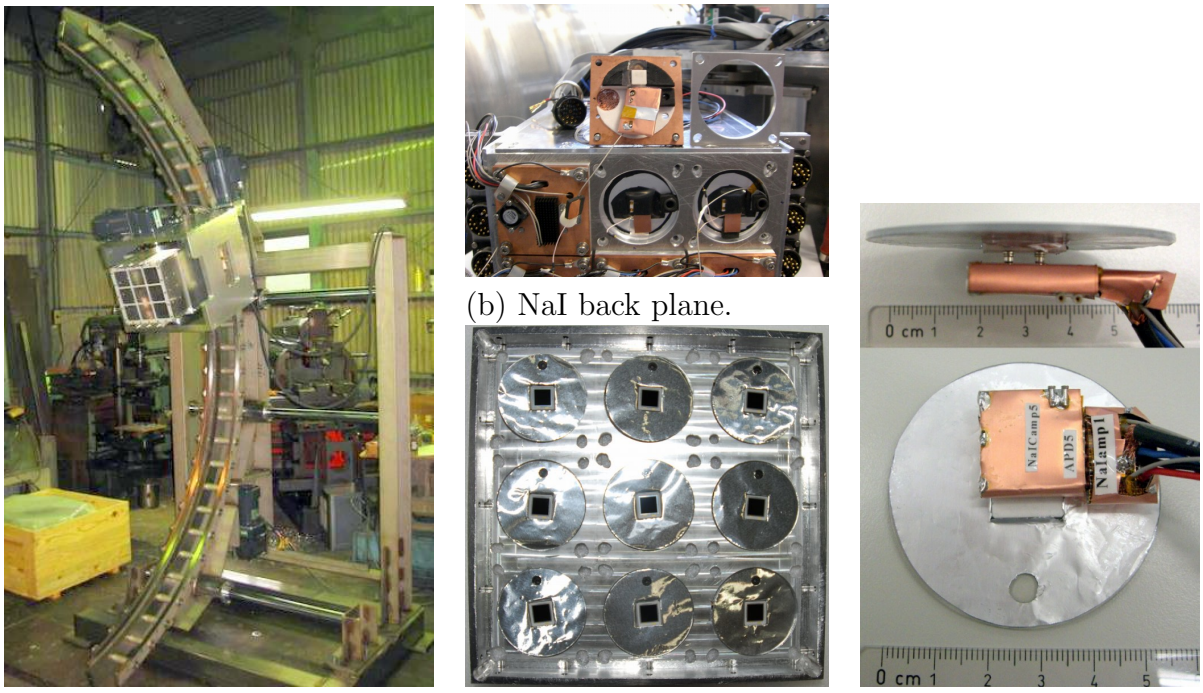

(a) NaI mover. (b) NaI back plane. (c) APDs alignment. (d) Amplifiers and APD.

Figure 3.54: Apparatus of the NaI detector for π^0 decay run.

40% of gamma rays are counted in plastic scintillator. However, for the efficient energy measurement it can be removed if there is no need to measure timing.

We use the APD (H8664-1010, Hamamatsu Photonics) with a 10 mm × 10 mm active area and 2 mm thickness. It works with 410 V and 50 gain typically and detects scintillation photons from the NaI crystal without shifting wavelength. One primary amplifier integrates charges and converts its to amplitude, then shaping amplifier forms and amplifies the signal. The charge amplifier is gn0261 (GNomes Design co.,ltd.) developed by Hiroshima University with a 19 mm × 19 mm size and 0.8 V/pC gain. On the other hand the shaping amplifier is a small handmade amplifier with a size of 13 mm × 18 mm and has two outputs (Figures 3.54 (d) and 3.55). The waveform is analyzed in two different waveform sampler, both a DRS chip and a digitizer in the trigger board as later described in Sections 3.9.4 and 3.9.5, then the pulse height is estimated. Figure 3.56 shows a sample of a waveform obtained from the DRS with enough time window for a peak estimation.

The design principle of the APD module is the following.

- Detect photons in APD with light guide.
- Amplify and shape signal from APD.
- The temperature of APD is controlled with a Pt-100 temperature sensor and a Peltier device.
- Heat radiator made of copper and fan to ventilate air inside module.
- Optical contact to lead laser (not used).

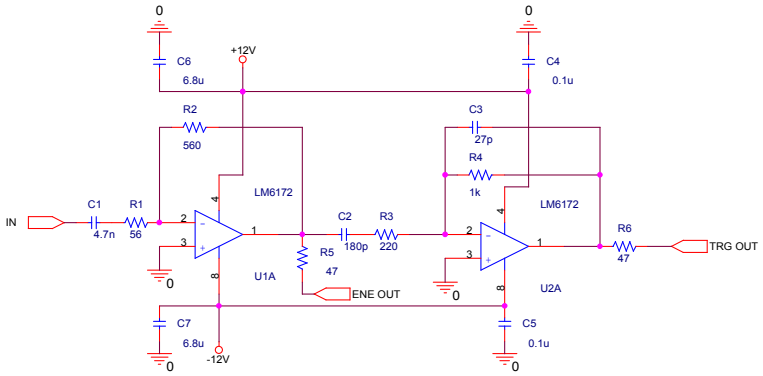

Figure 3.55: Shaping amplifier.

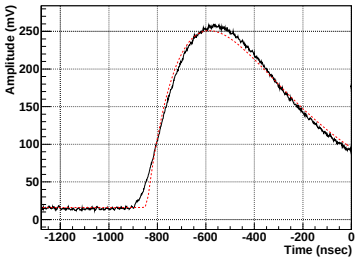

Figure 3.56: Sample of waveform from NaI+APD signal and a fit with dotted line.

- Blue LED (Surface Mount Device type) coupled to NaI for a APD monitor.
- Both charge amplifier and shaping amplifier and easily replaceable.

Beside the optical window of the NaI, all the electronic parts are housed in a small space of cylindrical shape, 52 mm diameter with 10mm thickness. The module is attached at the back plane of the NaI crystal with a total module size of 64 mm × 64 mm × 10 mm except for screw and fan as shown in Figure 3.57.

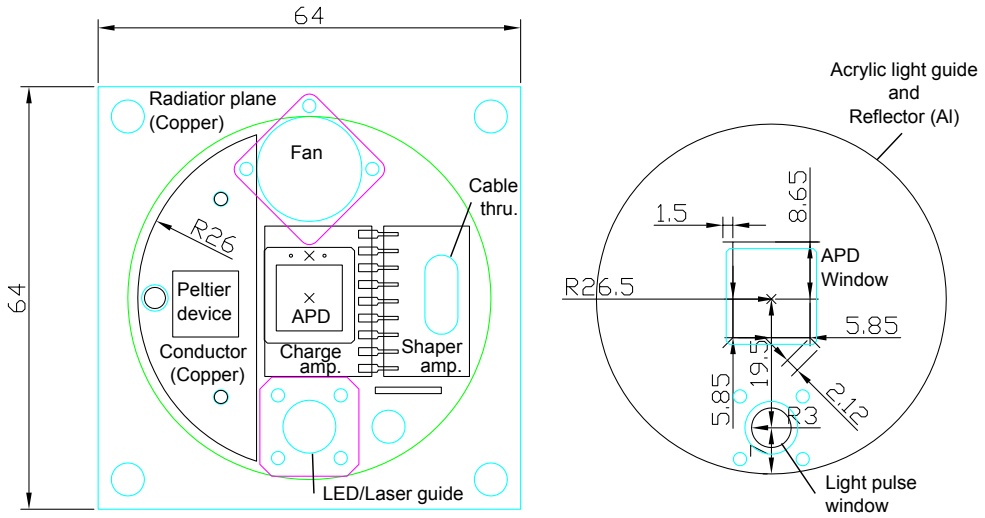

(a) APD module (b) Light guide

Figure 3.57: Layout of the APD module.

The APD can get less noise at low temperature, however, it is difficult enough to cool the all detector down because the APD shares a heat capacity with the NaI crystal. The purpose of thermal control is to keep the gain of APD constant by cooling only around the APD. With a help of the slow control system of SCS-2000, very precise thermal control is enabled within 0.08% stability with the cooling ability of the 10 °C lower than room temperature. Figure 3.58 shows the stability of the controlled temperature around the

APD for two days in the lowest graph and the active voltage control for the Peltier device in the top graph, and the thermal monitor of backplane and room temperature in the middle graph. The details of the calibration and performance are given in Appendix C.1.

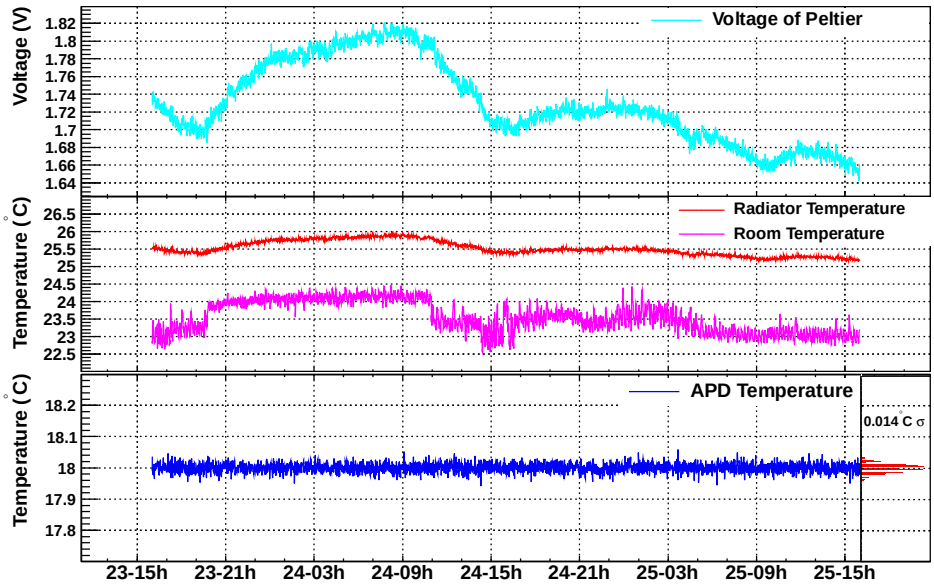

Figure 3.58: Thermal control and monitor of the central NaI crystal.

3.7.5 Pre-shower counter in front of the NaI

In front of the central NaI crystal, two layers of plastic scintillators are put for a timing measurement (Figure 3.59). A lead converter of 5 mm thickness is put in the front to make a shower of charged particles into the plastic scintillator. The converter or the counter can be removed in case of unnecessary to measure timing and the efficiency of the energy measurement accordingly increases. The scintillation is read out by two PMTs at both sides of the scintillator with a light guide along the ϕ-direction. The PMTs are H6152 made by Hamamatsu Photonics with photocathode of 17.5 mm ϕ and fine mesh dynode to work in the magnetic field.

3.8 Cockcroft-Walton proton accelerator

3.8.1 Purpose and principle

A Cockcroft-Walton (CW) proton accelerator dedicated for the MEG experiment is installed at the downstream side of the MEG detector for the calibration of the LXe detector. Gamma rays from nuclear reaction of the proton in various targets are very useful for the constant and frequent monitor of the scintillation light yield of the LXe detector, as well as the estimation of energy response of whole detector. The normal target for the muon beam can be replaced by the target for the CW. The replacement can automatically be done by inserting the beam pipe with the CW target from the downstream side using a bellows system. Frequent calibration is possible because the target exchange needs only a few minutes, on the other hand it is absent during the π^0 run because the downstream side is occupied with the hydrogen target.

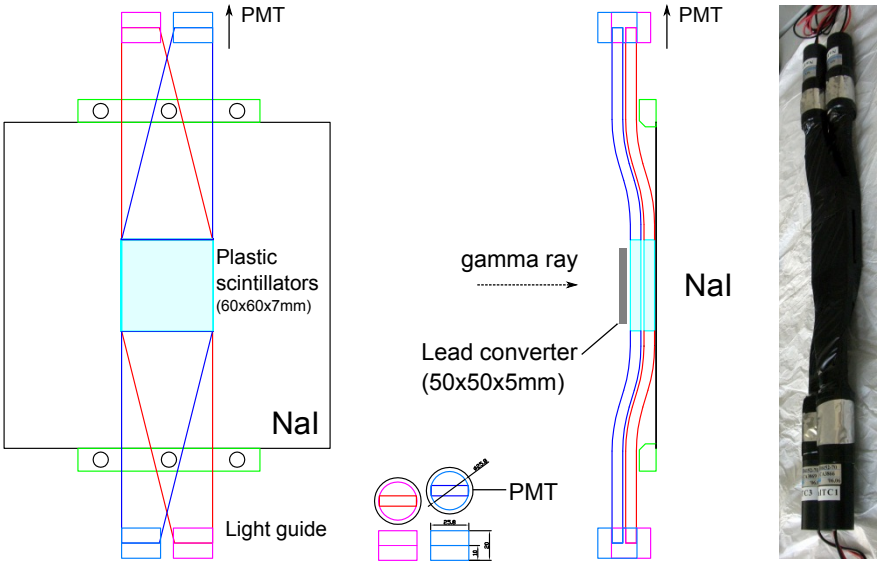

Figure 3.59: Timing counters in front of the NaI (Front view, side view and a picture).

The normal target made of lithium tetraborate ($Li_2B_4O_7$) provides reactions from a lithium and a boron. The most useful energy peak at 17.7 MeV is obtained from the resonant reaction in lithium, ${}^{7}_{3}\mathrm{Li}(p,\gamma){}^{8}_{4}\mathrm{Be}$ with a resonance energy at $T_p = 440$ keV ($\Gamma_R \simeq 12.5$ keV). The 17.7 MeV clear peaks can be a source of precise light yield monitor within 1% and allows to estimate a correction factor to make the detector response uniform over whole acceptance of the detector.

Another gamma-ray peaks from boron are coincidently given by the nuclear reaction, ${}^{11}_{5}\mathrm{B}(p,\gamma){}^{12}_{6}\mathrm{C}$ with a resonance at $T_p = 163$ keV ($\Gamma_R \simeq 5.3$ keV). Available energies are 11.7 MeV depending on the incident proton energy and another 4.44 MeV from ${}^{12}\mathrm{C}^{*}$ at coincident time, therefore it allows the timing measurement between timing counter and the LXe detector, as well as the confirmation of the energy scale or the light-yield monitor. Figure 3.60 shows peaks in the LXe detector obtained in CW run.

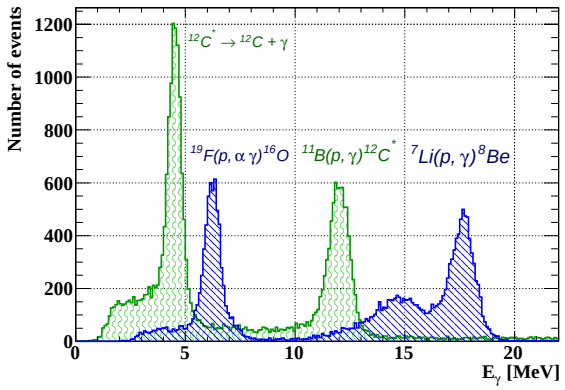

Figure 3.60: Energy peaks in the LXe detector with a use of the CW accelerator.

3.8.2 Cockcroft-Walton accelerator

For the calibration of the LXe detector, the CW accelerator for the MEG experiment produces the proton beam up to 1 MeV with a intensity of 10^{12} sec^{-1}. Detailed property is noted in Table 7 and Figure 3.61 shows the inside of the accelerator. The accelerator is placed at the small separated area beside the πE5 area. From the downstream side the accelerated protons are transported to the center of the MEG detector and the beam direction is opposite and parallel to the muon beam line (Figure 3.62). The gamma rays are produced at the center of the COBRA magnet as well as the gamma rays from RD, therefore we can calibrate the LXe detector at the same condition as in the muon data taking.

Table 7: Properties of MEG CW accelerator.

	Nominal	Measured at PSI
Terminal energy range (keV)	$300 - 900$	$200 - 1100$
Energy ripple (RMS eV)	< 500	< 50
Angular divergence (mrad×mrad)	5×5	$\sim 4 \times 4$
Spot size at 3 m (cm×cm)	$< 3 \times 3$	< 1
Energy setting reproducibility (%)	0.1	OK
Energy stability (FWHM %)	0.1	OK
Range of current (μA)	$1 - 100$	$0.1 - 135$
Current stability (%)	3	OK
Current reproducibility (%)	10	OK
Duty cycle (%)	100	OK
Start-up time (min)	< 20	< 15

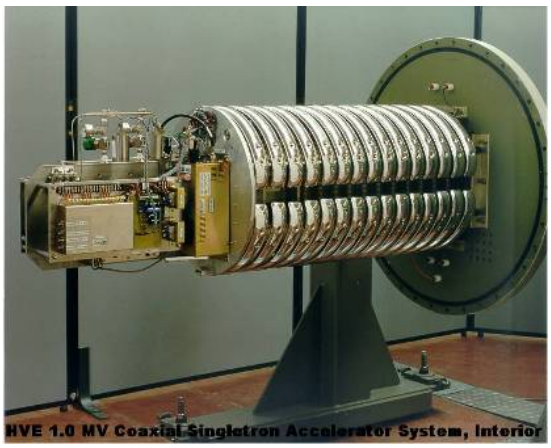

Figure 3.61: Electrode cascade inside the CW accelerator.

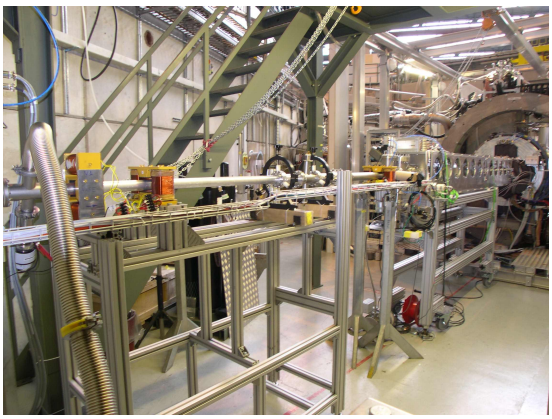

Figure 3.62: CW beamline installed at the down stream side of the MEG detector.

3.8.3 Beamline and target

We had tested various targets with changing proton energy. The current target made of a thick lithium tetraborate ($Li_2B_4O_7$) crystal disk is mounted at the end of the proton beam line. We can select the reaction of $^{7}_{3}\mathrm{Li}(p,\gamma)^{8}_{4}\mathrm{Be}$ or $^{11}_{5}\mathrm{B}(p,\gamma)^{12}_{6}\mathrm{C}$ with the same target by setting the proton kinematic energy to 500 or 700 keV, respectively.

Figure 3.63 shows a resonance of lithium and excitation curve for a thick target. The right side peak of the proton beam in the figure is higher but it can interact with a thick lithium target on a flat resonance. The emitted gamma-ray energy depends on both a proton energy and an emitted angle from proton, thus the lithium peak energy and the higher energy of the boron peaks should be calculated. The peak energy from lithium is estimated to be 17.7 MeV with a 0.8% width in sigma in the case of our usual setup (500 keV and FWHM $<$ 0.5 keV), on the other hand the higher peak from boron gets 12.0 MeV energy.

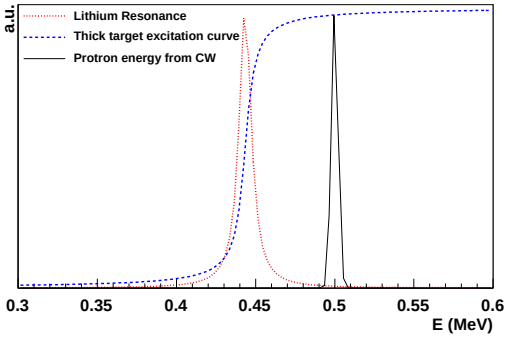

Figure 3.63: Energy spectrum and resonance of the lithium target.

3.9 Electronics and data acquisition

3.9.1 MIDAS

The MEG experiment uses MIDAS (Maximum Integration Data Acquisition System) developed at PSI as a DAQ system [51]. MIDAS works on many platforms and provides a graphical interface with a full control on a web browser as a HTML format from a HTTP server. The parameters of setup are written in the online database (ODB) and some parameters can be shown in graphical history plots for a monitor. After front-end programs running on different machines collect data, event builder generates events from buffers and logger system writes data. Thanks to the independent treatment of hardwares, any access to specific hardware are possible with user's implementation, though drivers for typical DAQ hardware such as CAMAC, FASTBUS and VME are already available.

3.9.2 Slow control system

To control all hardwares remotely in the same way, most of modules for the control have a communication based on the Midas Slow Control Bus (MSCB) developed at PSI. Modules are grouped by purpose or physical location in the area and internally synchronized via the MSCB bus, then each group has an external access with USB or Ethernet adapter.

A slow control frontend program runs in one of the online machines for the DAQ and all groups are centralized in it to be operated by the DAQ system. In addition, both a manual control with Character-based User Interface (CUI) and a control with a Graphical-User-Interface (GUI) programs such as LabVIEW (by National Instruments) are remotely possible.

One of the main purpose to use the slow control systems (SCS) is to store a log of various monitors. The log is recored by external programs such as the MIDAS DAQ system or LabVIEW. All measured values are stored in MIDAS at beginning of each taken run. Some of them are also recorded in MIDAS during a run with a constant slow rate of 0.1 Hz independently from normal DAQ.

There are various modules of the SCS developed for the MEG experiment. The most modules can be operated under a stand-alone control with a programmable firmware even if these lose commands from an external system, which allows the safe control and minimizes traffic. For example, all HV dividers in the MEG are based on the system and control HV under specified limit of voltage and current, ramp it up gradually, equip with auto-recovery and provide measured voltages and currents to the DAQ. For the most controls we use SCS-2000 device with many functions. It accepts up to eight daughter cards and a back panel to supply input or output channels up to 64, eight channels per a card, is attached. The various cards such as ADC, DAC, some kinds of relays, current source, voltage meter, capacitance meter, LED pulser are available. The systems in the MEG experiment are listed in Table 8.

Table 8: Running systems based on SCS for the MEG experiment.

COBRA and BTS monitor, Beam status,
HV of LXe, TIC, DCH and NaI, Environment monitor such as temperature,
VME crate monitor, Gas system for DCH, Purifier of xenon,
Control of 1000L LXe tank, Operation of LXe, LED pulser for LXe,
CW accelerator and beam line, Operation of AmBe source (since 2010),
Operation of the liquid hydrogen target,
NaI mover system, NaI thermal control

3.9.3 Data acquisition

Because plenty of data mainly from over a thousand waveforms is recorded, there are a few separated stages on DAQ for a reduction of data. At early stage in frontends before data are concentrated to MIDAS, some data reductions for waveforms are performed by suppressing zero-signal waveform or re-binning uninteresting region except for peaks or a baseline, which can be customized by run or event type. All events both from triggered data and periodical monitor are stored in a special data format for MIDAS, then compressed and transferred to a archive system and also to a storage system of analysis clusters. The data transfered to cluster are analyzed immediately and various plots are generated to show data quality. The analyzed result is stored as a ROOT format in a few separated files for the result of the reconstruction and for the raw data such as waveform or temperatures. The information of run is recorded in MySQL database commonly used

in whole MEG analysis. During data taking, a display to monitor a quality of a real-time data is provided by the same analyzer program.

3.9.4 Trigger system

Except for the timing fiber z-counter, all signal waveforms from detectors are taken, while signals for a trigger are arranged by each detector. The DCH does not take part in a $\mu^+ \to e^+\gamma$ trigger because of a slow signal and a necessity of a complex analysis to reconstruct events. Therefore the trigger for the muon decay is based on fast PMT signals from the LXe detector and timing counter, which allows to acquire high-rate muons with less dead time. With a help of a late readout of capacitor buffer arrays in the waveform digitizer (DRS), the trigger system also has an ability to take coincident π^0-decay events between fast PMT signals from the LXe detector and slow APD signals from the NaI detector arriving a hundred nano seconds later. The topology of the trigger system has a tree structure with triple layers and roughly selects kinematics of the gamma energy and time difference and opening angle. Because the timing z-counter was absent in 2008 and 2009 run, the positron information only from the timing ϕ-counter determines the trigger without precise direction match between a positron and a gamma. Nevertheless, the system shows enough trigger performance.

Trigger structure The following signals are formed for the trigger system.

- LXe inner face (216 PMTs, 1 channel per PMT)
- LXe lateral faces (288 PMTs, 1 channel per 4 PMTs)
- LXe back+up+down faces (342 PMTs, 1 channel per 4 PMTs except one case with 1 channel per 2 PMTs)
- TICP bars (60 PMTs, 1 channel per PMT)
- TICZ fibers
- DCH wires (64 wires, 1 channel per wire)
- Auxiliary channels (NaI, LED, Beam)
- Cosmic ray counters for DCH calibration

Two types of trigger boards make a tree structure with three layers and branches are classified by a part of the detectors. At the first stage seen by incoming signals, trigger boards of VME 6U named Type1 accept signals in flash analog to digital converters (FADC, AD9218, Analog Devices) and digitizes it at 100 MHz with 10 bits bin resolution to acquire waveforms. Type2 trigger boards of VME9U at the second layer collect outputs from Type1 boards with five boards and finally into one Type2 board and it makes a trigger for DRS.

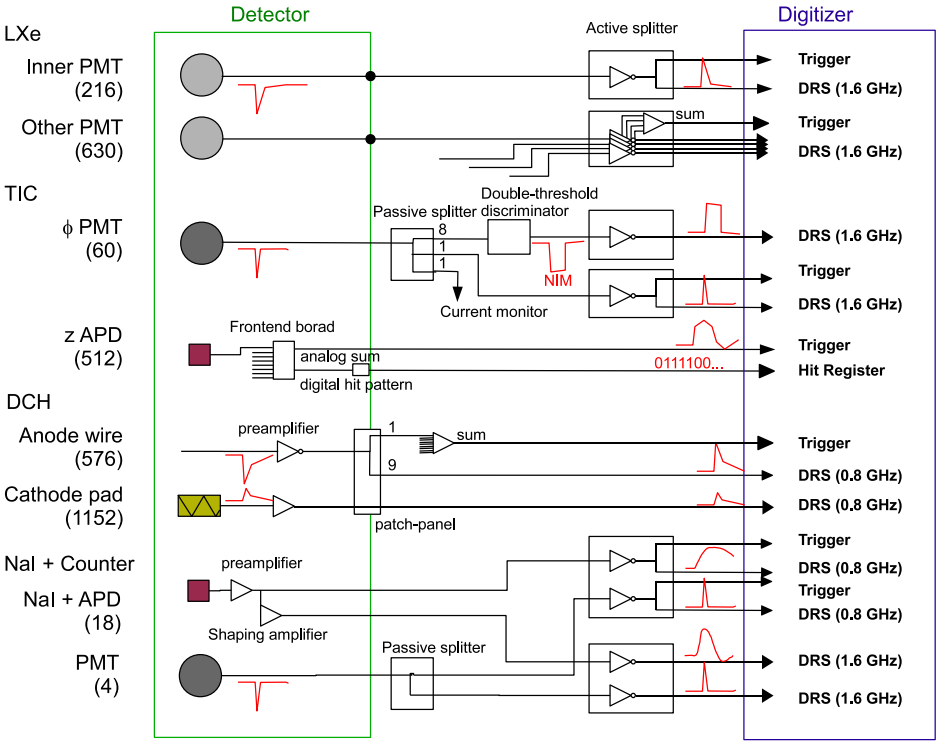

Figure 3.64: Flow of signal processing from detectors to the trigger and the waveform digitizer (DRS).

Signal from gamma ray to trigger The signal from the LXe detector and the timing ϕ-counter goes into active splitter boards, each with 16 input channels, to split the signal for the waveform digitizer (DRS) and the trigger. The amplifiers with a high 1900 MHz bandwidth (THS4509, Texas Instruments) of the active splitters send one of split signals to DRS with inverting its polarity from negative to positive. Another split signals from the amplifiers with a 320 MHz bandwidth (AD8138, Analog Devices) are brought into the trigger with summing a part of them. Figure 3.64 shows the signal flow from the detectors to the trigger system and the waveforms digitizer. From the inner face of the LXe detector all the 216 channels go to the trigger, while outputs from 288 PMTs on lateral faces and 342 PMTs on other faces are grouped every four PMTs.

Signal from positron to trigger The each signal from 60 PMTs of timing ϕ-counter is split to three in a passive splitter with a ratio of 8:1:1. The output of ten percent is for a current monitor to check the lifetime of PMTs. Another ten percent goes to active splitter, which is split to two signals with the same amplitude as the input. One of them is sent to a trigger board and the amplitude drops by 30% due to the limited bandwidth. Another is acquired with DRS to determine the charge and the amplitude but the timing. The largest 80% signals are shaped with double-threshold discriminator (DTD) which generates output of NIM signal. The lower threshold (25 mV) allows a good timing performance with a less effect of a time walk as possible, while the higher threshold prevents a fake signal due to noise or delta-ray hits. The output of 50ns-width NIM signal is acquired also by the DRS.

Other signals to trigger For various calibrations other detectors such as the NaI detector, cosmic-ray telescope counters for DCH calibration and neutron generator can participate in trigger. Other trigger signals from pedestal, LED, laser and proton current are also fed to the trigger system. Although the information of the primary proton current provided at PSI is not currently used for triggers, it is useful to monitor beam status and can optionally treat triggers depending on beam status if it were necessary.

Trigger algorithm Trigger algorithm is programmable on FPGA (XILINX Virtex-IIpro) and we define up to 32 trigger types as listed in Table 9. By each trigger type we count the number of triggered events and record live and dead time for each trigger type. Rate of each trigger can be adjusted by a pre-scale factor for each trigger type. These facility enables to count intrinsic triggered events as well as DAQ events.

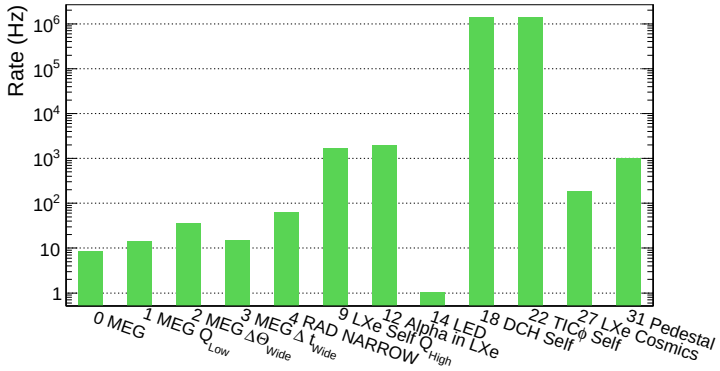

Figure 3.65: Trigger rate by each trigger type in the $\mu^+ \to e^+\gamma$ taking run.

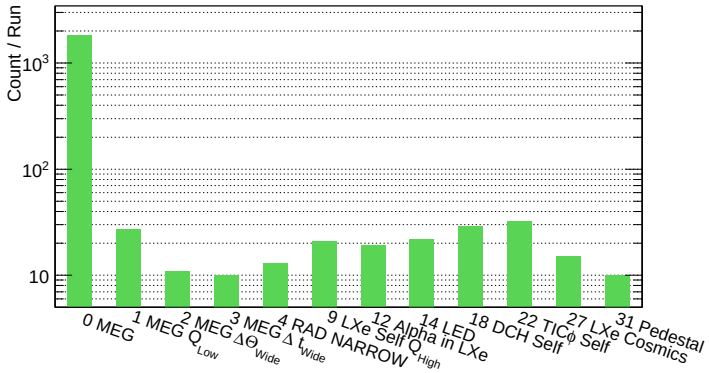

Figure 3.66: Taken events by each trigger type with pre-scaled in the $\mu^+ \to e^+\gamma$ taking run.

Thanks to the customized program and waveforms in trigger boards, flexible and complicated trigger are possible. For example, it is possible to select alpha events in the trigger under high-rate gamma-ray background by using information of waveform.

The DAQ has typically 84% live time and the triggered event rate of $\mu^+ \to e^+\gamma$ candidate was 5 Hz and total DAQ rate is 6.5 Hz.

Table 9: Trigger definition and pre-scaling factor (Prsc) in the MEG 2009 run. Approximately $Q_{low} \sim 30$ MeV, $Q_{high} \sim 40$ MeV, $T_N \sim 20$ ns, $T_{wide} \sim 40$ ns and $T_0 \sim 100$ ns are adopted.

Id	Trigger type	Prsc.	Logic
0	$\mu^+ \to e^+\gamma$	1	$(Q_{LXe} > Q_{high}) \wedge (\lvert T_{e\gamma}\rvert < T_N) \wedge (\Theta_{e\gamma} < \Theta_N)$
1	$\mu^+ \to e^+\gamma$, low energy	50	$(Q_{LXe} > Q_{low}) \wedge (\lvert T_{e\gamma}\rvert < T_N) \wedge (\Theta_{e\gamma} < \Theta_N)$
2	$\mu^+ \to e^+\gamma$, wide angle	500	$(Q_{LXe} > Q_{high}) \wedge (\lvert T_{e\gamma}\rvert < T_N) \wedge (\Theta_{e\gamma} < \Theta_{\rm wide})$
3	$\mu^+ \to e^+\gamma$, wide T	200	$(Q_{LXe} > Q_{high}) \wedge (\lvert T_{e\gamma}\rvert < T_{wide}) \wedge (\Theta_{e\gamma} < \Theta_N)$
4	$\mu^+ \to e^+\nu_e\overline{\nu}_\mu\gamma$ narrow / Dalitz decay in π^0	1000	$(Q_{LXe} > Q_{low}) \wedge (\lvert T_{e\gamma}\rvert < T_N)$
5	$\mu^+ \to e^+\nu_e\overline{\nu}_\mu\gamma$ wide T / CW-B	-	$(Q_{LXe} > Q_{low}) \wedge (\lvert T_{e\gamma}\rvert < T_{wide})$
6	π^0 with NaI	-	$(Q_{LXe} > Q_{high}) \wedge (Q_{NaI} > Q_{thr})$ $\wedge_i (Q_{NaI,4} > Q_{NaI,i}) \wedge (\lvert T_{\gamma\gamma}\rvert < T_0)$ $\wedge$ PMT patch on LXe $\wedge$!(Id=7)
7	π^0 w/o pre-shower	-	$(Q_{LXe} > Q_{high}) \wedge (Q_{NaITC} > Q_{thr}) \wedge (\lvert T_{\gamma\gamma}\rvert < T_N)$
8	NaI alone	-	$(Q_{NaI} > Q_{thr})$
9	LXe alone High	20000	$(Q_{LXe} > Q_{high})$
10	LXe alone Low / CW-Li / α	-	$(Q_{LXe} > Q_{low})$
12	α selection	22000	$(Q_{LXe} > Q_0) \wedge \alpha$ selection
14	LED	10	100 Hz pulse from LED module (1 Hz in the physics run)
16	Michel DCH track + TC hit	-	DCH hits $\wedge$ TIC hits
17	DCH track w/o outer	-	DCH self
18	DCH track	10^7	DCH self
19	Cosmic DCH	-	Outer tagging CR counters
20	DCH single chamber	-	DCH single self
21	Cosmic Counter alone	-	Cosmic-ray on TIC
22	TC alone w/ bar mult.	10^7	
23	CR counter coinc.	-	
24	TC Pair	-	
27	LXe Cosmic	2500	
28	NaI counter alone	-	
31	Pedestal	20000	Clock for pedestal

3.9.5 Waveform digitizer

We have two different waveform samplers. One is for the trigger purpose and another for the analysis. The slower FADC of 10 ns width/bin described in Section 3.9.4 is used for the trigger and the faster Domino Ring Sampler (DRS) chip with gigahertz sampling is adopted for the analysis. Compared with conventional ADC or TDC, the shape of waveform gives more useful information such as pileup events, timing, noise, saturation and time constant to be used for particle identification.

The fast waveform digitizer with switched capacitor arrays, DRS, is developed at PSI [52]. Since 2009 the MEG experiment has been using the fourth version of DRS (DRS4) for the LXe detector, PMTs of the timing counter and the drift chambers. The DRS4 has 950 MHz bandwidth at a variable sampling rate up to 6 GHz with 1024 cells, each with more than 11 bits resolution. The charge in the cells is slowly read out later with commercial FADC and each bin is digitized by 30 ns read-out time, that is totally a few kHz in one chip. New feature of on-chip Phase Locked Loop (PLL) is implemented for sampling frequency, which allows sampling speed in a range from hundreds MHz to 6 GHz. Each chip has nine channels and ninth channel can be used to record the external clock to synchronize all the DRS chips. If all the eight channels read the same signal, the number of cells increased up to 8192 or if half of the channels are used as a buffer, the dead time can be reduced.

Four DRS4 chips are mounted on the cards with 16 channels and two cards are inserted on VME board. Each card receives a 20 MHz global clock signal from master quartz and divides it to four DRSs with 0.78 MHz clock. In 2009 the four out of eight channels in DRS4 are used to record four signals of the LXe detector at 1.6 GHz sampling. That means that there is possibility by using four spare channels to improve internal timing accuracy with by doubling the sampling speed up to 3.2 GHz or to reduce dead time by using spare as a buffer. These features can be switched on only with a firmware upgrade. For drift chambers and APDs of the NaI detector sampling rate is set to 800 MHz (500 MHz in 2008) thanks to 500 ns delay in trigger.

3.9.6 Computer resource and online frontend

In the MEG experiment four frontends for the trigger and five frontends for the waveform acquisition with DRS are running. The frontends are running on different online computers. The online computers with DRS frontends are connected to each VME crate with an optical fiber. One of the trigger frontends sends command to start or stop run with run information as a master. The event builder on a powerful online computer accumulates information from all frontends and constructs an event, then logger system stores each event as data. In parallel, a slow control frontend collects information such as high voltages, temperatures and pressures from each slow control system, then the event builder constructs these as a different event type. Online computer provides DAQ interface via HTTP protocol and ODB database. The run information is stored in ODB and SQL database, and a header of run data.

When each run is finished, the data are transfered to offline cluster, in order to analyze the data, and also stored in an archive system with compressed in a GZIP format. The plots to check the data quality are automatically generated and the analyzed data are stored on offline clusters for further analysis.

In 2009 it took five minutes to take 2000 events, which is the typical number of events for each run. The data rate is 16.6 MB/s or 1.4 TB/day and the data is compressed by a factor of two. The total data size was 38 TB in 2009.

3.9.7 Monitor and analysis with ROME framework

Analysis and monitor framework in the MEG experiment base on the Root based Object oriented Midas Extension (ROME) developed at PSI [53]. The analyzer is called 'MEGAnalyzer' and provides an event display in both online and offline analysis. The MEGAnalyzer reads raw data in the MIDAS format or analyzed data in the ROOT format and writes the analysis results in ROOT format.

The ROME is a source code generator to provide a basic framework of analysis as an extension of ROOT library for a general purpose. A C++ class is automatically created according to a XML file that describes input and output parameters or tasks for a data analysis. Created framework can read configuration parameters from XML file or databases such as MySQL or sqlite. The ROME also provides remote connection for a display or a remote access to files. The user can just insert analysis code in the skeleton class generated by ROME. The online analysis allows a real time monitor of DAQ with analyzing data even though data is not recorded. The tasks or outputs can be disabled by flags in configuration XML file.

The monitor of the MEGAnalyzer can display a positron tracking and scintillation light distribution of a gamma ray, waveforms, trigger information such as trigger rate, hit map in timing counter and drift chambers and histograms of various results. The MEGAnalyzer plays a major part of the analysis such as calibrations, event reconstruction and selection, physics analysis and toy MC simulation with PDFs and also works in an interactive mode.

3.9.8 Monte Carlo simulation

The Monte Carlo simulation comprises two parts. One is the detector simulation and another is for the electronics simulation and event mixing.

The simulation of the detectors and kinematics of particles is based on GEANT3.21 [54]. The beam transportation can also be simulated, however normally events start from the target at the center of the MEG detector. Both calculated and measured magnetic field for the COBRA magnet and BTS are available. A drift of electrons or ions can be simulated with energy loss in gases or materials and drift according to an electrical field in a drift-chamber cell calculated with GARFIELD [27]. The scintillation photons in the scintillation bars of the timing counter are determined by taking attenuation and reflection into account, and finally detected with a fluctuation of the Poisson statistics. The scintillation photons in the liquid xenon are generated in each energy deposit based on W values depending on particle type. The propagation of scintillation light is simulated with various parameters such as reflections, absorption, Rayleigh scattering, transmission of quartz PMT window and light speed. The event can be generated for the signal, Michel decay, radiative muon decay and separated positron or gamma ray of each decay as well as other backgrounds such as annihilation in flight of positron. Various calibration events such as cosmic ray, ^{241}Am alpha source, LED and π^0 decay or a beam transportation are also simulated.

After all event kinematics and response of the detector are simulated, the MEGBartender, which is based also on the ROME framework, can simulate electronics and waveform and also mix simulated events. The MEGBartender generates raw data such as waveform in the same format as in the data. To generate waveforms of the DCH and the LXe detector, actual measured response is used. The 5.4 keV soft X-ray from ^{54}Mn source causes a single-electron avalanche in drift chamber and its signal can be an impulse response. For the LXe detector measured average waveform is used to obtain an impulse response. The signal is synthesized by convoluting hit information with the impulse response. The signal in timing counter is generated with digital filters in software and random fluctuations. The output data from the MEGBartender can be analyzed in the MEGAnalyzer in the same way as for the real data.

4 Method of Event Reconstruction

4.1 Waveform analysis

4.1.1 Drift chamber

The drift chamber has the largest number of channels, with two channels from anodes and four channels from cathode per each chamber cell. However, the number of hit wires is limited and the most channels are quiet. In order to reduce data size, online frontend of DRS can discard zero-signal waveform without recording. Common HV, circuit and ground may bring a common-mode noise on the DCH amplifiers. Although recording the channel with null signal is sometimes useful to subtract common noise from the signal waveform on an event basis, we do not use it currently. At the beginning of 2009 run we optimized the method of the zero-signal suppression.

Even for hit channels we can reduce data size by rebinning the part of the waveform outside the region around the baseline and the signal peak. Because of ionization clusters in single particle track, multiple peaks can appear. The following procedure is repeated to find the signal and obtain its charge. The maximum peaks in anode waveform over a certain threshold is recognized as a peak, then the width is taken by a full width at another threshold and that region is masked for next peak search. Time of each peak is taken at single threshold and charge is integrated in optimized 50 ns window, which is common for six channels in the same cell.

4.1.2 Timing ϕ-counter

There are two signal outputs from each PMT of the timing ϕ counter; a squared NIM pulse and raw PMT signal as described in Section 3.9.4. The PMT time is obtained by a template fit with NIM pulse. The template is formed from the averaged signal. The leading edge position and baseline are free parameters in the fit, while the scale should be constant because the pulse is the NIM standard. The NIM pulse delayed from a raw PMT signal by about 20 ns and the integrated window for the raw signal is 30 ns wide. From the raw signal the charge and the amplitude between estimated baseline and peak are calculated. The charge is for the gain equalization and the amplitude is for the time-walk correction because NIM pulse is made at a certain threshold as described in Section 3.9.4.

4.1.3 Liquid xenon detector

In the online frontend the data size of the waveform of the LXe detector is reduced with rebinning by merging eight bins of the waveform histogram except for the important part of the waveform such as baseline, leading edge and peak. The rebinning suppression is enabled by threshold or event type, for example in pedestal trigger there is no suppression.

We applied some types of shaping for the waveform.

- The summed waveform over the PMTs with a charge above a certain threshold is used for the determination of the time window for the charge integration, a particle discrimination and a pileup identification.

- The high-pass filtered waveform suppresses pileup since the signal with narrow width (48 ns) allows a short integrated region. The advantage of high pass filter is that the baseline is set to zero and the fluctuation of the baseline calculation disappears.

- The low-pass filtered waveform, in a way of moving average, allows to reduce high-frequency noise, spikes and the fluctuation of DRS cells, thus the waveform is smoothed.
- Template of noise for each DRS channel reduces biases around starting point of trigger, which appeared in new version, DRS4.
- Template subtraction of the cell pedestal for each DRS channel is effective.
- Correction of saturation is performed by scaling the template waveform according to the time-over-threshold (ToT).

The following methods are tried, but these are not applied in current normal analysis.

- The Fast Fourier Transform (FFT).
- The differential waveform indicates the peak time of the raw signal at zero-crossing time even if pileup exists.
- Event-by-event common noise reduction is implemented to compensate coherent noise of low frequency.
- Fit with a waveform template or a function are not used because it takes a lot of time.

The optimization of the shaping parameters was performed regarding the noise of DRS, the pile up and the fluctuation of the baseline. The gamma-ray reconstruction uses a high-pass (HP) filtered charge to reduce a pileup easily. For the calibration of the PMTs we use a normal-integrated (NI) charge without high-pass filter because the waveform in the LED run differs from that of gamma rays.

Timing calculation uses raw waveform without any filters and shaping not to distort leading-edge shape. To determine the PMT time independently of pulse height, we estimate the leading timing at 30% of its amplitude. Because the fluctuation of charge is less than that of amplitude, in fact, the timing is determined by charge corresponding to 30% height with using the known relation between charge and amplitude.

4.1.4 NaI detector

Due to a trigger arrangement of both slow NaI signals and fast counter signals to be taken at different sampling speeds, some unused channels exist. The flow of each input channel is shown at the bottom in Figure 3.64. Each signal from four PMTs of the two timing counters in front of the NaI and is taken by both 800 MHz (or 500 MHz in 2008) and 1.6 GHz DRS. For the analysis only 1.6 GHz DRS is used.

The amplifier of APD has two output channels. The faster waveform sampled by 1.6 GHz DRS did not join in both analysis and trigger. It is noisy but provides optional use of a fast trigger because of the fast leading edge. Another channel is taken by both 800 MHz DRS (Figure 3.56) and 1.6 GHz DRS (not used at all) and also by trigger waveform digitizer. For the analysis the low-pass filtered waveform of 800 MHz DRS or trigger waveform can be used. The charge from APD is integrated in the charge amplifier, thus the amplitude of the waveform determines the energy. Hence, it is no problem that the

tail of the waveform is out of range even in 800 MHz sampling as long as the peak can be estimated. Finally, the amplitude is taken from trigger waveform in 2009 analysis because spikes sometimes appear around a peak in DRS waveform.

4.2 Gamma-ray reconstruction

4.2.1 Scintillation photons

Scintillation photons in the liquid xenon are detected by 846 PMTs in the LXe detector. The distribution of the PMT outputs allows to reconstruct the timing, the position and the energy. Generally the number of scintillation photons in each PMT is obtained from the integrated charge of PMT with taking the quantum efficiency (QE), the collection efficiency (CE) and the gain into account. We reconstruct the number of photo-electrons,

$$N_{pe,i} = C \times Q_i/(G_i \times CE_i \times e), \tag{39}$$

and the number of scintillation photons,

$$N_{pho,i} = N_{pe,i}/(QE_i), \tag{40}$$

where i means the index of PMTs, G_i is the gain of PMT, e is the elementary electric charge, C is a constant factor from an attenuation related with electronics, QE_i is a QE and CE_i is a CE of PMT. The calculation of those parameters using LEDs and alpha sources in the detector are described in Section 6.2 and 6.3. Separate treatment of QE and gain is sometimes useful because QE depends on temperature while gains are sensitive to magnetic field and decrease by aging effect. The $N_{pe,i}$ is used to determine statistical error and the $N_{pho,i}$ is an important parameter to reconstruct events in the LXe detector.

4.2.2 Position reconstruction

The position of the event vertex can be estimated from the light distribution on PMTs. The position is necessary also for the timing and the energy reconstructions in the LXe detector. The incident angle or direction are difficult to be reconstructed because a gamma ray around signal energy region 52.8 MeV forms an electro-magnetic shower. The direction of the gamma-ray is, therefore, determined by the line connecting the reconstructed position of the gamma-ray and the vertex position on the target, which is reconstructed by the positron tracking. Especially a performance near the inner face is important since the gamma ray around signal energy is converted within a few centimeter after entering the liquid xenon. The main reconstruction methods tried in the MEG experiment are the followings:

- Method i) Weighted mean of PMT's position
- Method ii) Linear fit with Monte Carlo simulation
- Method iii) Fit with light distribution on a face
- Method iv) Least squares method

The method i) is an useful way for the fast check or for the calibration such as an identification of alpha sources in the LXe detector or cosmic ray. The deeper event from the inner face shows a better performance because many PMTs can detect photons. However the shower development or the event at the detector edge give a bias for the reconstruction.

The second method is not currently applied because the parameters for the scintillation light propagation in the Monte Carlo simulation is not well tuned.

The third method is to fit a light distribution along the inner face and its peak indicates the position of u and v [55]. The depth from the inner face, w, is determined by the width of fitted distribution so that the wider distribution indicates the deeper depth.

The approach iv) is the current best way and is adopted for the MEG analysis in 2008 and 2009. This method is optimized for gamma rays from the target and uses some local PMTs on the inner face near the incident position. The reconstruction using only the inner face is due to the following reasons:

1. Most events are close to the inner face.
2. To avoid the shower fluctuation in the outer face.
3. The densest area of PMTs with the closest distance each other.

The position (u, v, w) is determined by minimizing $\chi^2_{position}$ defined as

$$\chi^2_{position} = \sum_i^{PMT} \frac{N_{pho,i} - c \times \Omega_i(u,v,w)}{\sigma_{pho,i}(N_{pho,i})}, \tag{41}$$

where c is the free parameter for fitting as well as (u, v, w) and $\Omega_i(u, v, w)$ is the solid angle subtended by the photo-cathode of the i-th PMT, which is calculated numerically. The statistical uncertainty of the number of scintillation photons, $\sigma_{pho,i}(N_{pho,i})$, is defined from that of photo electrons, $\sigma_{pe,i}(N_{pe,i}) = \sqrt{N_{pe,i}}$, as

$$\sigma_{pho,i}(N_{pho,i}) = \sigma\left(\frac{N_{pe,i}}{QE_i}\right) \tag{42}$$

$$= \sqrt{\frac{N^2_{pe,i}}{QE^4_i}(\sigma(QE_i))^2 + \frac{1}{QE^2_i}(\sigma_{pe,i}(N_{pe,i}))^2}. \tag{43}$$

We assume that $\sigma(QE_i) = 0$ for simplicity, then $\sigma_{pho,i}(N_{pho,i}) = \sqrt{N_{pho,i}/QE_i}$ is obtained.

To avoid the shower fluctuation and pile-up gamma-ray, $\chi^2_{position}(u, v, w)$ is minimized in the fit around the limited number of PMTs. After the first fit with a selection of typically 45 PMTs around the PMT observing the largest number of photons, the second fit in a more restricted area with about 15 PMTs is performed. Then biases along u and w axis, which are observed in the MC, are corrected with the correlation estimated by MC simulation. These biases are caused by the slant incidence of the gamma-ray on the inner face, therefore there is no similar bias for v direction. The fluctuation of the shower development is also considered with a difference of $\chi^2_{position}$ as two fitting results from different PMT selections. A correction is applied by the difference with comparing to the MC. The performance including these correction is evaluated with actual measurement later in Section 7.1.

4.2.3 Timing reconstruction

The timing of the gamma-ray hit is calculated from the arrival time of photons at each PMT,

$$t_{hit,i} = t_{pmt,i} - t_{delay,i} - t_{offset,i}, \tag{44}$$

where $t_{hit,i}$ is the timing at vertex position, $t_{pmt,i}$ is the timing from the waveform analysis and $t_{offset,i}$ is the offset of each channel.

The delay time $t_{delay,i}$ occurs by a propagation time $t_{prop}(d, v_{eff})$ in the liquid xenon estimated from the distance d between PMTs and the vertex position and the effective velocity of scintillation light v_{eff}, then we can obtain

$$t_{delay} = t_{prop}(d, v_{eff}) - t_{indir}(\eta) - t_{walk}(N_{pe}), \tag{45}$$

where $t_{indir}(\eta)$ is a correction for the effect of the indirect photons using the incident angle η between the vertical axis of PMT surface and vertex position, which is caused by the reflection and the scatter at a large η.

Current estimation of $t_{pmt,i}$ is done at 30% of the peak height of the waveform instead of at a fixed threshold. The time-walk correction $t_{walk}(N_{pe})$ is nevertheless introduced as a function of N_{pe}, but the effect is usually tiny except when a large pulse appears.

Finally we can determine the hit time t_{LXe} with minimizing χ^2_{time} defined as

$$\chi^2_{time} = \sum_i \frac{(t_{hit,i} - t_{LXe})^2}{(\sigma_{t,i}(N_{pe}))^2}, \tag{46}$$

where $\sigma_{t,i}(N_{pe})$ is time resolution of each PMT as a function of the number of photoelectrons [56].

4.2.4 Energy reconstruction

For the reconstruction of the gamma-ray energy, a simple sum of all the number of photons with a fixed weight is the current best estimation. The weight is determined as the reciprocal of the coverage of the photo-cathode of the PMT on the face of the detector. The weight is constant and independent of the reconstructed position and the charge. The energy is then calculated from the sum of the number of photons after corrections related to the solid angle for shallow events ($w < 3$ cm), the reconstructed position and the measured light yield. Therefore the conversion formula can be described as below:

$$\text{Energy} = F(u,v,w) \times S(u,v,w) \times T(t) \times C \times \sum_i^{846} (N_{pho,i} \times W_i), \tag{47}$$

where (u, v, w) is the coordinates in the liquid xenon detector defined in Equations 32, 33, 34. $F(u, v, w)$ is a non-uniformity correction factor by the reconstructed position, $S(u, v, w)$ is a correction factor by the solid angle, $T(t)$ is a correction to compensate the change of light yield, C is conversion factor from the number of photons to energy, W_i is the constant weight and $N_{pho,i}$ is the number of photon (Section 4.2.1) of the i-th PMT.

4.2.5 Non-uniformity correction

For convenience we introduced the coordinates of u, v, w based on the geometry of the most illuminated inner face as described in Section 3.6.4. The faces are located in the (u, v, w)-coordinates (Figure 3.41) as:

- inner : u-v plane, $w = 0$ (cm),
- outer : u-v plane, $w = 38.4$ (cm),
- top : w-u plane, $v = 74.3$ (cm),
- bottom : w-u plane, $v = -74.3$ (cm),
- up : upstream side,
- down : downstream side.

Current energy reconstruction has a dependence along u, v and w and six faces of detector have a different behavior. This is because the vertex position is not taken into account in the reconstructed number of photons with constant weights. The non-uniformity in the current method is discussed here to know what kind of a position dependence exists.

The non-uniformity of the detector response projected to each face can be explained roughly with a simplified model. For example the solid angle of each detector face, with ignoring the ϕ-curvature of detector, is described as below,

$$\begin{aligned}\Omega_{Face}(x,y,z) = \frac{A_{Face}}{4\pi}\Bigg\{ &\arctan\left(\frac{(X_{Max}-x)(Y_{Max}-y)}{z\sqrt{(X_{Max}-x)^2+(Y_{Max}-y)^2+z^2}}\right)\\ &+\arctan\left(\frac{(X_{Max}-x)(Y_{Max}+y)}{z\sqrt{(X_{Max}-x)^2+(Y_{Max}+y)^2+z^2}}\right)\\ &+\arctan\left(\frac{(X_{Max}+x)(Y_{Max}+y)}{z\sqrt{(X_{Max}+x)^2+(Y_{Max}+y)^2+z^2}}\right)\\ &+\arctan\left(\frac{(X_{Max}+x)(Y_{Max}-y)}{z\sqrt{(X_{Max}+x)^2+(Y_{Max}-y)^2+z^2}}\right)\Bigg\}, \end{aligned} \tag{48}$$

where x and y are the axes parallel to the face with a range of $[-X_{Max}, X_{Max}]$, $[-Y_{Max}, Y_{Max}]$, respectively, while z-axis is vertical to the face, which is located at $z = 0$. A factor A_{Face} is an effective area of the face for the photon detection.

For the signal MC the detected total number of photons on the inner face is fitted with this function as shown in Figures 4.1 (a), (b), (c) along u, v and w, respectively, which shows a good agreement. In the total number of photons of all faces, a horizontal dependence of u, v shows double peaks in a shape of '$\mathcal{M}$' as shown in Figure 4.1 (d), or four peaks in u-v plane, which is also described by summing the functions over the six faces. Double peaks along parallel axes come from the dependence of vertical faces at both sides as shown in Figure 4.1 (c). This model implies that the non-uniformity exists intrinsically by the geometry and the three-dimensional correction is required. Actual non-uniformity is, however, more complicated due to the reflection, the curvature, the attenuation and

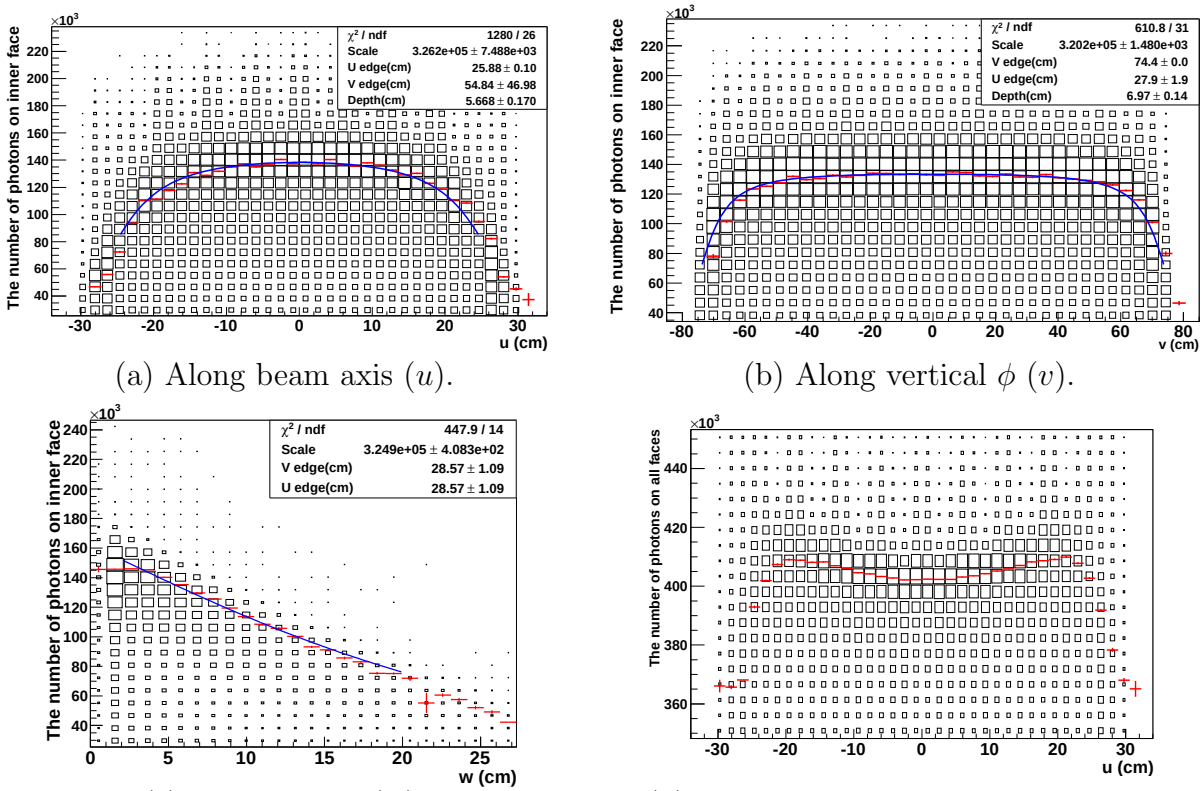

(a) Along beam axis (u). (b) Along vertical ϕ (v).

(c) Along depth (w). (d) Total photons in all faces, along u.

Figure 4.1: Position dependence of the reconstructed scintillation photons only in the inner face on (a) u, (b) v and (c) w. The red plots are the peaks scanning along axis and the blue line is the function of the opening angle (Equation 48). Position dependence of the reconstructed scintillation photons along u is shown in (d), where two peaks appear compared to (a) because of the photons from side walls.

the global bias of the calibration. Thus we finally use actual measurement of the non-uniformity for the correction, which will be shown in Section 6.5.1.

This model also suggests that the (u, v) dependence depends on gamma-ray energy because the event distribution along depth and the shower development depends on the energy. The difference is actually observed in 17.7, 54.9 and 82.9 MeV peaks. However, if we correct the three-dimensional dependence, the effect should become smaller.

The non-uniformity is intrinsic in our current reconstruction method, but there is a slight difference between the measurement and the MC in the asymmetry or in the position of the double peaks. These can arise from biased estimation of QE or imperfect knowledge of the scintillation photon propagation in the liquid xenon. However, the discrepancy between the data and the MC is not an issue for the energy reconstruction if the non-uniformity is corrected by the measured dependence.

4.2.6 Pileup search and correction

Pileup in muon beam The LXe detector has no segmentation with homogeneous liquid xenon. Pileup of the background gamma-ray occurs frequently according to the acceptance of the detector with 10% solid angle, a DC muon beam rate, typically about

3×10^7 Hz and waveform time window of 640 ns or 48 ns integrated region. Possible sources of the gamma-ray background are, however, not only direct gamma rays from radiative muon decay, but also annihilation in flight (AIF) of positrons and bremsstrahlung of positrons and so on. Therefore it is considered that low energy gamma rays are piled up with a large energy deposit to be able to make a trigger. The MC simulation roughly estimated that gamma rays above 0.5 MeV are piled up around the signal energy region with around 0.1 probability in the case of 3×10^7 Hz muon intensity.

Pileup identification There are implemented two simple ways to identify pileup events. One is to look for peaks in the light distribution observed by PMTs on the inner face. The number of the identified peaks during the muon decay run is shown in Figure 4.2 (a). Another method is to find the pileup in the time-domain. This method is complementary to the previous spatial method because the timing difference can discriminate pileups even if gamma rays arrive at the similar position with a different time. Thanks to the all waveforms taken, it is one possibility to find multiple peaks in each waveform or partially summed one. The other possibility is to find the event with a large χ^2/NDF in the fitting of the time reconstruction described in Equation 46. The threshold of χ^2/NDF to reject pileups is adjusted to 3 as shown in Figure 4.2 (b). This method is effective only to identify pileups. Unfolding the pile-up is done in the same way as in the spatial method, as described in next paragraph.

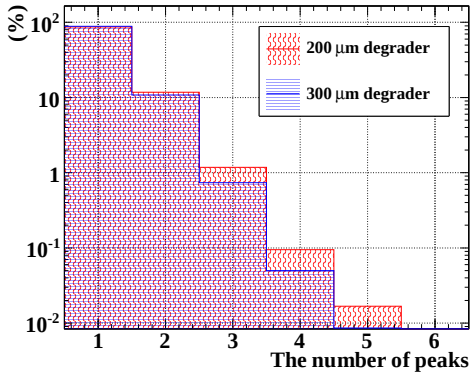

(a) Distribution of the number of peaks in the spatial light distribution.

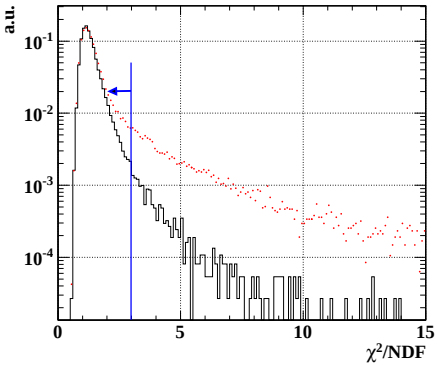

(b) Distribution of χ^2/NDF of the time reconstruction. Dotted plots show that of data and solid line shows that of signal MC without pileups.

Figure 4.2: Pileup discrimination by spatial or timing selection.

Pileup elimination It is quite important to correctly reconstruct the pileup event instead of just discarding it since the probability of the pileup is as large as 7%. We eliminate a small pileup by comparing the distribution of the PMT outputs with the expected distribution. A look-up table of the expected PMT outputs is prepared with the measured distribution with 17.7 MeV gamma-ray in the CW run. The table contains

average output of each PMT for each mesh ($1.55 \times 1.55 \times 1.55$ cm^3) for the reconstructed position. If the pileup is found, the elimination is performed in the following procedure.

1. Reconstruct energy in the usual way.
2. Fit PMT scintillation-photon distribution with the expected distribution stored in the table except for pileup region.
3. Calculate the expectation of outputs around pileup region based on the first reconstructed energy.
4. Replace photons of some PMTs around pileup region with those of the expectation.
5. Reconstruct energy again with replaced outputs of PMTs.

The light distribution in Figure 4.3 shows the elimination effect on 2D PMT development view.

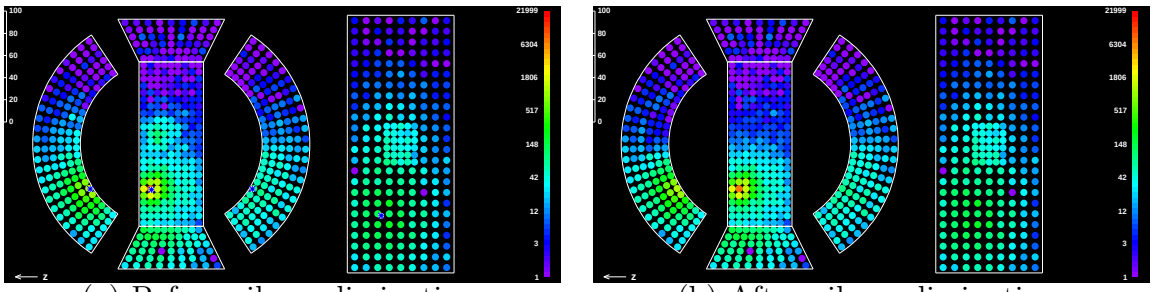

(a) Before pileup elimination. (b) After pileup elimination.

Figure 4.3: Photon distribution in PMTs with eliminating pileup.

With using the same table, dead PMT channels are also recovered. Replaced the number of scintillation photons of the dead channel are estimated from the photon averaged over the three PMTs at the symmetric locations along u and v direction.

The replacement depends on the table, and it is not appropriate for cosmic ray, ^{241}Am-alpha sources on wires and LED runs. This is because the light distribution of gamma rays from central targets, such as muon or proton target, differs from that for the special calibration sources. The monitor of the light yield is performed without the elimination to avoid uncertainties such as the different energy region and light distribution by calibration and the change of non-uniformity.

Different pileup depending on beam status The probability density function (PDF) of gamma-ray energy for the accidental background is prepared for pile-up and non-pileup events separately.

In the case of π^0 run, the source of pileup is different from that for the muons because there are many high energy and low energy backgrounds. The background in the π^0 run comes from the π^0 decay (a flat distribution between 54.9 and 82.9 MeV) and from the radiative capture of the charged pion (129 MeV gamma-ray and 8.9 MeV neutron). Additionally many positrons, electrons and muons are also expected because the Wien filter is not used in π^0 run. The difference of the background condition between the pion and the muon beam is taken into account in the estimation of the energy resolution in π^0 run.

4.3 Positron reconstruction

4.3.1 Strategy of position reconstruction

In the positron spectrometer, positron tracks are reconstructed by drift chamber and timing z-counter with combined analysis. Although there is no vertex detector, the extrapolation of positron tracks gives vertex position. The analysis flow for the positron is the following.

1. Reconstruct positron timing and position in the TICP
2. Reconstruct timing from the leading edge of anode-wire waveform and z position of the hit by the vernier method for each wire in DCH
3. Cluster finding
4. Track finding
5. Track fitting with the Kalman filter

The positron track is reconstructed by using the Kalman filter in order to include the multiple Coulomb scattering, the energy losses and the magnetic field effectively.

4.3.2 Hit z-position reconstruction in drift chamber

At first we compute asymmetries of charges for anode wires and for vernier pads. On the anode wire the asymmetry between both ends is estimated. One of cathodes in the vernier structure is read out at one side of down stream or up stream, while another cathode at another side as shown in Figure 3.25 and we take the asymmetry between these for both inner and outer foils. These asymmetries denoted as ϵ_a for anode wires, ϵ_1 and ϵ_2 for cathode pads, are calculated from a general equation,

$$\epsilon = \frac{Q_U - Q_D}{Q_U + Q_D}, \tag{49}$$

where Q_U is the charge read out at the upstream side and Q_D at the downstream side.

The parameter ϵ_a gives a rough z position with considering load impedance r and the resistance on wire, $\rho = 2200\ \Omega/\mathrm{m}$ as

$$z = -\left(\frac{r}{\rho} + \frac{L}{2}\right) \cdot \epsilon_a, \tag{50}$$

where the length of wire L depending on the wires.

In the vernier pads the precise z position in a zig-zag period is obtained from the angle $\alpha = \arctan(\epsilon_2/\epsilon_1)$. Because of the phase difference of π between upstream and downstream readout on the plane and the phase difference of $\pi/2$ between inner and outer pad, the hits on a ϵ_1 - ϵ_2 plane shows a circle with phase of α corresponding to the 5 cm zig-zag period. Figure 4.4 shows the vernier α-circle. Finally the combination of the global reconstruction from the wires and the local position in the vernier period gives the precise z-position. Each line in Figure 4.5 indicates the n-th vernier periods on α-charge division plane. Position is described from equation $z = l \cdot (\alpha/2\pi + n - n_0)$, where n_0 is the count of the central vernier and n is the vernier turn from down stream side, and l is the 5 cm period of vernier.

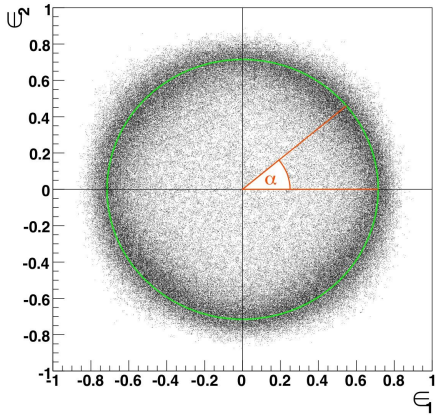

Figure 4.4: Vernier circle.

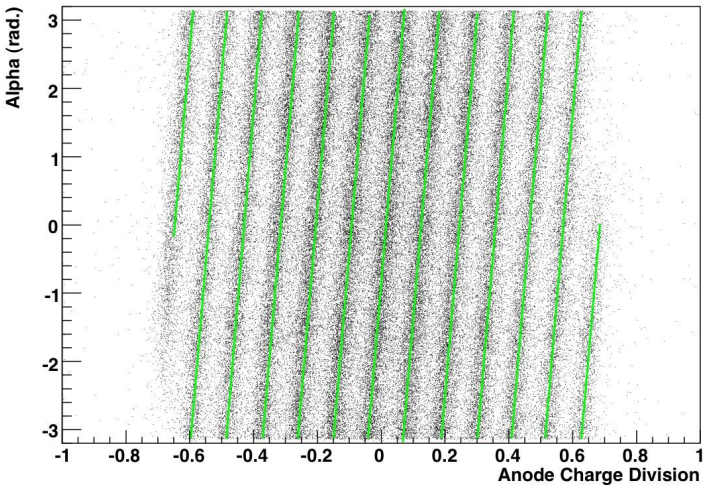

Figure 4.5: Phase on vernier circle and anode charge division.

4.3.3 Hit-timing reconstruction in timing-counter bar

The timing measured in the timing z-counter, T_{TC}, is defined as the timing at the first hit on the counter. The hit time on the k-th scintillator bar (k = 0-29), $T_{TC,k}$ is obtained from measured time at PMTs at both ends, $t_{i,k}$ and $t_{o,k}$, with correcting time walk effect by using pulse height $A_{i,k}$ and $A_{o,k}$ from inner PMT close to target and outer PMT around the edge of detector, respectively. With the factor of the time walk correction, $f_{j,k}(A_{j,k})$, distance from the hit point to the PMT, $d_{k,j=i,o}$, the longitudinal length of bar L and the effective velocity v_{TC} in the bar (14.5 cm/ns), there is a relation as

$$t_{j,k} = T_{TC,k} + \frac{d_{k,j}}{v_{TC}} + f_{j,k}(A_{j,k}) \ (j = i, o), \tag{51}$$

$$L = d_{k,i} + d_{k,o}, \tag{52}$$

therefore with using the number of scintillation photons in each PMT, $N_{i,k}$ and $N_{o,k}$, the reconstruction of $z_{TC,k}$ and $T_{TC,k}$ is obtained as

$$|z_{TC,k} - z_{offset,k}| = \frac{v_{TC} \cdot |t_{o,k} - t_{i,k}|}{2} + \frac{L}{2}, \tag{53}$$

$$T_{TC,k} = \frac{\sum_{j=i,o} \sqrt{N_{j,k}} \cdot (t_{j,k} - f_{j,k}(A_{j,k}) - d_{k,j})}{\sum_{j=i,o} \sqrt{N_{j,k}}}. \tag{54}$$

In 2008 we assume a model of time walk correction,

$$f_{j,k}(A_{j,k}) = b_{j,k} + c_{j,k}\frac{1}{\sqrt{A_{j,k}}} \ (j = i, o), \tag{55}$$

where $b_{j,k}$ and $c_{j,k}$ can be determined by a least χ^2 method with collecting triple hits in adjacent three bars ($k-1$, k, $k+1$) as

$$\chi^2 \equiv \sum_{\text{all triple events}} \left(t_{j,k} - \frac{(t_{j,k-1} + t_{j,k+1})}{2} \right)^2 |_{d_k = d_{k-1} = d_{k+1}, T_k = T_{k-1} = T_{k+1}}. \tag{56}$$

This correction improves the time resolution at least by a factor two. Additional logarithmic term is introduced in 2009 and the time walk correction of Equation 55 is replaced. With a lower threshold $D_{j,k}$ in DTD (described in Section 3.9.4) the correction factor in 2009 is described as

$$f_{j,k}(A_{j,k}) = b'_{j,k} + c_{0,j,k}\sqrt{\frac{D_{j,k}}{A_{j,k}}} + c_{1,j,k}\log\left(\frac{D_{j,k}}{A_{j,k}}\right) \ (j = i, o). \tag{57}$$

The unknown factors, $b'_{j,k}, c_{0,j,k}, c_{1,j,k}$, are evaluated from the averaged waveform shape.

4.3.4 Track finding and fitting

After all hits information are constructed both in drift chamber and in timing counter, reconstruction of positron tracking can proceed. Rough principle is described here to find positron tracking and fit it with considering a loss of energy and the magnetic field to extract momentum.

Cluster finding A cluster means a collection of hits in single module by a single charged particle. Separately from each cluster of each chamber, another larger cluster among several modules is called a 'track candidate', which is a collection of previous clusters by a single track to be recognized by track finding in next step. Each drift chamber module consists of two layers with shifting radially by a half size of the cell each other, thus typically a minimum of two hits is found from a positron track in a chamber. Single hit in a chamber is also recognized as a cluster if it is finally alone. Each layer has nine cells along R, then at first we cluster hits along R, then along z.

In each module, hits within three radially adjacent cells are clustered temporarily, then split if more than a few centimeter deviation along z from average in a category is observed. The z average depends on the selection into a category, thus refinement proceeds by removing and reassembling hits with many iterations. Next we connect clusters between modules.

Track finding In order to connect modules, at first step we search for tracking seeds with three clusters in modules. The search requests a radius larger than 24 cm, that is because there are possibilities that

- clusters existing at both side,
- many clusters in the same track,
- high momentum,
- less hits than inside R.

What we know is the distance from the wire but not the direction from wire, namely a circle from the wire with free angle in x-y plane and we have to solve so called 'left-right ambiguity'. The seeds of three clusters enable to suggest possible tracks with connecting hits on the circles.

At first we look for clusters with a radius larger than 24 cm except for modules at both ends along ϕ. The seed requires that the cluster radius at the middle module of the three

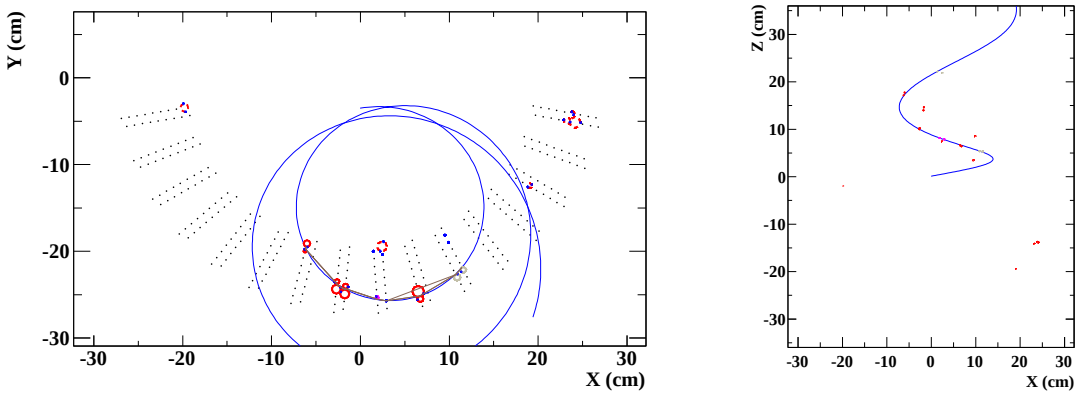

(a) $x - y$ view (b) $x - z$ view

Figure 4.6: Event display of positron tracking. Fitting with Kalman filter is performed for clusters in a track candidate.

is shortest, difference of the radius is smaller than 2 cm and at least one cluster must contain multi-hit cluster. Three modules must be adjacent within one skipped module and the difference of z must be within 4 cm per one interval of modules. If the seed is found, rough track time is estimated.

Then we extract seeds at both side and find connection to other clusters in other modules. Finally we reconstruct the tracking time in DCH from all hits on the track and search for matched hit on the timing counter. The tracking time is extrapolated from timing counter with considering a propagation time and a momentum, which is estimated by track fitting described in the next section.

Track fitting To obtain both a momentum and a precise track, track fitting is performed for the found track. Our analysis method relies on the Kalman filter, which is based on linear dynamic systems of a Bayesian model [57, 58]. It is effective for tracks with small number of hits or noise by environment, thus suitable for the positron tracking in MEG experiment.

The features of the Kalman filter are

- include effects of multiple scattering, energy loss and non-uniform magnetic field,
- three-dimensional and complex trajectory can be reconstructed,
- error propagation is taken into account.

The Kalman filter recursively estimates parameters set by each measurement in order. For the fit there are five free parameters, namely two position, two direction and one momentum of positron with in advance provided magnetic field and materials. Fit example is shown in Figure 4.6.

5 Run

Since in 1999 the MEG experiment was approved at Paul Sherrer Institut there was a long-term development such as the liquid xenon gamma-ray detector and the positron spectrometer. At the end of 2007 we finished the construction of the detector and successfully performed an engineering run where we estimated the detector performance and tested the $\mu^+ \to e^+\gamma$ trigger as well. In 2008 we successfully took the first physics data for three months. With some improvements for the detectors the stable data acquisition was carried out for two months in 2009.

5.1 First MEG physics run in 2008

5.1.1 Overview of 2008 run

The MEG experiment started the first physics data taking on 12 September, 2008 and it continued for three months. During the run, the drift chamber was suffered from a discharge problem. Thanks to the purification, the light yield of xenon was improving. Two π^0 decay runs were performed to measure the performance of the LXe detector in its all acceptance. The first π^0 run in 2008 started at the end of July and ended on 1 September before the MEG physics data taking to evaluate all the performance. The second π^0 data was taken for a short days period 18 to 23 in December to confirm the performance partially after the light yield increased. The regular shutdown period for three months at PSI started at the end of December, then for next 2009 run we fixed problems of the drift chambers, the LXe detector and so on.

5.1.2 Run

Physics run During the physics run in 2008, 9.5×10^{13} muons stopped on the target in total. For the purpose of the monitoring, calibrations and normalization eleven different trigger types were mixed in the run. The live time was 85% amounted to 3.3 Msec in total. The dedicated run for the radiative decay (RD) events were performed under the lower beam rate by a factor 25 and lower gamma-ray energy threshold of 25 MeV, although RD trigger was mixed also in the physics run. The RD data mixed in the physics run are useful for the normalization of muons and the background estimation, while the successful observation of RD enables the estimation of the detector performance such as the relative timing and the positron energy.

π^0 run In 2008 the performance was evaluated in all the acceptance of the LXe detector by moving the NaI detector on 3×8 meshes, each with 3×3 PMT size on the inner face of the LXe detector. At each position 200-300k events were taken and took six hours at each position. Every day during π^0 run, calibration data using LEDs, alpha sources and cosmic rays were taken for three hours. The lead collimator in 2008 had vertical or horizontal slits of 1 cm width with 1.8 cm thickness and 1.1M events were taken in total.

There was the second π^0 run with changing beam rate, to evaluate the performance after the improvement of the light yield by 40% and to measure the dependence of the performance or backgrounds on the beam rate.

5.1.3 Detector status

Drift chamber The drift chamber system suffered from a discharged problem in 2008. Because of a frequent discharge, the HV applied to the drift chambers were unstable for some channels and some were out of operation, thus the detection efficiency was much lower than expected especially at the end of 2008 run. The frequency of the discharge gradually increased, and finally in all 32 planes of 16 modules, only 12 planes worked at a nominal voltage (1850 V) and other 6 channels at a lower voltage. Figure 5.2 (a) shows the history of the biased HV for each cells.

The discharge was caused by the helium gas at the end of the plane where HV was biased. To avoid an annihilation of positrons there is a helium in the COBRA magnet except for around timing counters and 50% helium in drift chambers. To avoid the multiple scattering of the muon and positron, the inner bore of the COBRA is filled with helium gas. The chamber gas is the mixture of helium and ethane. The helium gas permeated to the weak part in the PCB little by little during the 2008 run.

Timing ϕ counter Till the end of October there was one broken channel on trigger side and it was fixed.

Timing z counter Timing z counter for z tagging of positron was not ready and not used. Nevertheless the 2008 run could be performed with a reasonable trigger efficiency even without the z-counter since the timing ϕ counter can also estimate z position in the trigger by using the time difference between the PMTs at both ends.

LXe detector Three dead channels of PMTs existed with problems about one of signal cables and two of HV lines. Additionally one strange shape of waveform and one unstable gain of the PMT were also found. During the run other two PMTs got a large decrease of the gain. However, it is not severe because these all were apart from a detection face.

5.2 MEG run in 2009

5.2.1 Overview of 2009 run

Before the 2009 physics run started the discharge problem of drift chamber was investigated and fixed. The drift chamber was stably operated in whole 2009 run as shown in the HV history in Figure 5.2. Additionally, the waveform digitizer chip (DRS) was upgraded and the yield of liquid xenon scintillation light recovered before the 2009 run started. Because other project using the same beam channel the MEG experiment got muons in the later half of the year. The physics data taking was performed for two months in 2009, which is 55% shorter than three-month run in 2008. The produced protons during the MEG physics run is shown in Figure 5.1. Thanks to the improvement of the positron efficiency, the observed number of muon decays increased by a factor of two compared to the run 2008. There were two setups of muon momentum degrader. A 200 μm thick degrader was used at the first half of runs, then 300 μm-thick degrader was used for the second half.

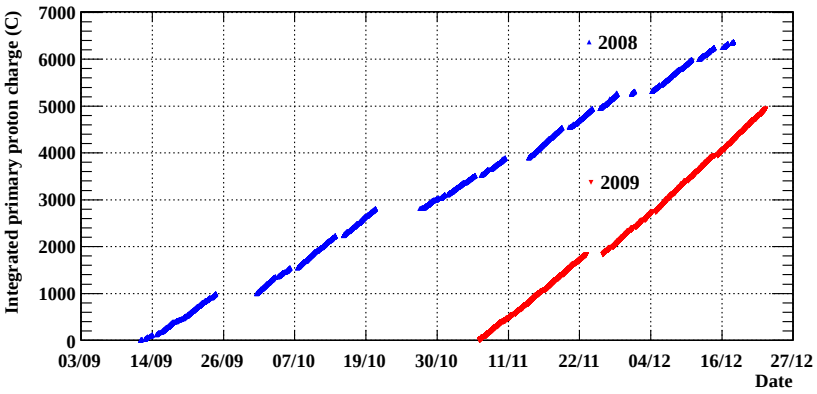

Figure 5.1: Integrated muons at PSI during the MEG data taking.

5.2.2 Degrader setting

In 2008 the Mylar degrader had 300 μm thickness at the center of BTS magnet outside the COBRA magnet. The 2009 physics run started with 200 μm degrader to shift the stopping distribution inside of target to the center. This was estimated in the Monte Carlo simulation but it was not totally optimized. At the end of November 2010, the degrader thickness was reverted to 300 μm because it was found that in 200 μm degrader the event distribution had a larger asymmetry along beam axis and the positron hits in the timing counter at the down stream side four times larger compared with up stream side. The stopping efficiency of the muon target is estimated to be about 56% and 82% for 200 μm and 300 μm degrader, respectively. There were different background and event distribution between 200 μm and 300 μm degraders, which is taken into account in the physics analysis.

5.2.3 Run

Physics run Delivered muon rate at the primary proton current of 2 mA is shown in Table 10. For example stopping rate in 300 μm degrader at 2.2 mA is $2.9 \times 10^7 \mu^+ \cdot \mathrm{s}^{-1}$. The muon rate was optimized with the beam slits by considering the background. Twelve types of the trigger are mixed in the physics run as shown in Figures 3.65 and 3.66. The 200 μm degrader run started at the end of October and ran for 18 days with 10 Hz DAQ rate and 75% live time, while the 300 μm degrader run was taken for 26 days with 6Hz DAQ rate and 84% live time. LED monitoring run was performed everyday during the physics data taking. Full sets of calibration data were taken three times a week, which includes LED data with beam on and off, LED gain calibration, alpha source data and the CW data. In total 94 TB data was collected and run finished at the end of December.

π^0 run The period of π^0 run is shorter than 2008 π^0 run and statistics for one measurement at the region in 3 $\times$ 3 PMT size also reduced from 300k to 200k events. The run was performed for twelve days from the middle of October. Different lead collimators with long slits along beam axis are prepared for the position measurement at two different positions on the inner face.

Table 10: Muon rate delivered at the center of the detector in 2 mA primary proton current.

Beam tuning	200 μm Degrader	300 μm Degrader
2008 setup	$(4.3 \times 10^7 \mu^+ \cdot \mathrm{s}^{-1})$	$3.7 \times 10^7 \mu^+ \cdot \mathrm{s}^{-1}$
2009 setup	$3.7 \times 10^7 \mu^+ \cdot \mathrm{s}^{-1}$	$3.2 \times 10^7 \mu^+ \cdot \mathrm{s}^{-1}$

5.2.4 Detector status

Recovery of the positron efficiency In 2008 discharge on drift chambers frequently happened as noted in Section 5.1.3. Figure 5.2 (b) shows history of the HV applied for all cells in 2009 run. Compared with previous 2008 (a) it is quite stable during physics data taking. Accordingly positron efficiency recovered.

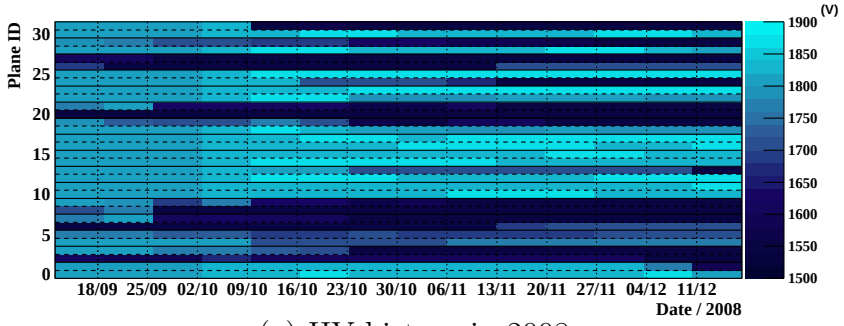

(a) HV history in 2008.

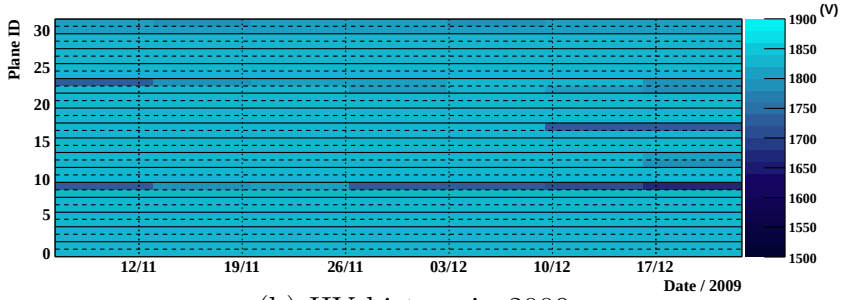

(b) HV history in 2009.

Figure 5.2: HV history applied for each drift chamber cell in 2008 (a) and 2009 (b).

The LXe detector A new liquid purification system of O_2 getter was installed, which can remove oxygen and also water. The liquid xenon circulated through the purifier at 180 liter/h transfer speed with new pump, then about 8k liters liquid xenon was circulated corresponding to nine times volume of the LXe detector. Before the 2009 run, the light yield increased about 2.5 times from the lowest in 2008 or 1.6 times from the end of 2008 by the purification.

Some bad channels of PMTs were fixed and some PMTs with larger gain shift, which is described later in Section 6.2.2, were replaced. Evacuation pump and cooling pipe were also updated.

New version of DRS waveform digitizer For the LXe detector and the drift chamber the DRS was upgraded from version 2 to 4, while the timing ϕ-counter used the same version of DRS (version 3). New version of DRS has less effect of temperature drifts, a good linearity up to 1 Volt, no ghost pulses due to residual charge, better timing accuracy with 20 MHz global synchronization between boards and ability of faster sampling up to 6 GHz, though the sampling rate and bins were kept at the same as 2008 setup of 1.6 GHz and 1024 cells. Cross talks with a clock signal disappeared in new version. Other small problems occurred in 2009 that the baseline got some biases around starting cells of triggered point and a few spike structure. It was, however, not a big issue since it can be solved in offline analysis by means of the templates of cell pedestals and baselines.

Trigger The signal received at the trigger board is three times larger compared with DRS boards because of the attenuation register 1/3 at the input of DRS. Sometimes the trigger suffered from the saturation, for instance, for the shallow event where the the some PMTs in the inner face receive larger amount of light. The dynamic range of the trigger improved from 1 to 2 Volt by replacing frontend cards for a part of PMTs of the LXe detector. Thanks to the improved discrimination of the waveform shape at the trigger side because of the improved light yield, alpha particles were able to be separated from gamma rays in online (Figure 5.3). It allows to mix the trigger for the alpha events in the physics run in order to monitor the detector performance.

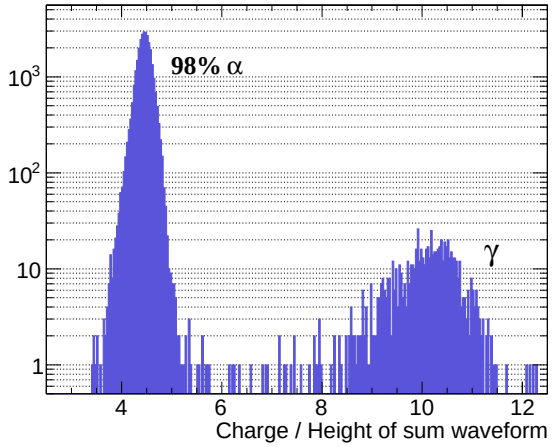

Figure 5.3: Triggered events as alpha particles with a selection efficiency of 98% in muon beam. Horizontal axis shows a ratio of charge to height for a precise discrimination in offline analysis as described later in Section 6.3.3.

Part III
The Liquid Xenon Gamma-Ray Detector

6 Calibration and Monitor of the Liquid Xenon Detector

6.1 Outlook of calibrations

For a long-time run, it is very important to keep a quality of a gamma-ray measurement by a monitor and a calibration. First concern is the light yield of scintillation photons in liquid xenon, which depends on a purity and it might change. Second concern is an aging effect of PMTs due to the high-rate environment. However, these can be overcome by a precise and frequent monitor. One of the important purposes in this section is to ensure the stability or to trace the change.

The excellent detector performance is important for the MEG experiment to achieve a good sensitivity of $\mu \to e\gamma$, such as the better timing resolution thanks to the fast response of the liquid xenon scintillation. Especially, the energy calibration is the most important. As indicated by Equation 18, the number of accidental background is proportional to a square of a gamma-ray energy resolution and it is a dominant factor. Therefore the energy reconstruction with a good resolution, long-term stability, and uniform response for all gamma-ray interaction points is crucial to suppress backgrounds of the $\mu \to e\gamma$ decay.

In order to calibrate and monitor the LXe detector, various methods are prepared for the MEG experiment. For a frequent monitor and calibration of PMTs, alpha sources and LEDs are used. The nuclear reaction of protons, ${}^{7}_{3}\mathrm{Li}(p,\gamma){}^{8}_{4}\mathrm{Be}$, by using Cockcroft-Walton (CW) accelerator with the lithium target enables to trace a light yield of a scintillation light by gamma rays at 17.7 MeV. The π^0 run to measure two gamma rays from a neutral pion decay is the most powerful way to know the detector performance about the energy, the timing and the position around a $\mu \to e\gamma$ signal region in the whole acceptance of the detector. Before moving on the explanation of each method, all calibration sources are summarized in Table 11 with its characteristics and purposes.

6.2 Gain of PMTs

6.2.1 Gain calculation

The LEDs attached on the lateral faces of the LXe detector are useful light sources to monitor and estimate gains of all PMTs. The gain calculation by LEDs is based on statistics of the collected number of photo-electron, N_{pe}, which is independent of the amount of photons and the wavelength. Observed charge, q, from PMT output is given by gain, G, and a conversion constant, e, as an equation, $q = G \cdot e \cdot N_{pe}$, where the gain does not include a collection efficiency of the first dynode from cathode. By counting many LED events, the mean of the charge and the number of photoelectrons obey an

Table 11: Calibration sources for the LXe detector.

Type	Purpose	Source	Energy	Interval
LED	PMT gain, timing	blue light	~470 nm λ	a few days/mixed
^{241}Am	QE, Xe property	α	5.5 MeV	a few days/mixed
Cosmic ray	light-yield monitor	μ	a hundred MeV	dedicated/mixed
^{241}Am ^{9}Be	light-yield monitor	γ	4.4 MeV	dedicated
CW proton	light-yield monitor energy and timing	γ	4.4, 12.0, 17.7 MeV	a few days
π^- beam	energy, timing, position, detection efficiency, light-yield monitor	γ, neutron, e	54.9-82.9, 129.4 MeV 8.9 MeV	a year
Thermal neutron capture	light-yield monitor	γ	9 MeV	(under testing)

equation,

$$\overline{q} = G \cdot e \cdot \overline{N}_{pe}. \tag{58}$$

The variation of the observed charge contains a noise from electronics or charge calculation as σ_0, a fluctuation of a photon propagation before reaching a PMT and a power of LED pulser as σ_{LED} and a resolution on the single photoelectron as σ_G^2, by an equation,

$$\sigma_q^2 = (G^2 + \sigma_G^2) \cdot e^2 \cdot (\sigma_{pe}^2 + \sigma_{LED}^2) + \sigma_0^2 \tag{59}$$

We assume that the intensity of photons from LEDs is constant and the number of photoelectrons obeys Poisson statistics when the photons are converted to photoelectrons at the photocathode. The Poisson distribution gives a relation between the deviation and the mean of photoelectrons, $\sigma_{pe}^2 = \overline{N}_{pe}$. By Equations 58 and 59, we obtain a relation between the mean and variance of charge and the gain,

$$\begin{aligned} \sigma_q^2 &= (G^2 + \sigma_G^2) \times e^2 \times \sigma_{pe}^2 + \sigma_0'^2 && (60)\\ &= (G^2 + \sigma_G^2) \times e^2 \times \overline{N}_{pe} + \sigma_0'^2 && (61)\\ &= \frac{(G^2 + \sigma_G^2) \times e}{G} \times \overline{q} + \sigma_0'^2, && (62) \end{aligned}$$

where σ_0' is a constant term and differs from a pedestal of σ_0 because it contains σ_{LED} and the gain. The number of photons coming into PMT, N_{pho}, is calculated by a relation of $N_{pho} = N_{pe}/QE$, where a quantum efficiency, QE, is described later in Section 6.3.1.

We took nine steps with different LED intensities in beam off condition as shown in charge distributions of Figure 6.1. Each step contains 3000 events and in total it took half an hour for one gain measurement. We can obtain a relation between charge $\bar{q}$ and variation σ_q^2 as shown in Figure 6.2, and then the slope of plots is regarded as the gain. Figure 6.3 shows a charge map of PMTs when one LED flashing, while Figure 6.4 shows that of ten LEDs flashing which can illuminate all the PMTs at the same. Figure 6.5

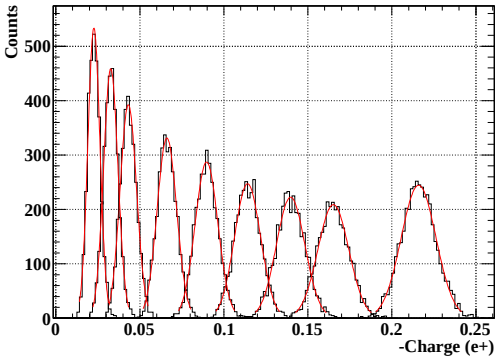

Figure 6.1: Nine LED peaks by various intensities.

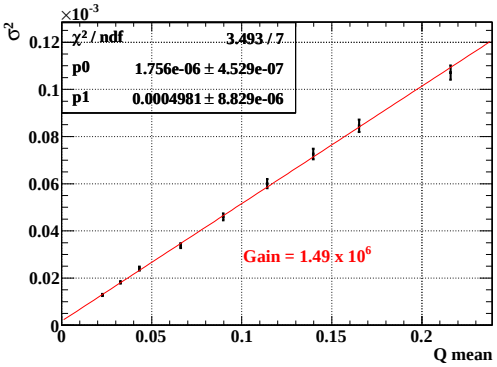

Figure 6.2: Gain estimation from the slope on charge mean and variance (σ^2) plane.

shows the relation of the mean and the variance of charge from each LED and all LEDs on upper figure and the slopes of those in lower figure, which suggests that calculated gains are independent of a light intensity and a LED.

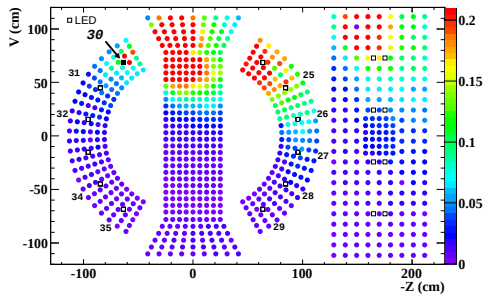

Figure 6.3: Charge map of PMTs from one LED. The number shows id of each LED and LED of id=30 illuminate the detector.

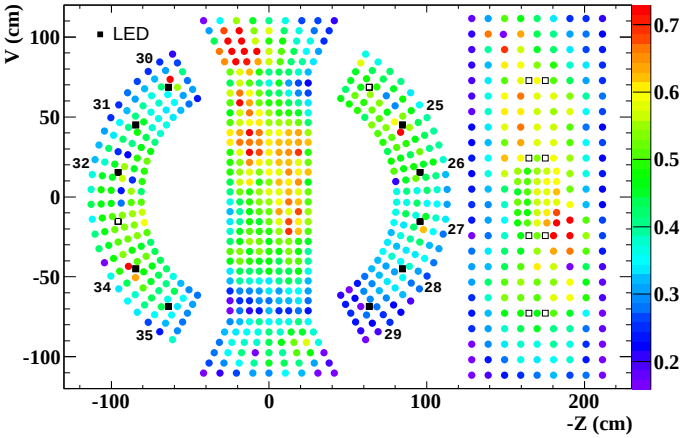

Figure 6.4: Charge map of PMTs from nine LEDs. All PMTs obtain enough charges at the same time.

Usual gain calibration was taken everyday or three times per week depending on the detector situation. Additionally the most intense step was taken everyday and every time when we start or stop using beam to monitor the variation of PMT gains relatively. LEDs are flashed with 100 Hz during the usual calibration and LED data with 1 Hz are mixed in MEG physics data taking.

6.2.2 Gain shift

By means of PMT calibration methods described above, a long-term stability of all PMTs were checked. However, temporally there was the PMT gain increase or decrease depend-

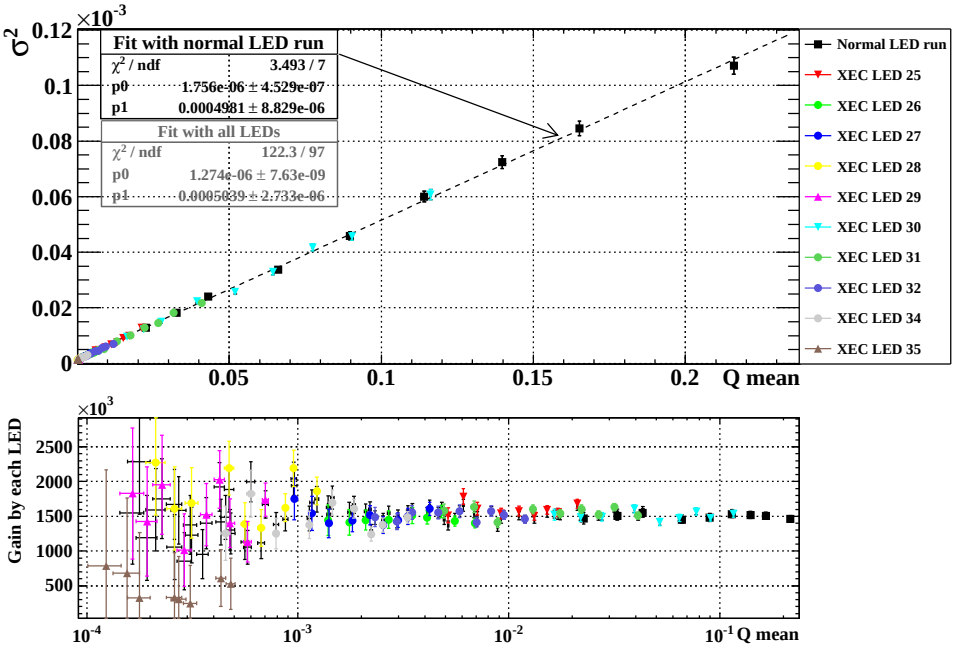

Figure 6.5: Relation between the slope on charge mean and variance (σ^2) by each LED light.

ing on the beam intensity when we started using the beam as shown in Figure 6.6, which is named 'gain shift'. This was confirmed by different methods such as LED peaks, alpha peaks, and gain calculation by means of LEDs. This gain shift is not coming from the pileup effect but the PMT itself since the gain calculation relies on the statistics of photoelectrons which is independent of the beam intensity. A monitor with constant LED light in Figure 6.6 shows a gradual increase clearly after starting a delivery of muons into the target. The contribution of beam switching time is a small, about ten seconds. As shown in Figure 6.7, gain shift factors depend on individual PMTs and the mean value is about 2%. Some PMTs have a larger gain increase, while several PMTs has less effect or nothing.

We know that it is related with a manufacturing process and indirectly with a cathode blue sensitivity (SKB). As shown in Figure 6.8 larger gain shifts are observed by PMTs which have larger serial number than 1000.

The shift is correlated with a beam intensity so that we can correct it with monitoring constantly. In order to correct this gain shift, LED data such as shown in Figure 6.6 are used. Exponential function with three time constants describes the gain shift well. Fit results indicate that the transition is faster in opening the beam blocker than in closing the blocker and it takes 5 minutes for the gain shift to be stabilized within 10% when beam blocker is opened and 20 minutes when the beam blocker is closed. Therefore after the beam blocker is opened or closed we wait 15 minutes before starting physics data taking and wait 30 minutes before starting a regular calibration, respectively. During the waiting time, LED flashing runs are taken to monitor and correct the shift.

We prepare different functions for each PMT, for different beam condition of muons and pions, and for both the beam blocker opened and closed, and shape of the transition seems to be no change for each prepared set. Typical shift of total number of photons is

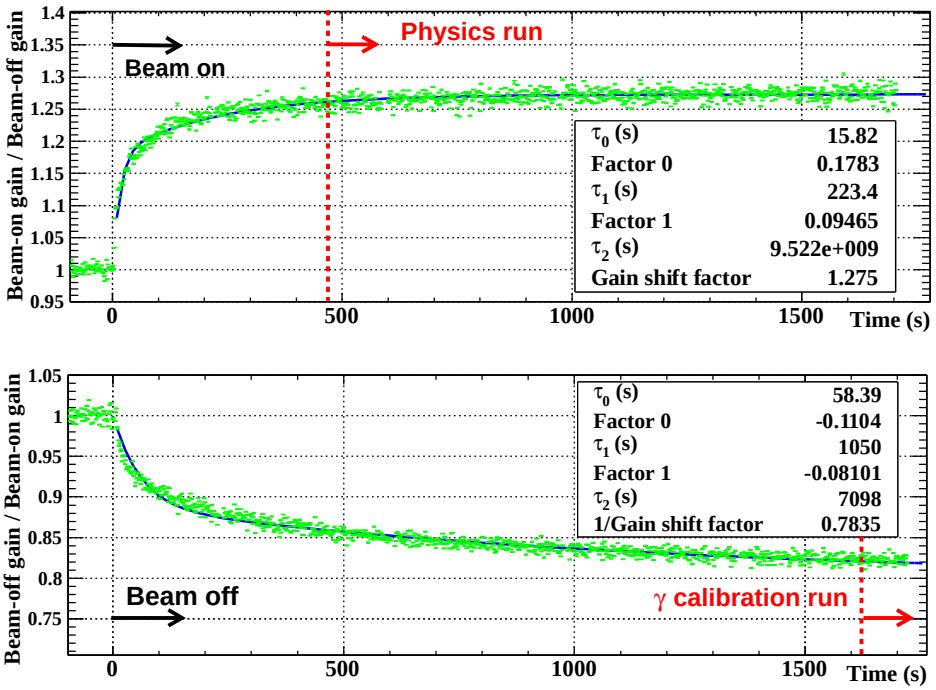

Figure 6.6: Gain shift of a worst PMT after beam blocker opened in upper figure and closed in lower.

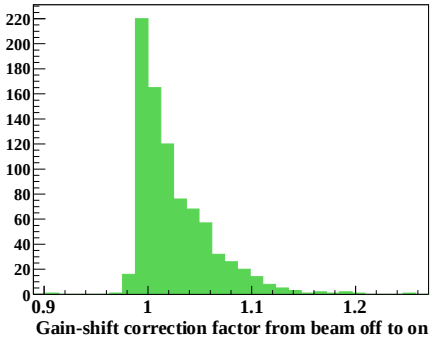

Figure 6.7: Gain shift factor from beam off to on of all PMTs.

about 2%. Because the most scintillation light is detected on the inner face, the larger gain shifts appears on the inner face. The larger shift is observed in a π^- beam because we do not use the Wien separator in the π^- beam and many electrons and muons exist.

6.2.3 Gain adjustment

Before physics data taking started, gains were adjusted by following reasons:

- Equalize each PMT performance such as timing response.
- Keep a pulse height within a dynamic range of waveform sampling boards

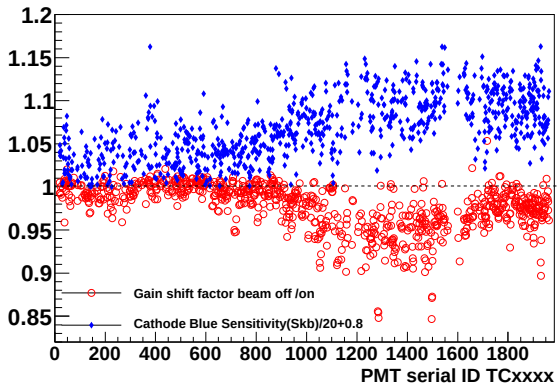

Figure 6.8: Gain shift factor (Beam off / Beam on) and Cathode blue sensitivity by PMT serial number, plotted by red circles and blue dots, respectively. Both values shifted by the serial number according to the change of manufacturing plant.

Normally a gain of a PMT with same resistive divider is in proportion to V^{kn}, where V is a bias voltage, n is the number of dynode stage and k is a factor determined by a material of dynodes. However, the PMTs for the MEG experiment use two Zener diodes in the last two stages shown in Figure 3.36, thus the equation is approximately modified,

$$\text{Gain} \propto (V - 0.95Z - V_0)^{11k}, \tag{63}$$

$$Z = Z_1 + Z_2 = 130 \text{ (Volt.)}, \tag{64}$$

where Z is the total voltage at two Zener diodes and V_0 is an offset by a loss in cables. Figure 6.9 shows the relation between HV and gain of a PMT as well as a fit result with Equation 63.

In 2008 and 2009 we adjusted all gains to 1.8 $\times 10^6$, without considering QE values in a simple way, by a few iteration for a determination of HV set with using the relation. Applied HV in 2009 is shown in Figure 6.10, which is enough lower than maximum bias voltage of PMTs about 1200 V. That allows a large increase of gain even if it decreases, for example, a shift of 200 V higher voltage from the 2009 set brings ten times larger gain.

6.2.4 Monitor of gain

Figure 6.11 shows calculated gains and LED peaks of a certain PMT on inner face, in which the values of LED peaks are scaled to the gain value of the right-most point. We can see a decrease of gains for a long time scale and it depends on a beam rate and particle. This aging effect can be seen in all PMTs especially on the inner face of the detector, shown in Figure 6.12. The decrease is independent of the gain shift effect. Figure 6.13 shows that the gain dropped to 90% in average during 2009 run. However, we can keep the gain for next several years by increasing HV because this drop is recovered by only about 5 V increase of HV and applied HV is sufficiently lower than maximum HV (Figure 6.10).

One can see more stable monitor result with LED peaks than with the gain calculation although those tendencies are the same as shown in Figure 6.11. Therefore we calculated the absolute gain by averaging some sets of LED calibrations at a stable condition without

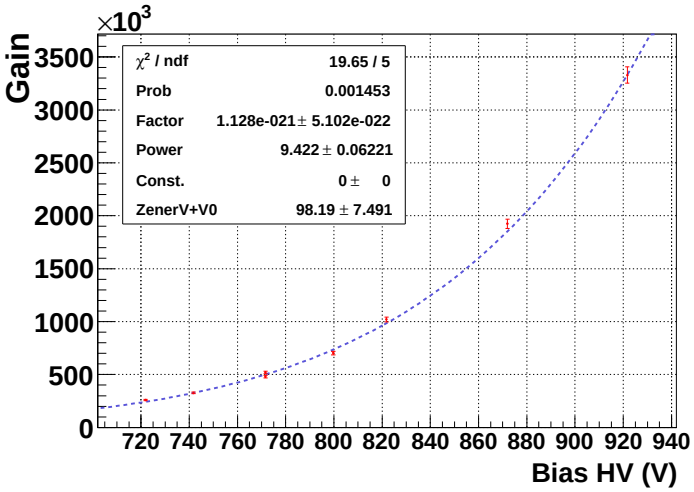

Figure 6.9: Gain - HV curve and fit.

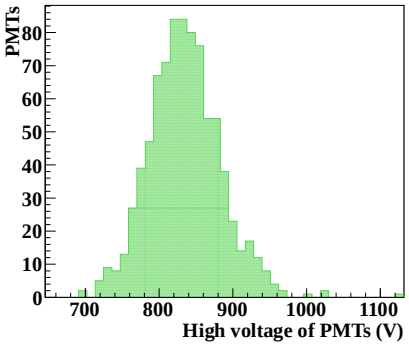

Figure 6.10: Determined HV set in 2009. Maximum voltage rating is 1200 V.

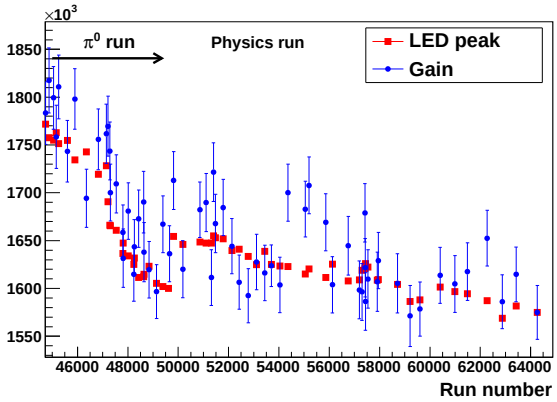

Figure 6.11: History of gain and scaled LED peak of a certain PMT. The shift just after the π^0 run is due to a different magnetic field of BTS. The red square dots from LED are scaled to the gain value adjusted by the absolute gain of blue dots and enable the gain monitoring stably.

the beam for a few days. After that the gain is traced relatively by means of LED peaks. A simple linear interpolation is applied for the MEG run only in 2009 and for the π^0 run in both 2008 and 2009, between each measurement point. The peak of LED contains not only a gain but also CE, QE for blue-light LED and a digitizer, and these are corrected. The gain calculation is still continued to avoid a disagreement from an aging of LED or the LED pulser. Thanks to the faster LED one-step run for a peak estimation than nine-step LED calibration set, the LED one-step run is frequently taken during the calibration set and in beam on. After all the gain calibration are applied, LED peaks mixed in physics data taking show a stability in Figure 6.14, which is within about 1% in sigma (Figure 6.15).

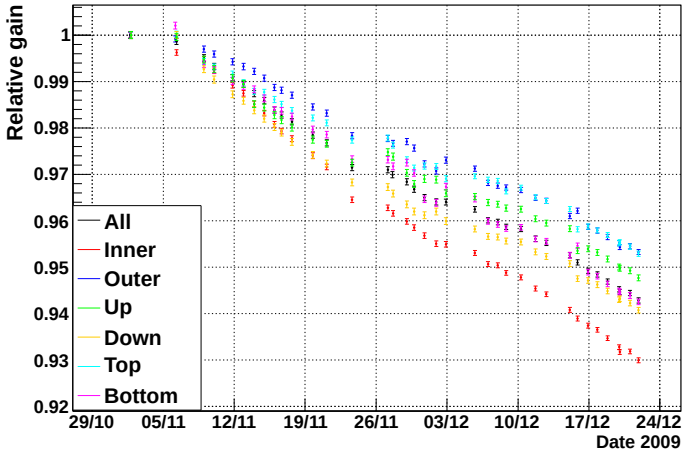

Figure 6.12: Relative change of averaged gains on PMTs by each face in muon beam (2009).

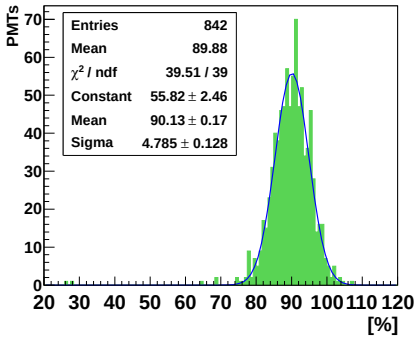

Figure 6.13: Relative gain decrease of PMTs in all the 2009 runs. There were gains of two PMTs decreasing largely.

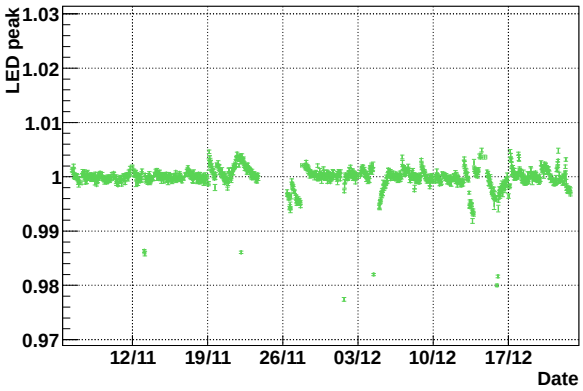

Figure 6.14: LED peaks mixed in the MEG 2009 run. Some lower points come from a beam break, a wrong gain interpolation and a low proton current.

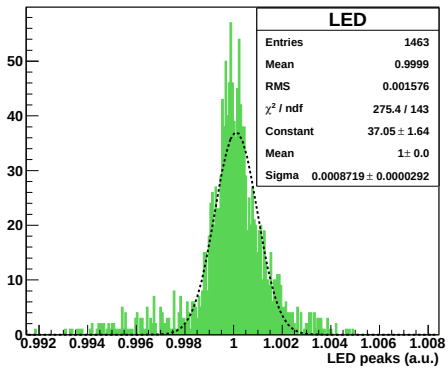

Figure 6.15: LED peaks in the MEG 2009 run within 0.09% in σ.

6.3 Alpha sources and quantum efficiency

6.3.1 Quantum efficiency

A QE of a PMT can be estimated by point-like alpha sources. Since we know the installed alpha positions, we can estimate the photoelectrons observed by each PMT by means of MC simulation. Then, QE is extracted from the comparison between the measured photoelectrons and estimated ones by the MC, with considering the calculated gain by LED. This method enables the estimation of QE times gain, and we can separate QE from the gain. The collection efficiency is included in the QE, while the transmittance of

the quartz PMT window is not in the QE because the MC simulation calculates it. The wavelength of scintillation light from alpha particles is the same as that from gamma rays, thus the estimated QE from alpha sources can be applied for the gamma-ray detection.

In liquid xenon phase the reconstructed positions from alpha sources make rings around alpha wires because a range of scintillation photons about 40 μm from the wire is near compared with a 100 μm diameter of the wire and the wire makes a shadow, while in gaseous state the reconstructed shape is like a point because of sufficiently far generation of scintillation photons from the wire in the range of about 7 mm. The MC-data correlation of peaks from observed photons by each source are shown in Figure 6.16 and its slope indicates a QE as a difference from MC. The events are selected for each PMT to avoid shadow positions behind wire and sources which has a large incident angle to the PMT. The QE is obtained by averaging some sets of estimations to reduce statistical fluctuations. The obtained QE is normalized in such a way that the mean of all QEs takes 0.16 to avoid the change of other properties such as the light yield. It is possible to calculate QE both in liquid and gas where the wavelength of scintillation is the same. The QE in gas is less influenced by absorption and scattering in xenon but is influenced by the effect of reflection on the wall and on the PMT window, and by a possible effect caused by temperature gradient in the detector. Therefore the QE set to be used in the 2009 data is estimated in liquid phase.

A fine tuning for the MC such as reflection, attenuation lengths and light speed improved agreement with actual data, however the MC for the QE estimation is sensitive to these parameters and a small remained discrepancy between the data and the MC makes it difficult to estimate QE. For instance, on a photo-cathode, different incident angles of photons from sources at different positions with respect to a PMT direction bring a bias even if disagreement of a reflection, a photon polarization or a response of photo-cathode for a slant injection is small between data and the MC. We could not overcome a small disagreement in a large incident angle between data and MC, thus we correct it by the angle in the QE calculation. In addition, a global bias is observed as a difference of non-uniformity of reconstructed scintillation photons between the data and the MC. The QE is corrected globally by using 17.7 MeV gamma ray from ${}^{7}_{3}\mathrm{Li(p,}\gamma){}^{8}_{4}\mathrm{Be}$ to eliminate asymmetries of peaks between PMTs at symmetric positions on each face of the detector. Figure 6.17 shows the QE distribution of all PMTs which is applied for all 2009 data.

6.3.2 Absorption and scattering

The scintillation light from excimers (Xe_2^*) is not absorbed by a liquid xenon in itself, but is absorbed by a contamination in xenon and causes Rayleigh scattering that is the most dominant. In general the attenuation factor $I(x)$ and attenuation length λ_{att} are described with absorption length λ_{abs} and diffusion length λ_{dif},

$$I(x) = I_0 e^{-x/\lambda_{att}}, \tag{65}$$

$$\frac{1}{\lambda_{att}} = \frac{1}{\lambda_{abs}} + \frac{1}{\lambda_{dif}}. \tag{66}$$

The inversed scattering length, h, is described by

$$h = \frac{1}{\lambda_R} = \frac{\omega^4}{6\pi c^4}\left[kT\rho^4\kappa_T\left(\frac{\delta\epsilon}{\delta\rho}\right)_T + \frac{kT^2}{\rho c_v}\left(\frac{\delta\epsilon}{\delta T}_{\rho}\right)\right], \tag{67}$$

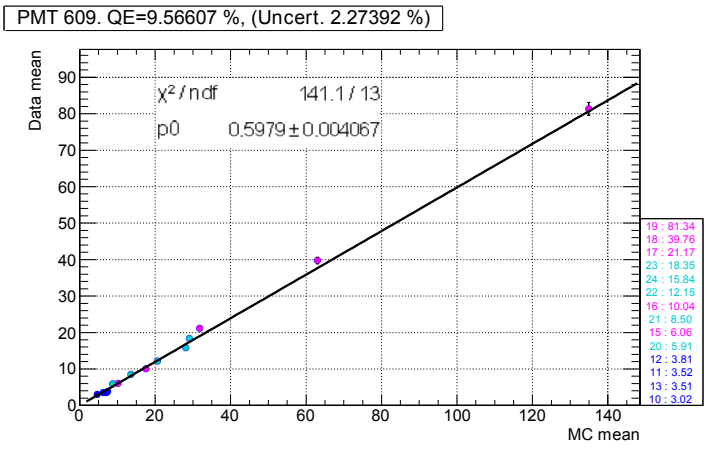

Figure 6.16: Comparison of alpha peaks between constant QE (16%) in MC and data.

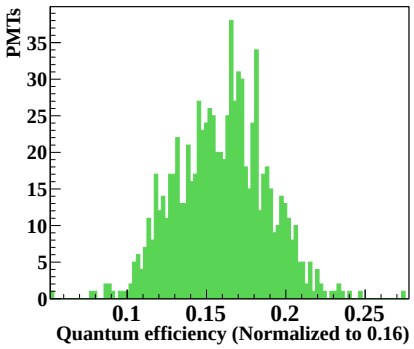

Figure 6.17: Estimated QE of all PMTs.

where ω is the angular frequency, c is the velocity of light, k is Boltzmann constant, T is the temperature, ρ is the liquid density, κ_T is the isothermal compressibility, c_v is the heat capacity at constant volume, and ϵ is the dielectric constant.

The optical properties of liquid xenon are poorly known and it is the most difficult point to reproduce events in the MC. The pairs of alpha source and PMT have exactly known distances and it is useful to estimate the attenuation length or the light speed in xenon. To obtain those we compare the charges in liquid xenon with those in gas xenon or in the MC. Since the attenuation in gas phase is long enough because of the low density, we can estimate attenuation length in liquid by taking the ratio of charges. Figure 6.18 shows the relation between the ratio of liquid to gaseous xenon and distance, and 65 cm attenuation is observed in 2009 data. Another way is to use the MC instead of gas. It allows us to check each optical parameter of MC such as attenuation, scattering length or reflection in the MC.

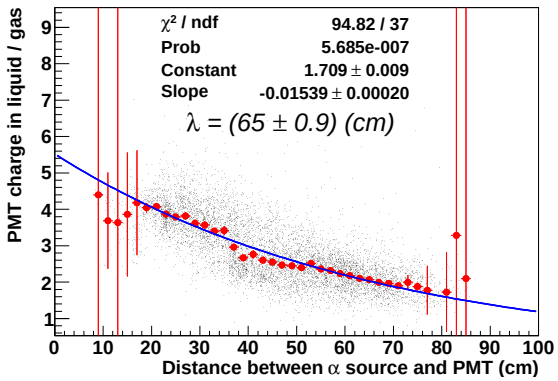

Figure 6.18: Attenuation length by charge ratio in liquid / gas from α source and distance between source and PMT in 2009 run.

6.3.3 Particle discrimination

Since there is a different density of energy deposit between alpha and gamma ray, the dominant scintillation process of fast or slow time components differ. Using all waveform information from PMTs, we can recognize the difference of time components clearly. Figure 6.19 shows averaged and normalized waveforms from alpha and gamma-ray events. We have two ways to distinguish particles by estimating time constants as a result of a fit with a function model, or by using a charge-height ratio. The charge over height ratio of summed waveform has an sufficient ability to separate alpha events from gamma ray, which is the simplest and fastest method. The discrimination is useful to estimate gamma-ray peaks in similar energy region of alpha or to take alpha events efficiently. As shown in Figures 6.20 and 6.21, the separation improved with the increase of the light yield by the purification.

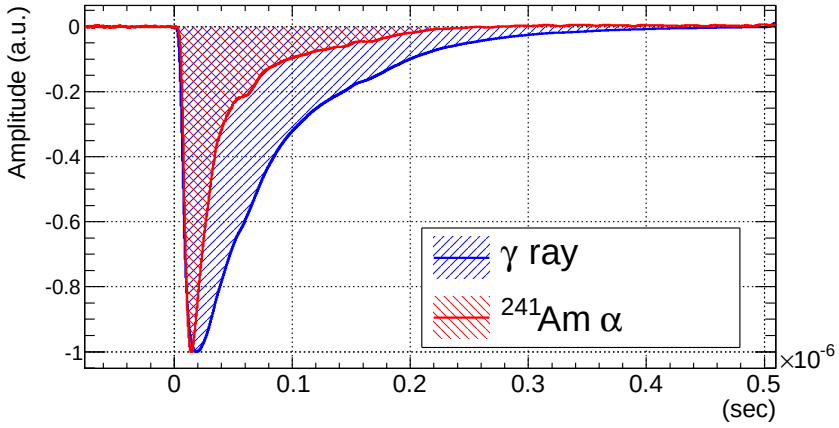

Figure 6.19: Averaged waveform from alpha events and gamma-ray events.

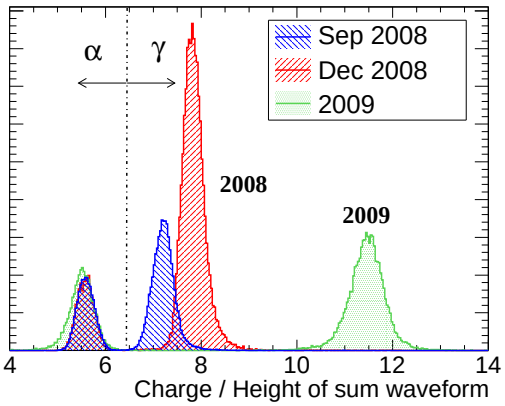

Figure 6.20: Alpha-gamma identification by a charge-height ratio.

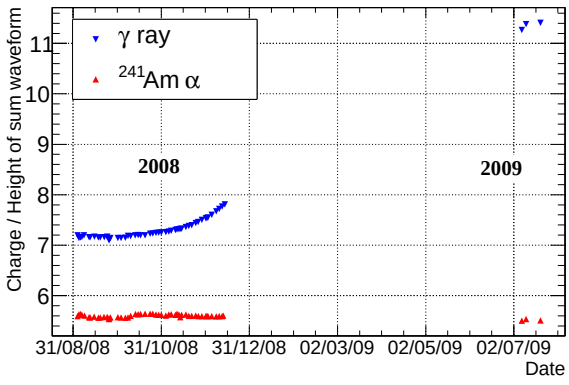

Figure 6.21: History of a charge-height ratio with purification.

6.4 Light yield

6.4.1 Light-yield monitor

The monitor of the light yield is crucial because the light yield directly relates with the energy scale that is determined at 54.9 MeV peak in a certain period of π^0 run. We had a precise light-yield monitor during beam-off periods by various sources. In 2008 we performed purification even during physics data taking, then in 2009 the purification was stopped before physics run started because the increase of the light yield seemed to be saturated. That indicates that the 2008 data needs a correction for the light yield, and we have to confirm a long-term stability in 2009.

It is the most precise method to use 17.7 MeV gamma-ray peaks from lithium target by the CW proton accelerator. However, the CW beamline can not be used during π^0 run because it must be removed to install the hydrogen target. Instead, during π^0 run, peaks of 54.9 and 82.9 MeV gamma rays from π^0 decay can be used for the monitor. For the monitor during a few days to change the beamline from π^- to muon beam and CW proton beam, other sources of gamma rays from americium-beryllium (AmBe) and cosmic rays are useful. In order to combine the time-dependent transitions from different energies and periods, we took several types of monitoring runs with overlapping periods because a linear response of reconstructed scintillation photons is not ensured.

Other sources are sometimes used to support the monitor. Monitoring by alpha sources is not always the same as that by gamma rays. That is because the dominant scintillation process differs between alpha particles and gamma rays. A degree of suppression in each process depends on particles contaminating xenon. Thus, events from alpha sources are not suitable to monitor the gamma-ray energy, but can be used to check the stability of the detector. For a consistency check, an edge of gamma rays from radiative muon decays can be used for the monitor in the muon beam. The edge includes the energy resolution that might change by time, thus it is not used for the calibration or the precise monitor. Monitoring sources mixed in physics data taking, such as cosmic rays or alpha particles, do not have enough statistics to perform a precise calibration or a monitor but enable to check a long-term stability.

Following sections from 6.4.2 to 6.4.7 show the stable light yield in 2009 monitored by each calibration source. Even if there is a light-yield change, it can be corrected by the monitor as shown in Section 6.4.8 that describes a light-yield correction in 2008.

6.4.2 Monitor during π^0 run

The π^0 run plays an important role in a performance evaluation of the LXe detector. One of the important purposes is to determine the energy scale by a 54.9 MeV peak near the signal energy of 52.8 MeV. Therefore the energy scale obtained in the π^0 run ought to be extrapolated to the MEG run exactly.

As shown in Figure 6.22, the inner face is divided into 24 patch positions, and data are taken for each patch position separately to select back-to-back two gammas from π^0 decay. The NaI detector is moved to the opposite side of each patch during calibration. Each patch consists of 3×3 PMTs. In a specified patch, a special trigger to select a gamma direction is issued if the maximum charge in inner face is observed in one of the nine PMTs. For the back-to-back selection of two gammas, the trigger also requires the maximum signal at central crystal among nine crystals, or hits in pre-shower counter in

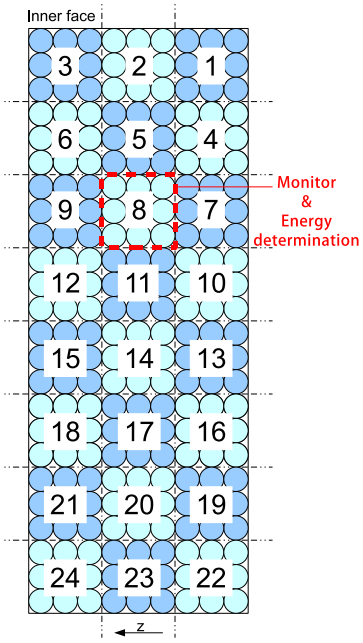

Figure 6.22: Software-collimator patches on the inner face for π^0 run. Circles show the location of PMTs and are divided into 3×8 patches by 3×3 PMTs region ($\Delta u \times \Delta v = 18.6 \times 18.6$ (cm^2)). The collimator patch #8 in dotted red box is used for the light-yield monitor and the determination of the energy scale.

front of the central NaI. The former is used for the energy measurement and later is for the timing measurement. The interaction of gamma rays in lead converter worses energy resolution, thus these are separately used by purpose. The online selection of maximum deposit in central NaI makes analysis effective because it is hard to use the events with a gamma ray entering the surrounding eight NaIs due to worse resolution by gamma-ray leaks. The distribution of triggered opening angle is shown in Figure 6.23, where the events with the opening angle larger than 170° are selected. It agrees well with the expectation of the angle 11°, which is the size of a patch viewed from the target. In order to acquire better resolution of the NaI, we also apply a cut by an energy ratio of the central NaI to the all NaIs, to be larger than 0.6.

Reconstructed scintillation photons of 54.9 MeV energies at 24 patches differ because of the position-dependent response as described in Section 4.2.5. Therefore we select one of the divisions for a constant monitor to be taken frequently. The central upper position, 'patch #8' of dotted box in Figure 6.22, is frequently taken for the monitor. It enables to monitor the change of the light yield independently of the position dependence.

The opening angle is calculated from the reconstructed position of the LXe and the central position of the NaI. This opening angle information is used to correct the expected energy using the theoretical correlation between energy and opening angle. The two gamma rays around edge of the patch makes higher 54.9 MeV-like peak or lower 82.9 MeV-like peak, thus it is corrected by theoretical energy dependence of opening angle. Figure 6.24 shows the correction factor for each energy and it is effective for edge events. To avoid a shift of opening angle by a misalignment of the NaI position, both peaks at 54.9 and 82.9 MeV in the LXe detector and also the other gamma-ray peak at the

NaI detector are monitored because the change of peaks by the shift of opening angle is opposite between two gamma rays, and thus it can be separated from the light-yield change.

The runs at patch #8 were taken everyday just after or before the calibration set of LED, alpha and cosmic ray run. Typically it takes for half an hour to complete the run with 50k events for each calibration. Figure 6.25 shows the monitor of the light yield at patch #8 position as blue circles, while peaks from other patches are red plots. The peaks from patch #8 agree with others and show the stable operation in π^0 run.

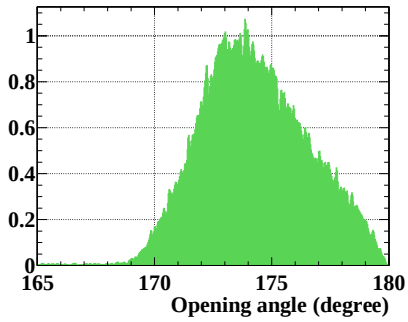

Figure 6.23: Opening angle distribution triggered by 3 × 3 PMTs region.

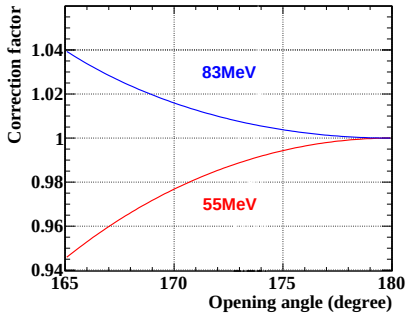

Figure 6.24: Correction factor by opening angle for 82.9 MeV and 54.9 MeV.

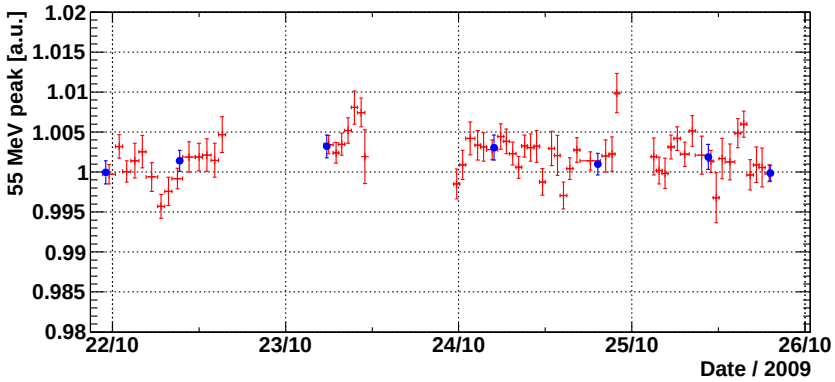

Figure 6.25: 54.9 MeV peak history in 2009 π^0 run. Blue circle plots show the monitoring at patch #8.

6.4.3 Monitor with the CW accelerator

The CW calibration run around 30k events was taken to collect 17.7 MeV lithium peaks once per a few days during physics run. Figure 6.26 shows 4.4 MeV and 12.0 MeV peaks from boron and Figure 6.27 shows 17.7 MeV and broad 14.6 MeV peaks.

The light-yield stability during 2009 run is ensured with 17.7 MeV lithium peaks as shown in Figure 6.28, and its projection in Figure 6.29 shows the stability within 0.25%

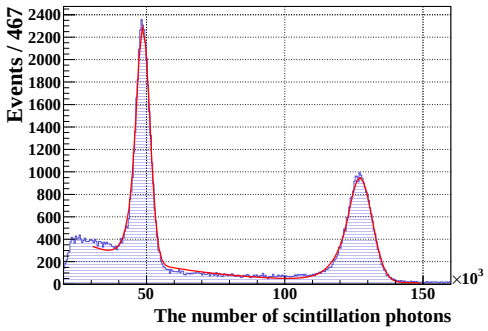

Figure 6.26: Boron peaks of gamma rays in CW run.

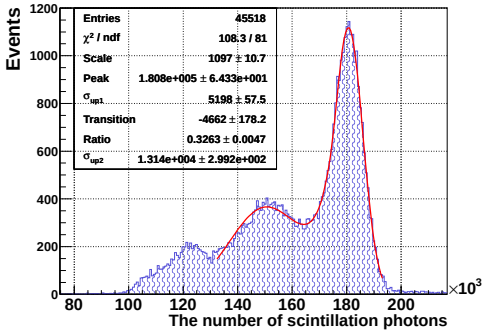

Figure 6.27: Lithium peaks of gamma rays in CW run.

in σ. Thus, we concluded that the light-yield in 2009 was stable within 0.25% precision by the lithium peak monitor. The resolution was also stable as shown in Figure 6.30.

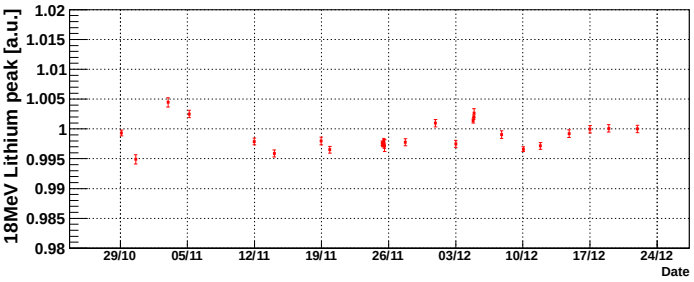

Figure 6.28: Monitor with 17.7 MeV peaks in 2009 CW run.

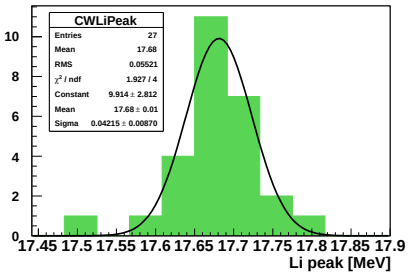

Figure 6.29: 17.7MeV Lithium peaks in 2009 within 0.25% stability.

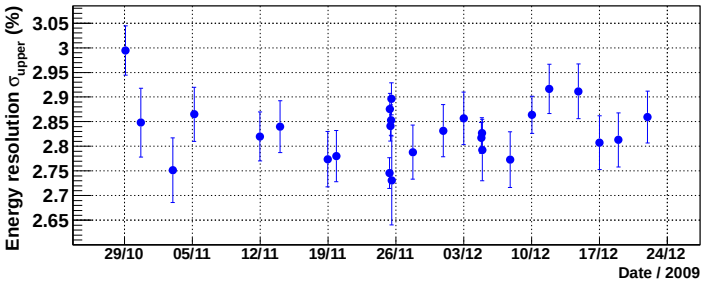

Figure 6.30: Stability of energy resolution at 17.7 MeV in 2009 CW run.

6.4.4 Cosmic-ray monitor

The Landau distribution from cosmic rays is obtained by selecting muons penetrating outer face and inner face, as shown in Figure 6.31. The benefit of the cosmic-ray monitor is that it is always available and it is mixed in the physics run.

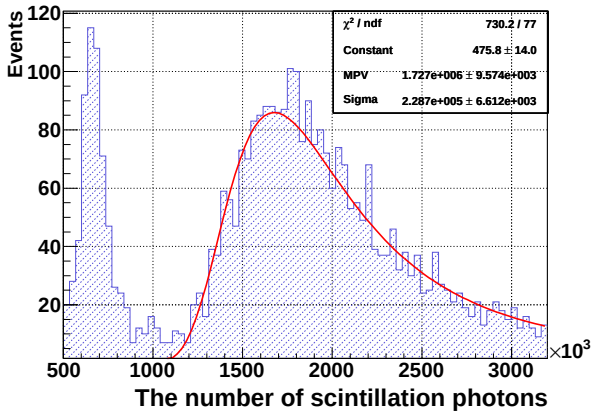

Figure 6.31: Landau peak of cosmic ray.

6.4.5 AmBe monitor

The americium-beryllium source, ^{241}Am-^{9}Be, provides a 4.4 MeV gamma ray from the bound-excited state of ^{12}C*, which is produced in the $^{9}_{4}\mathrm{Be}(\alpha, \mathrm{n})^{12}_{6}\mathrm{C}^{*}$ nuclear reaction after ^{241}Am emits 5.5 MeV alpha particle [59]. Another reaction of $^{9}_{4}\mathrm{Be}(\alpha, \mathrm{n})^{12}_{6}\mathrm{C}$ emits a 8 MeV neutron.

There are two major backgrounds; alpha and neutron backgrounds. The alpha contamination from ^{241}Am immersed in liquid xenon can be easily separated by the particle identification using pulse shape. The neutron background originates from the source itself. In the case of the monitor during π^0 run, it comes also from the π^- beam, and thus this background could change as a function of time. It is difficult to estimate the background shape and rate with a dedicated different run without the source. Therefore, we estimate the background spectrum using the AmBe run data itself as shown as a light blue line in Figure 6.32 [60]. By subtracting the estimated background, the peak of 4.4 MeV gamma ray clearly appears as shown as a gray filled histogram in the figure. Estimated energy resolution agrees with an expectation from other calibration runs but its precision is low because of the background, thus the same 4.4 MeV peak from the lower boron peak in CW run is suitable to see an energy dependence of energy resolutions.

The connection between π^0 and physics run is important because the energy scale is estimated in π^0 run. The monitor with both AmBe source and cosmic ray confirms the stability of the light yield in 2009 between 54.9 MeV π^0 and 17.7 MeV CW monitor.

6.4.6 Alpha monitor

The alpha peaks are constantly taken with LED run to estimate QE, but it is not used for a light yield monitor of 'gamma ray' because of the different scintillation process described

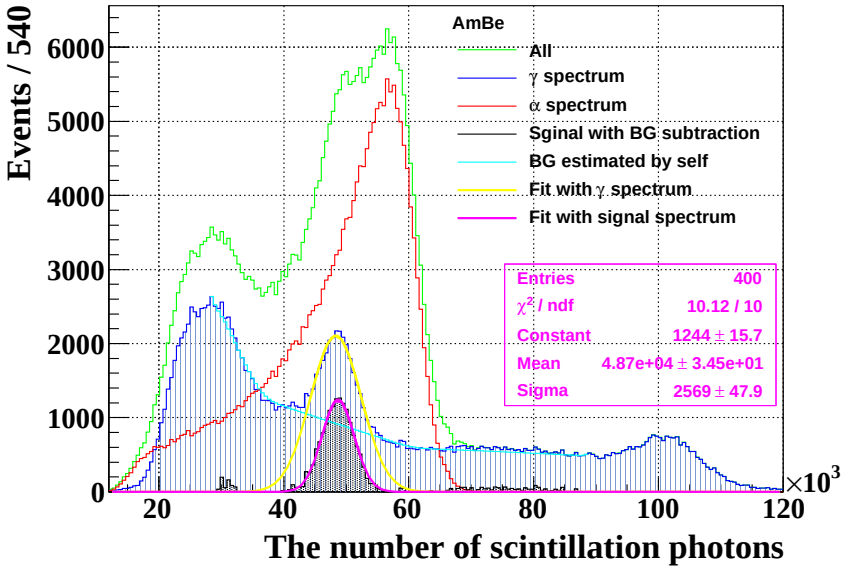

Figure 6.32: 4.4 MeV gamma-ray peak from AmBe source.

in Section 3.6.2. The monitor of alpha peaks is still significant to monitor the purity of xenon by alpha particles and stability of the detector including the waveform digitization and the gain calculation. Figure 6.33 shows the summed peak over all 25 sources, which enables more precise monitor than using peaks from each source.

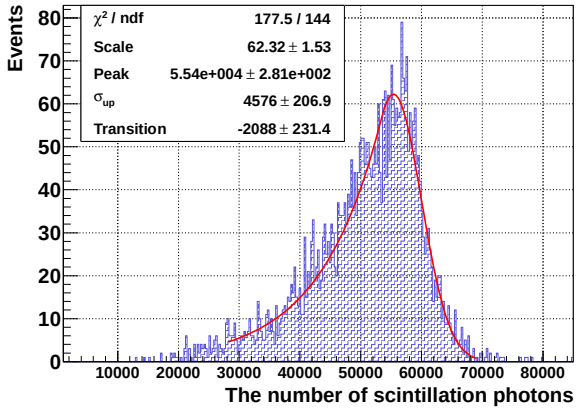

Figure 6.33: Alpha peak of all sources.

6.4.7 Monitor during muon beam

The stability of the LXe detector could be confirmed by beam-off calibration set. Then, it is important to check the stability in physics run when the muon beam is used. The mixed events of alpha sources in physics data taking allow the monitor once per day, while those of cosmic rays two in a week. The monitors are shown in Figure 6.34 and the peaks from alpha sources and cosmic rays seem to be stable within each precision of monitors.

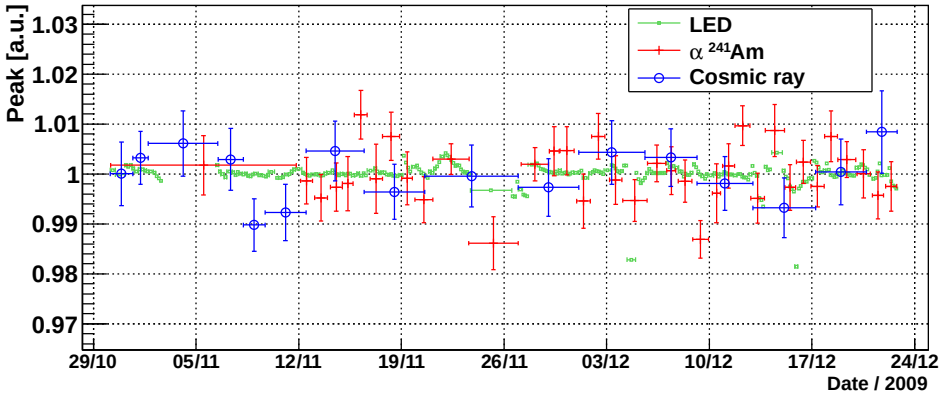

Figure 6.34: Peak of alpha, cosmic ray and LED in muon beam (The same LED peaks as in Figure 6.14).

6.4.8 Combined monitor of the light yield in 2008

In 2008, to trace the change of the light yield, the peak of 54.9 MeV at patch #8 and 17.7 MeV peak from lithium were combined with the help of cosmic rays and AmBe source (Figure 6.35). Instead of using the number of photons per energy, we obtain the relative change of the light yield by scaling each peak history in such a way that the average of peaks during overlap period are the same values between histories. This method reduces the uncertainties such as a linearity of energy response and unknown cosmic-ray peak energy.

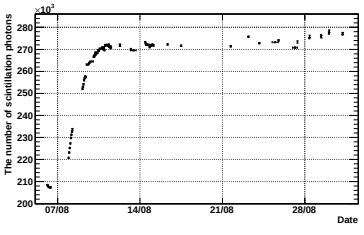

(a) 54.9 MeV in August.

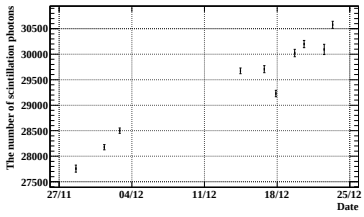

(b) 4.4 MeV AmBe.

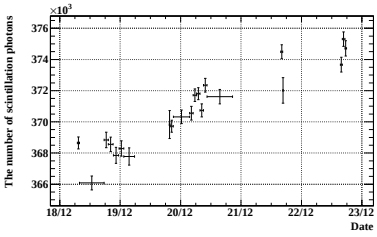

(c) 54.9 MeV in December.

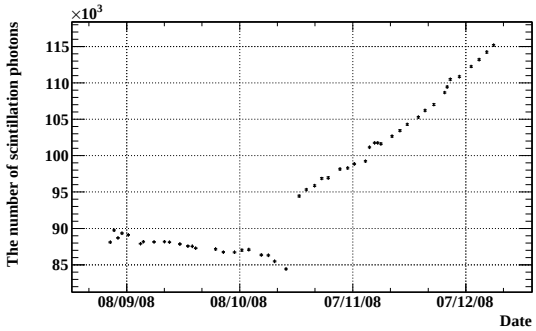

(d) 17.7 MeV CW Lithium.

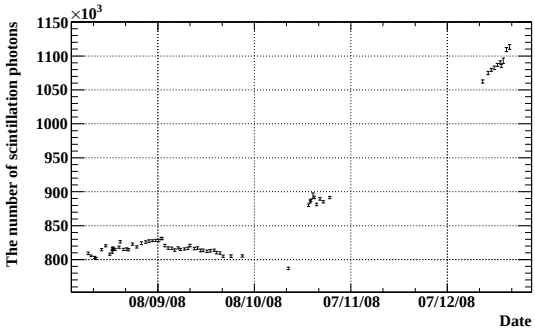

(d) Cosmic ray (Beam off).

Figure 6.35: Peak history in 2008.

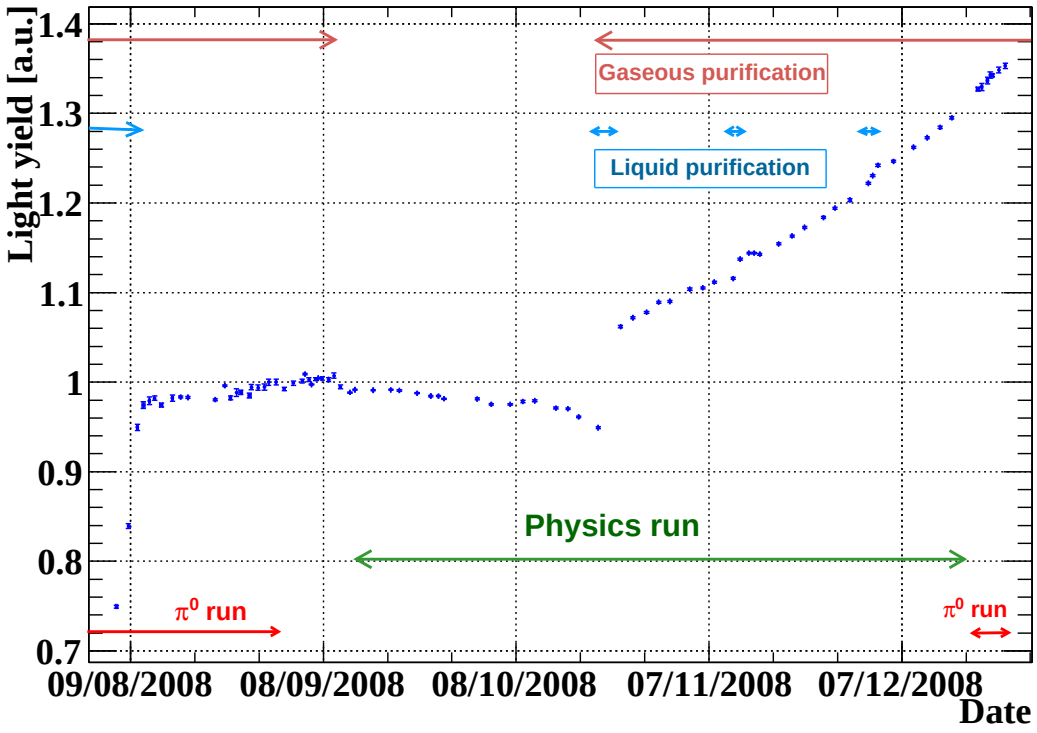

Figure 6.36: Combined history in 2008.

Figure 6.36 shows the change of the light yield in 2008. It was constructed with light-yield histories shown in Figure 6.35. To make a smooth history, points taken near each other were merged with taking average. After that a simple linear interpolation is applied. We confirmed that the peaks from alpha sources stayed constant during 2008 data taking, which differed from the other results from gammas. This can be explained by the different contribution of the scintillation process described in Section 3.6.2, and the history of alpha peaks was not used for the light yield correction. The constructed light yield history was used in 2008 to extrapolate the energy scale that was obtained at the end of August in π^0 run.

Figure 6.37 shows the light yield from 2008 to 2009. The red plots shows the peaks of 17.7 MeV by CW calibration and blue plots are taken from cosmic-ray Landau peaks. Before physics run in 2009 we performed a purification for xenon and the light yield was much improved. We confirmed the stable light yield in all monitors, therefore we do not apply the light yield correction for 2009 data.

6.5 Uniformity

6.5.1 Non-uniformity correction

Although the reconstructed scintillation photons has the non-uniformity response, the uniform energy response is available by the non-uniformity correction based on actual measurement in calibration runs. We made correction factors along u and v by 17.7 MeV peaks in CW run and depth correction functions by 54.9 MeV peaks in π^0 run in 2009 (by 17.7 MeV in 2008). In 2008 we observed the change of non-uniformity with the

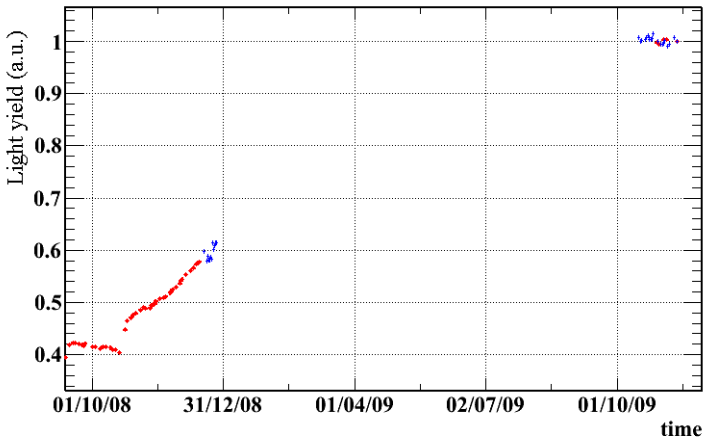

Figure 6.37: Light yield history from 2008 to 2009. The 17.7 MeV peak in CW run (red plots) and cosmic-ray Landau peak (blue plots) show the consistent improvement.

improvement of light yield, therefore we prepared two sets of correction tables before and after the purification started. Thanks to the stable light yield we prepared only one set of non-uniformity correction in 2009.

The correction factor is estimated with both two dimensional relation on u-v plane and one dimensional relation along depth, w. In particular, the peak transition along depth depends on both the energy scale and the position on u, v. Therefore the depth correction in 2009 is made from 54.9 MeV peak in π^0 run with separated three u positions, while only one u-division in 2008. The lateral walls are near each other than the top and bottom faces, thus peaks have larger dependence along u direction than v direction. This is the reason why we separate depth correction along u direction rather than v direction. Figure 6.38 shows factors of depth correction in 2008 and 2009.

The remained u-v correction is estimated after the depth dependence is corrected. Ideally the use of 54.9 MeV peaks is the best way to observe 52.8 MeV signal, however π^0 run are taken separately by 24 patches, and those may contain additional uncertainty coming from time-dependent variation. In addition, the larger gain decrease in π^- beam than that in muon beam makes it difficult to trace gain correctly, which may also bring gaps between patches. On the other hand 17.7 MeV gamma rays are available for the whole region of inner face at the same time which avoid any time-dependent variation. Thus we adopted lithium peaks for u-v non-uniformity correction. We estimate peaks by one PMT size window (6.2 cm $\times$ 6.2 cm) for w deeper than 2 cm with shifting by 1/3 PMT width along u and v to make a smooth peak transition. Thus the windows are overlapped and 24 selection windows are defined along u and 72 along v. Figure 6.39 shows the correction factor on u-v plane, which is inversed non-uniformity response.

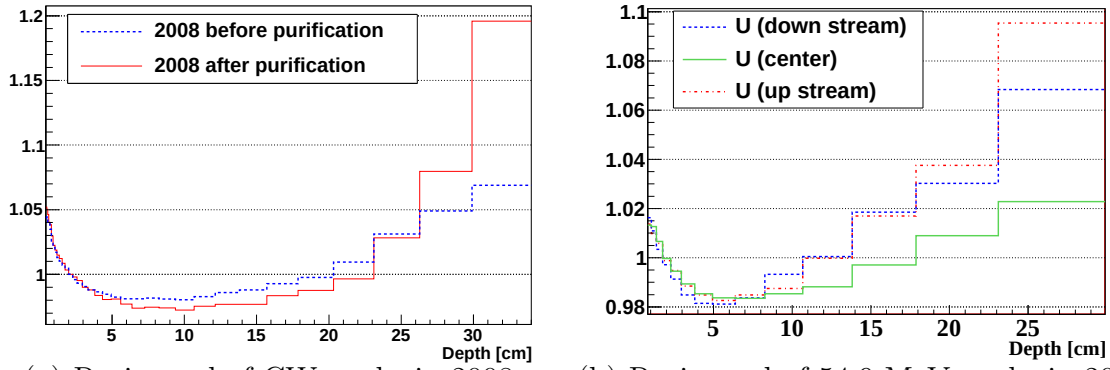

(a) Reciprocal of CW peaks in 2008. (b) Reciprocal of 54.9 MeV peaks in 2009.

Figure 6.38: Correction factor along depth (w). In 2009 factors are separately estimated along the beam axis u by three sets.

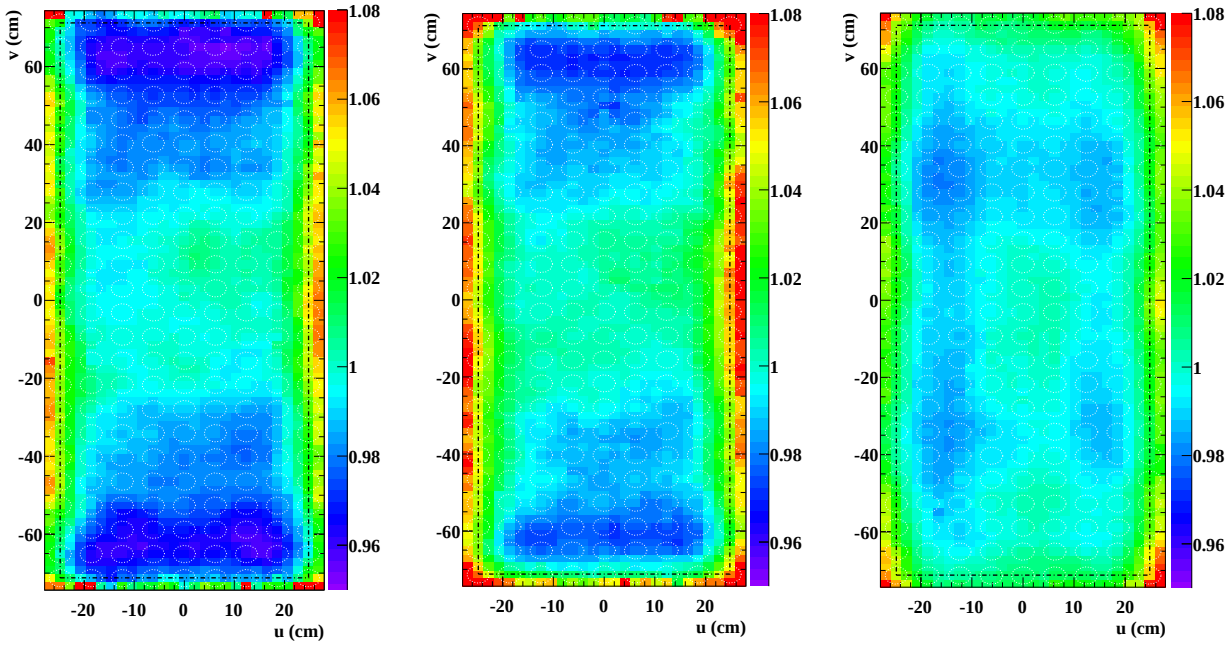

(a) Before purification in 2008. (b) After purification in 2008. (c) In 2009.

Figure 6.39: Correction factor on u-v plane (as the reciprocal of the peak). Acceptance region is shown in black dotted box and white circles indicate PMTs. QE set is the same between (a) and (b), but different between 2008 and 2009. The light yield improved between the sets. The factor in 2009 is calculated after the depth dependence is compensated by the factor in Figure 6.38 (b).

7 Performance of the Liquid Xenon Detector

7.1 Position

The position resolution of the liquid xenon detector along two directions, (u, v), is evaluated in a dedicated π^0 run at a certain part of the inner face. Lead collimators with slits were mounted in front of the gamma-ray window. Resolutions are measured by an event distribution of reconstructed positions around the slits. Because it takes too much time to measure position resolutions at all positions in the acceptance region, position dependence was estimated from the MC and the comparison with data was done at limited positions. In 2008 π^0 run, the agreement of position resolution between the data and the MC was checked. A QE estimation with a displacement of alpha source wires or unexpected errors from optical properties in MC such as the reflection and the attenuation length could make a global bias in the position reconstruction. In 2009, a global bias of the reconstructed position along beam axis z was measured in addition to the position resolution.

7.1.1 Collimator run in 2008

The lead collimators with slits which were used in 2008 measurement are shown in Figure 7.1. Each width of the slit is 1 cm, and the thickness of the lead collimator is 1.8 cm. Figure 7.2 (a) shows a reconstructed event distribution along u axis taken with the lead collimator that is shown in the Figure 7.1 (right one). Three peaks and two inner edges come from three horizontal slits and both sides of lead. The outer edges out of the lead collimator come from a bias on trigger, which selects collimator regions in 2 $\times$ 3 PMT size. A fitted red line is a combination of triple Gaussians for slits and two Error functions for edges with a floor. Figure 7.2 (b) is the same setup in the π^0 MC.

Figure 7.1: Lead collimator with 1.8 cm thickness in 2008 (a 2-inch PMT is shown for a reference). The lead on the left side has vertical slits of 1 cm width and the two leads on the right side have a 13 cm-length horizontal slit. Between two leads with the horizontal slit, another collimation is possible by these gap as shown in picture. The lead with horizontal slits in 2009 has a three times longer length.

Table 12 shows the sigmas from the fitting, which includes the width of slits and the beam spread in the hydrogen target of $\sigma_x = \sigma_y = 8$ mm and $\sigma_z = 25$ mm. The average of σ_v in slits is 6.9 mm in data and 6.5 mm in MC, and then the difference between data and MC is estimated to be 1.8 mm. The difference is added to the position dependent resolution map obtained from the signal MC. The difference probably originates from a precision of the PMT calibration, which is not included in the MC. The standard deviation of the difference between measured and expected mean of v position is 0.7 mm.

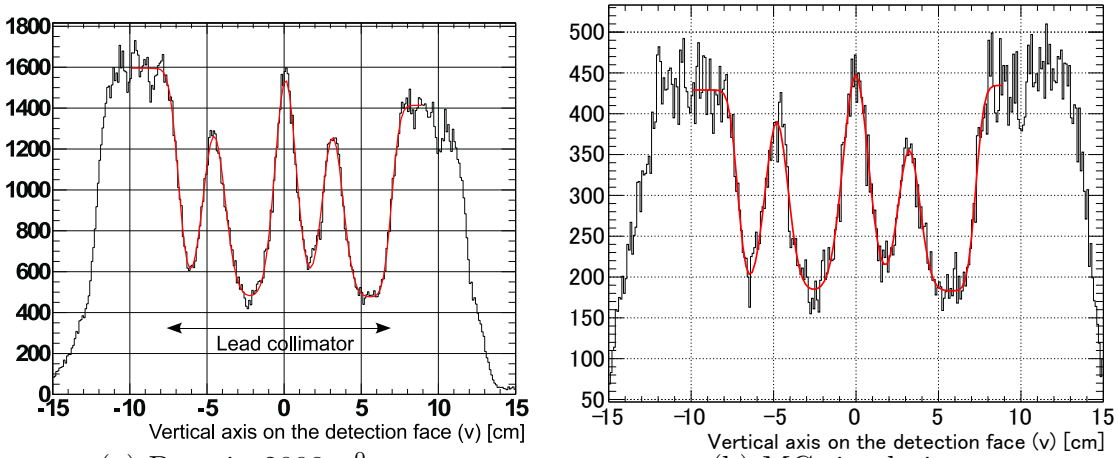

(a) Data in 2008 π^0 run. (b) MC simulation.

Figure 7.2: Event distribution through slits sliced along v. The selection is applied for all energy regions from two gammas, w deeper than 2 cm and a range of -15 cm $< u <$ 5 cm.

Table 12: Sigmas fitted in slits and edges along v (w >2 cm). Central slit in MC is omitted due to a difference of the geometry between data and MC.

	slit1	slit2	slit3	edge1	edge2
σ_v in 2008 Data (mm)	7.2	6.8	6.7	4.7	4.2
σ_v in MC (mm)	6.8	-	6.5	3.9	4.2
σ_v in MC truth (mm)	4.7	-	4.9	2.3	2.8

The resolution along u direction can be also estimated with vertical slits as shown in Figure7.3. However, it is more complicated for the following reasons:

- Slant angle of incident gamma rays makes a different response by u due to the cylindrical shape of the detector.
- Not independent from the depth resolution σ_w.
- The faces of the slits are perpendicular to the inner face, and are not parallel to gamma rays.
- Beam spread along z is wider (σ_z = 25 mm) than along ϕ ($\sigma_x = \sigma_y$ = 8 mm) and its projection along u on the inner face is about 5.8 mm.
- The length of a gamma-ray shower is projected on u, especially around large $|u|$.

Figure 7.3 shows an event distribution through vertical slits along u direction. The average of σ_z in six points is 6.1 mm with about 1 mm bias around center and those are comparable with the result along v.

The reconstruction method is the same for u and v, thus in principle the resolutions are similar to each other except for depth contribution. The position resolution along u and v strongly depends on the depth, which can not be seen in data but can be estimated in the

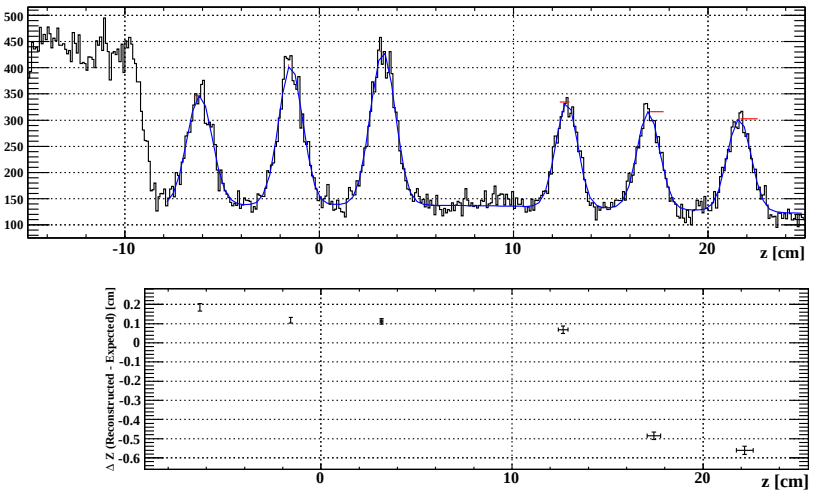

Figure 7.3: Event distribution through slits sliced along u (z) in 2008 π^0 run. The upper distribution is fit by six Gaussians with a floor as a continuous line and the expectation of slit positions is marked on the top of peaks. The plots in the lower shows the difference between the reconstruction and the expectation of u by the u position of slits.

MC. The difference between the data and the MC is applied to the position dependent resolution on u, v and w obtained in the MC.

7.1.2 Collimator run in 2009

In 2009 we prepared two collimators with long horizontal slits and 18 mm thickness. Two collimators have the same dimension except for the width of slits, 10 mm and 5 mm, and each has a long slit and three short ones to cover the entire z position at different v positions. The 10 mm-slits collimator was put at the v center of the detector as shown in Figure 7.4 and another with 5 mm slits at the lower part of the detector.

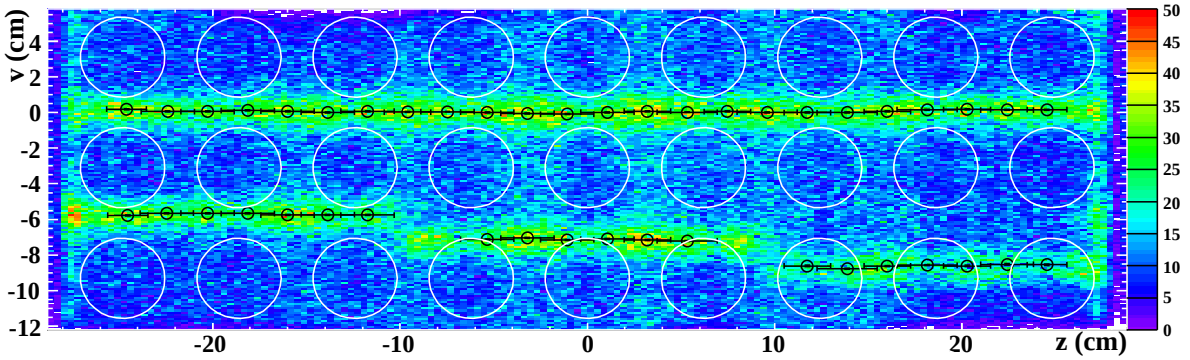

Figure 7.4: Event distribution of 10 mm slits in 2009 π^0 run. Circle plots show peaks in slits fitted by scanning along u. Large white circles indicate the active area of PMTs.

Figure 7.5 shows a double Gaussian fit of projection for v with 2.1 cm width cut along u. Figure 7.6 is projection for u by each three short-length slit with 10 mm width cut

for v around the slits. These are fitted with an error function on a flat floor. The peak positions are shown in black circles in Figures 7.7 (a) and (c) for 10 mm and 5 mm slits, respectively. The sigmas are shown in Figure 7.8 for 10 mm slits and Figure 7.9 for 5 mm slits. Average of sigmas on the 10 mm and 5 mm slits data are 6.8 mm and 6.5 mm in σ_v (Figure 7.10), respectively, and it agrees with 2008 result.

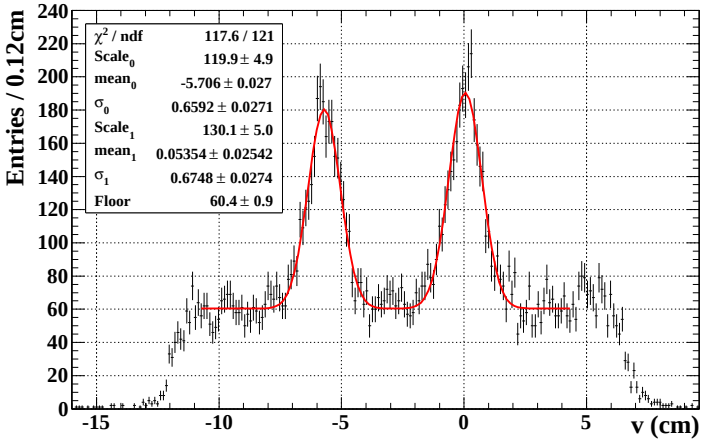

Figure 7.5: Cross section along vertical v ($w > 2$ cm).

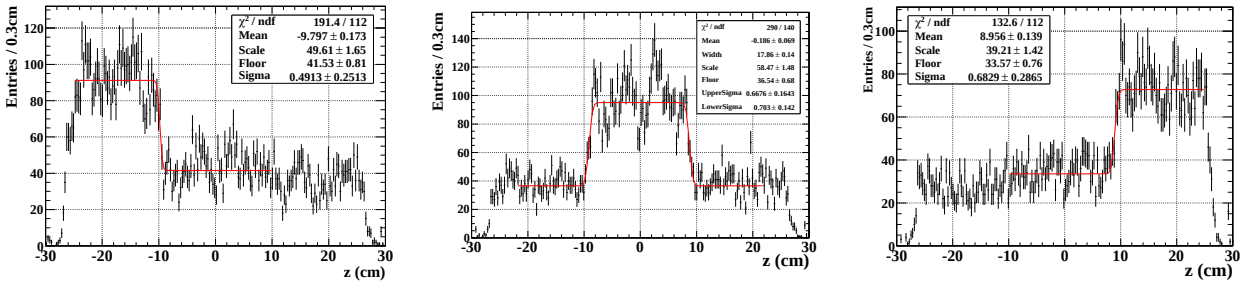

Figure 7.6: Longitudinal cross section of three slits along z ($w >$2 cm).

7.2 Time

The timing performance of the MEG detector is evaluated with a coincident radiative muon decay as a time difference between the LXe detector and the positron spectrometer. The single timing performance of the LXe detector was estimated by the measurement of two gamma rays of π^0 decay using the opposite plastic counters in front of the NaI as a reference. Another method was performed to measure an intrinsic time resolution, where the difference of reconstructed times by subdividing PMTs in the LXe detector into two groups were compared.

7.2.1 Intrinsic time resolution

The difference of reconstructed time from two divided groups of PMTs indicates the intrinsic time resolution. We performed the estimation on π^0-decay data near the signal

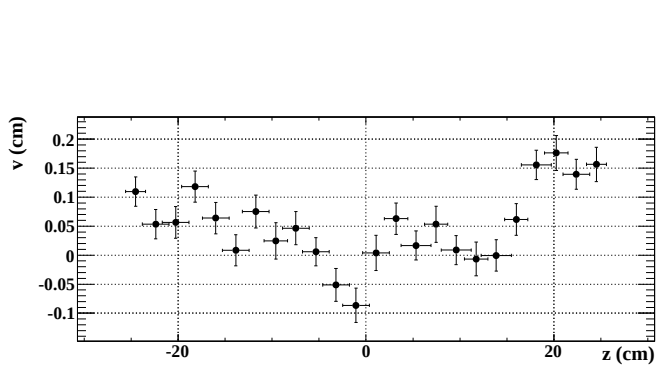

(a) 10 mm vertical slit.

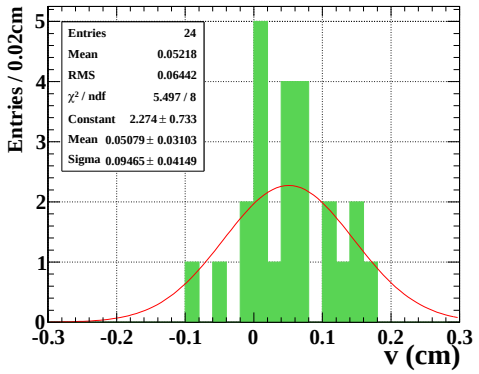

(b) Projection of (a) on v.

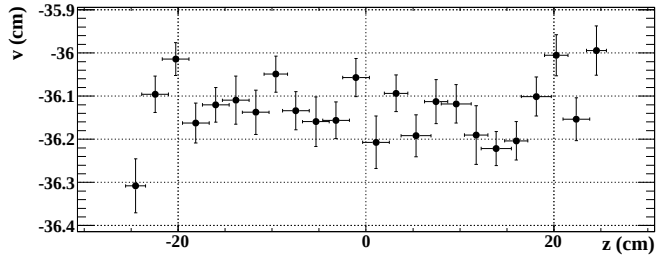

(c) 5 mm vertical slit.

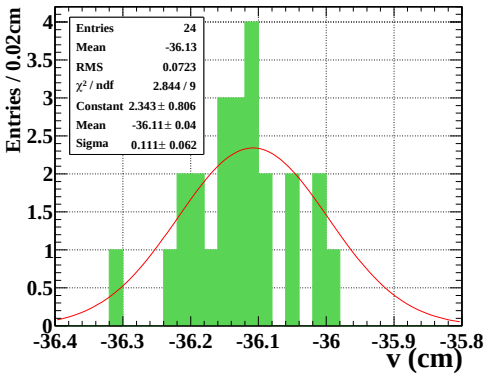

(d) Projection of (c) on v.

Figure 7.7: Peaks on the long slit by scanning along z with width of $\Delta z = 2.1$ cm.

energy. The word '*intrinsic*' means that it includes a precision of timing estimation at each PMT and electronics such as cable or synchronization but no fluctuation of scintillation light in the detector from a reflection or per-event shower development. It gives some useful information such as position or the number of photons dependence of timing and the difference between data and MC. PMTs are subdivided into two groups (odd and even index number group) as shown in Figure 7.11. Its uniform and symmetric division allows the same treatment with the same statistics of photons each other. The normal time reconstruction is performed for each group and two obtained timings are compared.

The statistics of photons becomes half by two divisions, but that effect for the intrinsic time resolution is canceled out after the time difference is divided by two. Half of the time difference between the odd-number and even-number group of PMTs is regarded as the intrinsic time resolution, defined as $\sigma((t_{even} - t_{odd})/2)$. It resulted in 37.5 ps at 54.9 MeV and 30.5 ps at 82.9 MeV. Figure 7.17 shows that the dependence of the resolution on energy is fit with $1/\sqrt{E_\gamma}$.

The dependence on position is also checked. Figure 7.12 shows a map of the intrinsic time resolution of two groups. In the figure the u-v window for the scan is set to 1×1 PMT size and energy ranges around 54.9 MeV (40 MeV $< E_\gamma <$ 60 MeV) and 82.9 MeV (70 MeV $< E_\gamma <$ 90 MeV) are selected. Figures 7.13, 7.14 and 7.15 show the resolution along depth w, u and v.

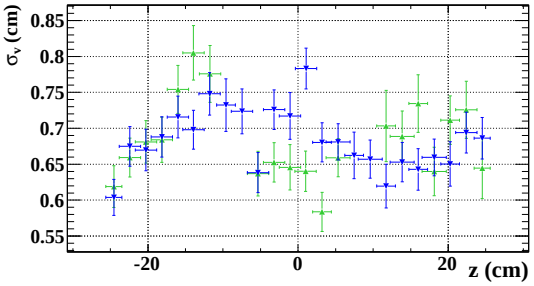

Figure 7.8: σ_v in 10 mm slits.

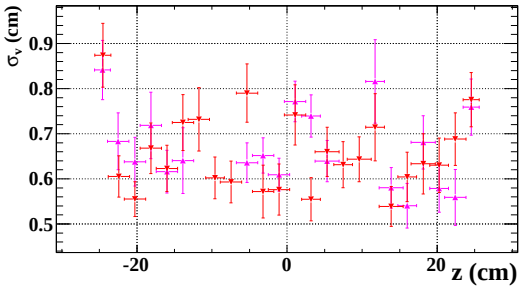

Figure 7.9: σ_v in 5 mm slits.

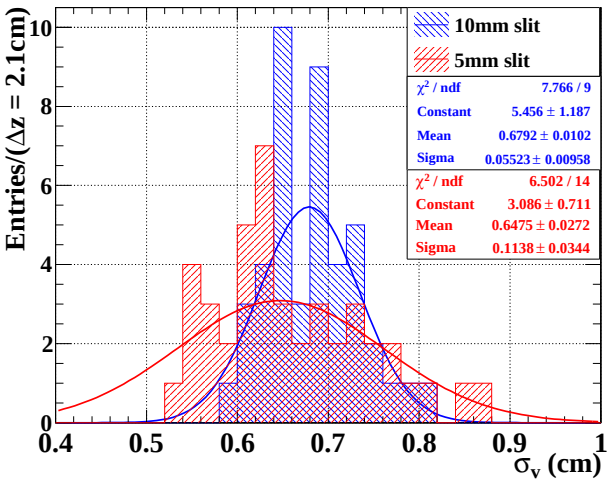

Figure 7.10: Distribution of the position resolution σ_v in 5 mm and 10 mm slits (Fittings on slices in z with 1/3 PMT width).

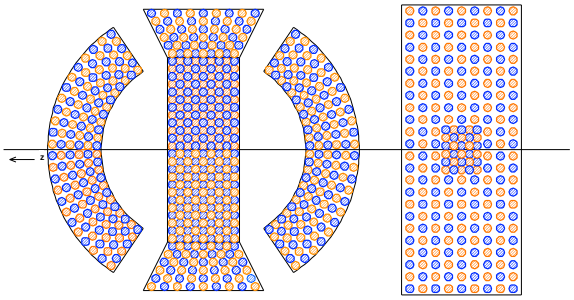

Figure 7.11: PMT grouping scheme for the intrinsic time resolution study. PMTs shown in blue circles belong to odd group, and those in orange circles belong to even group.

7.2.2 Absolute time resolution

The coincident time of two gamma rays are measured with scanning the whole acceptance by moving the NaI detector at 24 positions (Figure 6.22). At each scanning position 50k events were taken with using the plastic scintillators and the lead converter in front of the NaI. Absolute time resolution was measured from the time difference between the LXe and pre-shower detectors.

Figure 7.16 shows the time difference between two detectors, which is estimated to be

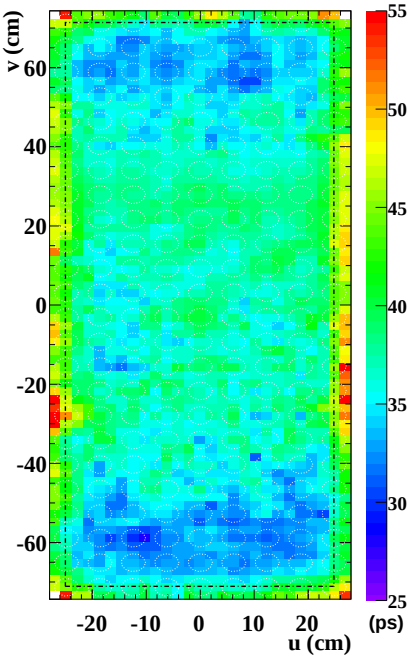

Figure 7.12: u-v map of intrinsic time resolution.

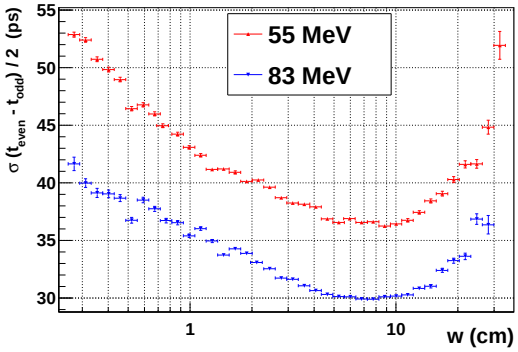

Figure 7.13: Intrinsic time resolution as a function of depth.

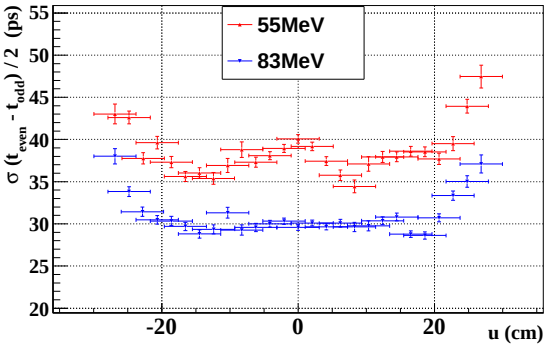

Figure 7.14: Intrinsic time resolution as a function of u (at v-center).

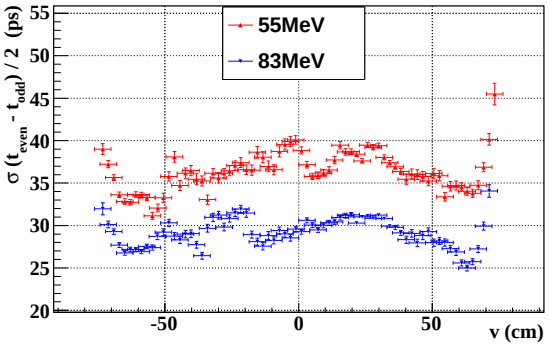

Figure 7.15: Intrinsic time resolution as a function of v (at u-center).

171 ps in sigma of Gaussian distribution at 54.9 MeV and 163 ps at 82.9 MeV. In this distribution, main three components are considered,

- Resolution of the reference pre-shower counter : 72 ps in σ,
- Contribution from beam spread : (58 ± 2) ps in σ,
- Time resolution of the LXe detector : to be estimated,

therefore time resolution of the LXe detector is calculated by subtracting contributions of reference pre-shower counter and the beam spread to be 144 ps at 54.9 MeV and 134

ps at 82.9 MeV, respectively. A dependence of the resolution on the energy was shown in Figure 7.18, which results in $\sqrt{659^2(\mathrm{MeV})/E_\gamma + 146^2}$ ps with a fit.

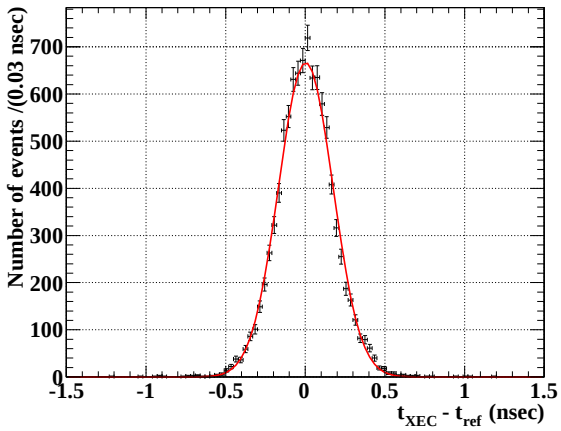

Figure 7.16: Time difference between the LXe detector and pre-shower timing counter in front of the NaI.

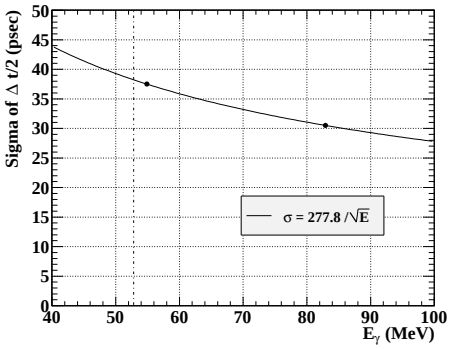

Figure 7.17: Intrinsic time resolution as a function of the energy.

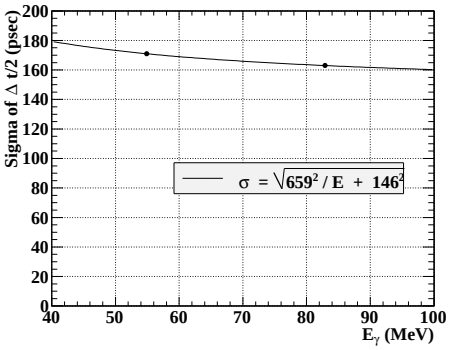

Figure 7.18: Absolute time resolution as a function of the energy.

7.3 Energy

7.3.1 Energy resolution

The energy resolution and scale of the gamma-ray detector are determined at 54.9 MeV peak in π^0 run. Precise determination of the energy scale and measurement of the resolution are quite important to improve sensitivity of the experiment.

The energy peak is estimated with a combination of Gaussian function for higher energy part and exponential function for a tail. These two functions are smoothly connected at transition point lower than the peak energy. Only in π^0 run, the pile-up elimination

is not applied. Instead of that, to obtain the energy resolution in π^0 run, we considered a difference of pedestal between muon beam and charged pion beam by a following procedure.

1. Prepare two pedestal distributions of the number of scintillation photons mixed in a corresponding π^0 runs and also in physics run (200 μm or 300 μm degrader separately).

2. The histograms prepared in the first step are scaled by averaged non-uniformity correction factor at each position.

3. Fit 54.9 MeV peak at the position by Exponential-Gaussian function convolved with the pedestal histogram in the π^0 runs.

4. The Exponential-Gaussian component in the previous fitting function is a intrinsic resolution excluding a contribution of the pedestal distribution. Generate peak distribution from the Exponential-Gaussian function with convolving the pedestal histogram in the physics run, which is corresponding to the distribution during physics data taking without pileup elimination.

5. Fit the constructed 54.9 MeV peak with Exponential-Gaussian function.

Figure 7.19 shows the energy peak at 54.9 MeV fit with the function at 3 × 3 PMTs region of upper central part (patch #8). The selection is applied for events deeper than 2 cm, opening angle larger than 175° and around 82.9 MeV peak at the NaI.

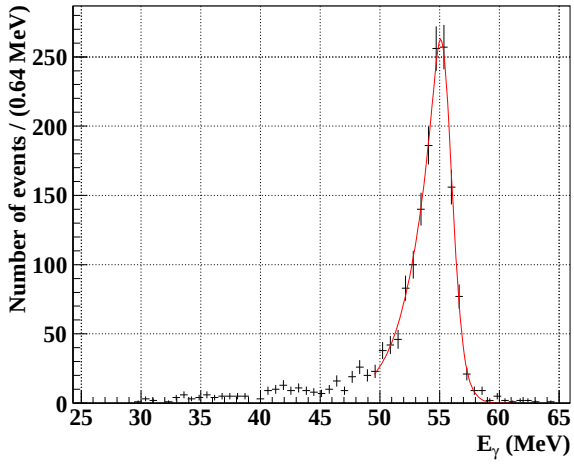

Figure 7.19: Energy peak of 54.9 MeV in π^0 run.

7.3.2 Uniformity of reconstructed energy

The non-uniformity correction factors of energy scale are estimated using 17.7 MeV peaks as described in Section 6.5.1. Figure 7.20 shows the distribution of peaks at various positions by scanning the inner face with selections of one PMT size at 17.7 MeV or 1.5 × 1.5 PMT size at 54.9 MeV. The broad distribution of 17.7 MeV peaks becomes sharp by

the correction with 0.1% width in sigma. Although the correction factors were estimated at 17.7 MeV, we have also confirmed the factors by 54.9 MeV mean distribution, which is as narrow as 0.28% in sigma.

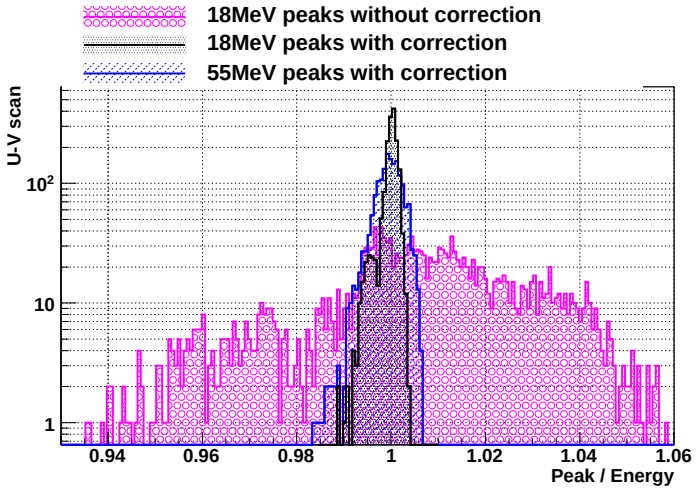

Figure 7.20: Peak distribution at 17.7 and 54.9 MeV by u-v scan. The non-uniformity correction is not applied for broad distribution by 17.7 MeV peaks, and it gets sharp after the correction. Peak at 54.9 MeV becomes also sharp with the same non-uniformity correction.

7.3.3 Linearity of reconstructed energy

The linearity of the energy scale is checked using gamma rays from 4 to 129 MeV. Because we determine the energy scale at 54.9 MeV, which is close to 52.8 MeV signal energy, the existence of non-linearity is not severe and it can be corrected even if it exists. Within a 10-10^2 MeV region, we confirmed a good linearity shown in Figure 7.21, and a correction of non-linearity in the reconstruction is not necessary. The 5.5 MeV peak of alpha particles is not on the line because the dominant scintillation process differs from that of gamma rays and W value is also different.

7.3.4 Energy dependence of energy resolution

The energy resolutions in Figure 7.22 are estimated by means of gamma rays of 4.4 MeV and 12.0 MeV from boron and of 17.7 MeV from lithium in CW run, and of 54.9, 82.9 and 129 MeV in π^0 run at patch #8 position of 3 × 3 PMT size. The resolution of 4.4 MeV AmBe peak is not shown here because it is not so reliable when subtracting neutron backgrounds and its origin is the same as the reaction of the lower boron peak. At patch #8 of the energy determined position, the energy resolution as a function of energy is obtained by fit in Equation 68,

$$\frac{\sigma_{upper}}{E} = \left(\frac{10.4}{\sqrt{E}} \oplus 1.2\right) (\%) \text{ (at patch \#8, } w > 2 \text{ cm)}. \quad (68)$$

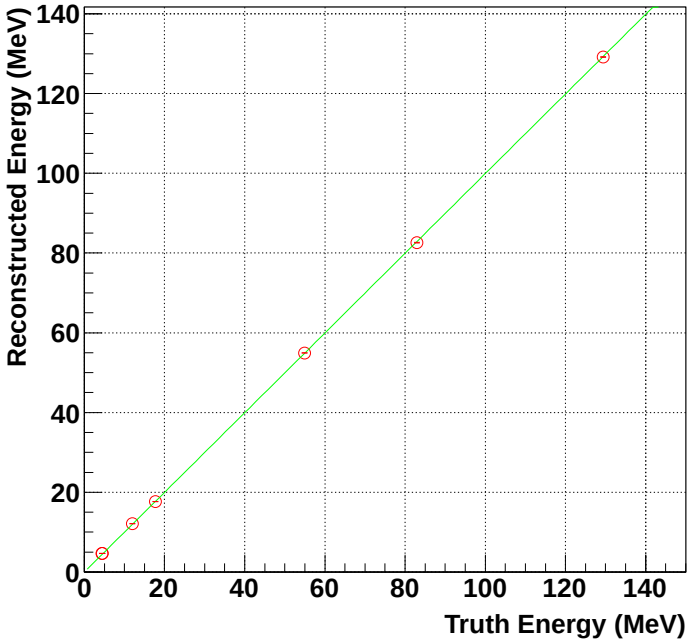

Figure 7.21: Linearity of reconstructed energy in 4.4, 12.0, 17.7, 54.9, 82.9 and 129 MeV.

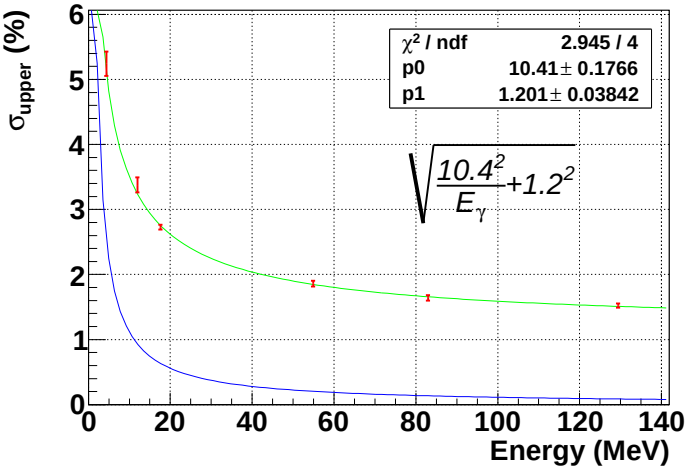

Figure 7.22: Energy resolution at 4.4, 12.0, 17.7, 54.9, 82.9 and 129 MeV. The lower line shows the contribution of pedestal.

7.3.5 Position dependence of energy resolution

Energy resolution in CW run and π^0 run The energy resolution depends on a reconstructed position largely. The dependence is investigated in CW Lithium run and π^0 run as shown in Figure 7.23. Resolution is worse in the shallow part and around the edge of the acceptance. The dependence is taken into account in the physics analysis. Figure 7.24 shows energy resolutions. Each entry is taken by a window of one PMT size at 17.7 MeV or 2×2 PMT size on the inner face. In the figure, the energy resolution in

sigma at 17.7, 54.9 and 82.9 MeV is simply averaged to be 2.8, 2.2 and 2.0 %, respectively. In both figures peaks in π^0 run are raw without pedestal subtraction. Following section shows a estimation of the energy resolution at 52.8 MeV $\mu^+ \to e^+\gamma$ signal.

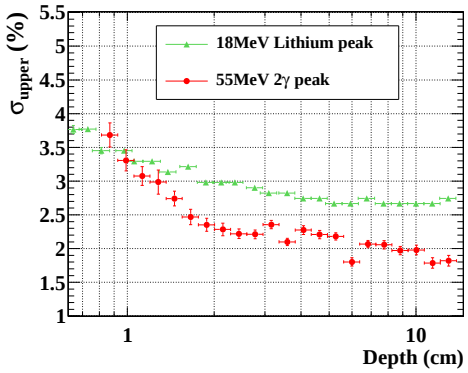

σ_{upper} by w.

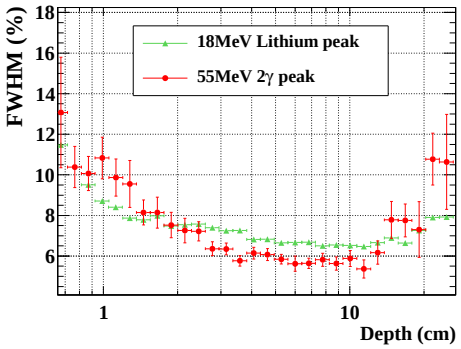

FWHM by w.

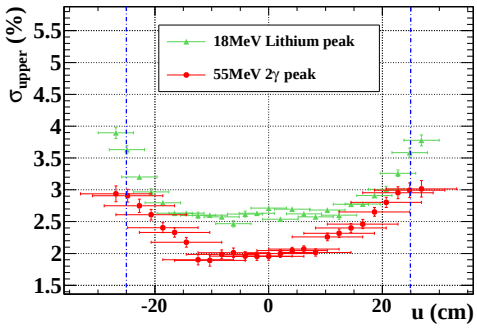

σ_{upper} by u ($w > 2$cm).

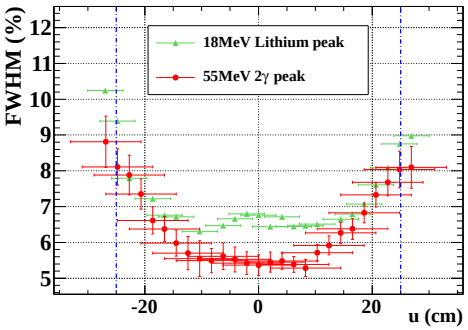

FWHM by u ($w > 2$cm).

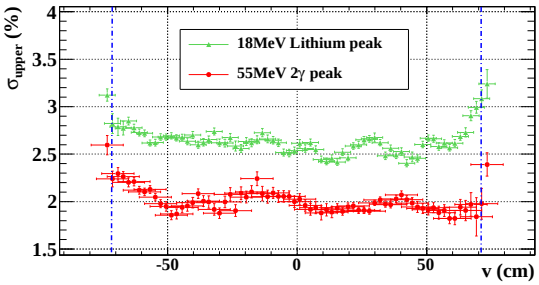

σ_{upper} by v ($w > 2$cm).

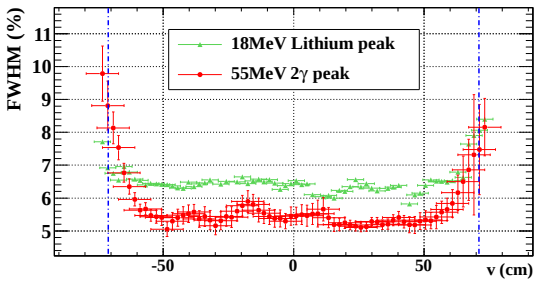

FWHM by v ($w > 2$cm).

Figure 7.23: Energy resolution in σ_{upper} and in FWHM along (u, v, w) - directions. Blue dotted lines show the acceptance edges. FWHM at 17.7 MeV is derived from only the higher peak in the fitted function.

The energy resolution at different u and v positions are evaluated by a window of PMT-unit size, therefore a ratio of active to inactive area of inner-face PMTs is same in any scanning points. That means no resolution dependence on position within a PMT appears. In order to look at a fine structure of the energy resolution correlated with the optical window of the PMT, a narrow window of 5 mm $\times$ 186 mm size, corresponding to 0.08 $\times$ 3 PMT size, is selected for events at patch #8 position. Figure 7.25 shows resolutions in sigma or FWHM as a function of u and v at 54.9 MeV. There may be a little correlation with center of PMTs, however it is a trivial and there is no strong

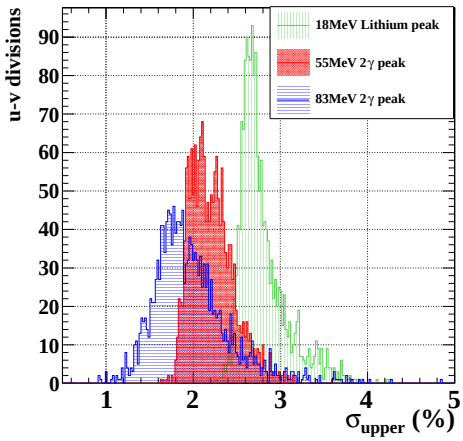

Figure 7.24: Energy resolution in σ_{upper} at 17.7, 54.9 and 82.9 MeV by u-v divisions.

dependence. Therefore the fine structure of energy resolutions within one PMT on the inner face is averaged.

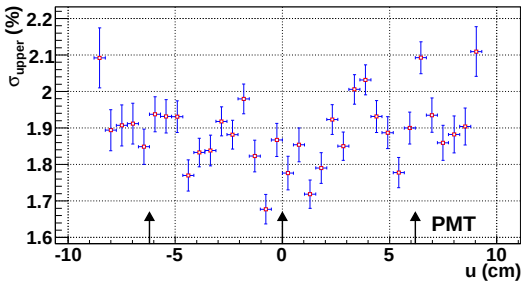

(a) σ_{upper} by u.

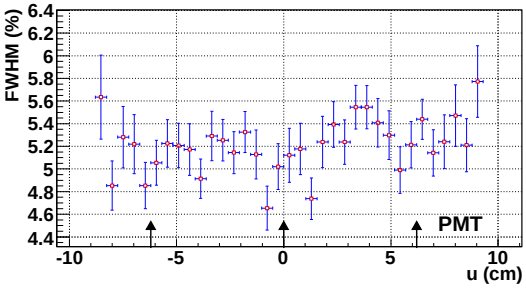

(b) FWHM by u.

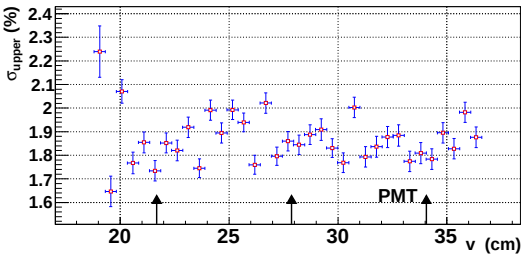

(c) σ_{upper} by v.

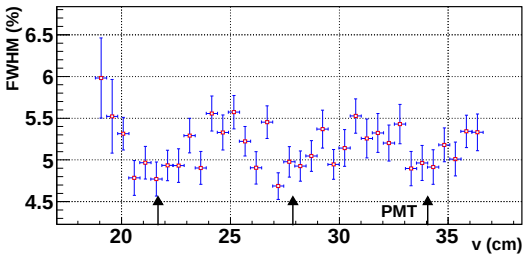

(d) FWHM by v.

Figure 7.25: Energy resolution at 3 × 3 PMTs region of patch #8 position with a fine scan. Events are selected by 5 mm × 186 mm window to check the resolution structure within a 1-PMT size window. Arrows show the center of PMTs.

Signal PDF of gamma-ray energy in 2009 The signal-energy PDF is based on 54.9 MeV resolution in π^0 run and expressed by the Exponential-Gaussian function. Parameters are prepared for each three dimensional position. The PDF is estimated by one PMT-size step in u and v directions with selecting 2 × 2 PMTs region within the acceptance, and w is divided into five windows, [0, 0.5], [0.5, 1], [1, 2], [2, 12] and [12, 38.6] (cm).

The procedure to obtain position dependent PDF at 52.8 MeV signal is described below:

1. The energy resolutions on the inner face are measured at 9 × 24 positions with 2 × 2 PMT size window selection in one-PMT size step ($w > 2$ cm). The obtained resolutions are shown in Figure 7.26.

2. In five depth divisions and wide range of $w > 2$ cm for the normalization, the resolution is also estimated by three divisions along u axis. The five depth-dependence resolutions are normalized with that in the wide range.

3. The energy dependence of sigma and transition point is estimated from 4.4, 12.0, 17.7, 54.9, 82.9 and 129 MeV peaks at patch #8 position. From the relations of sigma and transition as shown in Figures 7.27 and 7.28, respectively, conversion factors into the signal energy are calculated.

4. The resolutions obtained at the first step are scaled to take into account dependence on depth and energy using factors estimated at the second and the third steps.

The effect of the energy dependence is trivial for the resolution about 1% relatively. On the other hand the effect of the depth dependence is large particularly for a lower tail in shallow depth. Figure 7.29 shows a function obtained from a fitting on the 54.9 MeV data, and PDFs for signal at different depths. Averaged resolutions of sigmas in the whole acceptance are 2.1% (2 cm $\leq w <$ 38 cm), 2.8% (1 cm $\leq w <$ 2 cm) and 3.3% (0 cm $\leq w <$1 cm).

7.3.6 Systematic uncertainty

The candidates of uncertainties, which are related with gamma-ray energy scale, are listed below,

- Difference between expectations and other peaks of 82.9 MeV and 129 MeV : 0.3%,
- Uniformity at 54.9 MeV energy in the whole acceptance : 0.3% (in Section 7.20),
- Uncertainty of light yield monitor : 0.3% (in Section 7.3.2),
- Uncertainty of gain : 0.09% (in Section 6.2.4, Figure 6.15),
- Statistical uncertainty of fitting 54.9 MeV peak : 0.05%.

The first listed uncertainty includes the uncertainties of the non-linearity, the peak correction by the opening angle and the peak estimation by the fit. The non-linearity of energy is not an issue because the 54.9 MeV peak for the energy determination is near to the signal 52.8 MeV energy. The shift of the opening angle from the back-to-back angle, however, brings higher shift of 54.9 MeV-like peak and lower shift of 82.9 MeV-like peak by the correction, while a 129 MeV peak is not corrected by the angle. The second term indicates that the discrepancy of non-uniformity between 17.7 MeV peak used to make the u-v correction and 54.9 MeV peak for the confirmation is within its range. We do not observe jumps or a gradient decrease in the light-yield monitor, then the stability of the light yield in third, which includes the precision of the monitor in CW run and

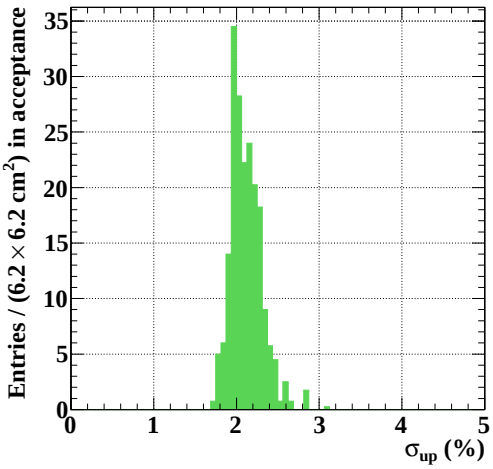

(a) Distribution of upper σ in acceptance (%)

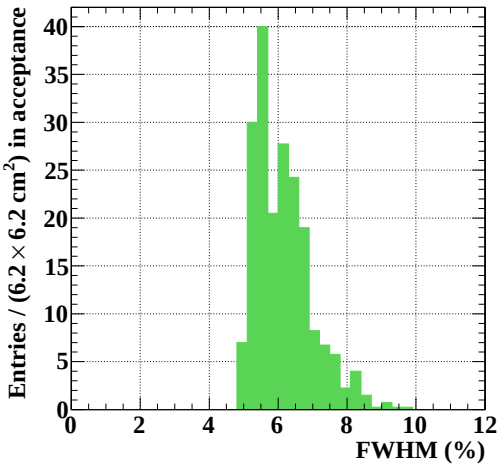

(b) Distribution of FWHM in acceptance (%)

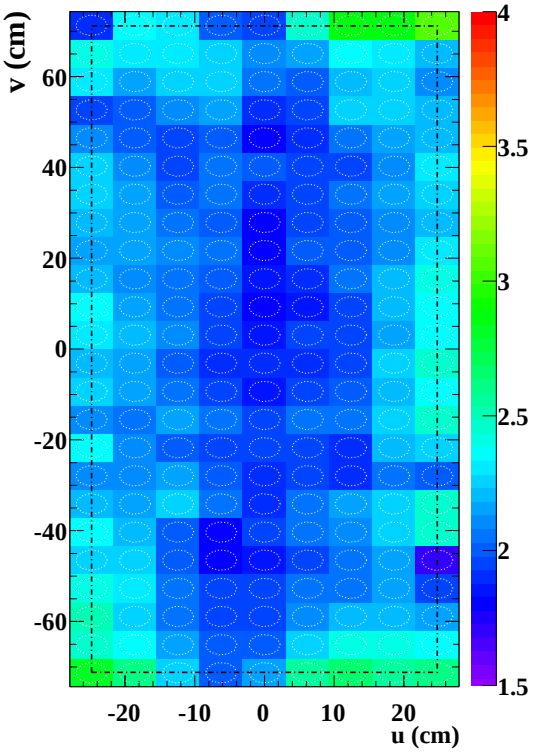

(c) Map of upper σ (%)

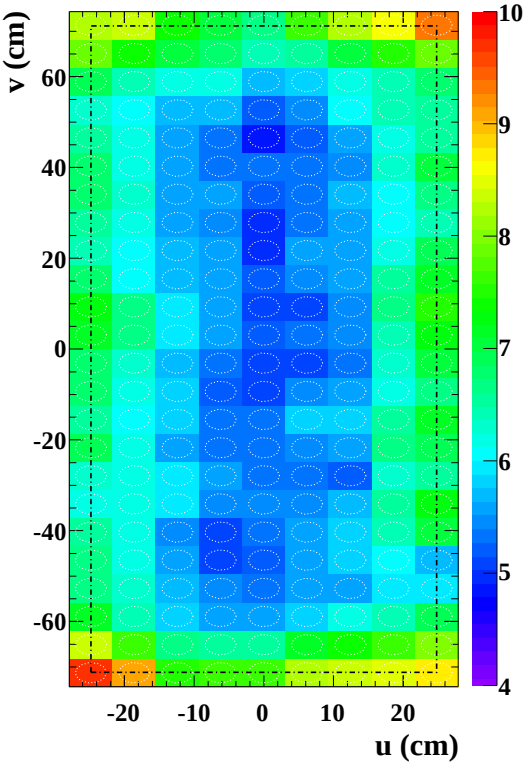

(d) Map of FWHM (%)

Figure 7.26: Energy resolutions at 54.9 MeV on inner face ($w > 2$ cm). The difference of pedestal between π^- and μ^+ beam is considered in the fit.

gain calibrations, is not used. The gain uncertainty is taken from the confirmation of the stability by the LED peaks in beam, therefore it includes all about the PMT gain such as gain calculation, shift and the stability of electronics. Final uncertainty of peak

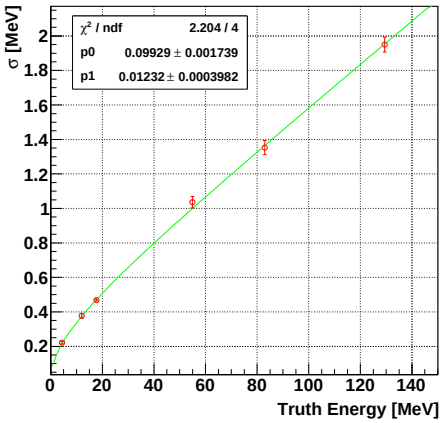

Figure 7.27: Energy dependence of energy resolution σ_{upper}.

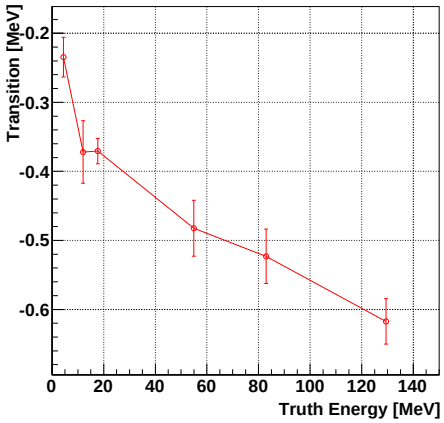

Figure 7.28: Energy dependence of transition point from Exponential to Gaussian in PDF.

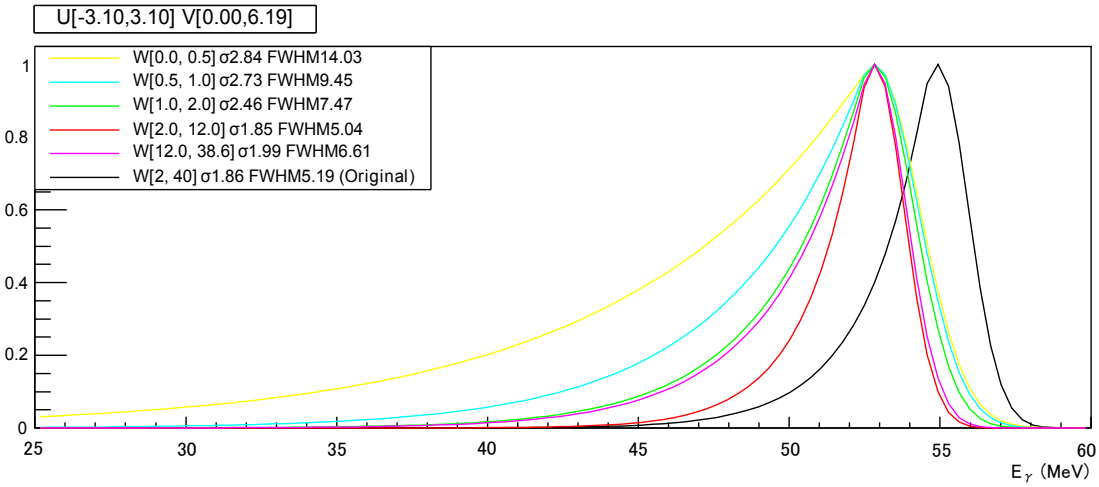

Figure 7.29: Signal energy PDF of gamma rays normalized by height instead of area. Conversion is applied with the energy correction, then the depth correction.

determination by the fit is doubly counted, thus the uncertainty of the energy scale is

$$\Delta E_\gamma = (0.3 \oplus 0.3 \oplus 0.09 \ominus 0.05)\% = 0.43\%. \tag{69}$$

7.4 Background

7.4.1 Cosmic ray

Cosmic ray background can contaminate physics data. The ratio of collected photons by outer face to inner face is an effective parameter to discriminate cosmic rays from gamma rays. This is because most cosmic muons penetrate the detector with a long path and illuminate many PMTs on several faces, while gamma rays from the target are mostly converted near the inner face and the inner face detects many scintillation photons from

gamma rays. In addition to that, the depth from inner face is introduced to improve the selection efficiency. The cosmic-ray cut is performed on depth(w)-ratio(R) plane as shown in Figure 7.30 to reject deep events and to keep middle depth events,

$$(w < a_1 \times R + b_1) \wedge (w > a_2 \times R + b_2), \tag{70}$$

where parameter is optimized to be $(a_1, b_1, a_2, b_2) = (15, 22, -400, 120)$ after a fine adjustment of b_1 with considering the efficiency. This selection has 56% rejection power of cosmic rays with 99% gamma-ray efficiency. It is applied for physics analysis.

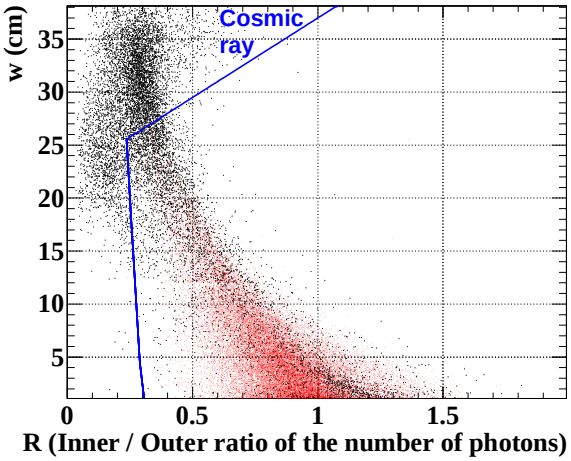

Figure 7.30: Depth and photons ratio of inner and outer face. Black square is cosmic ray and red plot is gamma rays in the signal MC.

7.4.2 Background distribution

We prepared following inputs to extract position-dependent background PDF of gamma-ray energy,

- A histogram of energy deposit in radiative muon decay (RD) in MC,
- A histogram of energy deposit in annihilation in flight (AIF) in MC,
- Pedestal distribution of energy mixed in physics data with 200 or 300 μm degrader separately,
- Comic ray spectrum in real data,
- Trigger efficiency for higher veto threshold to avoid cosmic rays,
- Trigger efficiency for threshold around lower energy.

All estimation of background distributions can be done at $t_{e\gamma}$ sideband before opening blind region. Data periods with 200 μm or 300 μm degrader are separately treated with corresponding pedestal data because of different event distributions. Two types of trigger efficiency curves are considered for cosmic-ray veto and the threshold at the low energy.

Veto energy threshold for cosmic ray is around 63-64 MeV, and lower energy threshold around 42-44 MeV.

The cosmic-ray spectrum in physics data has a higher edge because of a veto threshold in trigger. In cosmic-ray run with no beam, this veto efficiency can be checked by an event ratio of cosmic rays with veto to that without veto as shown in Figure 7.31. Higher cut off has about 9% resolution in σ. It is worse than expectation (about 3%) because some signal heights from PMTs are saturated on the trigger board. The veto threshold relatively differs by reconstructed position because of the non-uniformity effect of the reconstructed number of photons. Thus, the estimation is performed by different depth divided at 2 cm and also by three ($w \leq 2$ cm) or four ($w > 2$ cm) divisions along v direction to separately treat around top and bottom faces within 1.5-PMT region along v from v edge. Instead of the using veto efficiency curve directly, the cosmic ray with veto and without beam is fitted by polynomial function and used for the background component.

The lower threshold efficiency in Figure 7.32 is estimated from an event ratio of data with different lower thresholds, that is data triggered with id 0 over that with id 1 (Id is defined in Table 9). This efficiency does not affect the physics analysis because it is sufficiently low, but can be used for the studies in E_γ sideband data.

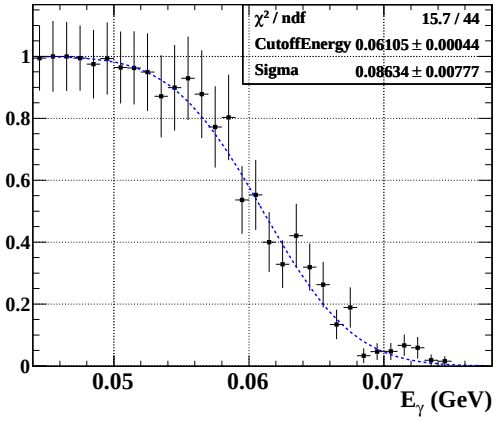

Figure 7.31: Veto efficiency curve.

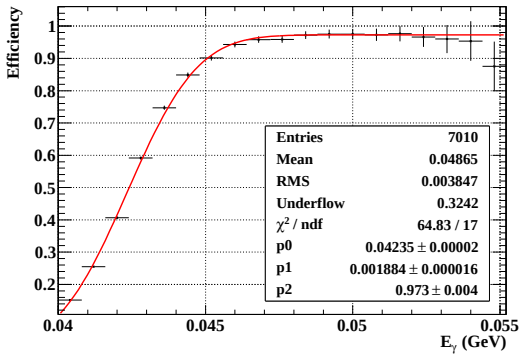

Figure 7.32: Lower trigger threshold efficiency.

Finally the background spectrum is fitted with the gamma-ray spectrum of RD and AIF, the cosmic ray and the trigger efficiencies. The spectrum is sum of two RD and AIF histograms weighted with each rate, convolves a pedestal with taking the pileup elimination into account and is smeared by the detector resolution. Energy scale, the detector resolution, the trigger threshold and the fraction of cosmic ray are extracted as free parameters. Figure 7.33 shows a background histogram in 300 μm degrader run and a fit result superimposed with each component. The energy scale and sigma as a result of the fitting is used to check the uniformity, the stability and the scale of energy independently from other calibrations.

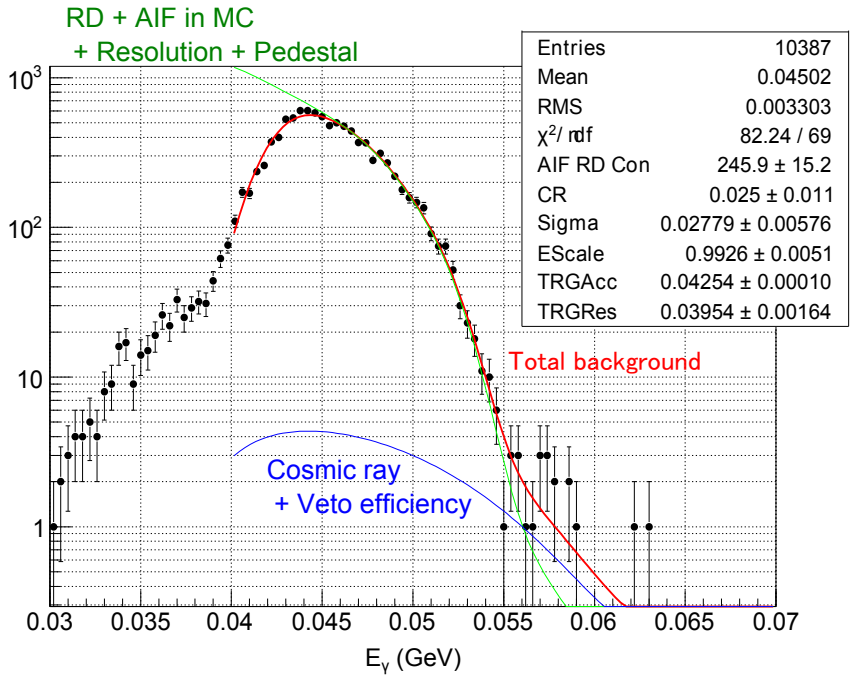

Figure 7.33: Background spectrum (300 μm degrader) from $t_{e\gamma}$-sideband data. Fitting results from RD decay, AIF, cosmic ray and trigger efficiency of lower threshold are shown with each component. RD and AIF are estimated in the MC and smeared by a resolution as free parameters. Cosmic ray is taken from beam-off data with including veto efficiency and the lower-threshold efficiency is fitted as free parameters.

7.5 Efficiency

7.5.1 Detection efficiency

The LXe detector has a sufficient stopping power for a gamma ray with $\sim$14 X_0 radiation length. However, in order to reach liquid xenon from the target, gamma rays ought to penetrate the 0.075 X_0 window of the LXe cryostat and COBRA magnet of 0.197 X_0. Therefore gamma rays may not be detected or sometimes lose the energy before reaching liquid xenon. In the signal MC at 52.8 MeV, Figure 7.34 shows event distribution of the first conversion point of a gamma ray in radius on x-y plane, and 58% of events is with the liquid xenon. Lower tail of a gamma energy peak mainly due to the energy deposit in materials before reaching liquid xenon and the energy leak near the face. The fact is indicated by the MC simulation as shown in Figure 7.35, where a difference between energy deposit in xenon and reconstructed energy is symmetric.

The gamma detection efficiency is used for normalization in physics analysis as described later in Section 9.3. The efficiency in the whole acceptance was estimated with the signal MC, and the consistency with data was checked. Counting two gamma rays from π^0 decay with tagging one in the NaI detector is a useful way to confirm the absolute detection efficiency. Then the difference between the data and the π^0 MC is regarded as a systematic uncertainty.

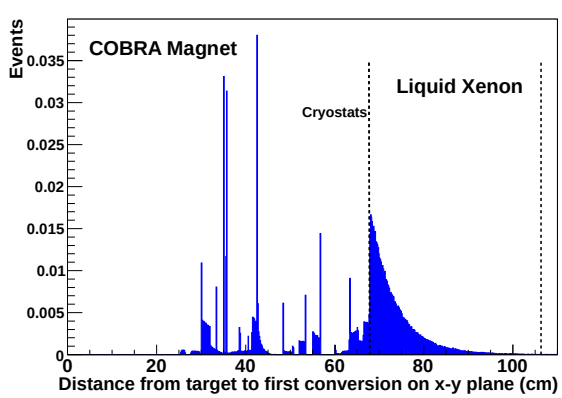

Figure 7.34: First conversion point of gamma rays in the MC simulation. Radius on x-y plane shows that a conversion sometimes occurs before reaching liquid xenon.

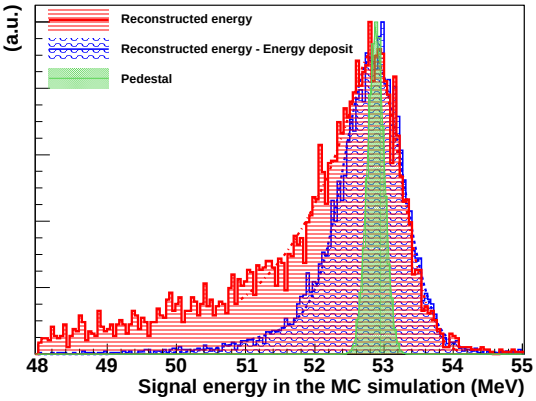

Figure 7.35: Signal gamma-ray energy in the MC simulation. Reconstructed energy has a lower tail originated from energy loss. A difference between reconstructed energy and true energy deposit in xenon shows a symmetric distribution. Pedestal distribution is superimposed with shifted.

7.5.2 Measurement of two-gamma decay

We had dedicated run to take two gamma-ray decays triggered by the NaI detector. One concern is a contamination of neutron backgrounds from $\pi^- p \to \gamma n$, which is coincident with a gamma ray in the tail from 129 MeV energy peak in the NaI detector.

By selecting gamma rays around 82.9 MeV in the NaI detector without any position selections in the LXe detector, one can obtain energy spectrum in the LXe detector as shown in a red dashed line in Figure 7.36. The procedure to obtain the detection efficiency is following,

1. Gamma rays appear in the energy range of 54.9-82.9 MeV and 129 MeV at the NaI detector. Fit 129 MeV energy in the NaI detector with an exponential-Gaussian function.

2. By using the fitting result in the previous step, estimate the tail contribution from 129 MeV in 82.9 MeV region where is the same selected region in the fifth step.

3. Make a template of 9 MeV neutron energy spectrum in the LXe detector by selecting 129 MeV peak at the NaI detector.

4. Scale the 9 MeV template of the LXe by the ratio obtained in the second step (blue histogram).

5. Make a template of 54.9 MeV gamma-ray energy spectrum in the LXe detector by selecting 82.9 MeV region at the NaI detector (red histogram).

6. Subtract neutron template (blue dashed histogram, in the fourth step) from raw 54.9 MeV distribution (red histogram, in the fifth step), then obtain a 54.9 MeV

energy spectrum (green distribution) only from π^0 decay without neutrons.

7. Set a lower energy threshold according to a window of physics analysis. The difference between $\mu \to e\gamma$ signal and lower edge of two gamma rays from π^0 decays is considered in the threshold, scaled by its peak ratio of 54.9(MeV)/52.8(MeV).

8. The number of events higher than the lower threshold normalized by total integration is regarded as detection efficiency

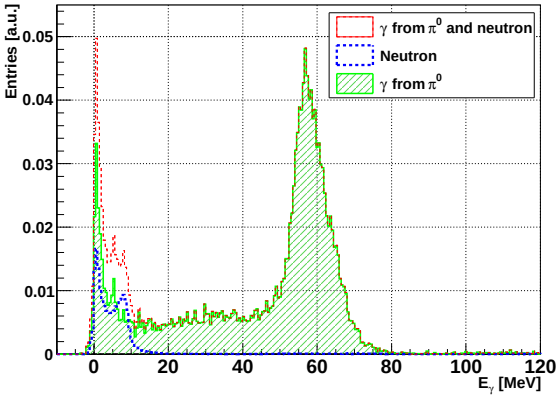

Figure 7.36: Energy spectrum in the LXe detector triggered by the NaI detector in π^0 run.

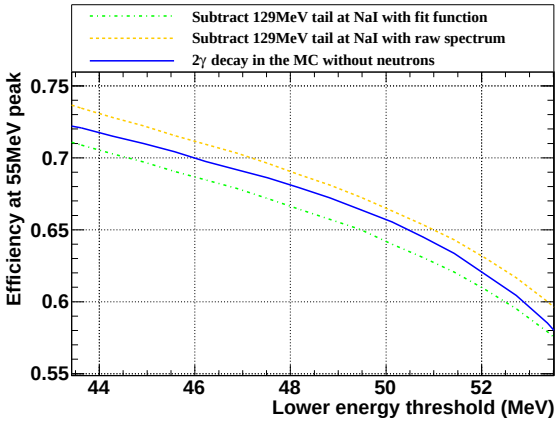

Figure 7.37: Detection efficiency curve as a function of lower energy threshold. A continuous line is the estimation from the MC, and dotted lines are actual measurement with different estimations of neutron background. 50 MeV energy corresponds to the lower edge of physics analysis region.

The detection efficiency is shown as a function of lower energy threshold in dotted lines in Figure 7.37. The measured efficiency in π^0 run is different from the signal efficiency because the energy and position distributions are different; therefore we use the data only for validating MC. The signal efficiency used in physics analysis is calculated from MC. In the π^0 setup, measured efficiency from the real data is 64-67 %, and the absolute difference from that in MC with the same setup is 2%. We use the difference as a systematic uncertainty in the physics analysis.

7.5.3 Efficiency for analysis

Finally, the gamma-ray detection efficiency is calculated from the signal MC with the 2% error estimated from difference between real data and MC in π^0 run. The detection efficiency is defined by a probability that the reconstructed energy of a signal gamma ray is within analysis region, that is larger than 48 MeV in 2009.

The detection efficiency depends on the position on the inner face, thus we estimated it by eight divisions. For example, at corners or edges, the efficiency is 55-56% and at center, it is 68%. In order to calculate the normalization factor, we need to know a conditional

probability to detect and reconstruct a gamma ray once a positron is triggered. Thus we take a weighted average of efficiencies with taking the angle distribution of positron detection into account, and it is estimated to be 64.7%. Taking analysis efficiency of a gamma ray, 89.3%, into account, the conditional probability, $\epsilon_{e\gamma}^{LXe}$, is resulted in $\epsilon_{e\gamma}^{LXe} = 0.647 \times 0.893 = 0.578$.

Part IV
Combined Analysis and Performance

8 Performance of Positron Detector

8.1 Time resolution of timing counter bars

High-energy positron from $\mu^+ \to e^+\nu_e\overline{\nu}_\mu$ sometimes penetrates a few bars and it can be used for the calibration. Time offset of each scintillation bar is calibrated in $\mu^+ \to e^+\nu_e\overline{\nu}_\mu$ by collecting positron hits in two adjacent scintillator bars. Time offsets of bars are calibrated relatively between bars. Although the averaged time of flight between bars is estimated to be 200 ps in MC simulation, the difference of time between bars can be also calculated event by event by using a positron track. When calibrating the time offset in $\mu^+ \to e^+\nu_e\overline{\nu}_\mu$ we considered the time of flight between bars based on the reconstructed track.

The width of the time difference distribution of the two hits gives the time resolution. For a single bar resolution, the width is divided by squared root of two assuming that the two have the same resolution. Figure 8.1 shows the time difference between bar 1 and 0, and Figure 8.2 shows the time resolution of each bar in 2008 and in 2009. The periodical worse resolutions come from the accuracy of the clock synchronization over different DRS chips because internal synchronization for four channels in a chip is better than that between chips with a use of different clocks. One worst point of bar 15 in 2008 is because the DTD channel had a defect. The averaged resolution is 76 ps in 2008 and 75 ps in 2009. We also checked a quality of calibration by using the CW-Boron run. Once the LXe detector detects a 4.4 MeV low energy gamma of coincident two gamma rays from boron as a reference time, then the other 12.0 MeV gamma allows a measurement of timing at a timing counter bar.

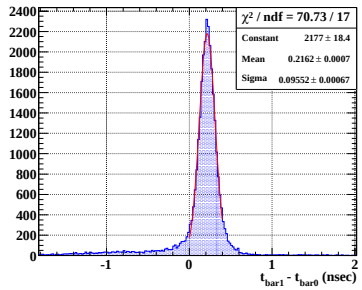

Figure 8.1: Time difference of two bars in double-hit events.

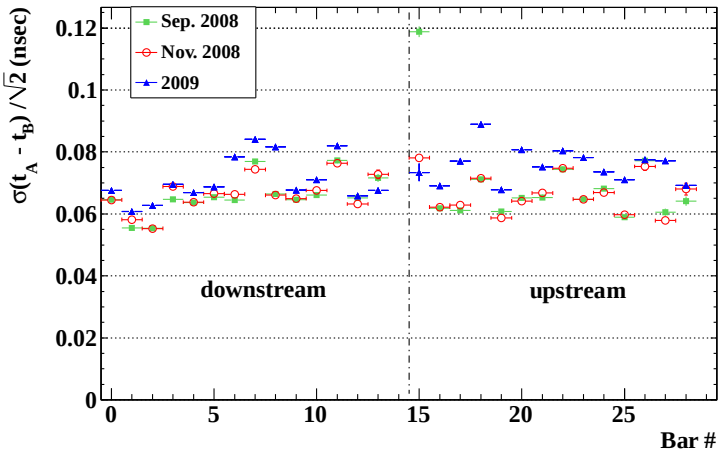

Figure 8.2: Time resolution of single bar for each two bar set.

8.2 Quality of positron reconstruction

The quality of positron tracking is categorized into two in order to treat the different performance with two sets of PDFs for the $\mu^+ \to e^+\gamma$ physics analysis. Mainly a difference along z and r between drift-chamber and timing-counter hit, Δz and Δr, separates the quality. That is the difference between the extrapolated track by only the drift chamber and the hit reconstruction only by the timing counter. Low quality is selected within $|\Delta z| < 12$ (cm), $|\Delta r - 1.8| < 5$ (cm) and the number of hits larger than seven, while the high quality is more strict within $|\Delta z| < 6$ (cm) and $|\Delta r - 1.8| < 3$ (cm), the number of hits larger than ten and less uncertainties of the momentum, the angle and the chi squared of fit. In Figure 8.3 the filled area shows a high-quality region of Δz and Δr.

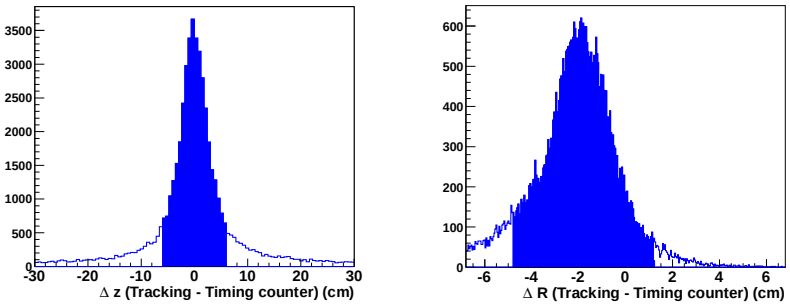

(a) Δz (b) Δr

Figure 8.3: z or r difference between tracking and timing-counter hit. The filled area is high-quality region.

8.3 Positron energy

In actual data we have two ways to obtain the resolution of positron momentum. The first method is to fit the energy distribution of normal muon decay, $\mu^+ \to e^+\nu_e\overline{\nu}_\mu$, with a convolved function of a theoretical prediction in the SM and a double Gaussian distribution as the resolution contribution of a core and a tail. Figure 8.4 illustrates the Gaussian in a dotted line and convolved function in a solid line. These estimations of low and high quality are separately shown in Figures 8.5 (a) and (b). We fit only high energy region (> 50 MeV) to exclude possible momentum dependence of the resolution. The energy scale of the positron is determined by the Michel spectrum. There is a discrepancy between upstream and downstream side, thus it is corrected by a shift about 64 keV.

The other way is to estimate the energy resolution by the difference between two independent energy reconstructions of only one-turn track in the events observed as two-turn track. In the MC a true resolution defined as a difference between reconstructed and generated energies can be checked. The systematic uncertainties associated to the double turn method have been evaluated by comparing true and measured resolutions in MC samples with different single hit resolutions and by comparing resolutions from two different methods. Statistical uncertainties are negligible compared to them.

The resolution is described by triple or double Gaussian. In 2009 the two-turn method is used and the resolution is described with double Gaussian, estimated to be 0.39 MeV

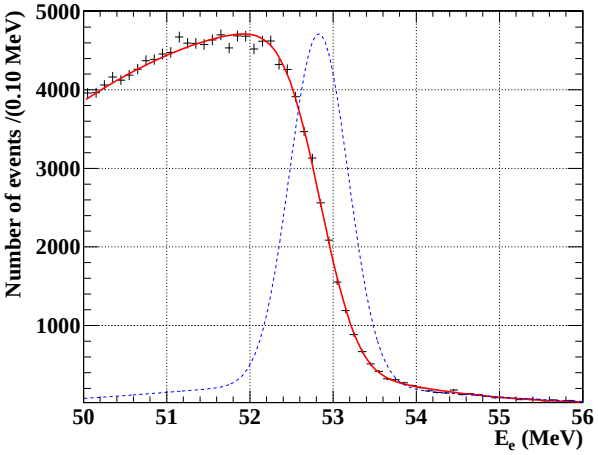

Figure 8.4: Energy distribution of positrons from muon decays, $\mu^+ \to e^+\nu_e\overline{\nu}_\mu$.

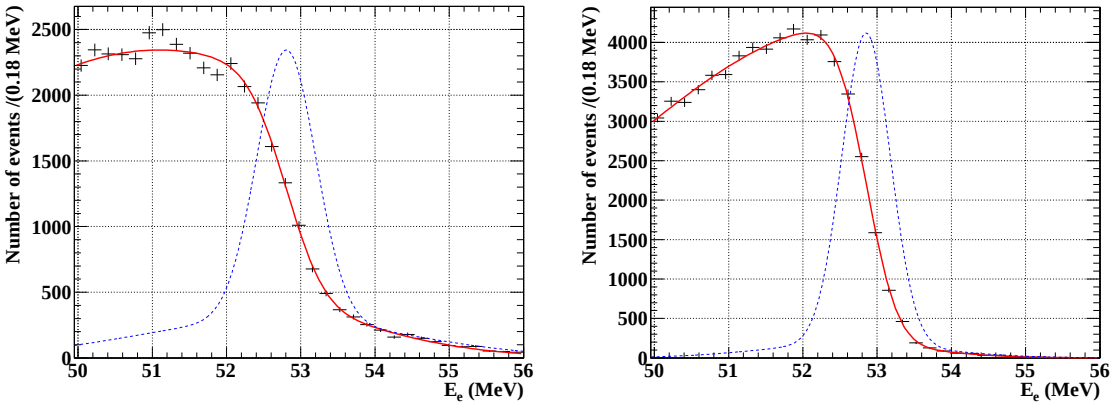

(a) Low-quality tracking (b) High-quality tracking

Figure 8.5: Energy distribution of tracking positrons from muon decays, $\mu^+ \to e^+\nu_e\overline{\nu}_\mu$, by two categories of the tracking quality.

as the core resolution (σ_{core}) in 79% fraction (f_{core}) with 1.71 MeV sigma as a tail (σ_{tail}) in 21%. The typical energy performance is summarized in Table 13 with the two qualities of positron tracking.

Table 13: Resolution of signal positron energy E_e with double-turns method

E_e	Global	High Quality	Low Quality
σ_{core} (MeV)	0.390±0.003	0.340±0.004	0.414±0.004
f_{core}	0.788±0.003	0.907±0.008	0.740±0.005
σ_{tail} (MeV)	1.71±0.02	0.907±0.008	1.76±0.02

8.4 Positron angles

The resolution of emission angle ϕ_e is taken from actual data in the two turn method. Typical ϕ_e resolution is given in Table 14 and expressed in double Gaussian with zero means.

Table 14: Positron ϕ_e of signal

ϕ_e	Global	High Quality	Low Quality
σ_{core} (mrad)	7.08±0.05	6.03±0.13	7.42±0.07
f_{core}	0.852±0.004	0.878±0.017	0.831±0.005
σ_{tail} (mrad)	26.6±0.4	16.2±0.8	27.6±0.4

The resolution of θ_e is also estimated from double turns and expressed in Gaussian with correcting the difference of a measured value from true one in the signal MC. Table 15 summarizes θ_e resolution with tracking qualities.

Table 15: Positron θ_e of signal

θ_e	Global	High Quality	Low Quality
σ (mrad)	11.15±0.03	9.72±0.05	11.63±0.04

8.5 Decay vertex resolution

The position of the decay vertex is determined by the extrapolated positron tracking because there is no vertex detector and the LXe detector has a poor determination of a gamma-ray direction. There are two ways to estimate the position resolution of positron tracking in data. One is to see holes on the target and the other is to estimate the difference of each separated turn of the track, which is recognized with over two turns.

The vertex resolution in 2009 is obtained from the hole method along minor vertical axis (Y) and major axis on the plane (Z) as listed in Table 16. In the case of the two-turn

method, the resolution is calculated as 2.3 mm and 2.8 mm along minor and major axis respectively.

Table 16: Vertex position resolutions from views of the holes on the muon target

Vertex (Z,Y)	Global	High Quality	Low Quality
σ_Z (cm)	0.344±0.007	0.330±0.009	0.360±0.015
σ_Y (cm)	0.328±0.007	0.302±0.009	0.42±0.04

9 Combined analysis of a Gamma ray and a Positron

9.1 Relative angle, $\theta_{e\gamma}$ and $\phi_{e\gamma}$

The direction of a positron emission on the stopping target is determined by extrapolating positron tracks to the crossing points on the target. The emission angle of a gamma ray is calculated from the position in the LXe detector and the vertex position expected by a positron. The opening angle $\Theta_{e\gamma}$ between these two directions is obtained from two dimensional angle of gamma ray and positron,

$$\cos\Theta_{e\gamma} = \sin\theta_\gamma\cos\phi_\gamma\sin\theta_e\cos\phi_e + \sin\theta_\gamma\sin\phi_\gamma\sin\theta_e\sin\phi_e + \cos\theta_\gamma\cos\theta_e. \quad (71)$$

We use a two dimensional angles of the polar θ and the azimuthal ϕ directions from beam axis. The difference of these angles is defined as

$$\theta_{e\gamma} = \theta_\gamma - (\pi - \theta_e),\ \phi_{e\gamma} = \phi_\gamma - (\pi - \phi_e), \quad (72)$$

so that these make peaks at zero for the signal events.

The $\mu^+ \to e^+\gamma$ decay is physically identified with opening angle of $\Theta_{e\gamma}$ between a positron and a gamma ray. In the PDF point of view it is desirable to adopt $\theta_{e\gamma}$ and $\phi_{e\gamma}$ as observables with a better expression of the position dependent resolution, instead of $\Theta_{e\gamma}$. This is because the resolutions in the MEG detector with a cylindrical symmetry depends strongly on θ and a dependence of resolutions on θ is different from that on ϕ. Practically the resolutions of relative angles are calculated from those of z and ϕ for both the LXe and the DCH detectors and those of vertex position with measured positions.

9.2 Relative timing $t_{e\gamma}$

The coincident radiative decay, $\mu^+ \to e^+\nu_e\overline{\nu}_\mu\gamma$, has a peak of the relative timing on the flat accidental floor. The time resolution from RD includes all contributions of timing from the LXe detector, positron tracking and electronics. Even before opening the blind region, the coincident timing peak appears in the lower E_γ sideband and it is useful to know a combined timing performance.

Figure 9.1 shows the peak in E_γ sideband in a range of 40 MeV $\leq E_\gamma \leq$ 47 MeV, 45 MeV $\leq E_e \leq$ 55 MeV and within 300 mrad opening angle. The peak is fitted with double Gaussian function and timing resolution resulted in 149±10 ps in 70% fraction as core sigma and 250 ps sigma. To evaluate the performance at the signal region, we correct

small gamma-energy dependence of the timing resolution, and it is estimated to be 142 ps in sigma. We carefully checked the stability of $t_{e\gamma}$ and confirmed the constant peak within 15 ps.

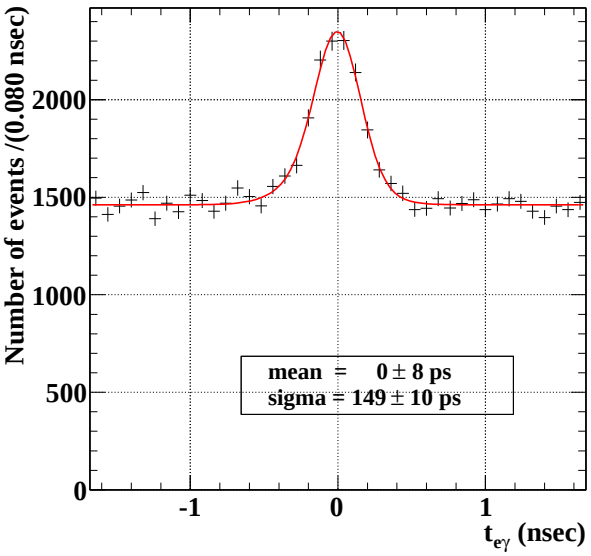

Figure 9.1: Time difference between positron and gamma ray in 2009.

9.3 Normalization factor for $\mu^+ \to e^+\gamma$

9.3.1 Principle

A difficulty to determine the normalization factor is the treatment of the detection efficiencies. It is not independent of time, especially in 2008 due to HV discharge problems in the drift chamber, and also of emission angles.

We have three methods to count muons by counting primary protons, gamma rays from radiative decays or positrons from Michel decays. In the first method to count the protons, monitored the intensity of the beam offered from PSI and a measured ratio of stopping muons in the target to primary protons allows to estimate the total number of muons. In order to calculate the normalization factor from protons, we have to know the detection efficiencies in all the detectors.

Secondly, by counting radiative muon decays both in the LXe detector and in positron spectrometer, both the detection efficiency of these detector and the direction match efficiency in the trigger can be taken into account, however, the statistics is very low.

By the following reasons the best way to count muons is to use positrons from normal Michel decays, $\mu^+ \to e^+\nu_e\overline{\nu}_\mu$, in the positron spectrometer.

- $\mu^+ \to e^+\gamma$ candidate is counted relatively from another channel of the Michel decay and it is suitable to estimate branching fraction.
- The change of detection efficiency such as HV problem or missing channels is compensated by taking only positrons from Michel decays simultaneously with physics data.

- The change of beam intensity is also included in counted positrons thanks to continuous data taking of Michel positrons during physics run.
- The detection efficiency of positron tracker can be almost compensated between $\mu^+ \to e^+\gamma$ and $\mu^+ \to e^+\nu_e\overline{\nu}_\mu$.
- Share the analysis cut for the positron with the signal event.
- Stopping efficiency in muon target does not need to be known.

For the gamma-ray detector we could acquire the detection efficiency in MC and check a consistency between measurement and MC with using two gamma-ray decay in π^0 run (Section 7.5.1). The method allows to obtain a branching fraction of $\mu \to e\gamma$ normalized by $\mu^+ \to e^+\nu_e\overline{\nu}_\mu$ and $\mu^+ \to e^+\nu_e\overline{\nu}_\mu\gamma$, that is $\Gamma(\mu^+ \to e^+\gamma)/\Gamma(\mu^+ \to \mathrm{e}^+\nu_\mathrm{e}\overline{\nu}_\mu(\gamma))$. Because we do not use low energy positrons, the obtained total fractions are almost the same as that of $\mu^+ \to e^+\nu_e\overline{\nu}_\mu$, $\Gamma_{total} \simeq \Gamma(\mu^+ \to \mathrm{e}^+\nu_\mathrm{e}\overline{\nu}_\mu)$.

9.3.2 Counting the Michel decay, $\mu^+ \to e^+\nu_e\overline{\nu}_\mu$

The total number of the Michel decay (MD), N_{MD}, is estimated from the event triggered with only timing ϕ counter (Trigger id #22 as described in Table 9) mixed in the MEG physics data taking simultaneously. It consists of some efficiencies and acceptances,

$$N_{MD} = N_\mu \times T_{e\nu\overline{\nu}} \times \mathcal{B}_{e\nu\overline{\nu}} \times f_{e\nu\overline{\nu}}^{E_e \in E_{selection}} \times \frac{1}{P_{e\nu\overline{\nu}}} \times \epsilon_{e\nu\overline{\nu}}^{trig} \times A_{e\nu\overline{\nu}}^{TIC} \times \epsilon_{e\nu\overline{\nu}}^{DCH} \times A_{e\nu\overline{\nu}}^{DCH}, \quad (73)$$

where each factor is denoted as the following:

- $N_\mu \times T_{e\nu\overline{\nu}}$: The number of stopped muons during a livetime, $T_{e\nu\overline{\nu}}$
- $\mathcal{B}_{e\nu\overline{\nu}}$: The branching ratio of Michel decay
- $f_{e\nu\overline{\nu}}^{E}$: The fraction of Michel spectrum above 50 MeV
- $P_{e\nu\overline{\nu}}$: The pre-scale factor of the TIC-self trigger
- $\epsilon_{e\nu\overline{\nu}}^{trig}$: The conditional trigger efficiency
- $A_{e\nu\overline{\nu}}^{TIC}$: The conditional acceptance of timing counter including the probability of DCH-TIC matching
- $\epsilon_{e\nu\overline{\nu}}^{DCH}$: The conditional tracking efficiency including the selection criteria
- $A_{e\nu\overline{\nu}}^{DCH}$: The geometrical acceptance of the drift chamber.

On the other hand the total number of $\mu^+ \to e^+\gamma$ signal, N_{sig}, is described as,

$$N_{sig} = N_\mu \times T_{e\gamma} \times \mathcal{B}_{e\gamma} \times \epsilon_{e\gamma}^{trig} \times A_{e\gamma}^{TIC} \times \epsilon_{e\gamma}^{DCH} \times A_{e\gamma}^{DCH} \times \epsilon_{e\gamma}^{LXe} \times A_{e\gamma}^{LXe}, \quad (74)$$

where the similar terms are defined as the same way in previous expressions, while other contributions for the gamma-ray detector and trigger efficiency of gamma rays and a matching are introduced as below,

- $\epsilon_{e\gamma}^{LXe}$: The gamma-ray detection and the reconstruction efficiency including selection criteria
- $A_{e\gamma}^{LXe}$: The conditional acceptance of the gamma ray from $\mu^+ \to e^+\gamma$ decay

The pre-scale factor of signal, $P_{e\gamma}$, is equal to 1 and the monochromatic signal energy make a fraction of signal spectrum, $f_{e\gamma}^{E_{e\gamma}}$, is to be 1, thus these are omitted. The fraction of each term is

$$\frac{\mathcal{B}_{e\gamma}}{\mathcal{B}_{e\nu\bar{\nu}}} = \frac{N_{sig}}{N_{MD}} \times \frac{f_{e\nu\bar{\nu}}^{E_e \in E_{selection}}}{P_{e\nu\bar{\nu}}} \times \frac{\epsilon_{e\nu\bar{\nu}}^{trig}}{\epsilon_{e\gamma}^{trig}} \times \frac{A_{e\nu\bar{\nu}}^{TIC}}{A_{e\gamma}^{TIC}} \times \frac{\epsilon_{e\nu\bar{\nu}}^{DCH}}{\epsilon_{e\gamma}^{DCH}} \times \frac{1}{\epsilon_{e\gamma}^{LXe}} \times \frac{1}{A_{e\gamma}^{LXe}}. \tag{75}$$

What we have to estimate is k factor defined as

$$1/k = \frac{1}{N_{sig}} \cdot \frac{\mathcal{B}_{e\gamma}}{\mathcal{B}_{e\nu\bar{\nu}}} \tag{76}$$

$$= \frac{1}{N_{MD}} \times \frac{f_{e\nu\bar{\nu}}^{E_e \in E_{selection}}}{P_{e\nu\bar{\nu}}} \times \frac{\epsilon_{e\nu\bar{\nu}}^{trig}}{\epsilon_{e\gamma}^{trig}} \times \frac{A_{e\nu\bar{\nu}}^{TIC}}{A_{e\gamma}^{TIC}} \times \frac{\epsilon_{e\nu\bar{\nu}}^{DCH}}{\epsilon_{e\gamma}^{DCH}} \times \frac{1}{\epsilon_{e\gamma}^{LXe}} \times \frac{1}{A_{e\gamma}^{LXe}}. \tag{77}$$

The inefficiency of the Michel decay trigger originated from a high rate compared with a live time of trigger scaler. The intrinsic trigger rate by the Michel decay is about 10^7 Hz, while the trigger signal to be used is 80 ns width window to make a coincidence with the LXe detector. Therefore the inefficiency from accidental pileup as a ratio of actual to measured rate, $(R_{true}/R_{measure} - 1)$, is easily estimated to be 20% in 200 μm thickness degrader and 15% in 300 μm. This difference is because the triggered rate in 200 μm degrader is higher than in 300 μm at the timing counter, although actual Michel trigger is lower.

The direction match efficiency between a positron and a gamma ray, ϵ_{DM}, is a dominant difference of $\epsilon_{e\gamma}^{trig}$ from $\epsilon_{e\nu\bar{\nu}}^{trig}$, which was estimated with signal and radiative events in MC. The efficiency to $\Theta = 180^\circ$ region is estimated by extrapolating the efficiencies at each opening angle, to be $\epsilon_{DM} = (83.5 \pm 2(\text{stat.}) \pm 0.5(\text{syst.}))\%$.

The each factor in 2009 was evaluated to be below:

- N_{MD} : The number of observed Michel decays, 18,096 events, 5% error,
- $f_{e\nu\bar{\nu}}^{E_e \in E_{selection}}$: Fraction of Michel spectrum, 0.114±0.002,
- $P_{e\nu\bar{\nu}}$: Pre-scale factor, 10^7 (inefficiency correction : 1.17),
- $\epsilon_{DM} \equiv \epsilon_{e\gamma}^{trig}/\epsilon_{e\nu\bar{\nu}}^{trig}$: Reconstruction efficiency for positron, 0.84±0.02,
- $A_{e\nu\bar{\nu}}^{TIC}/A_{e\gamma}^{TIC} \times \epsilon_{e\nu\bar{\nu}}^{DCH}/\epsilon_{e\gamma}^{DCH}$: Timing counter efficiency given momentum distribution and reconstruction efficiency for positron, 1.12±0.06,
- $\epsilon_{e\gamma}^{LXe}$: The efficiency for the gamma inside the acceptance, 0.58±0.02,
- $A_{e\gamma}^{LXe}$: 0.99±0.01,

then the normalization factor is resulted in

$$1/k = (1.01 \pm 0.08) \times 10^{-12}. \tag{78}$$

9.4 Systematic uncertainty

The uncertainties in 2009 are listed in Table 17. The systematic uncertainty of E_γ is estimated in Section 7.3.6. As the relative angle, a large uncertainty is set because the z alignment of the LXe detector may have a shift of a few mm suggested by position measurements with a radio active source or cosmic rays, while the uncertainty of positron angles is about ± 1.5 mrad. The systematic uncertainty from correlation of $\delta E_e - \delta\phi_e$ is roughly estimated from the MC, where δ means the true resolution between the reconstruction and the generation. The systematic uncertainty for the relative time is taken from the uncertainty in fitting and the stability. The resolution of it is also taken from the fit uncertainty and the correction uncertainty by the gamma-ray energy. The effect of the systematic uncertainty for the physics analysis is small as discussed later in Section 10.7.4.

Table 17: Systematic uncertainty in 2009.

E_γ	E_e	σE_e	$\theta_{e\gamma}$, $\phi_{e\gamma}$	$\sigma\theta_{e\gamma}$, $\sigma\phi_{e\gamma}$	$\delta E_e - \delta\phi_e$ correlation	$T_{e\gamma}$	$\sigma T_{e\gamma}$	Normalization
0.43%	50 keV	15%	7.5 mrad	10%	50%	15 ps	10%	8%

Part V
Physics Analysis on 2009 Data

10 Analysis for the $\mu^+ \to e^+\gamma$ Search

This part shows the analysis to calculate the branching ratio of $\mu^+ \to e^+\gamma$ from 2009 data. What we exactly calculate is the branching fraction, but its ratio is approximately equal to the branching ratio of $\mu^+ \to e^+\gamma$,

$$Br(\mu^+ \to e^+\gamma) \simeq \frac{\Gamma(\mu^+ \to e^+\gamma)}{\Gamma(\mu^+ \to e^+\nu_e\overline{\nu}_\mu)}, \tag{79}$$

because the 8% error of normalization factor counted by Michel decay in Equation 78 is much larger than difference between $\Gamma(\mu^+ \to e^+\nu_e\overline{\nu}_\mu)$ and a total Γ_{total}.

A maximum likelihood analysis is performed to extract the number of signal from the data. Thus, we define a likelihood function with probability density functions (PDFs) of observables.

A confidence interval of the best fit number and a sensitivity of the branching ratio are estimated in a frequentist approach. To construct confidence interval, a frequency probability of the 2009 data is estimated in many simulated experiments with each assumption of the number of events. The sensitivity with null-signal assumption is calculated with taking average of branching-ratio upper limits by many generated experiments.

In order to avoid some human biases, we blinded the region around $\mu^+ \to e^+\gamma$ until calibration and analysis had been fixed [61]. However, the above analysis can be done in sidebands beside the blind region with the same procedure as that for the blind region even before opening the blind region. The result of the maximum likelihood fit in the null-signal sideband region gives useful information such as backgrounds and a sensitivity. The blind procedure is not necessarily for a likelihood analysis rather than a cut analysis, but it would make the analysis reliable.

10.1 Strategy

Our analysis proceeds with blinding a signal. The blind region is a little wider than the analysis region because a precision of reconstructions is worse at the early stage of the calibration. The analysis procedure is below:

1. Event pre-selection and process with blinding as soon as data taken.
2. Repeat calibration and reprocessing with improving quality before opening blind region.
3. Estimate resolution, PDF and determine selection.
4. Study in the $T_{e\gamma}$ sidebands such as a maximum likelihood fit and a sensitivity calculation. Some predictions of backgrounds in the blind region are available.
5. Optimize and fix the analysis procedures.

6. Open blinded region.

7. Maximum likelihood fit for analysis region.

8. Calculate confidence interval of branching ratio.

From the second to the fourth process, there are developments of the event reconstruction and an iteration in order to improve calibrations and analysis before the final physics analysis.

10.1.1 Event selection and blinding

Pre-selection As soon as physics data is taken, a first analysis is performed. During the first process a event pre-selection is performed and the original raw data is blinded only in physics run. The purpose of pre-selection is to reduce data size and accordingly to make the following physics analysis fast. Mixed calibration or monitoring sources are out of selection for the physics analysis and these become accessible as well as normal dedicated calibration runs. At the first analysis the quality of calibrations is low or not done, thus the pre-selection is enough loose to avoid a loss of good events and uses only timing information of PMTs in the LXe detector and timing counter.

The pre-selection is defined as,

- -6.875 ns $< t_\gamma - t_{TICHIT} < 4.375$ ns,
- $|t_{track} - t_{TIC}| < 50$ ns,

where t_γ is the gamma-ray emission time at the center of target and t_{TICHIT} is a hit timing from the timing-counter bar. There is no use of tracking information at this stage. In the first window there is a wider region for a late t_{TICHIT} not to lose hits after multi-turn. The second condition requires at least one track, associated with the trigger, is found. The events are decreased by 0.3-0.4 factor with a pre-selection. Data out of pre-selection is never used and analyzed except for calibrations, while the selected events has some reprocessing and provides regions of a signal, blinded, an analysis and a sideband beside a blind box.

Blind region The blinding process for the pre-selected events uses two information of a gamma-ray energy and a time difference,

- $|E_\gamma - m_\mu/2| < 4.8$ MeV,
- $|t_{e\gamma}| < 1$ ns,

and the blind box is opened after all analysis and calibration are fixed. The blind region is shown in Figure 10.1, as well as sidebands. The sideband of $t_{e\gamma}$ gives a useful information about accidental backgrounds because it is independent from $t_{e\gamma}$. Another useful knowledge is obtained at lower E_γ sideband, where we can see the $t_{e\gamma}$ peak from radiative muon decays. Those two allow to estimate backgrounds level in blind box before opening it.

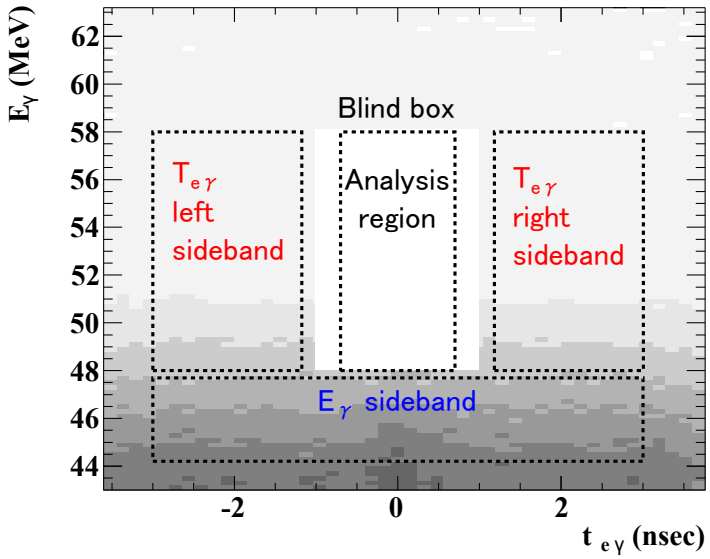

Figure 10.1: Event distribution on E_γ - $t_{e\gamma}$ plane. Blind region is shown in a blank box.

10.1.2 Analysis region and acceptance cut

The analysis window is considered separately from a signal window of cut analysis. In general, the signal window is defined as a narrow window according to the resolution of the detector for observed kinematics in order to discriminate signals from background events well. While the our analysis window uses a fitting region for the likelihood analysis and it can be defined in wider range. Because all events both from signal and background in the region are fitted simultaneously, ideally the result is independent on the selection of the window.

We defined the analysis region in 2009 run as follows:

- $|t_{e\gamma}| < 0.7$ ns,
- 50 MeV $< E_e <$ 56 MeV,
- 48 MeV $< E_\gamma <$ 58 MeV,
- $|\phi_{e\gamma}| < 50$ mrad and $|\theta_{e\gamma}| < 50$ mrad.

Lower energy limit of gamma-ray energy is high enough to avoid the bias from the trigger threshold and upper energy limit is also set. The window is narrower than the analysis in 2008 except for the same region of positron energy.

Additional cuts for the acceptance and the quality of the reconstruction are applied. As the LXe detector, a gamma-ray position is reconstructed using only PMTs on inner face and energy leaks are larger around the edge of the detector. Therefore the acceptance selection is applied as $|u| < 25$ cm, $|v| < 71$ cm and all depths, where the acceptance region excludes a half size of PMT around edges of u and v. The quality of positron tracking is separated into two groups to apply different PDFs as described in Section 8.2. Additionally at least four hits in the drift chamber and a vertex position within 8.24 cm along longitudinal axis and 2.8 cm along vertical axis are required.

10.1.3 Experiments simulation

Our goal is to obtain a confidence interval of the number of signal by a distribution of a frequency probability. A frequency probability of the experiment is evaluated in many simulated experiments with each assumption of the number of signal and backgrounds. We can estimate a confidence region by scanning the numbers to be generated.

The effect of the statistical fluctuation by experiments can be taken into account with a generation of many experiments under the same setup and the performance but a different event set. It is important to simulate a large number of experiments for a rare-event observation such as the MEG experiment.

The simulated experiments are so called 'toy Monte Carlo (toy-MC) experiments' generated by toy-MC simulation to be distinguished from a usual full MC simulation of detectors started with particle generations. The toy MC uses only acquired performance of the detectors and measured data set without using any information of materials or interactions in the detectors' geometry. That means there is only statistical treatment in toy MC but no kinematics because PDFs and data set have all information of those. For a precise way, the PDFs are prepared event by event to express the exact detector performance. It is possible to use the same PDF set, associated with actual data set, for all toy-MC experiments because the performance of detectors are inherent in the detectors setup and the the experiment. Actual data set are used for the event generation, which contains a realistic information about a correlation of observables and a distribution of observed events with a trigger and detection efficiency and particle emissions. A random event pickup from data set provides associated PDF set in the event and the PDFs can be a seed of new event generation with a random selection of observables from that PDF.

Events in a certain experiment are generated by PDFs with a specified set of the number, $(N_{sig}, N_{RD}, N_{BG})$. Here we note that the number of $\mu^+ \to e^+\gamma$ events as N_{sig}, that of $\mu^+ \to e^+\nu_e\overline{\nu}_\mu\gamma$ events as N_{RD} and that of accidental background events, which is most dominant in the events, as N_{BG}. The number to be generated is usually fluctuated with Poisson distribution around specified number. One of advantages in toy MC is that we can arbitrary determine the true number of each event type, signal and two backgrounds in generation. It allows to evaluate the performance of the likelihood analysis by comparing the best fit result of the number with true generated number.

The strategy to simulate one experiment is below.

1. Prepare a data set from data in 2009.

2. Determine a set of number of events, $(N_{sig}, N_{RD}, N_{BG})$, to be generated and is randomly fluctuated with Poisson distribution except for the number to be fixed.

3. Select events from the data set randomly.

4. Form PDFs associated with the selected event for a specified event type.

5. Generate observed variables randomly from PDF distributions.

We prepare a data set based on actual data and it includes a detection bias by emission angle or trigger efficiency and a correlation between observables. It is difficult more or less to separate the data set by event type $(N_{sig}, N_{RD}, N_{BG})$ and accidental background is most dominant while others is less than that, so we determine to use a common list for

all event type. For a polarized muon we have to choose a different list between event type and a event distribution of signal depends on physics model.

10.1.4 Confidence region

There are some methods to extract confidence region of branching ratio. We adopted Feldman-Cousins approach to estimate the confidence level of $\mathrm{Br}(\mu \to e\gamma)$, which is the same as 2008 analysis [62]. Other methods are also tried for a consistency check.

From now on, the best fit values of N is represented with hat, $\hat{N}$, and type of event (data or j-th toy MC) on superscript and i-th sampling points on subscript. We introduce the Feldman-Cousins procedure. The confidence level around the point, $(\hat{N}^{data}_{sig}, \hat{N}^{data}_{RD}, \hat{N}^{data}_{BG})$, is estimated for each i-th sampling point, $(N_{sig,i}, N_{RD,i}, N_{BG,i})$. The scan of interesting region by collecting sampling points gives a contour of the confidence level on $(N_{sig}, N_{RD}, N_{BG})$. In order to estimate the confidence level at each i-th sampling point, we simulate many experiments by each sampling point that is used for the generation as the number of events. The j-th toy experiment at the i-th sampling point gives the best fit value of the maximum likelihood fit, $(\hat{N}^j_{sig,i}, \hat{N}^j_{RD,i}, \hat{N}^j_{BG,i})$. To order the results, a probability of data at sampling point, $(N_{sig,i}, N_{RD,i}, N_{BG,i})$, is compared to those of toy-MCs at the same point. Feldman-Cousins method uses a ratio of likelihood,

$$R_{data,i} = \frac{L(N_{sig,i}, N_{RD,i}, N_{BG,i})}{L(\hat{N}^{data}_{sig}, \hat{N}^{data}_{RD}, \hat{N}^{data}_{BG})}, \tag{80}$$

$$R^j_{MC,i} = \frac{L(N_{sig,i}, N_{RD,i}, N_{BG,i})}{L(\hat{N}^j_{sig,i}, \hat{N}^j_{RD,i}, \hat{N}^j_{BG,i})}, \tag{81}$$

and the confidence level is determined by the probability,

$$P(R^j_{MC,i} > R_{data,i}) = \sum_j^{N_{MC}} \frac{H(R^j_{MC,i} - R_{data,i})}{N_{MC}}, \tag{82}$$

$$H(R^j_{MC,i} - R_{data,i}) = \begin{cases} 1 \ (R^j_{MC,i} \geq R_{data,i}), \\ 0 \ (R^j_{MC,i} < R_{data,i}). \end{cases} \tag{83}$$

The scan by sampling points i gives the confidence distribution. Our final purpose is to extract the 90% confidence interval of N_{sig} from the confidence region on $(N_{sig}, N_{RD}, N_{BG})$. We checked no obvious correlation between the numbers of (N_{sig}, N_{RD}). Hence we assume that the number of signal and radiative decay are independent each other. The number of radiative background and accidental background, N_{RD}, N_{BG}, can be fixed to the best fit value respectively $\hat{N}^{data}_{RD}$, $\hat{N}^{data}_{BG}$ and we estimate the confidence level along N_{sig}.

10.1.5 Effect of systematic uncertainty

The systematic uncertainty can be taken into account at the calculation of confidence level by randomly fluctuating the PDFs according to the systematic uncertainties. Technically after experiments' simulation the PDFs are shifted when fitting in the range of systematic uncertainties such that the degree of shift is randomly determined by each experiment.

10.2 Maximum likelihood analysis

The goal of the maximum likelihood analysis is to obtain the best fit value of the number of $\mu^+ \to e^+\gamma$ signal, as well as prompt and accidental backgrounds. The reason why we separate backgrounds to two types is that we can estimate each PDF and mixing of two is different by an selection window and a beam condition such as a rate or a muon polarization. The likelihood function is also used to compare the probabilities at the given number of events.

10.2.1 Definition

A likelihood function $L(\vec{\theta}|\vec{X})$ is defined as

$$L(\vec{\theta}|\vec{X}) = \prod_{i=1}^{N_o} p(\vec{x_i}|\vec{\theta}), \tag{84}$$

where $\vec{x_i}$ is a set of observables in i-th event within the selected region, $\vec{X}$ is a set of $\vec{x_i}|_{i=0\sim N_o}$ in an experiment with an observed total number of events N_o, $\vec{\theta}$ is a set of unknown parameters of the likelihood. The function $p(\vec{x_i}|\vec{\theta})$ is a joint PDF for all observations of i-th event in a $\vec{\theta}$ set. The parameters $\vec{\theta}$ can be determined so that the likelihood is maximized with a given $\vec{X}$, which is $\vec{\theta}^{best}(\vec{X})$. These are the maximum likelihood fit method to obtain $\vec{\theta}^{best}(\vec{X})$. In the MEG experiment we define $\vec{\theta}$ by the number of event:

$$\begin{aligned} \vec{\theta} &= (N_{sig}, N_{RD}, N_{BG}), & (85)\\ N_o &= N_{sig} + N_{RD} + N_{BG}. & (86) \end{aligned}$$

However, it could be better to regard that parameters of $(N_{sig}, N_{RD}, N_{BG})$ have an experiment-by-experiment fluctuation. We redefine N_o with an unknown true value set of $\vec{\theta}_{true} = (N_{o,sig}, N_{o,RD}, N_{o,BG})$ in the performed experiment and introduce N instead of N_o as a mean in experiments,

$$\begin{aligned} N &= N_{sig} + N_{RD} + N_{BG} & (87)\\ N_o &= N_{o,sig} + N_{o,RD} + N_{o,BG}. & (88) \end{aligned}$$

We assume that the fluctuation of each number, $f(N_{o,j}|N_j)$ $(j = (sig, RD, BG))$, obeys the Poisson distribution $f_{poisson}(N_{o,j}|N_j)$ $(j = (sig, RD, BG))$ respectively, then the fluctuation of summed number N_o, $f(N_o|N)$, also shows a Poisson distribution $f_{Poisson}(N_o|N)$.

$$\begin{aligned} f(N_o|N) &= f_{Poisson}(N_{o,sig}|N_{sig}) \wedge f_{Poisson}(N_{o,RD}|N_{RD}) \wedge f_{Poisson}(N_{o,BG}|N_{BG}) & (89)\\ &= \prod_{j=(sig,RD,BG)} f_{Poisson}(N_{o,j}|N_j) & (90)\\ &= f_{Poisson}(N_{o,sig} + N_{o,RD} + N_{o,BG}|N_{sig} + N_{RD} + N_{BG}) & (91)\\ &= f_{Poisson}(N_o|N) & (92) \end{aligned}$$

Here we regard the $\vec{\theta}$ as an independent parameter set and use a reproductive property of Poisson distribution from Equation 90 to Equation 91.

Then we can define the extended likelihood function $L_{ext}(\vec{\theta}|\vec{X})$,

$$L_{ext}(\vec{\theta}|\vec{X}) = f(N_o|N)L(\vec{\theta}|\vec{X}) \quad (93)$$

$$= \frac{N^{N_o}\exp(-N)}{N_o!}\prod_{i=1}^{N_o} p(\vec{x_i}|\vec{\theta}), \quad (94)$$

where N means the positive expected number of occurrences in the Poisson distribution of observed total events in experiments.

10.2.2 Observables

From a kinematic point of view, four parameters of energies, opening angle and time difference, $(E_e, E_\gamma, \Theta_{e\gamma}, t_{e\gamma})$, can discriminate $\mu^+ \to e^+\gamma$ signal from backgrounds. With considering the detector responses of the drift chamber and timing counter, they have a different position performance between a z direction and a ϕ direction. Therefore we separate the opening angle $\Theta_{e\gamma}$ to $\theta_{e\gamma}$ and $\phi_{e\gamma}$.

Accordingly resolutions of the parameters, $\delta\vec{x} = (\delta E_e, \delta E_\gamma, \delta\theta_{e\gamma}, \delta\phi_{e\gamma}, \delta t_{e\gamma})$, are introduced to construct event-by-event PDFs. These resolution parameters are determined by the position on the LXe detector and emission angles of positrons. Other parameters of two thicknesses of the degrader and two categories of tracking quality also specify the PDFs, but we omit to express these in $\vec{x}$. We define this parameter set to specify the shape of PDF as $\delta\vec{x}$ and the set can be used to generate events in the toy MC. Then observables are selected,

$$\vec{x} = (E_e, E_\gamma, \theta_{e\gamma}, \phi_{e\gamma}, t_{e\gamma}, \delta E_e, \delta E_\gamma, \delta\theta_{e\gamma}, \delta\phi_{e\gamma}, \delta t_{e\gamma}). \quad (95)$$

The probability is expressed by each probability of event types,

$$p(\vec{x_i}|\vec{\theta}) = \sum_{j=(sig,RD,BG)} p(\vec{x_i}|\vec{\theta}, j)\frac{N_j}{N}. \quad (96)$$

Here we use PDFs of signal, radiative decay and accidental background defined below,

$$p(\vec{x_i}|N_{sig}, N_{RD}, N_{BG}, sig) \equiv S(\vec{x_i}) = S(\vec{x_i}|\delta\vec{x_i})p(\delta\vec{x_i}), \quad (97)$$

$$p(\vec{x_i}|N_{sig}, N_{RD}, N_{BG}, RD) \equiv R(\vec{x_i}) = R(\vec{x_i}|\delta\vec{x_i})p(\delta\vec{x_i}), \quad (98)$$

$$p(\vec{x_i}|N_{sig}, N_{RD}, N_{BG}, BG) \equiv B(\vec{x_i}) = B(\vec{x_i}|\delta\vec{x_i})p(\delta\vec{x_i}), \quad (99)$$

It is assumed that the function of $p(\delta\vec{x_i})$ is common because the performance of all the detectors is almost symmetric and is able to cancel out another asymmetry such as the event distribution, for example, it may be asymmetric depending on a muon polarization. Then we can define a likelihood function of $(N_{sig}, N_{RD}, N_{BG})$ as

$$L_{ext}(N_{sig}, N_{RD}, N_{BG}) \quad (100)$$

$$= \frac{N^{N_o}\exp(-N)}{N_o!}\prod_{i=1}^{N_o}\left(\frac{N_{sig}}{N}\cdot S(\vec{x_i}) + \frac{N_{RD}}{N}\cdot R(\vec{x_i}) + \frac{N_{BG}}{N}\cdot B(\vec{x_i})\right) \quad (101)$$

$$= \frac{N^{N_o}\exp(-N)}{N_o!}\prod_{i=1}^{N_o} p(\delta\vec{x_i}) \left(\frac{N_{sig}}{N}\cdot S(\vec{x_i}|\delta\vec{x_i}) + \frac{N_{RD}}{N}\cdot R(\vec{x_i}|\delta\vec{x_i}) + \frac{N_{BG}}{N}\cdot B(\vec{x_i}|\delta\vec{x_i})\right) \quad (102)$$

We use a negative log-likelihood (NLL) function to be minimized and it is suitable for a fit,

$$
\begin{aligned}
&- \ln L_{ext}(N_{sig}, N_{RD}, N_{BG}) + \sum_{i=1}^{N_o} p(\delta\vec{x_i}) + const. \\
&= N - \sum_{i=1}^{N_o} \ln \left(N_{sig} \cdot S(\vec{x_i}|\delta\vec{x_i}) + N_{RD} \cdot R(\vec{x_i}|\delta\vec{x_i}) + N_{BG} \cdot B(\vec{x_i}|\delta\vec{x_i}) \right). \quad (103)
\end{aligned}
$$

In our case MINUIT package is used [63]. From now on, we redefine $S(\vec{x_i})$, $R(\vec{x_i})$, $B(\vec{x_i})$ by $S(\vec{x_i}|\delta\vec{x_i})$, $R(\vec{x_i}|\delta\vec{x_i})$, $B(\vec{x_i}|\delta\vec{x_i})$, or simply express these by S, R, B, respectively.

10.3 Probability density function

The Probability density functions (PDFs) are based on measured data and some set are prepared separately by a certain period for a different condition of degraders. We estimate three types of PDFs, which is S, R and B for a signal, a prompt background from radiative muon decays and accidental background respectively.

Different conditions of experiment setup such as different years or a normal MC events can be considered in the same framework with regarding these condition as also observables and preparing a corresponding PDF set. Thus we prepared two separated PDF set for different degrader thickness of 200 or 300 μm, which is recognized by taken time. Some parts of PDFs can be separated for independent variables, and three types of PDF are defined as

$$S(E_e, E_\gamma, \theta_{e\gamma}, \phi_{e\gamma}, t_{e\gamma}) = S_1(E_e)S_2(E_\gamma)S_3(\theta_{e\gamma})S_4(\phi_{e\gamma}|E_e)S_5(t_{e\gamma}), \quad (104)$$

$$R(E_e, E_\gamma, \theta_{e\gamma}, \phi_{e\gamma}, t_{e\gamma}) = R_1(E_e, E_\gamma, \theta_{e\gamma}, \phi_{e\gamma})R_2(t_{e\gamma}), \quad (105)$$

$$B(E_e, E_\gamma, \theta_{e\gamma}, \phi_{e\gamma}, t_{e\gamma}) = B_1(E_e)B_2(E_\gamma)B_3(\theta_{e\gamma})B_4(\phi_{e\gamma})B_5(t_{e\gamma}). \quad (106)$$

Figure 10.2 shows PDFs with simply averaged in observed events, as a functions of observable.

10.3.1 Signal

The PDF is almost based on measured distribution. The signal PDF, S, is estimated as below.

$S_1(E_e)$ The positron momentum is expressed with double Gaussian. Not only emission angles but also the selection of the tracking quality determines S_1. In 2008 we extract S_1 with fitting theoretical Michel spectrum by convoluting its response. Currently in 2009 we estimate the momentum resolution with the two-turn method as described in Section 8.3.

$S_2(E_\gamma)$ The S_2 is position dependent and derived from 54.9 MeV gamma ray in π^0 decay. In 2009 the energy dependence of the energy resolution is considered.

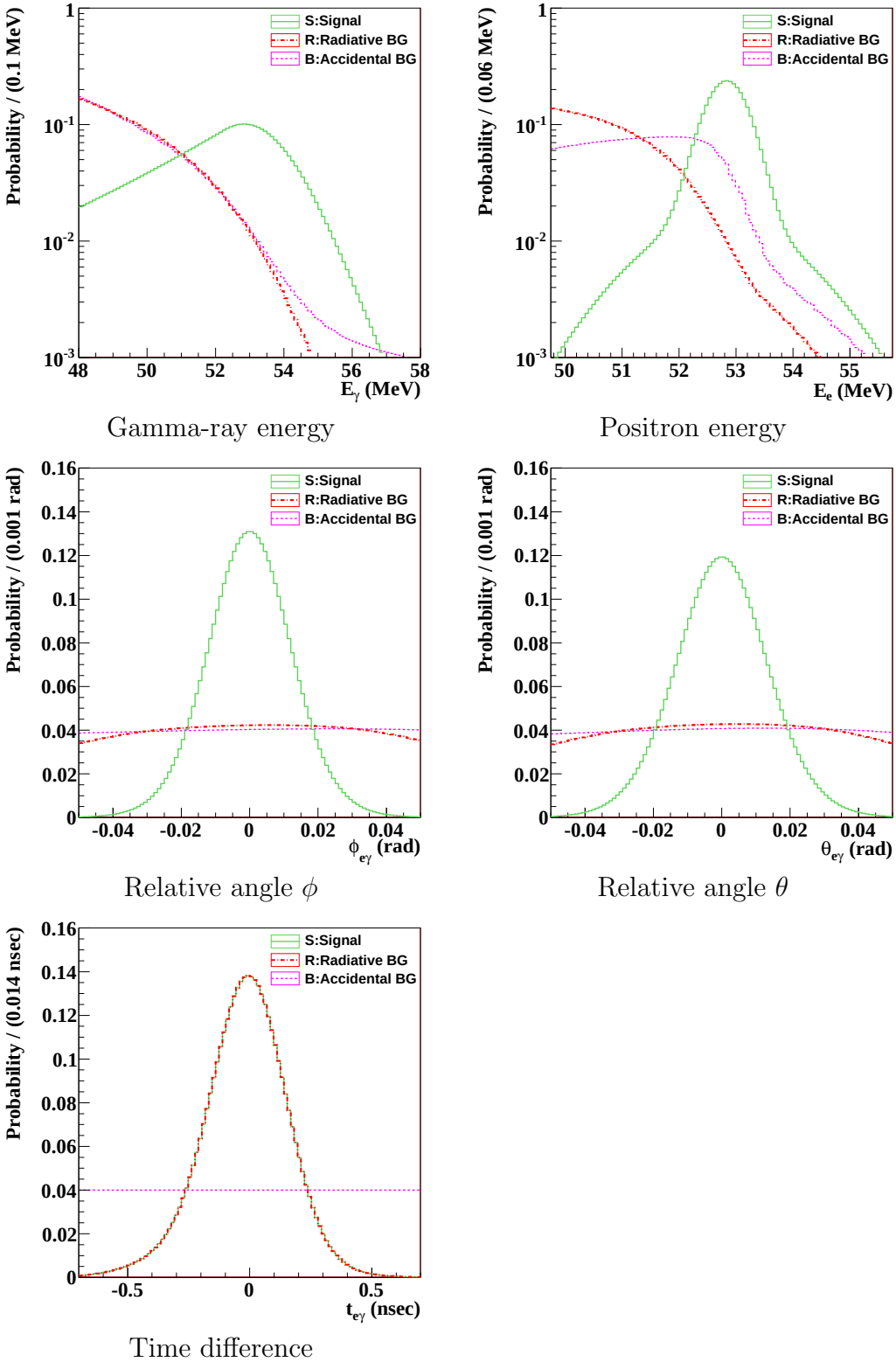

Figure 10.2: Averaged probability density functions (PDFs) by observables. In the figure the solid lines, the chain lines and the dashed lines show the PDFs of signal, of radiative background and accidental background (S, R, B), respectively.

$S_3(\theta_{e\gamma}), S_4(\phi_{e\gamma}|E_e)$ The angular resolution is constructed from resolutions of emission angles and a vertex position by a positron and (u, v)-resolution in the LXe detector. The difference between independent reconstructions of one turn, which is recognized as a two-turn track, gives the positron resolution of emission angles. Bias of this method is eliminated by the signal MC. The holes on the muon target are estimated as a vertex resolution. The position resolution of gamma-ray detection is evaluated in π^0 decay run by putting a lead-slit collimator in front of the LXe detector at a certain position, then a position dependence of resolution is extracted with the signal MC. The signal MC indicates that a reconstruction of $\phi_{e\gamma}$ has a bias depending on the positron energy, E_e. The dependence is treated in the conditional probability, $S_4(\phi_{e\gamma}|E_e)$.

$S_5(t_{e\gamma})$ The time difference between positron and gamma ray is derived from a radiative muon decay. We confirm a peak of $t_{e\gamma}$ from that decay and obtain S_5 with subtracting floor from accidental background. It contains a dependence of gamma-ray energy.

10.3.2 Radiative decay

The radiative decay has a kinematic correlation between observable parameters, which forbids a separate treatment of PDF.

$R_1(E_e, E_\gamma, \theta_{e\gamma}, \phi_{e\gamma})$ The R_1 is formed with the theoretical correlation of radiative muon decay folding with detector response of each signal PDF.

$R_2(t_{e\gamma})$ This PDF is the same as signal PDF S_5 from a peak of radiative decay.

10.3.3 Accidental background

To avoid a contamination of coincident radiative decays, those PDF elements are estimated from $t_{e\gamma}$ sideband data outside the analysis window.

$B_1(E_e)$ The positron energy spectrum in Michel decay is fitted by a theoretical Michel decay smeared by the resolution.

$B_2(E_\gamma)$ The PDF B_2 is position dependent and estimated by fitting $t_{e\gamma}$ sideband data with an expectation of a radiative muon decay and a positron annihilation flight in the MC with folding a detector response.

$B_3(\theta_{e\gamma}), B_4(\phi_{e\gamma})$ The background PDFs of opening angle $\theta_{e\gamma}$ and $\phi_{e\gamma}$ are estimated by fitting third-order polynomial function to the distribution observed in the sidebands.

$B_5(t_{e\gamma})$ The B_5 is a flat distribution because it is only accidental. The effect of trigger bias is not remained in the analysis region.

10.4 Result of the maximum likelihood fit

When we finished the optimization of the analysis and the background studies in the sidebands, we opened the blinding box and performed a likelihood analysis. Then the first result in 2009 data of the MEG experiment is revealed. After unblinding events in the analysis region, the numbers of signal, radiative muon decay and accidental background are estimated to be,

$$(\hat{N}_{sig}, \hat{N}_{RD}, \hat{N}_{BG}) = (3.0^{+6.9}, 35^{+24}_{-22}, 332^{+38}_{-36}),\ N_{obs} = 370, \tag{107}$$

where asymmetric errors are taken from MINUIT of fitting, that is 1.645 sigma MINOS errors. The negative error of $\hat{N}_{sig}$ is outside of the defined fit region and is not described.

Figure 10.3 shows the distribution projected onto each observable with averaged PDFs scaled with the best fit number of each type. The highest blue line of four lines is a total sum of all PDFs. Because we select the wide analysis window there is also radiative peak on the relative time window, while no obvious peak is seen in relative angle distributions. Figure 10.3 (f) shows contour plots on N_{sig}-N_{RD} plane and the black dot mark shows the best-fit value. The dashed-, solid-, dotted-lines show contours of the likelihood function at 1, 1.645, 2 sigma (0.5, 1.353, 2 ΔNLL), respectively.

10.5 Sensitivity of Run 2009

A higher tail of the likelihood from $\hat{N}_{sig}$ indicates a region to exclude the LFV events. In case of the previous experiment by the MEGA collaboration, the shape of likelihood distribution determined the upper limit on the branching ratio such that the area along N_{sig} takes 90% area [2]. While in our case the confidence interval is determined by many toy experiments with assuming various N_{sig} in toy MC, according to Feldman Cousin method described in Section 10.1.4. The upper limit of the branching ratio obtained in a single experiment suffers a statistical fluctuation. We consider the fluctuation by many simulated experiments with null signal and can obtain the sensitivity by the average of upper limits in the experiments.

The sensitivity of the experiment with the data statistics for the run 2009 is calculated as an upper limit averaged over an ensemble of the simulated 1500 experiments, where the same expected numbers of the RD and the accidental BG as the likelihood fit result on 2009 data and the null signal are assumed. The upper-limit calculation does not include the systematic uncertainties. Taking average of 90% branching-ratio upper limit as shown in Figure 10.4, it is calculated to be

$$S_{2009} = 6.1 \times 10^{-12}. \tag{108}$$

The result is improved from 2008 result, $S_{2008} = 1.3 \times 10^{-11}$, while it is from early data and not a final goal of the sensitivity in the MEG experiment.

10.6 Upper limit of $\mu^+ \to e^+\gamma$ branching ratio

In 2009 data the 90% C.L. upper limit for N_{sig} is estimated to be 14.5, while $N_{sig} = 0$ is inside the confidence interval of 90%. The systematic uncertainties are included in this calculation. The detailed effect of each uncertainty is discussed later. With normalization factor, the upper limit for the branching ratio is finally obtained as

$$\mathrm{Br}(\mu^+ \to e^+\gamma) < 1.5 \times 10^{-11} \text{ at } 90\% \text{ C.L.} \tag{109}$$

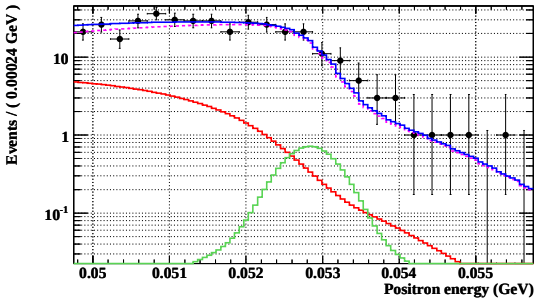

(a) Gamma-ray energy

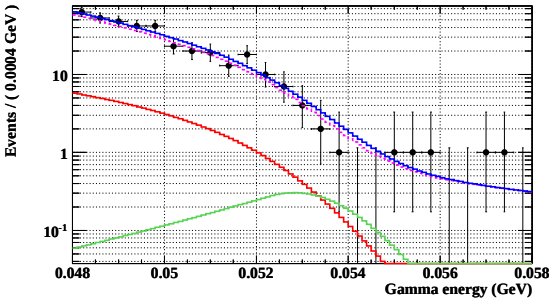

(b) Positron energy

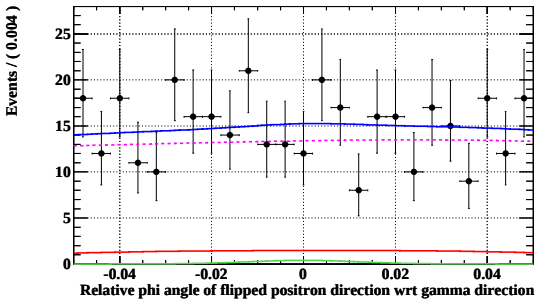

(c) Relative angle ϕ

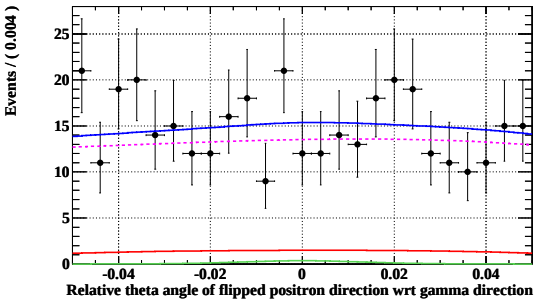

(d) Relative angle θ

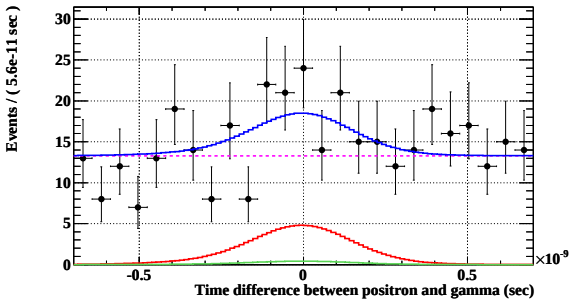

(e) Relative time

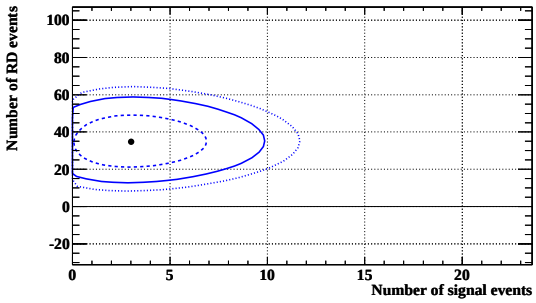

(f) Contour plots on N_{sig} and N_{RD}

Figure 10.3: Result of the maximum likelihood fit. Summed PDFs weighted with best fit values of each types are superimposed on (a)-(e). The notation of each PDF is the same as in Figure 10.2.

10.7 Discussion

10.7.1 Event distribution

The event distributions after the unblinding are shown in Figure 10.5 where the events near the signal are labeled with the order of the likelihood ratio defined as $S/(S+R+B)$. In the figure, (a) and (b) show E_γ and E_e, while relative time and $\cos\Theta_{e\gamma}$ are shown in (c) and (d). Separately, the events with a high-quality positron tracking are plotted in the figures (b) and (d). The most signal-like events in the analysis region remain even after high quality cut is applied in (b) and (d) out of all events without the quality selection in (a) and (c).

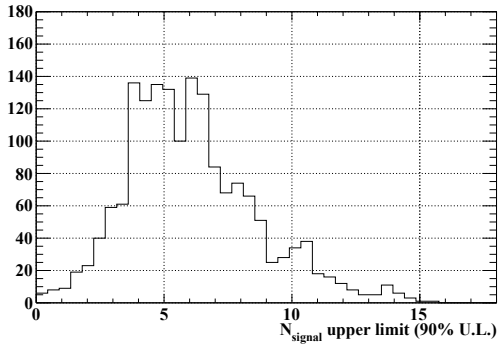

Figure 10.4: Distribution of N_{sig} upper limit at 90% confidence level in a toy MC.

10.7.2 Highly-ranked events

Table 18 shows properties such as E_γ, E_e, $t_{e\gamma}$, angles, positions and a proton current of highly ranked events by means of the relative signal likelihood. The Z_{TC} shows the reconstructed position of hit on z in the timing counter. The rank in the table is given by the likelihood ratio of signal to backgrounds and corresponding to the numbers in Figure 10.5.

Table 18: List of the highly ranked events by $S/(S+R+B)$.

Rank	E_γ, E_e (MeV)	$t_{e\gamma}$ (ps)	$\phi_{e\gamma}$, $\theta_{e\gamma}$ (mrad)	$\cos\Theta_{e\gamma}$	$(u,v,w)_{LXe}$ (cm)	Z_{TC} (cm)	Proton (μA)
1	52.3, 52.6	27	5, -20	-0.99978	1.6, -46.0, 3.1	-31.3	2178
2	52.1, 52.7	-72	16, -14	-0.99978	14.9, -8.3, 0.5	-61.5	2185
3	51.8, 53.0	-136	-12, 22	-0.99968	3.4, -62.9, 3.5	-35.3	1698
5	52.2, 52.6	287	14, -11	-0.99986	24.3, -42.5, 0.9	-89.2	2191
8	52.3, 52.5	-259	25, 11	-0.99964	9.5, -10.7, 4.7	-38.8	2186

We thoroughly checked ten signal-like events with a high rank by the signal likelihood. The high ranked events are almost categorized in high quality of positron tracking and there is no pile ups of gamma rays. For example, observables and PDFs of the highest-rank event are shown in Figure 10.6 to check which observable is dominant in a PDFs. Figure 10.7 shows the event display of the highest ranked event. On the left hand side two-dimensional display with positron tracks and light distribution in the LXe detector are shown, while the distribution are drawn in development view on the right hand side.

Figure 10.8 (a) shows the proton current and the time of highly ranked events. The third ranked event was taken when the proton current was low. We checked the quality of the gamma-ray energy. The peaks of LED events mixed during the physics run (Figure 10.8 (b)) shows the third event in several sudden jumps about 1.5 % due to gains misapplied between different intensities of proton beam that is not large compared to the 1-sigma region in Figure 10.5 (a). Except for that, through the check neither strange nor wrong reconstruction are found.

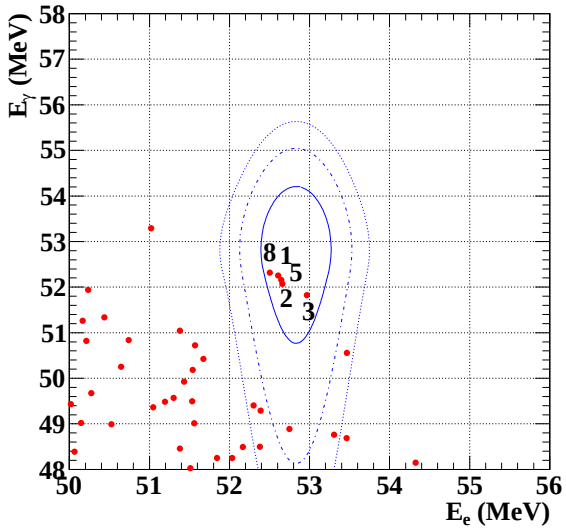

(a) E_γ and E_e

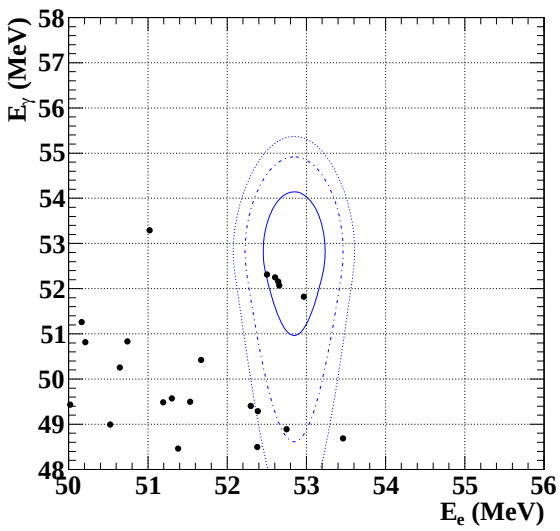

(b) E_γ and E_e
of only high-quality positron tracking

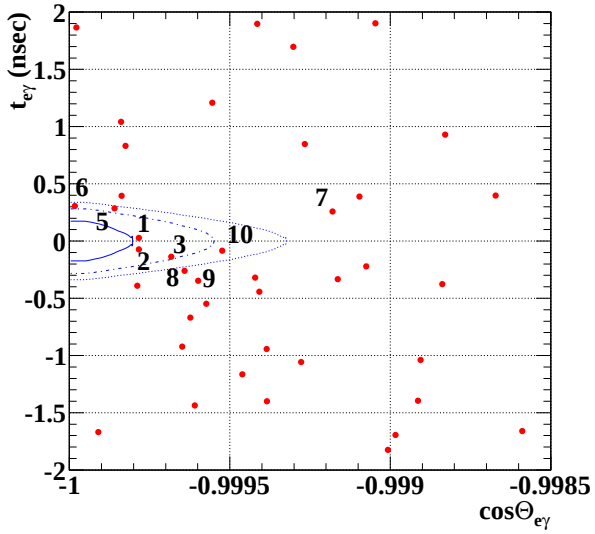

(c) Relative time and $\cos\Theta_{e\gamma}$

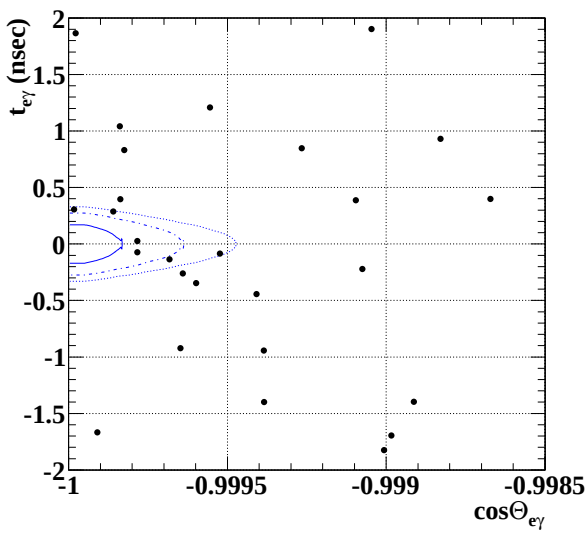

(d) Relative time and $\cos\Theta_{e\gamma}$
of only high-quality positron tracking

Figure 10.5: Distribution in analysis region. The signal 2D PDFs are superimposed as contours at 1, 1.64, 2 sigma as blue solid, dot-dashed, and dashed lines respectively. The number shows the rank by $S/(S+R+B)$.

10.7.3 Result in sideband data

The same analysis was performed with different event sets such as in sidebands. The likelihood fit with null signal is possible with sideband of $t_{e\gamma}$, which is very convenient way because the estimation of the upper limit sensitivity is also possible with the same PDF set.

Before opening blind box we estimated upper-limit sensitivities to be $3-5\times10^{-12}$ with shifting the analysis window along $t_{e\gamma}$. Figure 19 shows the best fit values in both

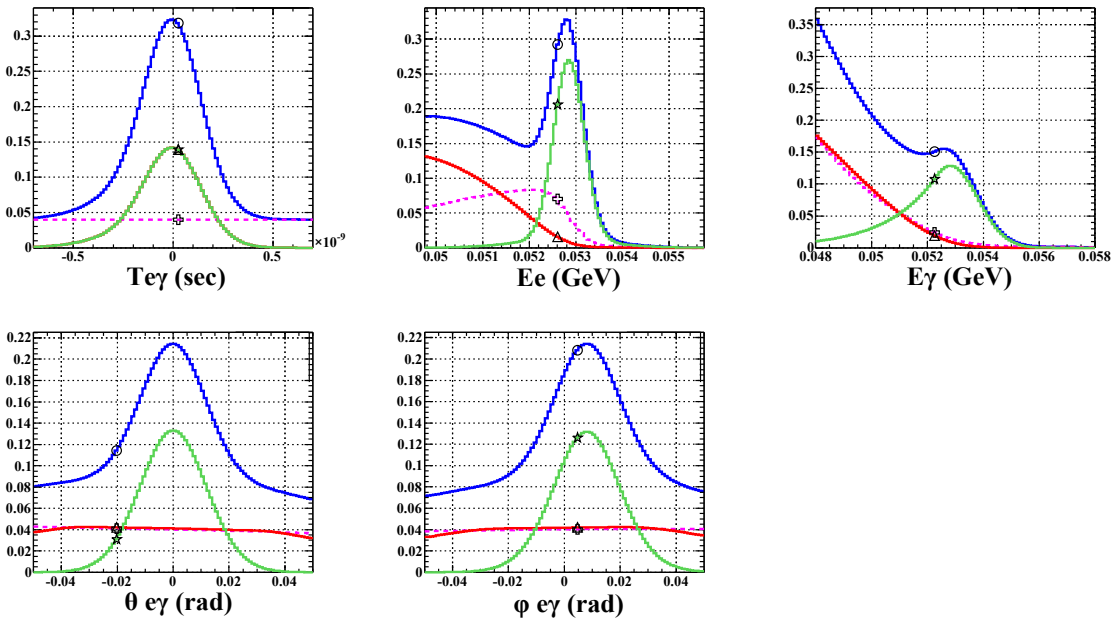

Figure 10.6: The observables in the highest-ranked event with PDFs ($t_{e\gamma}$(sec), E_e(GeV), E_γ(GeV), relative angles(rad)). Three-type of S, R, B and summed PDF in the event are drawn as green, red, magenta and blue lines. Mark superimposed on PDFs shows the measurement value and the probability in the event.

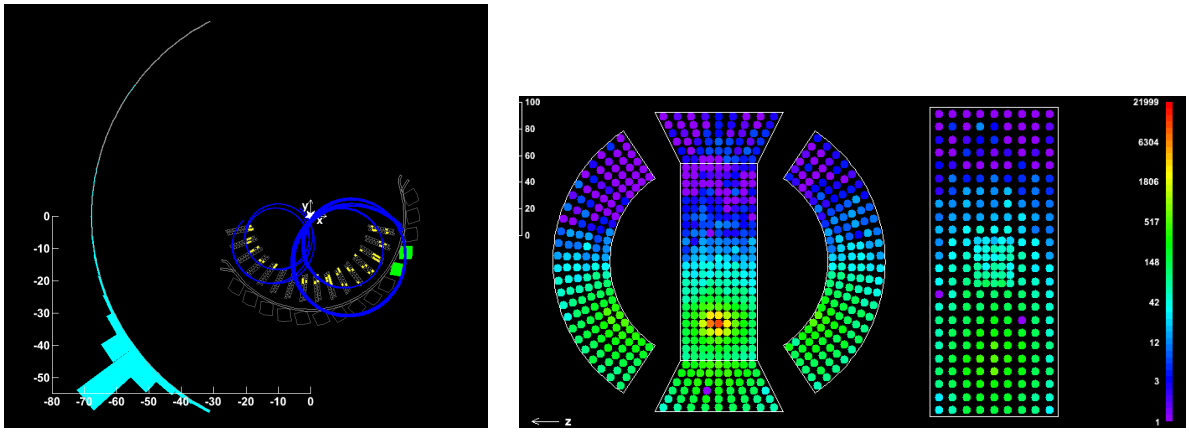

(a) 2D x-y display (b) Map of the number of photons by PMTs

Figure 10.7: Event display of the highest rank.

sidebands of $t_{e\gamma}$. The result in the analysis window differs from the final result because the systematic uncertainties are not considered.

10.7.4 Effect of the systematic uncertainty

The systematic uncertainty can be included in calculation of the confidence interval by fluctuating the likelihood function when performing the likelihood fit in each simulated experiment. All the uncertainties are fluctuated simultaneously in the C.L. calculation.

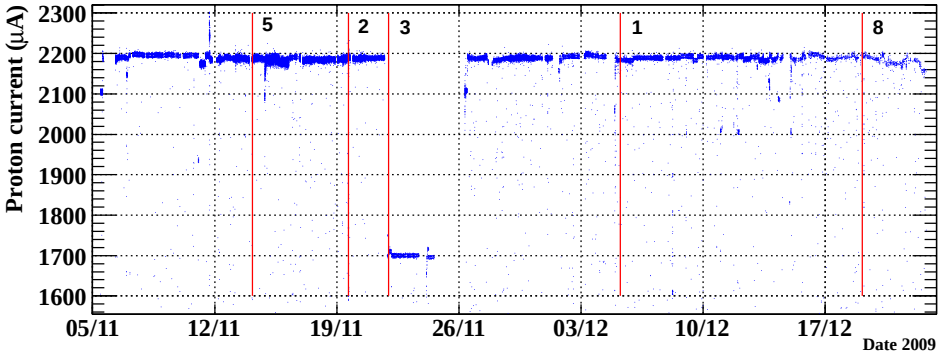

(a) Proton current.

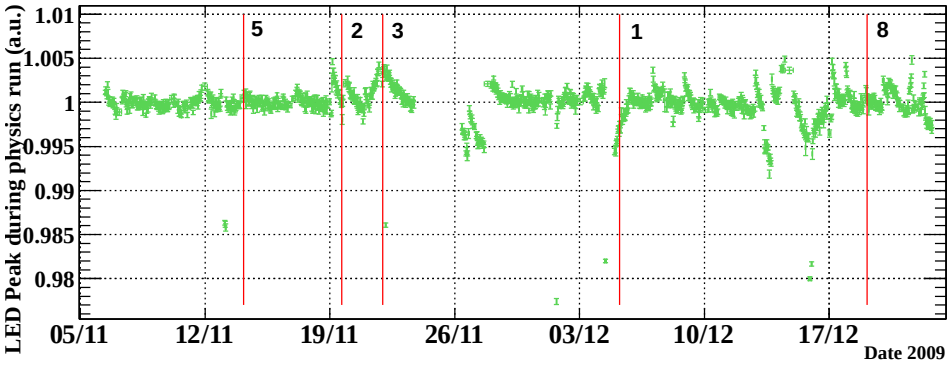

(b) LED peaks in the LXe detector, which is the same as Figure 6.14.

Figure 10.8: Muon beam (a) and LED peaks in the LXe detector (b) during physics run. The attached numbers are the rank listed in Table 18. The red lines beside the number show the time of the events taken.

Table 19: The best fit values and 90% C.L. upper limits (UL) on $t_{e\gamma}$ side bands with ± 2.5 ns offset shift. The systematic uncertainties are not included.

	events	$\hat{N}_{sig}$	$\hat{N}_{RD}$	$\hat{N}_{BG}$	N_{sig} UL	Br UL (10^{-12})
Analysis window	370	3.0	35	332	11.8	14.3
Negative $t_{e\gamma}$ sideband	290	0	0	290	4.5	4.5
Positive $t_{e\gamma}$ sideband	300	0	4.4	296	6.0	6.1

We estimated the contribution of each systematic uncertainty by individually shifting the parameter in PDF according to its uncertainty and see how the best fit value of N_{sig} is shifted. Figure 10.9 shows the best fit values of the number of the signal by shifting each parameter within uncertainties. The most dominant factor is a relative angle, and second ones are both energies secondary. However, the effect of the systematic uncertainty is small compared to the statistical uncertainty of the likelihood fit.

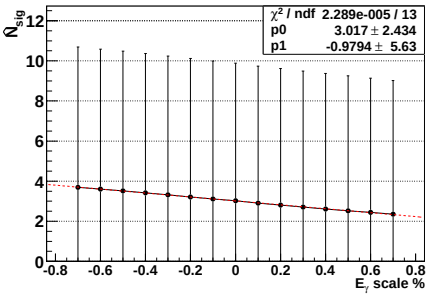

(a) E_γ : $0.42N_{sig}$ (0.43%)

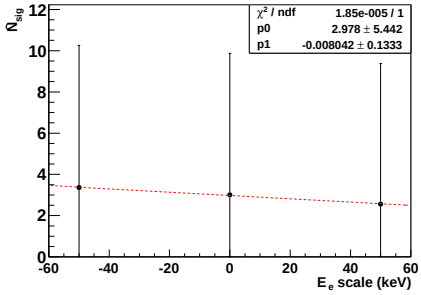

(b) E_e : $0.40N_{sig}$ (50 keV)

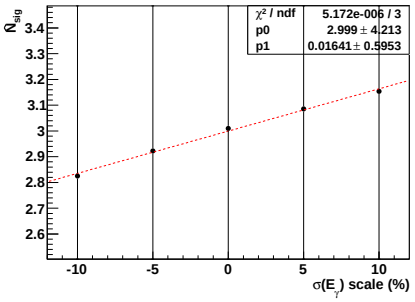

(c) $\sigma(E_\gamma)$: $0.3N_{sig}/0.1\sigma_{E_\gamma}$

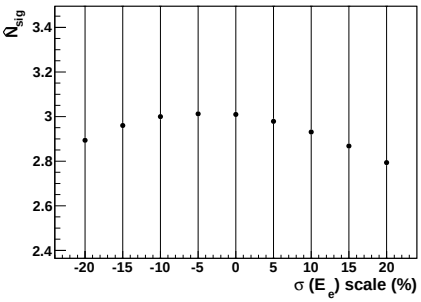

(d) $\sigma(E_e)$: $0.14N_{sig}$ (15%)

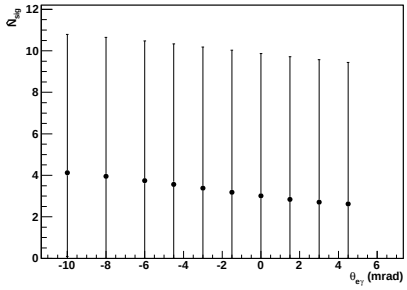

(e) $\theta_{e\gamma}$: $0.90N_{sig}$ (7.5 mrad)

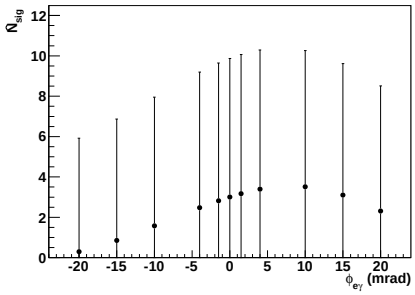

(f) $\phi_{e\gamma}$: $0.99N_{sig}$ (7.5 mrad)

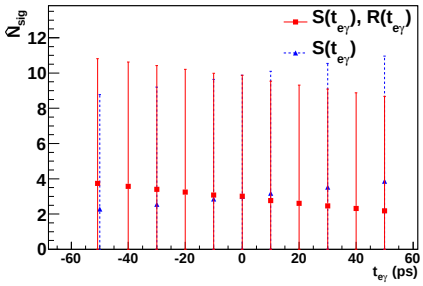

(g) $t_{e\gamma}$: $0.23N_{sig}$ (15 ps)

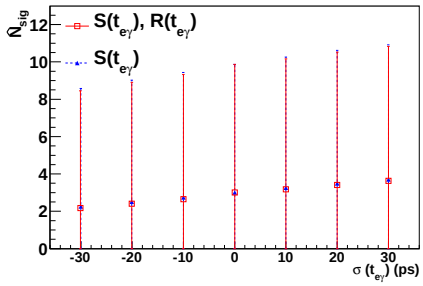

(h) $\sigma(t_{e\gamma})$: $0.35N_{sig}$ (10%)

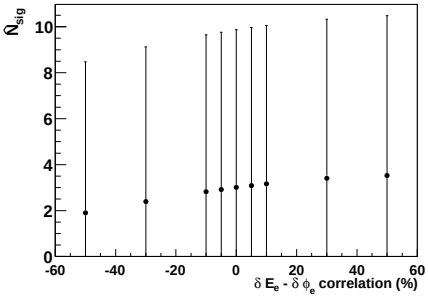

(i) $\delta E_e - \delta\phi_e$: $0.83N_{sig}$ (50%)

Figure 10.9: Effect to the best fit N_{sig} by each systematic uncertainty. Each notation shows a value, shift of the best fit of N_{sig} in the uncertainty and systematic uncertainty listed in Table 17.

10.7.5 Future prospects

The current statistics of muon decays is still low and we continue to take physics data for several years. Future prospects of the sensitivity for the $\mu^+ \to e^+\gamma$ are estimated by year as shown in Figure 10.10. The shown sensitivity in the figure is based on Bayesian inference for a fast calculation of 90% upper limit of the branching ratio, which differs a little from the previous result in Section 10.5. However, we have confirmed a consistency that these have similar results each other. In this method, the toy MC simulation by the data set in 2009 was performed for the sensitivity calculation with the expected number of events by year. Two types of PDFs are prepared for the event generation. One is the same performance in 2009 and the other is taken from an expected performance achieved by upgrades of the detectors and the analysis. The assumption of the performance in sigma is $\sigma_{E_e} = 32$ keV, $\sigma_{E_\gamma} = 1.5\%$ (2 cm $\leq w <$ 38 cm), 2.46% (1 cm $\leq w <$ 2 cm), 2.65% (0 cm $\leq w <$1 cm), $\sigma t_{e\gamma} = 100$ ps, vertex resolutions $\sigma_Z = 2.5$ mm, $\sigma_Y = 1.4$ mm and 8 mrad for both ϕ and θ angles. The sensitivity will reach a region lower than 10^{-12} within a few years.

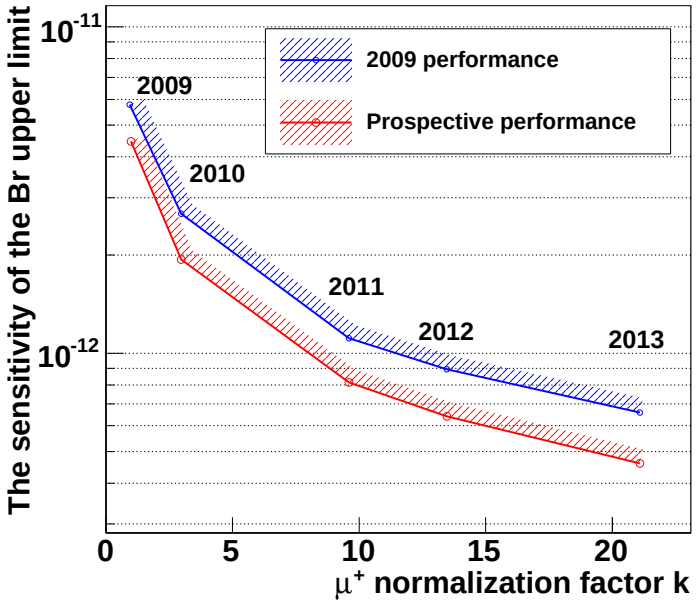

Figure 10.10: Future prospects of the sensitivity for a next few years as a function of k factor.

Part VI
Conclusion

The MEG experiment successfully took the physics data in the second year 2009 for two months. The enough purification for the liquid xenon brought the large increase of the light yield and it was quite stable during the run within 0.3%. The accumulated number of stopped muons in 2009 is about 6.5×10^{13}, while 9.5×10^{13} in 2008 because of the longer three-month run in 2008. Thanks to the investigation and the improvement for the discharge problem of the drift chamber before the 2009 run, the positron spectrometer was stably operated over whole period of the data taking and the muon decays observed in the detector increased largely compared to the 2008 run.

The obtained performance in 2009 is summarized in Table 20. We got large improvements for the performance of positron tracking especially.

Table 20: Resolution in 2009

Year	σ_{E_γ} (%)	$\sigma_{(u,v,w)}$ (mm)	ϵ_γ	σ_{E_e} (%)	σ_{ϕ_e} (mrad)	σ_{θ_e} (mrad)	Vertex $\sigma_{Z,Y}$ (mm)	ϵ_e	$\sigma_{t_{e\gamma}}$ (ps)	ϵ_{trig}
2009	2.1[1]	5, 6	0.58	0.74[2]	7.1[2]	11.2	3.4, 3.3	0.4	142[2]	0.84

[1] $w > 2$cm
[2] Core component

The branching-ratio sensitivity in 2009 is estimated to be

$$S_{2009} = 6.1 \times 10^{-12}.$$

This result is better than the previous 2008 result of the sensitivity, 1.3×10^{-11}.

The analysis in 2009 data concludes that the upper limit of branching ratio is

$$\mathrm{Br}(\mu^+ \to e^+\gamma) < 1.5 \times 10^{-11} \text{ at } 90\% \text{ C.L.},$$

and showed the improvement compared to the 2008 result, 2.8×10^{-11} (90% C.L.). The 90%-confidence interval still includes the region of $N_{sig} = 0$.

The presented analysis uses only 2009 data while the MEG experiment just started data taking and will run for a next few years. The result is still limited by the statistics of muons and a finer tuning and an improvement of the analysis is going on.

Appendix

A Radiative decay

A.1 Radiative-decay differential branching ratio

Equation 5 shows the differential branching ratio of RD [19]. The functions of $F(x,y,d)$, $G(x,y,d)$, and $H(x,y,d)$ are given in the SM as follows:

$$
\begin{aligned}
r &= \left(\frac{m_e}{m_\mu}\right)^2, \\
F(x,y,d) &= F^{(0)} + rF^{(1)} + r^2F^{(2)}, \\
G(x,y,d) &= G^{(0)} + rG^{(1)} + r^2G^{(2)}, \\
H(x,y,d) &= H^{(0)} + rH^{(1)} + r^2H^{(2)}, \qquad (110)\\
F^{(0)}(x,y,d) &= \frac{8}{d}\{y^2(3-2y) + 6xy(1-y) + 2x^2(3-4y) - 4x^3\} \\
&\quad +8\{-xy(3-y-y^2) - x^2(3-y-4y^2) + 2x^3(1+2y)\} \\
&\quad +2d\{x^2y(6-5y-2y^2) - 2x^3y(4+3y)\} + 2d^2x^3y^2(2+y), \qquad (111)\\
F^{(1)}(x,y,d) &= \frac{32}{d^2}\left\{-\frac{y(3-2y)}{x} - (3-4y) + 2x\right\} \\
&\quad +\frac{8}{d}\{y(6-5y) - 2x(4+y) + 6x^2\} \\
&\quad +8\{x(4-3y+y^2) - 3x^2(1+y)\} + 6dx^2y(2+y), \qquad (112)\\
F^{(2)}(x,y,d) &= \frac{32}{d^2}\left\{\frac{(4-3y)}{x} - 3\right\} + \frac{48y}{d}, \qquad (113)\\
G^{(0)}(x,y,d) &= \frac{8}{d}\{xy(1-2y) + 2x^2(1-3y) - 4x^3\} \\
&\quad +4\{-x^2(2-3y-4y^2) + 2x^3(2+3y)\} - 4dx^3y(2+y), \qquad (114)\\
G^{(1)}(x,y,d) &= \frac{32}{d^2}(-1+2y+2x) + \frac{8}{d}(-xy+6x^2) - 12x^2(2+y), \qquad (115)\\
G^{(2)}(x,y,d) &= -\frac{96}{d^2}, \qquad (116)\\
H^{(0)}(x,y,d) &= \frac{8}{d}\{y^2(1-2y) + xy(1-4y) - 2x^2y\} \\
&\quad +4\{2xy^2(1+y) - x^2y(1-4y) + 2x^3y\} \\
&\quad +2d\{x^2y^2(1-2y) - 4x^3y^2\} + 2d^2x^3y^3, \qquad (117)\\
H^{(1)}(x,y,d) &= \frac{32}{d^2}\left\{-\frac{y(1-2y)}{x} + 2y\right\} \\
&\quad +\frac{8}{d}\{y(2-5y) - xy\} + 4xy(2y-3x) + 6dx^2y^2, \qquad (118)\\
H^{(2)}(x,y,d) &= -\frac{96y}{d^2x} + \frac{48y}{d}. \qquad (119)
\end{aligned}
$$

B Engineering run in 2007

B.1 Overview of 2007 run

Detector and trigger setups and various calibrations (engineering run 2007) started in September in 2007. In December a trigger for $\mu^+ \to e^+\gamma$ was tested for a day and correctly worked with both gamma-ray and positron detectors. Data set taken for the drift chamber are cosmic rays and positrons from Michel decays in positive muon beam, and for the liquid xenon detector LEDs, alpha sources in both liquid and gas phase, cosmic rays, gamma rays with Cockcroft-Walton accelerator, gamma rays from radiative muon decays and two gamma rays in π^0 decay. Coincident events were able to be acquired between the timing counter and the drift chamber and also between the timing counter and the liquid xenon detector. The charge exchange reaction (CEX) run in π^- beam, in other words π^0 run, gives the first performance evaluation of the liquid xenon detector about timing, position and energy near the signal at a certain position of the detector. A successful trigger for the π^0 decay between the anti-tagging NaI detector and the LXe detector enabled it. The engineering run 2007 finished at the end of December which enable us to confirm all setup working, then some upgrades were performed for a next 2008 run.

B.2 The LXe detector status

The gains of PMTs were set to 1.5×10^6 and typical HV was 810 V. There were 17 dead channels out of 846 PMTs, some of that are fixed by changing cables and circuits after 2007 run finished. The liquid phase purifier worked for 205 hours, and the light yield increased by 1.6 times and saturated after 180-hours purification. That brought a longer absorption length from 60 cm to over three meters.

B.3 MEG engineering run in 2007

For two days on 16 and 17 in December the trigger for the $\mu \to e\gamma$ was tested with 4 Hz and 40 MeV lower threshold in the LXe detector.

B.4 π^0 run in 2007

For the first performance evaluation of the LXe detector, the π^0 decay data was taken for three days. The timing and energy resolutions was estimated with a region corresponding to 3×2 PMTs region at the three part of center, central lower and central upstream side on inner face, respectively 765k, 260k and 156k events were taken. Trigger rate was 12 Hz in the energy measurement and 2.5 Hz in the timing measurement. We also measured the position performance by the lead collimator with holes of 5 mm and 10 mm diameter and 18 mm thickness, which was mounted on the LXe detector's vessel at the lower part . During the run the APDs attached on the NaI had no thermal control but the change of the temperature was within a Celsius degree.

C Calibration of the NaI detector

C.1 Gain adjustment of APDs

The gain of the NaI detector is adjusted to detect gamma rays from a π^- beam in an energy region under the 150 MeV. The scintillation light of the NaI(Tl) is detected by an APD and signal charges from it are integrated by a charge amplifier, thus a gamma-ray energy is proportional to an amplitude of the output. All HVs of APDs are determined at 2.6 mV/MeV gain in 2008 and 3.2 mV/MeV in 2009 to be able to measure gamma rays without saturation in a DRS digitizer.

At the same time we can acquire all gains by cosmic rays, which is also used to adjust HV. The peak of cosmic ray is fitted with Landau distribution with an exponential tail as shown in Figure C.1. It is difficult to determine HVs of all APDs with using tens-MeV gamma rays from a target by each crystal because of energy leaks. To use a radio active source is inconvenient to calibrate all at the same time and the measurement of a MeV gamma ray is difficult with the same HV set for tens-MeV because of a noise from APD. Cosmic rays make peaks around 30 MeV and allow the same energy deposit in each crystal without any cut. The energy deposit in the NaI crystal is estimated by MC simulation and no selection for zenith angle is applied to treat all crystals in the same way. However, it should be taken into account that the gain of APD depends on a temperature. To know the gain dependence for HV and temperature, LEDs equipped in the NaIs are useful for a quick calibration. A linearity and a saturation region are measured with changing the width of LED pulse.

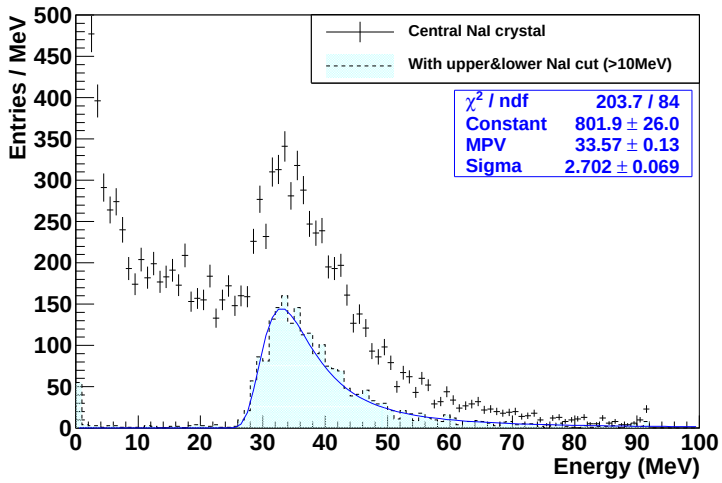

Figure C.1: Energy deposit of cosmic-ray muons in the central NaI crystal. The selection with upper and lower crystal gives a clear Landau peak, although HV is determined by plots distribution to treat all crystals as the same way.

Figure C.2 shows the thermal dependence of APD gains by changing a APD temperature with Peltier devices. The relation in Figure C.2 (a) is measured with LED peaks in a certain APD, which is under a room temperature because only around APD is cooling. Figure C.2 (b) describes relative change of gains in the all nine APDs. The shift of each curve is probably due to a variation of break down voltage that is fluctuated from 400 to

430 V. The temperature of APDs is typically kept at 18 degrees Celsius, while the gain has a 1-2 $\%/^{\circ}C$ dependence. With considering the stability of the thermal system within 0.1% as shown in Figure 3.58, the gain has a good stability under 0.2%.

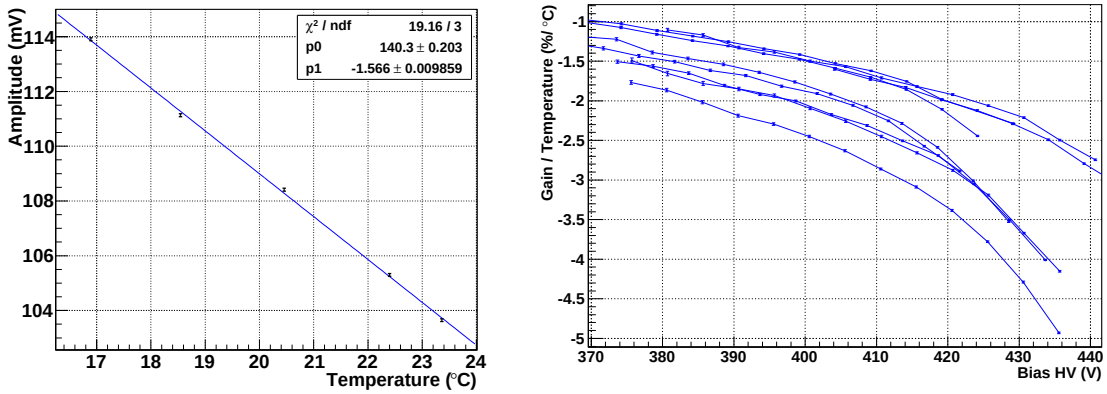

(a) LED peaks and APD temperatures.

(b) Gain shift by a Celsius and biased high voltage of nine APDs.

Figure C.2: Thermal dependence of APD gain measured by LED peaks.

For the HV determination, a constant LED peak is measured with different HVs to know gain-HV dependence quickly. The gain dependence by HV can be given by Equation 120,

$$\text{gain}_{\text{APD}} \propto \frac{1}{1 - \left(\frac{V}{V_{bd}}\right)^{-k}}, \tag{120}$$

where V is a bias voltage, V_{bd} is a break down voltage of APD, and k is determined with a fit. This relative change of LED peaks, as shown in Figure C.3, is scaled by the gain obtained from cosmic rays. The blue horizontal line shows a target gain and a corresponding HV is applied.

C.2 Performance of the NaI detector

The NaI detector measures MeV-scale gamma rays by the total energy deposited in NaI. To make a clear peak, the trigger requires the largest deposit in the central NaI and the reconstruction needs a cut such that a ratio of central NaI to sum of all is larger than 0.6. In 2009 analysis, the position on the NaI was fixed at the center of the detector.

Figure C.4 shows a peak from 17.7, 54.9, 82.9 and 129 MeV gamma rays. The linearity between reconstructed energy and true energy is shown in Figure C.5. There is a deviation of 129 MeV peak from a linear correlation of others, because the energy leak becomes dominant around over hundred-MeV scale which is much higher than critical energy of NaI. However, the response is linear in the interesting range of two gamma-ray region to be tagged in π^0 run.

Figures C.6 and C.7 show the energy resolutions of sigma and FWHM, respectively. The resolution of higher energy region obeys logarithmic function of energy, though leaks are somehow suppressed by the selection of central crystal deposit. An interesting energy

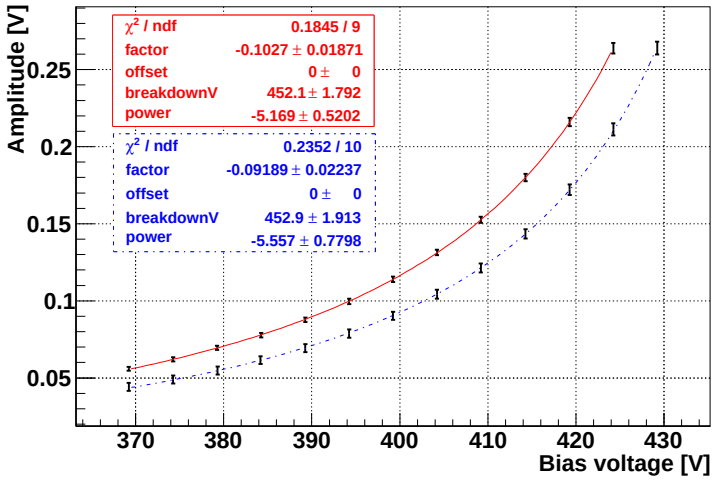

Figure C.3: HV-Gain curve of the central NaI crystal measured by LED peaks. Plots from DRS are fit with a red continuous line, while those from waveform taken in a trigger board with a blue dashed line.

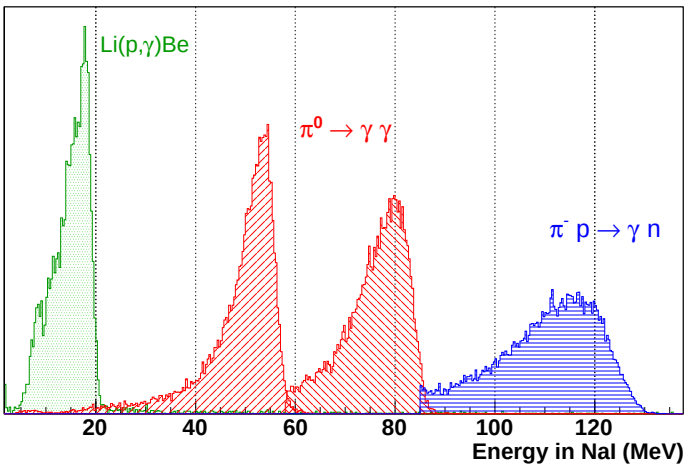

Figure C.4: Energy distribution of the NaI in CW and π^0 run.

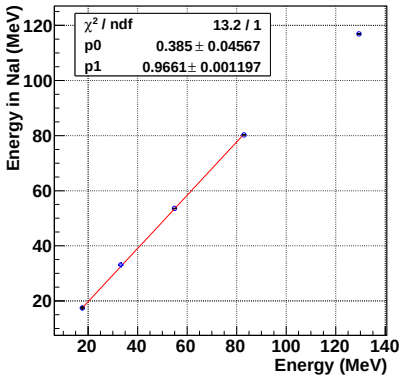

Figure C.5: Energy linearity.

region of two gamma rays from π^0 decay is fit as a continuous line and shows energy resolution as a function of energy in Equation 121,

$$\frac{\sigma_{upper}}{E} = \left(\frac{24.3}{\sqrt{E}} \oplus 0.5\right)\% \ (E < \text{a hundred MeV}), \tag{121}$$

while other dotted lines are obtained by functions with additional logarithmic term for high energy. A MC simulation indicates that the resolution at ten-MeV scale is limited by energy leaks. To achieve more efficient trigger and higher resolution, there is an update plan to replace 4×4 BGO crystals and PMTs instead of 3×3 NaIs and APDs. Thanks to higher stopping power of BGO than NaI, the total size of acceptance is almost the same with better resolution and much shorter length allows a use of PMTs geometrically.

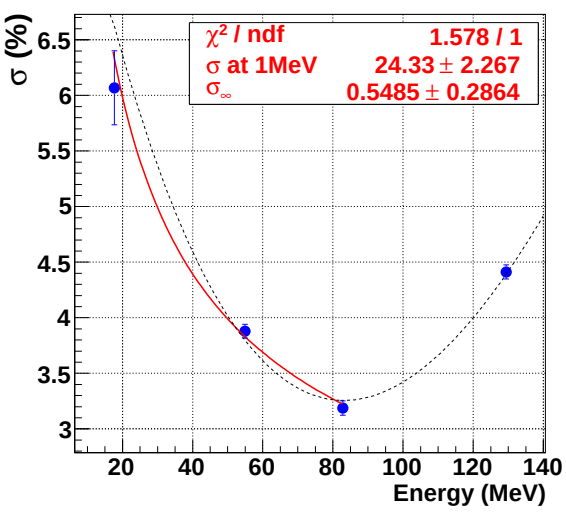

Figure C.6: Energy resolution in σ.

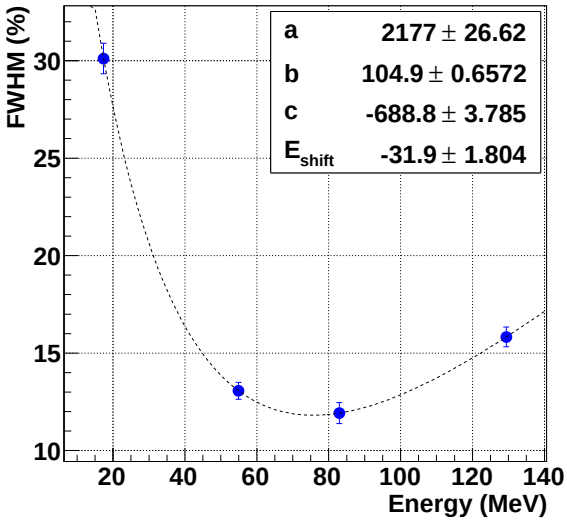

Figure C.7: Energy resolution in FWHM.

C.3 Gain adjustment of pre-shower counter

The magnetic field of the COBRA is symmetric on z axis, though the gain might change at different positions with a rotation of the NaI detector. The gains of four PMTs, attached with two plastic scintillators, are adjusted to have the similar gain. The adjustment is not so severe because a signal should be clear if gamma rays are converted in lead in front of those. Charges in PMTs are used to correct time-walk effect. The triggered events by PMTs for the timing measurement have a worse energy resolution in the NaI due to a large energy deposit in the lead converter, thus the events were not used for the evaluation of energy performance. The gain is adjusted with radio active source such as Sr-90 or cosmic ray.

Acknowledgment

Over the years I have experienced a research in the MEG experiment by a collaboration of the University of Tokyo, KEK, Waseda University, Paul Sherrer Institut, INFN and Pisa, University of Genova, University of Pavia, University Roma Sapienza, University of Lecce, and BINP, Novosibirsk, JINR, Dubna and University of California, Irvine.

I would like to express my great appreciation to my supervisor and also one of spokespersons in the MEG experiment, Prof. Toshinori Mori. He guided me to the world of the particle physics and supported the whole of my study.
I have greatly benefited from Japan Society for the Promotion of Science (JSPS), Japan Student Services Organization and the University of Tokyo. Them financial support made it possible to complete my study.

My first life in Switzerland started in 2005 with a kind help from Dr. Shuei Yamada, Dr. Kenji Ozone and Dr. Yasuko Hisamatsu. They gave me a useful knowledge and a powerful support in my life. I would like to express my special gratitude to Dr. Satoshi Mihara, Dr. Wataru Ootani, Dr. Toshiyuki Iwamoto, Dr. Hajime Nishiguchi and Dr. Ryu Sawada. Through our works I have learnt a lot of skills and close acquaintance from them. Meaningful discussions with Mr. Hiroaki Natori, Dr. Yusuke Uchiyama, Ms. Kinuyo Matsuda, Mr. Daisuke Kaneko, Ms. Xue Bai, Mr. Yuki Fujii and Mr. Teppei Chiba supported my research and they gave me a pleasant time. I want to thank them a lot.

I am deeply grateful to the members of the International Center for Elementary Particle Physics (ICEPP), the MEG collaborator and my friends. Although I could not mention all acknowledgment, my thesis would not be accomplished without any support. Finally, my deepest appreciation goes to my family.

December 2010,
Tokyo

Yasuhiro NISHIMURA

Bibliography

[1] Y. Fukuda *et al.*, "Evidence for Oscillation of Atmospheric Neutrinos", Phys. Rev. Lett. 81, 1562-1567 (1998)

[2] M. Ahmed *et al.*, "Search for the lepton-family-number nonconserving decay $\mu^+ \to e^+\gamma$ ", Phys. Rev. D **65**, 112002 (2002); M. L. Brooks *et al.*, New Limit for the Lepton-Family-Number Nonconserving Decay $\mu^+ \to e^+\gamma$, Phys. Rev. Lett. **83**, 1521-1524 (1999).

[3] T. Mori *et al.*, "Search for $\mu^+ \to e^+\gamma$ down to 10^{-14} branching ratio", Research Proposal to Paul Scherrer Institut, R-99-05 (1999), http://meg.web.psi.ch/docs/prop_psi/index.html/

[4] J. Adam *et al.*, [MEG collaboration], "A limit for the $\mu \to e\gamma$ decay from the MEG experiment", Nucl. Phys. B **834**, 1-12 (2010).

[5] K. S. Hirata *et al.*, "Experimental limits on nucleon lifetime for lepton+meson decay modes", Phys. Lett. B **220**, 308-316 (1989).

[6] J. Hisano, M. Nagai, P. Paradisi, and Y. Shimizu, "Waiting for $\mu \to e\gamma$ from the MEG experiment", Volume 2009, JHEP12, 30 (2009).

[7] Carl H. Albright and Mu-Chun Che, "Lepton flavor violation in predictive supersymmetric GUT models", Phys. Rev. D **77**, 113010 (2008).

[8] C.H. Albright and S.M. Barr, "Realization of the Large Mixing Angle Solar Neutrino Solution in an SO(10) Supersymmetric Grand Unified ", Phys. Rev. D **64**, 073010 (2001).

[9] M.-C. Chen and K.T. Mahanthappa, "Lepton flavor violating decays and soft leptogenesis in a supersymmetric SO(10) model", Phys. Rev. D **70**, 113013 (2004).

[10] Y. Cai and H.-B. Yu, "SO(10) grand unification model with S4 flavor symmetry", Phys. Rev. D **74**, 115005 (2006).

[11] R. Dermisek and S. Raby, "Bi-large neutrino mixing and CP violation in an SO(10) SUSY GUT for fermion masses", Phys. Lett. B **622**, 327 (2005).

[12] W. Grimus and H. Kühbock, "Fermion masses and mixings in a renormalizable $SO(10) \times Z_2$ GUT", Phys. Lett. B **643**, 182 (2006).

[13] P. Depommier *et al.*, "New Limit on the Decay $\mu^+ \to e^+\gamma$ ", Phys. Rev. Lett. **39**, 1113-1116 (1977); G. Azuelos *et al.*, "New Upper Limit on the Decay $\mu \to e\gamma\gamma$", *ibid.* **51**, 164-167 (1983).

[14] A. van der Schaaf *et al.*, "A SEARCH FOR THE DECAY $\mu^+ \to e^+\gamma$ ", Nucl. Phys. **A340**, 249-270 (1980); H. P. Povel *et al.*, "A NEW UPPER LIMIT FOR THE DECAY $\mu^+ \to e^+\gamma$ ", Phys. Lett. B **72**, 183-186 (1977).

[15] W. W. Kinnison *et al.*, "Search for $\mu^+ \to e^+\gamma$ ", Phys. Rev. D **25**, 2846-2868 (1982); J. D. Bowman *et al.*, "Upper Limit for the Decay $\mu^+ \to e^+\gamma$ ", Phys. Rev. Lett. **42**, 556-560 (1979).

[16] R. D. Bolton *et al.*, "Search for rare muon decays with the Crystal Box detector", Phys. Rev. D **38**, 2077-2101 (1988); R. D. Bolton *et al.*, "Search for the Decay $\mu^+ \to e^+\gamma$ ", Phys. Rev. Lett. **56**, 2461-2464 (1986).

[17] T. Kinoshita, A. Sirlin, "Radiative Corrections to Fermi Interactions", Phys. Rev. 113, 1652-1660, (1959).

[18] R. R. Crittenden *et al.*, "Radiative Decay Modes of the Muon", Phys. Rev. **121**, 1823-1832 (1961).

[19] Y. Kuno and Y. Okada, "Muon decay and physics beyond the standard model", Rev. Mod. Phys. **73** 151-202 (2001).

[20] T. Kinoshita and A. Sirlin, "RADIATIVE DECAY OF THE MUON", Phys. Rev. Lett. **2**, 177-178 (1959).

[21] C. Fronsdal and H. Überall, "μ-Meson Decay with Inner Bremsstrahlung", Phys. Rev. **113**, 654-657 (1959).

[22] Y. Kuno and Y. Okada, "Proposed $\mu \to e\gamma$ Search with Polarized Muons", Phys. Rev. Lett. **77**, 434-437 (1996).

[23] Y. Kuno, A. Maki, and Y. Okada, "Background suppression for $\mu \to e\gamma$ with polarized muons", Phys. Rev. D **55**, R2517-R2520 (1997).

[24] W. Wagner *et al.*, "PSI status 2008 - Developments at the 590 MeV proton accelerator facility", Nucl. Instr. Meth. A **600**, 5-7 (2009).

[25] 'The 590 MeV Ring Cyclotron of PSI', http://abe.web.psi.ch/accelerators/ringcyc.php.

[26] W. Ootani *et al.*, "Development of a Thin-wall Superconducting Magnet for the Positron Spectrometer in the MEG Experiment", IEEE Trans. Appl. Superconduct. **14**, 568-571 (2005).

[27] Garfield, Simulation of gaseous detectors, http://garfield.web.cern.ch/garfield/.

[28] H. Nishiguchi, "An Innovative Positron Spectrometer to Search for the Lepton Flavour Violating Muon Decay with a Sensitivity of 10^{-13}", Ph.D. Thesis, the University of Tokyo (2008), http://meg.web.psi.ch/docs/theses/nishiguchi_phd.pdf/.

[29] S. Mihara *et al.*, "Development of a liquid-xenon photon detector - toward the search for a muon rare decay mode at Paul Scherrer Institut", Cryogenics **44** 223-228 (2004).

[30] K. Ozone, "Liquid Xenon Scintillation Detector for the New $\mu \to e\gamma$ Search Experiment", Ph.D. Thesis, the University of Tokyo (2005), http://meg.web.psi.ch/docs/theses/ozoned.pdf/.

[31] Particle Data Group, Review of Particle Physics, http://pdg.lbl.gov/.

[32] D. Lide ed., "CRC Handbook of Chemistry & Physics 2004-2005", Crc Pr. I Llc. (2004).

[33] A.C. H. Hallett, "ARGON, HELIUM AND THE RARE GASES" Vol **I**, Chap IX, Interscience Publishers, Inc., Yew Nork/London (1961).

[34] C. W. Fabjan and F. Gianotti, "Calorimetry for particle physics", Rev. Mod. Phys. **75**, 1243-1286 (2003).

[35] J. Jortner, L. Mever, S. A. Rice, and E. G. Wilson, "Localized Excitations in Condensed Ne, Ar, Kr, and Xe", J. Chem. Phys. **42**, 4250-4253 (1965); N. Schwenter, E.-E. Koch, and J. Jortner, "Electronic Excitations in Condensed Rare Gases", Springer-Verlag, Berlin (1985).

[36] L. M. Barkov, A. A. Grebenuk, N. M. Ryskulov, P. Yu. Stepanov, and S. G. Zverev, "Measurement of the refractive index of liquid xenon for intrinsic scintillation light", Nucl. Instr. Meth. A, **379**, 482-483 (1996).

[37] V. N. Solovov *et al.*, "Measurement of the refractive index and attenuation length of liquid xenon for its scintillation light", Nucl. Instr. Meth. A, **516**, 462-474 (2004).

[38] T. Doke *et al.*, "Absolute Scintillation Yields in Liquid Argon and Xenon for Various Particles", Jpn. J. Appl. Phys. **41**, 1538-1545 (2002).

[39] A. Hitachi *et al.*, "Effect of ionization density on the time dependence of luminescence from liquid argon and xenon", Phys. Rev. B **27**, 5279-5285 (1983).

[40] G. M. Seidel, R. E. Lanou, and W. Yao, "Rayleigh scattering in rare-gas liquids", Nucl. Instr. Meth. A, **489**, 189-194 (2002).

[41] A. Braem *et al.*, "Observation of the UV scintillation light from high energy electron showers in liquid xenon", Nucl. Instr. Meth. A, **320**, 228-237 (1992).

[42] V. Y. Chapel, M. I. Lopes, R. Ferreira Marques, and A.J.P.L. Policarpo, "Purification of liquid xenon and impurity monitoring for a PET detector", Nucl. Instr. Meth. A, **349**, 500-505 (1994).

[43] N. Ishida *et al.*, "Attenuation length measurements of scintillation light in liquid rare gases and their mixtures using an improved reflection suppresser", Nucl. Instr. Meth. A, **384**, 380-386 (1997).

[44] Y. Yoshino *et al.*, "Absorption cross section measurement of water vapor in the wavelength region 120 to 188mm", Chem. Phys. **211** 387 (1996).

[45] A. Baldini *et al.*, "A radioactive point-source lattice for calibrating and monitoring the liquid xenon calorimeter for the MEG experiment", Nucl. Instr. Meth. A, **565**, 589-598 (2006).

[46] T. Haruyama *et al.*, "Development of a high-power coaxial pulse tube refrigerator for a liquid xenon calorimeter", Advances in Cryogenic Engineering **49**, 1459-1466 (2004).

[47] T. Iwamoto *et al.*, "Development of a large volume zero boil-off liquid xenon storage system for muon rare decay experiment (MEG)", Cryogenics **49**, 254-258 (2009).

[48] S. Mihara *et al.*, "Development of a method for liquid xenon purification using a cryogenic centrifugal pump", Cryogenics **46** 688-693 (2006).

[49] Samios, N. P., "Panofsky Ratio", Phys. Rev. Lett. **4**, 470-472 (1960).

[50] J. Spuller *et al.*, "A remeasurement of the Panofsky ratio", Phys. Lett. B **67**, 479-482 (1977).

[51] MIDAS, Maximum Integration Data Acquisition System, https://midas.psi.ch/.

[52] S. Ritt, "The DRS chip: cheap waveform digitizing in the GHz range", Nucl. Instr. Meth. A, **518**, 470-471 (2004); S. Ritt, "Design and Performance of the 5 GHz Waveform Digitizing Chip DRS3", Nucli. Sci. Symmp. Conf. Rec. IEEE **4**, 2485-2488 (2007); S. Ritt *et al.*, "Application of the DRS chip for fast waveform digitizing", Nucl. Instr. Meth. A **623**, 486-488 (2010).

[53] ROME, Root based Object oriented Midas Extension, https://midas.psi.ch/rome/.

[54] GEANT, Detector Description and Simulation Tool version 3.21, http://wwwasd.web.cern.ch/wwwasd/geant/.

[55] R. Sawada, "A Liquid Xenon Scintillation Detector to Search for the Lepton Flavor Violating Muon Decay with a Sensitivity of 10^{-13}", Ph.D. Thesis, the University of Tokyo (2008), http://meg.web.psi.ch/docs/theses/sawada_phd.pdf/.

[56] Y. Uchiyama, "Analysis of the First MEG Physics Data to Search for the Decay $\mu \to e\gamma$", Ph.D. Thesis, the University of Tokyo (2010), http://meg.web.psi.ch/docs/theses/uchiyama_phd.pdf/.

[57] R. E. Kalman, "A New Approach to Linear Filtering and Prediction Problems", Transaction of the AMSE-J. Basic Engineering **D82**, 35-45, (1985).

[58] R. Frühwirth, "APPLICATION OF KALMAN FILTERING TO TRACK AND VERTEX FITTING", Nucl. Instr. Meth. A, **262**, 444-450 (1987).

[59] S. Croft, Nucl. Instr. Meth. A, "The use of neutron intensity calibrated ^{9}Be(α, n) sources as 4438 keV gamma-ray reference standards" , **281**, 103-116, (1989).

[60] M. Morhac *et al.*, "Background elimination methods for multidimensional coincidence gamma-ray spectra.", Nucl. Instr. Meth. A, **401**, 113-132, (1997); M. Morhac *et al.*, "Efficient one- and two-dimensional Gold deconvolution and its application to gamma-ray spectra decomposition.", Nucl. Instr. Meth. A,, **401**, 385-408, (1997); M. Morhac *et al.*, "Identification of peaks in multidimensional coincidence gamma-ray spectra.", Nucl. Instr. Meth. A, **443**, 108-125, (2000).

[61] J. R. Klein and A. Roodman, "Blind Analysis in Nuclear and Particle Physics", Annu. Rev. Nucl. Part. Sci. **55**, 141-163 (2005).

[62] G. J. Feldman and R. D. Cousins, "Unified approach to the classical statistical analysis of small signals", Phys. Rev. D **57**, 3873-3889 (1998).

[63] MINUIT, Function Minimization and Error Analysis, http://lcgapp.cern.ch/project/cls/work-packages/mathlibs/minuit/home.html.